UNIVERSITY OF CALIFORNIA

SANTA BARBARA

Correlating the atomic-level compositions, structures, and reaction properties of Pt-zeolite catalysts

A dissertation submitted in partial satisfaction of the

requirements for the degree Doctor of Philosophy in Chemical Engineering

by

Tsatsral Battsengel

Committee in charge:

Professor Bradley F. Chmelka, Chair

Professor Phillip Christopher

Professor Song-I Han

Professor Eric F. McFarland

Professor Horia Metiu

March 2022

The dissertation of Tsatsral Battsengel is approved.

_____

Phillip Christopher

_____

Song-I Han

_____

Eric F. McFarland

_____

Horia Metiu

_____

Bradley F. Chmelka, Committee Chair

December 2021

Correlating the atomic-level compositions, structures, and reaction properties of Pt-zeolite catalysts

In loving memory of my mom, Enkhbayasgalan Batsukh

Thank you, mama, for everything good that happened in my life

Acknowledgment

I had the most enriching experiences of my life during the past five years in graduate school. “Graduate school is not a sprint, but it is a marathon”. My Ph.D. journey was indeed a marathon filled with numerous challenges, both academic and personal, which made me a better researcher, family member, and friend. I do not believe I could have overcome all these challenges and completed this thesis without the support and guidance of many. First, I would like to express my sincere gratitude to my research advisor Professor Bradley F. Chmelka. Brad, you are one of the most intellectually curious minds I have ever met, and I am so fortunate to call you my Ph.D. advisor. Your constant enthusiasm for research made my graduate school experience more exciting. I learned a lot from your meticulous approach to conducting research, and I will carry the same attitude in my future work. I thank you for providing me the opportunity to closely collaborate with numerous scientists from leading industries, *e.g.*, ExxonMobil, Chevron, and Chevron Phillips. Words cannot describe how much I appreciate your moral support during my grieving times after losing my mom. Thank you for your academic and personal guidance during the most important period of my life.

My gratitude extends to my committee members for their valuable time, advice, and great interest in my research studies. Thank you, Prof. Eric McFarland, for the delightful experience of working as your teaching assistant for the reaction engineering course. Thank you, Prof. Songi Han, for teaching my favorite classes taken at UCSB, *e.g.*, fundamentals of nuclear magnetic resonance and electron paramagnetic resonance, and for the opportunity to work in your lab and learn from your wise postdocs, Dr. Sheetal Jain and Dr. Asif Equibal. Thank you, Prof. Phillip Christopher, for providing me the privilege of working with Dr. Hossein Robatjazi and Prof. Joaquin Resasco. Thank you, Prof. Horia Metiu, for giving me valuable feedback, asking interesting and challenging questions about my projects.

My graduate school experience wouldn't have been as memorable and joyful as it is without the members of the Chmelka group. Especially, I would like to acknowledge

Dr. Zachariah Berkson and Dr. Nathan Prisco for mentoring me at the earlier stage of my research. I appreciate Dr. Matt Idso, Dr. Niels Zussblatt, Shona Becwar, Maxwell Berkow, Mike Schmidhorst, Matt Lertola, Dr. Philipp Selter, Dr. Federica Boscaro for the daily sharing of our research, occasional beach time, and group hangouts. Also, I am forever grateful for making many life-long friends during my residency in Santa Barbara. Beihang Yu, Nick Scherk, Chad Wangsanuwat, and many more friends from all over the world made my journey much more cheerful. I specifically thank my boyfriend, Chad Spensky, for his constant support and for being my best friend and listener.

I was fortunate to collaborate with numerous scientists from several industries for the past four years. It was my great pleasure to work with Dr. Randall Meyer, Dr. Allen Burton, Dr. Robert Carr, Dr. Pedro Serna, and Dr. Mobae Afeworki from ExxonMobil Research and Engineering. Especially, I appreciate Randall and Rob for the opportunity to work with them at Argonne National Laboratory in Illinois. I am grateful for my collaboration with the Chevron Phillips R&D team, Dr. Joseph Bergmeister, Dr. Gabriella Alvez-Manoli, Dr. Sikander Hakim, Dr. Steven Kim, Dr. Masud Monwar, Dr. Cori Demmelmaier. Particularly, I am thankful for the experience of visiting the Chevron Phillips research facility in Texas and having productive discussions with the team. I would also like to thank my collaborators from Chevron Energy and Technology company, Dr. Stacey Zones and Dr. Michael Girgis. I appreciate Stacey for not only his academic and career guidance but also his support and much-appreciated parent-like advice when I was overwhelmed with taking care of my 10-year-old brother and finishing my Ph.D. after the passing of my mom. Thank you, Stacey, I am extremely lucky to have you as my collaborator and mentor. My research endeavors have enormously benefited from collaborating with and learning from world experts in various scientific fields. I thank Dr. Lynne McCusker and Dr. Christian Baerlocher from ETH Zurich for interesting discussions about zeolite structures during their visit to UCSB. I appreciate Dr. Zhehong Gan, Dr. Ivan Hung, Dr. Joanna Paulino from the National High Magnetic Field Laboratory in Florida for hosting and mentoring me when I visited to use the high-field nuclear magnetic resonance spectroscopy

instruments. I appreciate Prof. Aaron Rossini and his talented students Dr. Amrit Venkatesh, Benjamin Atterberry, and Scott Carnahan from Iowa State University for our collaboration on indirect detection of ^{195}Pt in Pt-zeolite catalysts.

I spent a great deal of my graduate school period in the laboratories of the UCSB shared facilities. My research efforts came into fruition thanks to the top-notch maintenance and modification of state-of-the-art instruments by the spectroscopy facility members, Dr. Jerry Hu, Jaya Nolt, and Shamon Walker. I also thank Dr. Amanda Strom from the TEMPO facility and Dr. Youli Li from the X-ray diffraction facility of the Materials Research Laboratory at UCSB. I found my growing interest in science and engineering thanks to my high school teachers in Mongolia, Zurgaanjin and Buyandelger, Batchimeg Bold, Khosbayar Tsogvoo, and Batkhishig Jamts. Thank you for helping me build strong fundamental knowledge and skills that enabled me to attend world-class higher education institutes. I also thank my undergraduate mentors from the University of Michigan, Prof. Suljo Linic, Prof. Timothy Scott, and Dr. Scott Zavada for their valuable mentoring time and encouragement to obtain a graduate degree. My heartful gratitude extends to my late college friend and a fellow talented chemical engineer, Wei Tan, who shared her last few months of her life with me in Santa Barbara. I am forever thankful for her friendship and inspiration to keep exploring and traveling around this beautiful world.

I present my warmest gratitude to my parents. Thank you for providing me the fortune of being a big sister of two wonderful brothers, Batbayar and Bat-Enkh Battsengel. Thank you, Baaduu and Borko, for bringing me so much joy and support throughout my graduate school. Finally and most importantly, my heartfelt gratitude goes to my mom, who dedicated her entire life to making me who I am today. Although lung cancer has taken my mother away from me just a couple of months before my graduation, her wisdom continues to exist within me. One of the proofs of her continuation is this dissertation, and undoubtedly many more beautiful adventures of my life to come…

Tsatsral Battsengel, Santa Barbara, California, October 2021

Curriculum Vitae of Tsatsral Battsengel

EDUCATION

Ph.D. Chemical Engineering, University of California Santa Barbara, Dec 2021
Advisor: Bradley F. Chmelka

B.S. Chemical Engineering, University of Michigan, Ann Arbor, May 2016
Summa cum laude*,* minor in environmental engineering*,* College of Engineering Honors

PUBLICATIONS

- **Battsengel, T**., Meyer, R., Burton, A., Carr, R., Serna, P., Afeworki, M., Chmelka, B., Atomic-scale structures, framework interactions, and locations of Pt species in NaY-zeolite, *Journal of American Chemical Society*, pending submission
- **Battsengel, T**., Berkson, Z., Bergmeister, J., Alvez-Manoli, G., Hakim, S., Lim, S., Monwar, M., Cori Demmelmaier, C., Chmelka, B., Correlating the Atomic-Level Compositions, Structures, and Aromatization Properties of Pt-KL Zeolite Catalysts*, ACS Catalysis*, pending submission
- **Battsengel, T**., Girgis, M., Zones, S., Chmelka, B., Atomic-scale structures & hydroisomerization properties of bifunctional Pt-H^+USY zeolite catalysts, to be submitted
- Robatjazi, H., **Battsengel**, **T**., Finzel, J., Tieu, P., Xu, M., Hoffman, A., Qi, J., Chmelka, B., Bare, S., Pan, X., Halas, N., Christopher, P., Dynamic behavior of Al native oxide-supported metal catalysts: exposing uniform atomically dispersed species via strong metal-support interactions, submitted
- Zavada, S. R., **Battsengel, T**., Scott, T. F. Radical-Mediated Enzymatic Polymerizations. *Int. J. Mol. Sci*., **2016**, 17, 195

RESEARCH EXPERIENCE

- Graduate student researchers, UCSB Santa Barbara, CA, Jan 2017 - Present Experienced in leading research projects by designing & conducting hypotheses driven experiments, analyzing data, and communicating findings by written reports and presentations
- Visiting researcher, Argonne National Laboratory Chicago, IL, April 2019 Conducted X-ray absorption measurements on Pt-NaY zeolites with Dr. Randall Meyer from ExxonMobil Research & Engineering

- Visiting researcher, Chevron Phillips Chemical Company Kingwood, TX
  Oct. 2018

  Presented project update to the researchers, discussed & planned future direction of the project focused on understanding the effects of fluorine promoters on Pt-KL aromatization catalysts
- Visiting researcher, National High Magnetic Field Laboratory Tallahassee, FL
  June & Sep 2018

  Selected as one of five young scholars to get trained & conduct experiments on the world's highest magnetic field (36 T) for NMR on zeolite materials
- Undergraduate research assistant, U of Michigan Ann Arbor, MI 2013-2016
  Optimized synthesis process of plasmonic Ag-Pt core-shell nanoparticle catalysts in Prof. Linic's lab Experienced in radical-mediated polymer synthesis in Prof. Scott's lab, which led to a publication

TECHNICAL SKILLS

- Solid-state NMR techniques, including two-dimensional correlation experiments & dynamic nuclear polarization NMR methods to identify atomic-scale structures of heterogeneous materials
- Hydrothermal zeolite synthesis & preparation of Pt-zeolite catalyst materials
- Fundamental catalyst characterization methods, *e.g.*, electron paramagnetic resonance spectroscopy, X-ray diffraction, thermogravimetric analyses, electron microscopy, and X-ray absorption spectroscopy

LEADERSHIP

- Graduate student recruiting leader, department of chemical engineering 2019

  Organized research & social activities for 58 prospective students & successfully recruited 18 incoming Ph.D. students for the class of 2020, which led to the ChemE department distinguished service award
- Professional development co-chair, chemical engineering graduate student association 2018-19

  Organized professional development events including research poster fair for undergraduate chemical engineers, planned & hosted inaugural graduate student invited speaker events

  Found chemical engineering seminar series presented by ChemE graduate students & postdocs

- Co-founder of Mongolian Cultural Organization at the University of Michigan, which is now expanded to U.S. nationwide network led by Mongolian students 2012-Present

SELECTED CONFERENCE & SEMINAR PRESENTATIONS

- Annual American Institute of Chemical Engineering Meeting: Invited speaker, Boston, MA, Nov. 2021
  Advances in zeolite science and technology symposium organized by Dr. Stacey Zones, Chevron
  "Atomic-scale structures & hydroisomerization properties of bifunctional Pt-H^+USY zeolite catalysts"
- Chevron R&D seminar series: Speaker April 2021
  "Nanoscale structures and macroscopic properties of platinum-zeolite catalysts"
- Annual American Institute of Chemical Engineering Meeting: Invited speaker, Nov. 2020
  Advances in zeolite science and technology symposium organized by Dr. Stacey Zones, Chevron
  "Understanding atomic-scale compositions, structures, and properties of Pt-zeolite catalysts"
- International Catalysis Conference 2020: Speaker San Diego, CA, June 2020
  "Correlating atomic-level compositions, structures, and aromatization properties of Pt-KL catalysts"
- Annual American Institute of Chemical Engineering Meeting: Speaker Orlando, FL, Nov. 2019
  "Correlating treatment conditions and atomic-scale environments of Pt supported on NaY zeolite"
- 60th Experimental NMR Conference: Poster Asilomar, CA April 2019
  "Atomic-level insights into zeolite-supported Pt metal catalysts obtained by multinuclear solid-state NMR"
- Materials Research Outreach Program: Poster UCSB, CA, Jan. 2019
  "Physical distribution of Pt nanoparticles supported on NaY-zeolite directly related to calcination processes"
- BigMag workshop: Poster UCSB, CA, May 2018
  "Opportunities for high-field NMR and DNP for elucidating surface and heteroatom environments in complex heterogeneous materials"

- Amgen-Clorox Chemical Engineering Graduate Symposium: Poster
  UCSB, CA, Oct. 2017
  "Correlated compositions, nanoscale structures, and activities of heterogeneous platinum-zeolite catalysts"
- Chemical Engineering First-year Graduate Student Symposium: Poster
  UCSB, CA, Sep. 2017
  "Correlations of compositions, nanoscale structures, and activities of platinum-zeolite catalysts"
- Bi-monthly research update teleconference presentations:
  ExxonMobil Research and Engineering – Dec. 2018 – July 2019
  Chevron-Phillips Chemical Company – Oct. 2018 – Dec. 2020
  Chevron Energy Technology Company – Jan. 2021 – Dec. 2021

TEACHING EXPERIENCES

- Teaching assistant UCSB, CA, Spring 2020, Winter 2019, Winter 2018
  Reaction kinetics & Thermodynamics
- Instructional assistant U of Michigan, MI, 2015 & 2016
  Fluid mechanics & Introduction to material and energy balance

Abstract

Correlating the atomic-level compositions, structures,
and reaction properties of Pt-zeolite catalysts

by

Tsatsral Battsengel

Heterogeneous catalysts are used for approximately 80% of the chemical catalysts used in the world, among which metal supported on zeolite catalysts are particularly versatile and widely used in chemical industries. The reaction properties of these catalysts depend strongly on the compositions and nanoscale architectures of the zeolite support, as well as the types and locations of metal species within the zeolite pores, which are influenced by the catalyst synthesis and treatment conditions. Understanding the atomic-scale structures of metal-zeolite systems is crucial to the development of strategies to control metal dispersion and thereby improve catalyst performance. However, these types of catalysts are complex and challenging to understand on the atomic scale, because of the presence of broad distributions of chemical environments. Here, solid-state nuclear magnetic resonance (ssNMR) methods are used to elucidate atomic-scale structures of various types of metal-zeolite materials. The results and analyses are complemented by analyses of other powerful techniques, such as electron paramagnetic resonance, extended X-ray

absorption fine structures, X-ray diffraction, and high-resolution transmission electron microscopy.

Detailed understandings of atomic structures of various metal-zeolite systems are obtained by advanced ssNMR methods, with a focus on industrially significant platinum supported on zeolites, *e.g.*, bifunctional Pt on H^+USY zeolite catalyst used for hydroisomerization and Pt on F-KL zeolite catalyst used for the aromatization of straight *n*-hexane. For example, two-dimensional (2D) solid-state NMR techniques are used to identify covalent bonding environments of ^{27}Al and ^{29}Si sites of the zeolite and to reveal interactions between dilute promoter species and zeolite support sites. High external magnetic field (up to 35.2 T) and fast magic angle spinning (up to 55 kHz MAS) methods are used to obtain well-resolved NMR spectra which enabled to elucidate distinct chemical environments present in various zeolite catalysts. Ultrawideline ^{195}Pt NMR experiments are also implemented on high loading Pt supported on zeolite materials to identify types and distributions of ^{195}Pt moieties. Moreover, recent advancements in NMR instrumentation enabled to conduct *in-situ* variable temperature and pressure (up to 200 bar & 240 ^{o}C) ^{13}C and ^{1}H MAS NMR measurements, which provide opportunities to identify types of reactants and products under reaction conditions. The methods, analyses, and results discussed in this thesis are expected to be of broad importance in understanding correlations between reaction properties and atomic-scale structures of industrially significant zeolite catalysts.

List of Figures

List of Tables

Table of Contents

CHAPTER 1

1. Introduction and background

1.1 Motivation and objectives

Catalysis has a significant role in today's world; it is involved in energy conversion applications and various chemical manufacturing processes including petrochemical, polymer, food, and pharmaceutical industries. Several major inventions that revolutionized these industries by enabling more sustainable pathways of chemical conversions are the Haber-Bosch process of ammonia synthesis[1] from molecular nitrogen and hydrogen using an iron catalyst, the Houdry process of cracking of heavier petroleum[2] using solid-acid aluminosilicates, and the Fischer-Tropsch process[3] of forming hydrocarbons and oxygenated compounds from CO and H_2 over alkalized iron catalysts. The importance of the field of catalysis has been well documented in the history of the Nobel Prize. As of 2021, the groundbreaking inventions of 23 out of 187 Nobel Laureates were directly related to catalysis.[4,5] Thanks to these discoveries, the use, and importance of catalysts have only been increasing. Approximately 80% of the chemical catalysts used in the world are heterogeneous catalysts,[6] of which supported metal-zeolite catalysts are particularly versatile and widely used in chemical industries.[7–21]

These types of metal-zeolite catalysts are complex and challenging to understand on the atomic scale, because the overall catalytic performance of supported metal catalysts depends on various factors, including the types of support and metals. Moreover, within a metal particle, many different sites can participate in the reaction, thus adding more complexity to the understanding of these catalysts. It is of great

interest for both industrial and fundamental research to obtain atomic-scale insights about supported metal catalysts, a central theme in the science of heterogeneous catalysis, to guide the design of catalysts with improved performances. This doctoral dissertation work focused on investigating how catalytic properties of metal-zeolite catalysts, specifically focused on Pt-zeolite catalysts, are governed by atomic-scale structures and chemical compositions of the catalysts.

1.2 Heterogeneous zeolite catalysts

A catalyst is a substance that influences the rate of a chemical reaction by changing its reaction pathway without itself being consumed and without changing the equilibrium of the reaction. Heterogeneous catalysts are widely used in industries, because of their reusability and easy separation from the products. More than 40% of the heterogeneous catalysts used today in chemical industries are zeolites.[22] Zeolites are porous crystalline aluminosilicates, and their high internal surface-areas and shape-selective cages make them attractive as heterogeneous catalysts and as supports for metal ions and nanoparticles. Zeolite structures are composed of tetrahedral Si and Al bonded through bridging oxygen atoms. The Trivalent Al atom bonded to four oxygen atoms possesses a negative charge, which is balanced by extraframework cations such as H^+, Na^+, and K^+.[23–26] The porous character and adsorption capacity of aluminosilicate zeolites makes them extremely hydrophilic. The term “zeolite” is based on the Greek words for “to boil” and “stone”. The Swedish mineralogist A.F. Cronstedt observed the formation of a large amount of steam when heating the mineral, and named it zeolite.[27] Since the discovery of the natural zeolites

and finding of the importance in the application of catalysis, ion exchange, and gas separation, the quest to discover new types of synthetic zeolites has been strongly continuing.[28–45]Currently, there are over 240 different zeolite frameworks have been identified by the International Zeolite Association.[46] However, only about 17 are of commercial interest and produced synthetically**.**[47–49] In this dissertation, three of the most commonly used zeolite structures are studied: FAU, LTL, and CHA.

For zeolite catalysts, the shape selectivity of the structure plays a crucial role. Geometric shape constraints of the pores of the zeolite can influence the reactant, product, or transition states, hence directly affecting the overall selectivity. Firstly, the reactant shape selectivity arises when the difference in reactivity between competing reactants is caused by their different accessibility of the internal active sites of the zeolite. The reaction only proceeds when the molecule is small enough to enter the pore of the zeolite, while the bulkier molecules bypass the zeolite pores as illustrated in **Figure 1.1**. [50]

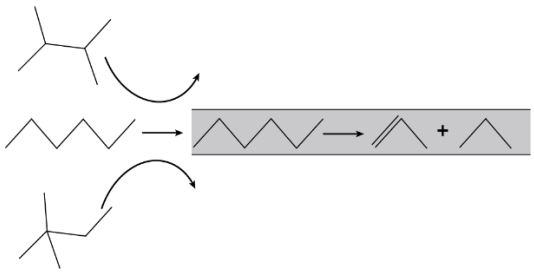

Figure 1.1. Schematic diagrams illustrating reactant shape selectivity of zeolites

Secondly, the product shape selectivity arises when the reactants are small enough to diffuse through the channels of the zeolite, but only the product molecules that are small enough can diffuse out of the zeolite pore as shown in **Figure 1.2**.[51]

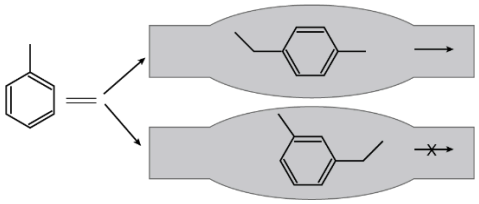

Figure 1.2. Schematic diagrams illustrating product shape selectivity of zeolites

Lastly, the transition state shape selectivity refers to the situation where the constraints of the size of the zeolite cage hamper the formation of transition states that are too bulky to be encaged in the pores as illustrated in **Figure 1.3**.[52]

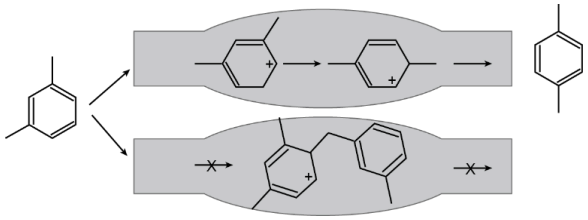

Figure 1.3. Schematic diagrams illustrating transition state shape selectivity

When small nanoparticles or single atoms of Pt are supported on zeolites, a broad variety of the combination of the pore structure and various possibilities of locations of Pt within the zeolite pore result in Pt-zeolite systems capable of catalyzing various types of reactions. Pt-zeolite catalysts are widely used for chemical conversions, including hydrocarbon cracking, reforming, and selective reduction of nitrogen oxides.[20,53–56] The reaction properties of Pt-zeolite catalysts depend strongly on the compositions and nanoscale architectures of the zeolite framework, as well as the types and locations of Pt species within the zeolite nanopores, which are influenced by catalyst synthesis and treatment conditions. Understanding the atomic-scale structures of Pt-zeolite systems is crucial to the development of strategies to improve and prolong catalyst activity and to reduce the amount of Pt required. Detailed

understanding of Pt environments in zeolite catalysts has till now been very limited, due in part to the broad distributions of local Pt environments, both within nanoscale clusters and due to diverse interactions near different framework sites, exchangeable cations, or adsorbed species. To overcome these challenges, powerful solid-state nuclear magnetic resonance (NMR) techniques, in combination with electron paramagnetic resonance (EPR), X-ray powder diffraction (XRD), extended X-ray absorption fine structure (EXAFS), scanning and transmission electron microscopy (SEM and TEM), thermogravimetric analyses (TGA), to obtain detailed insights on the locations and interactions of Pt species, as functions of treatment conditions.

Correlations between reaction properties and atomic-scale structures of various types of industrially significant zeolite catalysts, with a specific focus on Pt-supported zeolites, are investigated in this dissertation work. Chapter 2 discussed the effects of calcination temperatures on the types and locations of Pt moieties and their effects on the zeolite sites of support NaY zeolite. Chapter 3 revealed the atomic-scale structural changes of Pt/KL aromatization catalyst upon dilute fluorination. The specific types of fluorine species attached to the framework zeolite sites are unambiguously revealed and proposed to have promoting effects on *n*-hexane aromatization properties. Chapter 4 investigated structural differences in two types of bifunctional Pt-H^+USY catalysts used for *n*-hexadecane hydroisomerization. Different isomerization activities exhibited by two types of Pt-H^+USY are found to be due to the differences in the amount of siliceous disordered moieties in USY zeolites. Chapter 5 studied distributions of Al sitings in small pore CHA zeolites synthesized in different gel mediums. The effects of zeolite crystallization medium, *e.g.*, presence of structure-

directing agent and cations, are found to directly influence the distributions of Al sites in CHA zeolite despite keeping the bulk Si/Al ratio. In Chapter 6, different coordinations of Cu^{2+} in deNOx catalyst Cu-CHA zeolite are revealed by extensive analyses of EPR methods. Notably, EPR methods revealed two types of Cu coordination and dimers of Cu species, which are all crucial for understanding the catalytic activities of Cu-sites. The atomic-level structural information of various zeolite systems presented in this dissertation provides information that is crucial to the development of synthesis protocols to optimize treatment conditions, which can ultimately lead to the design of zeolite catalysts with higher performances.

1.3 Characterization of Pt-zeolite catalysts

Oftentimes, a combination of different characterization methods is used to obtain a structure-function correlation of various zeolite catalyst systems. These include sorption measurements (pore size and accessibility), solid-state NMR (short-range order and connectivity), electron microscopy, and powder diffraction methods (long-range periodicity, crystallinity).[11,32,34,57–60] In this dissertation, results and analyses of solid-state NMR methods are complemented by various other advanced methods, such as X-ray diffraction, synchrotron X-ray absorption, and high-resolution TEM methods to probe different length scales and chemical environments as illustrated in **Figure 1.4.**

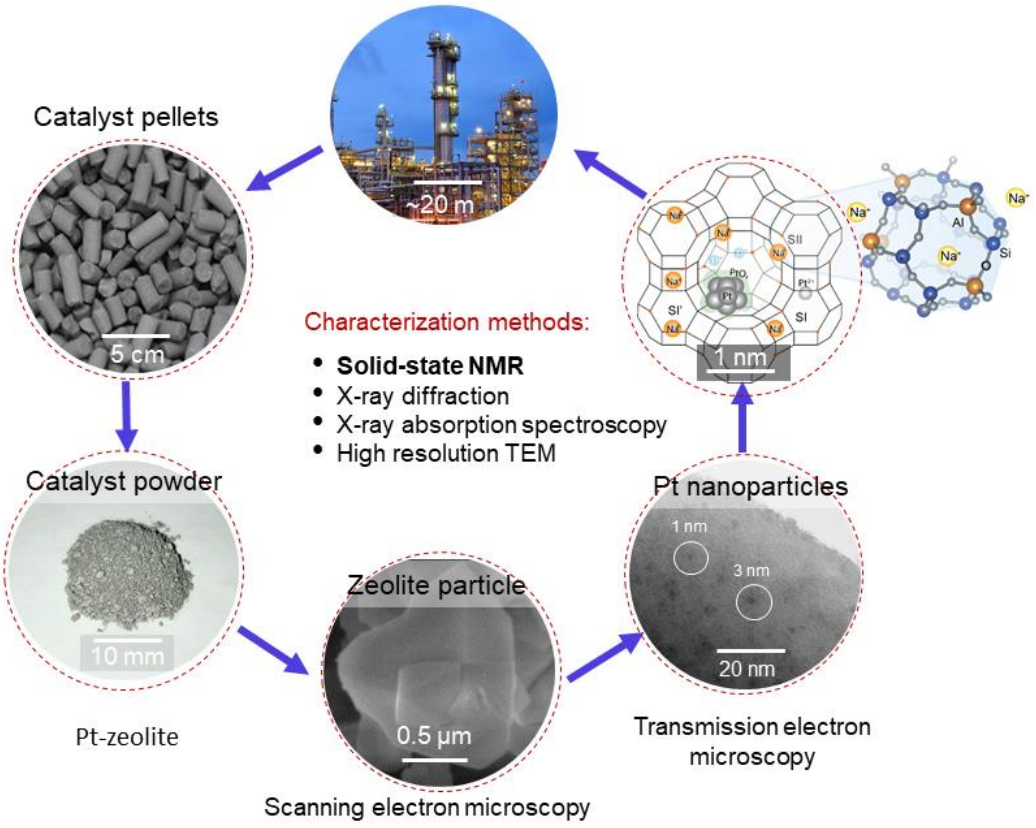

Figure 1.4. Characterization methods used to obtain a structure-function correlation of Pt-zeolite catalysts

Solid-state Nuclear Magnetic Resonance methods

NMR spectroscopy is a powerful technique for obtaining atomic-level structural information of zeolite materials.[10,14,61–83] The theory of NMR can be explained by rigorous quantum mechanics of nuclear-spin angular momentum, which is characterized by nuclear-spin-quantum-number *I*. Nuclei with non-zero spin quantum numbers ($I \neq 0$) are called NMR active because they have nuclear magnetic moments, $\boldsymbol{\mu}$, and can be studied by NMR. Nuclear magnetic moments are characterized by a magnetic quantum number, *m*, which has $2I+1$ possible values. When there is no external magnetic field, the $2I+1$ number of states are degenerates. In the presence

of a magnetic field, the states have different energy levels. The splitting between nuclear spin levels is called Zeeman splitting, which is very small energy compared to thermal energy. The population difference between the states is very small, and the fraction of the population at state *m* is defined by the Boltzman distribution.

$$\frac{N_m}{N} = \frac{e^{\frac{m\hbar\gamma B_0}{k_B T}}}{\sum_m e^{\frac{m\hbar\gamma B_0}{k_B T}}} \approx \frac{\left(1 + \frac{m\hbar\gamma B_0}{k_B T}\right)}{\sum_m \left(1 + \frac{m\hbar\gamma B_0}{k_B T}\right)} \approx \frac{1}{2I+1}\left(1 + \frac{m\hbar\gamma B_0}{k_B T}\right)$$

N_m is the number of nuclei in the m^{th} state, N is the total number of nuclei in all states. By applying the Taylor series at high-temperature approximation, the population ratio simplifies to become a linear function of an applied external field, an inverse function of absolute temperature.[84] At equilibrium, the different energy states are unequally populated, because populations of lower energy are slightly higher than other energy levels. For example, for ^{1}H (I = ½) at T = 293 K when external field B_0 = 9.4 T, fraction of population at m = ½ state is 0.500016, which means only 16 spins are contributing to the bulk magnetization in one million spins. Therefore, NMR spectroscopy has inherently very low sensitivity, and this is the main reason many researchers put a lot of effort to construct an NMR instrument with the highest field possible. Currently, the highest magnetic field available for NMR measurement is 35.2 T, and the instrument is located in the National High Magnetic Field Laboratory, Tallahassee, FL.[85] Several major NMR results of this dissertation work have utilized the 35.2 T magnets, and the high field enabled to obtain unprecedented spectral resolution which lead to more straightforward and unambiguous structural analyses of zeolite systems.

Nothing interesting will happen if the spins are just sitting in the magnet since the net magnetization will be equilibrated at thermal equilibrium. Therefore, short radiofrequency pulses are applied to perturb the thermal equilibrium, and the NMR signal is acquired during the time the perturbed bulk magnetization relaxes back to its thermal equilibrium. As an example, 90^{o} single-pulse and ^{29}Si spectrum of KL zeolite are shown in **Figure 1.5**. The aligned bulk magnetization of ^{29}Si nuclei to the external magnetic field represented by the red arrow is tilted to the transverse plane upon application of the rectangular 90^{o} pulse. While the bulk magnetization precesses back to its thermal equilibrium, transverse magnetization is detected as a free induction (FID) decay in the time domain. ^{29}Si NMR spectrum is plotted by taking Fourier Transform of the FID, which shows signal intensities at -96, -102, and -108 ppm (normalized frequency unit Hz/MHz). Each signal arises from ^{29}Si moieties with different numbers of Al neighbors Pulse sequences can be designed to selectively measure or remove certain interactions, or correlate different spin systems, which will be shown in the following discussions about two-dimensional NMR.

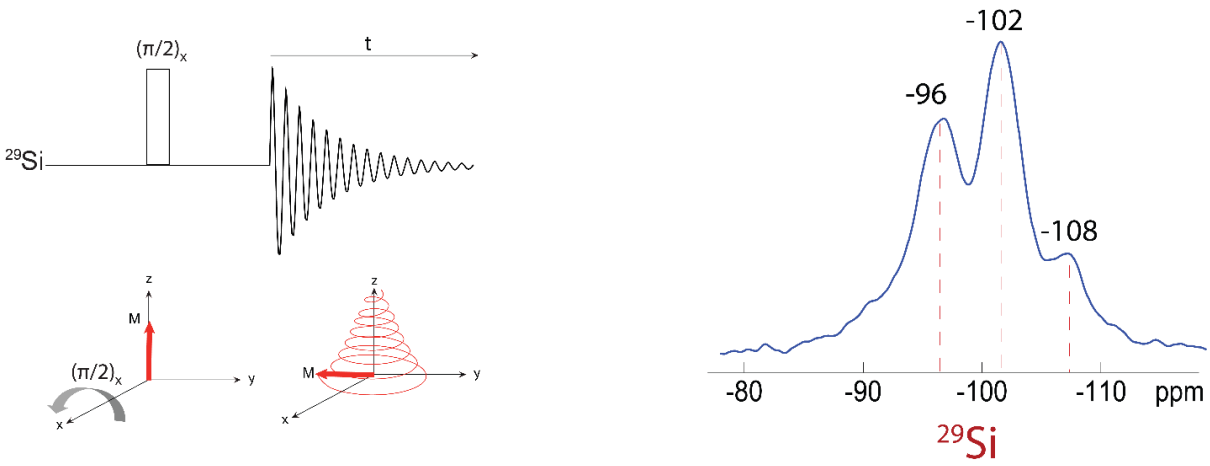

Figure 1.5. 90º Single-pulse and free induction decay, corresponding visualization of bulk magnetization below

Two-dimensional NMR

One of the highlights of NMR spectroscopy is its ability to correlate homo- and heteronuclear spin systems by two-dimensional (2D) NMR,[86] which has made a tremendous impact on systems that can be studied. In one dimensional NMR, the intensity of each peak is plotted as a function of frequency. In 2D NMR, each peak has two frequency coordinates and amplitudes, which is shown as a contour plot. Two-dimensional correlation NMR experiments have the general pulse sequence shown in **Figure 1.6a**. It starts with preparing spins to evolve in t_1, during which no observation is made. Multiple quantum excitations, which contain information about correlated spin systems, are allowed during t_1 since there is no need to have an observable signal during this evolution time. Then, the crucial step of transferring magnetization into observable coherence is implemented by applying radio-frequency pulses called mixing or sometimes refocusing pulses. Finally, the signal has to be observable free induction decay for normal detection time t_2. The two time-domains, t_1 and t_2, are

transformed into two frequency axes after Fourier transform. For example, solid-state 2D ^{27}Al{^{29}Si} *J*-mediated correlational spectrum of dehydrated KL zeolite is shown in **Figure 1.6b**. ^{27}Al and ^{29}Si moieties interacting through covalent bonds, *i.e.*, ^{27}Al-O-^{29}Si, give rise to correlated signal intensities

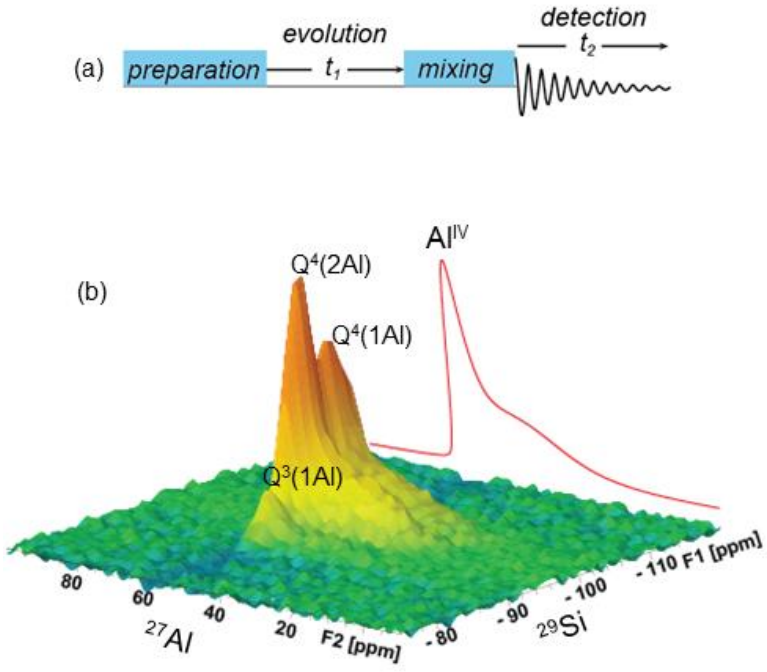

Figure 1.6. Two-dimensional NMR (a) pulse program, (b) 2D ^{27}Al{^{29}Si} *J*-HMQC spectrum of KL zeolite

There are various types of advanced pulse sequences for 2D NMR to provoke different interactions, such as dipolar and scalar, present in the spin systems of interest. The goal of any pulse sequence is to selectively keep a specific coherence transfer pathway and remove the unwanted ones. For example, one of the commonly used 2D NMR methods in this dissertation is dipolar- and *J*-mediated heteronuclear multiple quantum coherence (HMQC) experiments. The heteronuclear correlation experiment is first developed by Muller et. al.,[87] and later Bax[88] popularized the pulse

sequence known as HMQC, which has the pulse sequence shown in **Figure 1.7**. The HMQC pulse sequence starts with a 90° pulse on the *I* spin followed by τ delay. For *J*-mediated experiment, τ = 1/2J_{IS}, where J_{IS} is *J*-coupling strength between spin *I* and *S*. At the end of the delay, in-phase I magnetization is converted to antiphase $2I_YS_Z$ magnetization. A 90° pulse on the S spin converts this antiphase term into a zero- and double-quantum coherence. $2I_YS_X$, which evolve during the t_1 period. Centrally placed 180° pulse on I spin selectively refocuses the I spin evolution, leaving the coherence of S spin labeled. The second 90° pulse on the *S* spin changes the multiple quantum coherence to observable antiphase *I* spin magnetization. Finally, the second τ delay converts the antiphase term into an in-phase term before acquisition in time domain t_2. [89]

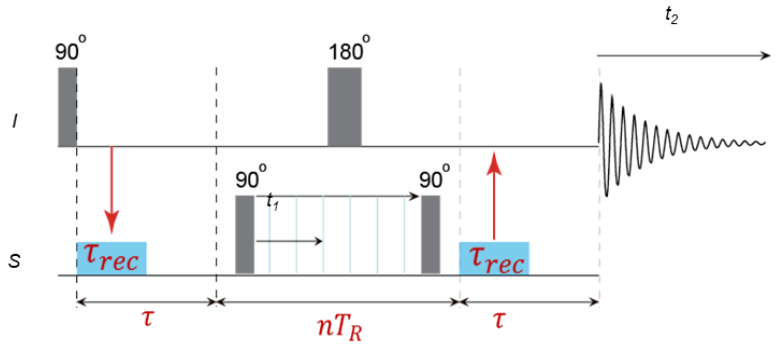

Figure 1.7. Dipolar-mediated HMQC pulse sequence. *J*-mediated HMQC experiment has the same pulse sequence, except the two recoupling pulses noted as τ_{rec} in the blue rectangle is not present.

Fast-MAS

In low viscosity liquids, molecules change orientations faster than the timescales of the anisotropic interactions, thus averaging out these interactions and resulting in a high-resolution NMR signal in the solution state. However, in solids, such rapid

molecular tumbling motion does not exist, and the resulting NMR signals are poorly resolved broad peaks, in which anisotropic interactions contribute significantly. Spinning the sample at a 54.7° angle concerning the applied magnetic field, also known as the Magic Angle Spinning (MAS), partially averages out these anisotropic interactions. The total Hamiltonian of an ensemble of spin *I* is expressed as:

$$\mathcal{H} \approx -\omega_0 I_z + \omega_\lambda \boldsymbol{d}_{\mathbf{0,0}}^{(\mathbf{0})}(\boldsymbol{\theta}) T_{0,0}^{\lambda} D_{0,0}^{(0)}(\Omega_{PAS}) \rho_{0,0}^{\lambda} + \omega_\lambda \boldsymbol{d}_{\mathbf{0,0}}^{(\mathbf{2})}(\boldsymbol{\theta}) T_{2,0}^{\lambda} \sum_{p=-2}^{2} D_{p,0}^{(2)}(\Omega_{PAS}) \rho_{2,p}^{\lambda}$$

The first term arises due to Zeeman interaction. The second and third term encompasses the isotropic and anisotropic internal interactions, respectively. (See reference for further detailed discussions) The bolded terms are spherical harmonics, and they express the angular dependence of the effective Hamiltonian. These terms vary as Legendre polynomials in cos θ.

$$d_{0,0}^{(0)}(\theta) = P_0(\cos\theta) = 1$$

$$d_{0,0}^{(2)}(\theta) = P_2(\cos\theta) = \frac{1}{2}(3\cos^2\theta - 1)$$

The root of the second-order Legendre polynomial is 54.7°, which zeros the anisotropic terms in the spin Hamiltonian. When anisotropic interaction is strong, such as ^{19}F-^{19}F dipolar interaction in the fluorine promoted Pt/KL catalyst, spinning at low speed (10-20 kHz) is not enough to obtain well-resolved spectra. Therefore, to suppress the strong dipolar spin interactions, ^{19}F measurements in this dissertation are conducted at a fast MAS rate of up to 55 kHz.

References

(1) Kandemir, T.; Schuster, M. E.; Senyshyn, A.; Behrens, M.; Schlögl, R. The Haber-Bosch Process Revisited: On the Real Structure and Stability of “Ammonia Iron” under Working Conditions. Angewandte Chemie - International Edition 2013, 52, 12723–12726.

(2) The Houdry Process. American Chemical Society, National Historic Chemical Landmark; 1996.

(3) Schulz, H. Short History and Present Trends of Fischer-Tropsch Synthesis. Applied Catalysis A 1999, 186, 3–12.

(4) The official website of the Nobel Prize - NobelPrize.org https://www.nobelprize.org/

(5) Wisniak, J. The History of Catalysis. From the Beginning to Nobel Prizes. Educacion Quimica 2010, 21, 60–69.

(6) Hollmann, F.; Studt, F.; Hu, X.; Yip, A. C. K. Heterogeneous Catalysis: Enabling a Sustainable Future. Frontierts in Catalysis 2021, 1, 667675.

(7) Meriaudeau Paul; Naccache Claude. Dehydrocyclization of Alkanes Over ZeoliteSupported Metal Catalysts: Monofunctional or Bifunctional Route. Catalysis Review 1997, 39, 5–48.

(8) Guisnet, M.; Alvarez, F.; Giannetto, G.; Perot, G. Hydroisomerization and Hydrocracking of N-Heptane on Pth Zeolites. Effect of the Porosity and of the Distribution of Metallic and Acid Sites. Catalysis Today 1987, 1, 415–433.

(9) Kubo, T.; Arai, H.; Tominaga, H.; Kunugi, T. Metal Catalysts Supported on Zeolite. I. A Study on Platinum Particles Disribution. Bulletin of the Chemical Society of Japan 1972, 45, 607–612.

(10) Xu, J.; Wang, Q.; Deng, F. Metal Active Sites and Their Catalytic Functions in Zeolites: Insights from Solid-State NMR Spectroscopy. 2019.

(11) Liu, L.; Lopez-Haro, M.; Calvino, J. J.; Corma, A. Tutorial: Structural Characterization of Isolated Metal Atoms and Subnanometric Metal Clusters in Zeolites. Nature Protocols 2020.

(12) Kosinov, N.; Liu, C.; Hensen, E. J. M.; Pidko, E. A. Engineering of Transition Metal Catalysts Confined in Zeolites. Chem. Mater 2018, 30, 31.

(13) de Vos, D. E.; Thibault-Starzyk, F.; Knops-Gerrits, P. P.; Parton, R. F.; Jacob, P. A. A Critical Overview of the Catalytic Potential of Zeolite Supported Metal Complexes Macromol. Symp 1994, 80, 157–184.

(14) Ahn, D. H.; Lee, J. S.; Nomura, M.; Sachtler, W. M. H.; Moretti, G.; Woo, S. I.; Ryoo, R. Characterization of Zeolite-Supported Pt-Cu Bimetallic Catalyst by Xenon-129 NMR and EXAFS. Journal of Catalysis 1992, 133, 191–201.

(15) Brito, L.; Pirngruber, G. D.; Guillon, E.; Albrieux, F.; Martens, J. A. Hydroconversion of Perhydrophenanthrene over Bifunctional Pt/H-USY Zeolite Catalyst. ChemCatChem 2020, 12, 3477–3488.

(16) Katsuno, H.; Fukunaga, T.; Sugimoto, M. New Modification Method of Pt/L Zeolite Catalyst for Hexanes Aromatization. Studies in Surface Science and Catalysis 1993, 75, 2419–2422.

(17) Fukunaga, T.; Katsuno, H. Halogen-Promoted Pt/KL Zeolite Catalyst for the Production of Aromatic Hydrocarbons from Light Naphtha. Catalysis Survey Asia 2010, 14, 96–102.

(18) Wang, Y.; Nishitoba, T.; Wang, Y.; Meng, X.; Xiao, F. S.; Zhang, W.; Marler, B.; Gies, H.; de Vos, D.; Kolb, U.; Feyen, M.; McGuire, R.; Parvulescu, A. N.; Müller, U.; Yokoi, T. Cu-Exchanged CHA-Type Zeolite from Organic Template-Free Synthesis: An Effective Catalyst for NH3-SCR. Industrial and Engineering Chemistry Research 2020, 59, 7375–7382.

(19) Derouane, E. G.; Vanderveken, D. J. Structural Recognition and Preorganization in Zeolite Catalysis: Direct Aromatization of n-Hexane on Zeolite L-Based Catalysts. Applied Catalysis Letter 1988, 45, L15–L22.

(20) Zhan, Z.; Manninger, I.; Paal, Z.; Bathomeuf, D. Reactions of N-Hexane over Pt-Zeolite Catalysts of Different Acidity. Journal of Catalysis 1994, 147, 333–341.

(21) D ’ippolito, S. A.; Gutierrez, L. B.; Vera, C. R.; Pieck, C. L. Pt-Mg-Ir/Al 2 O 3 and Pt-Ir/HY Zeolite Catalysts for SRO of Decalin. Influence of Ir Content and Support Acidity. “Applied Catalysis A, General” 2013, 452, 48–56.

(22) Friend, C. M.; Xu, B. Heterogeneous Catalysis: A Central Science for a Sustainable Future. Accounts of Chemical Research 2017, 50, 517–521.

(23) Chmelka, B. F. Zeolites: Large Molecules Welcome. Nature materials 2006, 5, 681–682.

(24) Li, G.; Pidko, E. A. The Nature and Catalytic Function of Cation Sites in Zeolites: A Computational Perspective. ChemCatChem 2019, 11, 134–156.

(25) Davis ’, M. E. Zeolites and Molecular Sieves: Not Just Ordinary Catalysts. Ind. Eng. Chem. Res 1991, 30, 1675–1683.

(26) Cejka, J.; van Bekkum, H.; Corma, A.; Schuth, F. Introduction to Zeolite Science and Practive, 3rd revised edition.; Elsevier, 2007; Vol. 168.

(27) Cronstedt, A. F. Observation and Description of an Unknown Kind of Rock to Be Named Zeolites. Kongl Vetenskaps Academiens Handlingar Stockholm 1756, 17, 120.

(28) Jensen, Z.; Kim, E.; Kwon, S.; Gani, T. Z. H.; Román-Leshkov, Y.; Moliner, M.; Corma, A.; Olivetti, E. A Machine Learning Approach to Zeolite Synthesis Enabled by Automatic Literature Data Extraction. ACS Central Science 2019.

(29) Zones, S. I.; Hwang, S. J. A Novel Approach to Borosilicate Zeolite Synthesis in the Presence of Fluoride. Microporous and Mesoporous Materials 2011, 146, 48–56.

(30) Goel, S.; Zones, S. I.; Iglesia, E. Synthesis of Zeolites via Interzeolite Transformations without Organic Structure-Directing Agents. Chemistry of Materials 2015, 27, 2056–2066.

(31) Davis, M. E. Zeolite Synthesis - Can It Be Designed. Interfacial Design And Chemical Sensing 1994, 561, 27–37.

(32) Bignami, G. P. M.; Dawson, D. M.; Seymour, V. R.; Wheatley, P. S.; Morris, R. E.; Ashbrook, S. E. Synthesis, Isotopic Enrichment, and Solid-State NMR Characterization of Zeolites Derived from the Assembly, Disassembly, Organization, Reassembly Process. Journal of the American Chemical Society 2017, 139, 5140–5148..

(33) Li, J.; Corma, A.; Yu, J. Synthesis of New Zeolite Structures. Chemical Society Reviews 2015, 44, 7112–7127.

(34) Derbe, T.; Temesgen, S.; Bitew, M. A Short Review on Synthesis, Characterization, and Applications of Zeolites. 2021.

(35) Dusselier, M.; Davis, M. E. Small-Pore Zeolites: Synthesis and Catalysis. 2018.

(36) Lobo, R. F.; Pan, M.; Chan, I.; Li, H.; Medrud, R. C.; Stacey, I.; Lobo, R. F.; Pan, M.; Chan, I.; Li, H.; Medrud, R. C.; Zones, S.; Crozier, P. A.; Davis, M. E. SSZ-26 and SSZ-33 : Two Molecular Sieves with Intersecting 10- and 12-Ring Pores Zones , Peter A . Crozier and Mark E . Davis Science 1993, 262, 1543–1546.

(37) Zones, S. 1. Conversion of Faujasites to High-Silica Chabazite SSZ-13 in the Presence of N,N,N-Trimethyl-l-Adamantammonium Iodide; 1991; Vol. 87.

(38) Zones, S. I. Direct Hydrothermal Conversion of Cubic P Zeolite to Organozeolite SSZ-13. Journal of the Chemical Society, Faraday Transactions 1990, 86 , 3467–3472.

(39) Zones, S. I. Synthesis of High Silica Zeolites Using a Mixed Quaternary Ammonium Cation , Amine Approach : Discovery of Zeolite SSZ-47. 2002, No. 5, 313–320.

(40) Chen, C. Y.; Rainis, A.; Zones, S. I. Reforming with Novel Borosilicate Molecular Catalysts. Materials Research Society Symposium Proc 1997, 454, 205–215.

(41) Zones, S. I.; Chen, C. Y.; Benin, A.; Hwang, S. J. Opportunities for Selective Catalysis within Discrete Portions of Zeolites: The Case for SSZ-57LP. Journal of Catalysis 2013, 308, 213–225.

(42) Xie, D.; Mccusker, L. B.; Baerlocher, C.; Zones, S. I.; Wan, W.; Zou, X. SSZ-52, a Zeolite with an 18-Layer Aluminosilicate Framework Structure Related to That of the DeNOx Catalyst Cu-SSZ-13. Journal of the American Chemical Society 2013, 135, 10519–10524.

(43) Smeets, S.; Xie, D.; McCusker, L. B.; Baerlocher, C.; Zones, S. I.; Thompson, J. A.; Lacheen, H. S.; Huang, H. M. SSZ-45: A High-Silica Zeolite with Small Pore Openings, Large Cavities, and Unusual Adsorption Properties. Chemistry of Materials 2014, 26, 3909–3913.

(44) Schroeder, C.; Mück-Lichtenfeld, C.; Xu, L.; Grosso-Giordano, N. A.; Okrut, A.; Chen, C. Y.; Zones, S. I.; Katz, A.; Hansen, M. R.; Koller, H. A Stable Silanol Triad in the Zeolite Catalyst SSZ-70. Angewandte Chemie - International Edition 2020, 59, 10939–10943.

(45) Eliášová, P.; Opanasenko, M.; Wheatley, P. S.; Shamzhy, M.; Mazur, M.; Nachtigall, P.; Roth, W. J.; Morris, R. E.; Čejka, J. The ADOR Mechanism for the Synthesis of New Zeolites. Chemical Society Reviews. Royal Society of Chemistry October 21, 2015, pp 7177–7206.

(46) Database of Zeolite Structures http://www.iza-structure.org/databases/

(47) Lauriente, D. H. , I. Y. The Chemical Economics Book; SRI Consulting, 2005.

(48) Sherman, J. D. Synthetic Zeolites and Other Microporous Oxide Molecular Sieves. PNAS 1999, 96, 3471–3478.

(49) Rabo, J. A.; Schoonover, M. W. Early Discoveries in Zeolite Chemistry and Catalysis at Union Carbide, and Follow-up in Industrial Catalysis. Applied Catalysis A: General 2001, 222, 261–275.

(50) Chen, N. Y. ,; Garwood W.E.; Dwyer F.G. Shape Selective Catalysis Industrial Applications; 1989; Vol. Chapter 5.

(51) Weitkamp, J. ,; Ernst, S.; Puppe, L. Catalysis and Zeolites Fundamentals and Applications; Springer: Berlin, 2001.

(52) Maesen, T. L. M.; Schenk, M.; Vlugt, T. J. H.; de Jonge, J. P.; Smit, B. The Shape Selectivity of Paraffin Hydroconversion on TON-, MTT-, and AEL-Type Sieves. Journal of Catalysis 1999, 188, 403–412.

(53) Guisnet, M. “Ideal” Bifunctional Catalysis over Pt-Acid Zeolites. Catalysis Today 2013, 218, 123–134.

(54) Xu, D.; Wang, S.; Wu, B.; Zhang, B.; Qin, Y.; Huo, C.; Huang, L.; Wen, X.; Yang, Y.; Li, Y. Highly Dispersed Single-Atom Pt and Pt Clusters in the Fe-Modified KL Zeolite with Enhanced Selectivity for n-Heptane Aromatization. ACS Applied Materials and Interfaces 2019, 11, 29858–29867.

(55) Moliner, M.; Gabay, J. E.; Kliewer, C. E.; Carr, R. T.; Guzman, J.; Casty, G. L.; Serna, P.; Corma, A. Reversible Transformation of Pt Nanoparticles into Single Atoms inside High-Silica Chabazite Zeolite. 2016, 138, 15743–15750.

(56) Hanaoka, T.; Miyazawa, T.; Shimura, K.; Hirata, S. Preparation for Pt-Loaded Zeolite Catalysts Using w/o Microemulsion and Their Hydrocracking Behaviors on Fischer-Tropsch Product. Catalysts 2015, 5, 88–105.

(57) Wan, W.; Su, J.; Zou, X. D.; Willhammar, T. Transmission Electron Microscopy as an Important Tool for Characterization of Zeolite Structures. Inorg. Chem. Front 2018, 5, 2836.

(58) Dartt, C. B.; Davis, M. E. Characterization and Catalytic Activity of Titanium Containing SSZ-33 and Aluminum-Free Zeolite Beta. Applied Catalysis A: General 1996, 143, 53–73.

(59) Pandya, K. I.; Heald, S. M.; Hriljac, J. A.; Petrakis, L.; Fraissard, J. Characterization by EXAFS, NMR, and Other Techniques of Pt/NaY Zeolite at Industrially Relevant Low Concentration of Platinum. Journal of Physical Chemistry 1996, 100, 5070–5077.

(60) Hunger, B.; Heuchel, M.; Clark, L. A.; Snurr, R. Q. Characterization of Acidic OH Groups in Zeolites of Different Types: An Interpretation of NH 3 -TPD Results in the Light of Confinement Effects. Journal of Physical Chemistry B 2002, 106, 3882–3889.

(61) Valerio, G.; Goursot, A.; Vetrivel, R.; Malkina, O.; Malkin, V.; Salahub, D. R. Al MAS NMR Chemical Shifts in Zeolite- Using Density Functional Theory: Correlation with Lattice Structure. Journal of American chemical Society 1998, 120, 11426–11431.

(62) Chmelka, B. F.; Ryoo, R.; S.B. Liu; L.C. de Menorval; Radke, C. J.; Petersen, E. E.; Pines, A. Probing Metal Cluster Formation in NaY Zeolite by Xenon-129 NMR,. Journal of American Chemical Society 1988, 110, 4465–4467.

(63) Yu, Z.; Zheng, A.; Wang, Q.; Chen, L.; Xu, J.; Amoureux, J. P.; Deng, F. Insights into the Dealumination of Zeolitehy Revealed by Sensitivity-Enhanced 27Al DQ-MAS NMR Spectroscopy at High Field. Angewandte Chemie - International Edition 2010, 49, 8657–8661.

(64) Dumesic et al., 13C NMR, Pt-L Zeolite for n-Hexane Conversion, J.Cat, 1994.

(65) Zhao, X.; Xu, J.; Deng, F. Solid-State NMR for Metal-Containing Zeolites: From Active Sites to Reaction Mechanism. Frontiers of Chemical Science and Engineering 2020, 14, 159–187.

(66) Brouwer, D. H.; Brouwer, C. C.; Mesa, S.; Semelhago, C. A.; Steckley, E. E.; Sun, M. P. Y.; Mikolajewski, J. G.; Baerlocher, C. Solid-State 29Si NMR Spectra of Pure Silica Zeolites for the International Zeolite Association Database of Zeolite Structures. Microporous and Mesoporous Materials 2020, 297.

(67) Morris, R. E.; Weigel, S. J.; Henson, N. J.; Bull, L. M.; Janicke, M. T.; Chmelka, B. F.; Cheetham, A. K. A Synchrotron X-Ray Diffraction, Neutron Diffraction, 29Si MAS-NMR, and Computational Study of the Siliceous Form of Zeolite Ferrierite. Journal of the American Chemical Society 1994, 116, 11849–11855..

(68) Gil, B.; Zones, S. I.; Hwang, S. J.; Bejblová, M.; Ejka, J. Č. Acidic Properties of SSZ-33 and SSZ-35 Novel Zeolites: A Complex Infrared and MAS NMR Study. Journal of Physical Chemistry C 2008, 112, 2997–3007.

(69) Žilková, N.; Gil, B.; Zones, S. I.; Hwang, S. J.; Bejblová, M.; Čejka, J. Acidic Properties of SSZ-33 and SSZ-35 Novel Zeolites: A Complex I.R. and MAS NMR Study. Studies in Surface Science and Catalysis 2008, 174, 1027–1032.

(70) Ernst, H.; Freude, D.; Wolf, I. Multinuclear Solid-State NMR Studies of Brønsted Sites in Zeolites. Chemical Physics Letters 1993, 212, 588–596.

(71) Peng, L.; Huo, H.; Gan, Z.; Grey, C. P. 7O MQMAS NMR Studies of Zeolite HY. Microporous and Mesoporous Materials 2008, 109, 156–162.

(72) Klinowski, J. Solid-State NMR Studies of Zeolite Catalysts. Colloids and Surfaces 1989, 36, 133–154.

(73) Jiao, J.; Wang, W.; Sulikowski, B.; Weitkamp, J.; Hunger, M. Si and Al MAS NMR Characterization of Non-Hydrated Zeolites Y upon Adsorption of Ammonia. Microporous and mesoporous materials 2005, 90, 246–250..

(74) Hwang, S. J.; Chen, C. Y.; Zones, S. I. Boron Sites in Borosilicate Zeolites at Various Stages of Hydration Studied by Solid State NMR Spectroscopy. Journal of Physical Chemistry B 2004, 108, 18535–18546.

(75) Greiser, S.; Hunger, M.; Jaeger, C. 29Si{27Al} TRAPDOR MAS NMR to Distinguish Qn(MAl) Sites in Aluminosilicates. Test Case: Faujasite-Type Zeolites. Solid State Nuclear Magnetic Resonance 2016, 79, 6–10.

(76) Qi, G.; Wang, Q.; Xu, J.; Wu, Q.; Wang, C.; Zhao, X.; Meng, X.; Xiao, F.; Deng, F. Direct Observation of Tin Sites and Their Reversible Interconversion in Zeolites by Solid-State NMR Spectroscopy. Communications Chemistry 2018, 1, 1–7.

(77) Qi, L.; Alamillo, R.; Elliott, W. A.; Andersen, A.; Hoyt, D. W.; Walter, E. D.; Kee; Han, S.; Washton, N. M.; Rioux, R. M.; Dumesic, J. A.; Scott, S. L. Operando Solid-State NMR Observation of Solvent-Mediated Adsorption-Reaction of Carbohydrates in Zeolites.

(78) Zhao, Z.; Xing, Y.; Li, S.; Meng, X.; Xiao, F. S.; McGuire, R.; Parvulescu, A. N.; Müller, U.; Zhang, W. Mapping Al Distributions in SSZ-13 Zeolites from 23Na Solid-State NMR Spectroscopy and DFT Calculations. Journal of Physical Chemistry C 2018, 122, 9973–9979.

(79) Brouwer, D. H.; Darton, R. J.; Morris, R. E.; Levitt, M. H. A Solid-State NMR Method for Solution of Zeolite Crystal Structures. Journal of American Chemical Society 2005, 127, 10365–10370.

(80) Feuerstein, M.; Hunger, M.; Engelhardt, G.; Amoureux, J. P. Characterisation of Sodium Cations in Dehydrated Zeolite NaX by 23Na NMR Spectroscopy. Solid State Nuclear Magnetic Resonance 1996, 7, 95–103.

(81) Pearson, J. G.; Chmelka, B. F.; Shykind, D. N.; Pines, A. Multiple-Quantum NMR Study of the Distribution of Benzene in NaY Zeolite. Journal of Physical Chemistry 1992, 96, 8517–8522.

(82) Zhang, W.; Bao, X.; Guo, X.; Wang, X. A High-Resolution Solid-State NMR Study on Nano-Structured HZSM-5 Zeolite. Catalysis Letters 1999, 60, 89–94.

(83) Li, S.; Huang, S. J.; Shen, W.; Zhang, H.; Fang, H.; Zheng, A.; Liu, S. bin; Deng, F. Probing the Spatial Proximities among Acid Sites in Dealuminated H-Y Zeolite by Solid-State NMR Spectroscopy. Journal of Physical Chemistry C 2008, 112, 14486–14494.

(84) Cavanagh, J.; Fairbrother, W. J.; Palmer, A. G.; Skelton, N. J.; Rance, M. Protein NMR Spectroscopy; 2007.

(85) Gan, Z.; Hung, I.; Wang, X.; Paulino, J.; Wu, G.; Litvak, I. M.; Gor'kov, P. L.; Brey, W. W.; Lendi, P.; Schiano, J. L.; Bird, M. D.; Dixon, I. R.; Toth, J.; Boebinger, G. S.; Cross, T. A. NMR Spectroscopy up to 35.2 T Using a

Series-Connected Hybrid Magnet. Journal of Magnetic Resonance 2017, 284, 125–136.

(86) Levitt, M. H. Spin Dynamics-Basics of NMR; 2013; Vol. 53.

(87) Müller, L. Müller / Sensitivity Enhanced Detection of Weak Nuclei 4481 Sensitivity Enhanced Detection of Weak Nuclei Using Heteronuclear Multiple Quantum Coherence. Journal of American Chemical Society 1979, 101, 4481–4484.

(88) Bax, A.; Griffey, R. H.; Hawkins, B. L. Correlation of Proton and Nitrogen-15 Chemical Shifts by Multiple Quantum NMR*. Journal of Magnetic Resonance 1983, 55, 30–33.

(89) Mandal, P. K.; Majumdar, A. A Comprehensive Discussion of HSQC and HMQC Pulse Sequences. Concepts in Magnetic Resonance Part A: Bridging Education and Research 2004, 20, 1–23.

CHAPTER 2

2. Correlated distributions of Pt, exchangeable cations, and framework sites in Pt-NaY zeolite

*Tsatsral Battsengel,[1] Randall Meyer,[2] Tom Willhammar,[3] Lynne McCusker,[4] Allen Burton,[2] Robert Carr,[2] Pedro Serna,[2] Mobae Afeworki,[2] Bradley F. Chmelka[1, *]*

[1] Department of Chemical Engineering, University of California, Santa Barbara, California 93106, United States

[2] ExxonMobil Research and Engineering Co., Annandale, New Jersey 08801, United States

[3] Department of Materials and Environmental Chemistry, Stockholm University, SE-106 91 Stockholm, Sweden

[4] Laboratory of Crystallography, ETH Zurich, CH-8093 Zurich, Switzerland

Keywords: Pt-NaY, metal distributions in zeolite, zeolite catalyst, solid-state NMR of zeolites

2.1 Abstract

The reaction properties of metal-zeolite catalysts strongly depend on the compositions and nanoscale architectures of the zeolite support, as well as the identities and locations of metal species and exchangeable cations within the zeolite pores, which are influenced by the catalyst synthesis and treatment conditions. Pt supported on faujasite zeolites, which consist of distinct cages with different nanoscale dimensions are prepared to understand the calcination temperature-dependent locations of Pt species within the

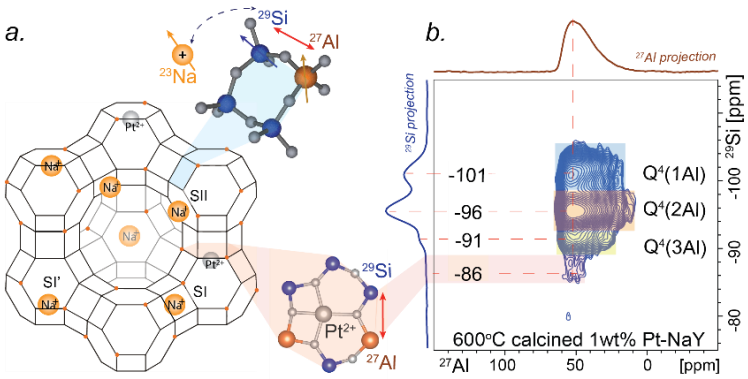

different cages of the zeolite framework and the effects of different Pt species on distributions of exchangeable cations. A combination of nuclear magnetic resonance (NMR), synchrotron extended X-ray absorption fine structure (EXAFS), X-ray diffraction (XRD) refinement analyses, and high-resolution transmission electron microscopy (HRTEM) results revealed calcination temperature-dependent locations of precious metal Pt sites in zeolites and distributions of ^{23}Na cations located in different cages of the faujasite zeolite. Pt species directly influence through-bond ^{29}Si-O-^{27}Al and through-space ^{29}Si-^{23}Na interactions, as revealed by solid-state two-dimensional (2D) NMR measurements. Calcination at high temperatures (873 K) results in Pt^{2+} cations at the center of the sodalite cage 6-ring of the Y-zeolite, whereas calcination at 673 K results in PtO_x species in supercage sites. Moreover, the Pt^{2+} cations charge-balance anionic framework sites and compete with Na^+ cations, which affect their mutual distributions. Such atomic-scale insights are expected to enable the design and synthesis of dispersed Pt, a central goal of metal-supported heterogeneous catalyst preparation.

2.2 Introduction

In zeolite-supported metal catalysts, the composition and nanoscale architecture of the zeolite support, as well as the types and locations of metal species within zeolite pores determine the reaction properties. Preparation conditions, *e.g.*, treatment temperature, of these catalysts, influence the speciation and distribution of the metals supported on zeolites.[1–6] Understanding the atomic-scale structures of metal-zeolite systems prepared under different conditions is crucial to the development of strategies to control metal active site distributions, and thereby improve catalyst performance.

Y zeolite with FAU framework structure is industrially significant zeolite support used for various catalytic reactions, such as isomerization and cracking.[7–9] Pt-NaY is especially useful for understanding how metals interact with the zeolite framework due to the distinct types of sub-nanometer cages of the faujasite framework with different local structures and dimensions. Y zeolite structure is composed of supercages (diameter 1.2 nm), sodalite cages (diameter 0.6 nm), and small hexagonal prisms (diameter 0.3 nm). Pt metals can be stabilized via strong basic lattice sites ligation or can be mechanically supported inside zeolite pores by encapsulation. While the effects of catalyst treatment, *e.g.*, calcination and reduction conditions, on the chemical reaction properties of Pt-zeolite catalysts have long been known, the atomic-level structures that account for these influences have remained elusive.[2,5,6,9–15] Previously, locations of Pt in NaY-zeolite have been inferred by indirectly detecting Pt species by nuclear magnetic resonance (NMR) spectroscopy of adsorbed ^{129}Xe or ^{13}CO,[4,16] infrared spectroscopy,[17] and H_2 temperature-programmed desorption analyses.[10] Due to dilute loadings of Pt and broad distributions of local chemical environments in the zeolite, Pt-zeolite systems have been challenging to characterize at an atomic-level, including the interactions of Pt with the framework atoms and locations of Pt within the zeolite. Recent advances in solid-state nuclear magnetic resonance techniques overcome some of these challenges by detecting local environments of framework ^{27}Al, ^{29}Si sites, distributions of ^{23}Na exchangeable cations, and directly acquiring ultrawideline ^{195}Pt spectrum, which is sensitive to chemical and coordination environments of platinum sites. Here, detailed structural insights are obtained on the locations and interactions of Pt species within the zeolite framework

as functions of calcination temperatures. Long-range structural order and distributions of extraframework charge density (Na^+ or Pt^{2+}) are revealed by Rietveld refinement analyses of the WAXS diffraction pattern. The atomic-scale compositions and structures are determined by solid-state nuclear magnetic resonance (NMR) spectroscopy, extended X-ray absorption fine structure (EXAFS), and high-resolution transmission electron microscopy (HRTEM) techniques. Pt-NaY with high Pt loadings (15 wt%) are used as a guide to analyzing results for industrially relevant Pt-NaY with an order of magnitude lower Pt content (<1 wt%) show calcination temperature-dependent differences in types, sizes, and locations of Pt species, and different interactions between Pt species and framework tetrahedral sites.

2.3 Materials and Methods

Synthesis of ion-exchanged and calcined Pt-NaY. NaY zeolite with a Si/Al ratio of 2.5 (Zeolyst International, Inc. CBV-100) was hydrated overnight in an atmosphere with 80% relative humidity before ion-exchanging platinum tetraamine salt, $Pt(NH_3)_4Cl_2 \cdot H_2O$ (Spectrum Chemical MFG Corp. CAS 13933-33-0). The desired amount of Pt tetraamine salt in an aqueous solution was added dropwise to a solution of NaY zeolite in deionized water, and the slurry solution was stirred for 15 h at 373 K with refluxing. The ion-exchange proceeds through reaction (1), and after filtering the slurry the solid was washed with ammonia solution and DI water to remove residual chloride ions.

$$Pt(NH_3)_4^{2+} + 2Cl^- + Na^+{-}Y \rightarrow Pt(NH_3)_4^{2+} {-}Na^+{-}Y + 2Na^+Cl^-_{aq} \quad (1)$$

A thin bed of ion-exchanged $Pt(NH_3)_4^{2+}Na^+$-Y was dried under vacuum at RT for 12 h before calcination under a continuous flow of O_2 (2 scfh/300 mg sample) with a heating

rate of 11 K/h up to the desired temperature (473 K, 673 K, and 873 K). After keeping the sample at calcined temperature for 2 h and allowing it to cool down to room temperature, the sample was sealed in glass ampules and stored in a dry glovebox. Pristine NaY was dried under vacuum from room temperature to 723 K for 5 h and held at that temperature for 2 h.

Elemental analyses of Pt-NaY at different stages of the preparation were obtained by X-ray fluorescence spectroscopy on Rigaku ZSX Primus IV spectrometer. Scanning electron micrographs were obtained using an FEI XL40 Sirion FEG digital scanning electron microscope at 15 000× magnification and 5 kV electron beam voltage.

Materials characterization. Wide-angle X-ray scattering (WAXS) powder patterns were acquired from 1 wt% Pt-NaY calcined at different temperatures to identify the distributions of extraframework charge densities. Samples were sealed in 1 mm quartz capillary were measured using a home-built instrument equipped with XENOCS Genix 50W X-ray microsource with a focus size of 50 μm at transmission mode A reference signal from Ag-behenate was acquired for a shorter time (120 s) compared to the acquisition time of the Pt-NaY samples (300 s).

Electron Microscopy images were acquired to identify the sizes of Pt particles. The zeolite samples were suspended in ethanol. Two types of Scanning Transmission Electron Microscopy signals were acquired: Annual Dark Field (ADF) and integrated Differential Phase Contrast (iDPC), The contrast of the first one is more sensitive to higher Z elements, *e.g.* Pt, while the latter results in higher resolution in zeolite framework. The microscope was operated at an accelerating voltage of 300 kV. The

images were acquired using a beam current of 20 pA, a convergence angle of 16 mrad, and a dwell time of 20 μs.

Extended X-ray absorption fine structure spectroscopy (EXAFS) experiments were performed at beamline 9-BM at Advanced Photon Source (APS) at the Argonne National Laboratory. Data were collected in transmission mode using an XAFS cell that has the capability of in-situ calcination and reduction. The in-situ reductions were performed with 4% H_2 (in He), whereas 20% O_2 (in He) was used for the in-situ oxidation treatments. A water-cooled Si(111) monochromator was used to scan X-ray energy from −250 to 1000 eV relative to Pt-L3 edge (11564 eV). Each sample (~20 mg) was pressed as a thin wafer inside the airtight EXAFS cell. Transmission XAFS measurements were carried out simultaneously with the pure Pt foil measured in reference mode for X-ray energy calibration and data alignment. Data processing and analysis were performed using the IFEFFIT package.[18] After appropriate background subtraction, data ranges were assessed based on the quality of data generally between k = 3-14 $Å^{-1}$ and for R= 1.2-3.3 Å. EXAFS analysis was done model-independently, and the results were not biased in favor of any assumed model about the short-range order of elements in these samples. Specifically, the analysis was employed by fitting theoretical FEFF6 calculations to the experimental EXAFS data. The value of amplitude reduction factor, S02, was determined to be 0.82 by a fit of the reference foil with a fixed coordination number of 12 to reflect the fcc structure of Pt and was fixed in the analysis of the Pt-NaY samples. The parameters describing electronic properties (*e.g.*, correction to the photoelectron energy origin) and local structural environment (coordination numbers N, bond length R, and the Debye-Waller

factor, σ^2) around absorbing atoms were varied during fitting with a simultaneous fit of k^1, k^2, and k^3.

Solid-state nuclear magnetic resonance (NMR) spectroscopy measurements were used to reveal molecular compositions and atomic structures of Pt-NaY and NaY zeolite materials. Y zeolite with a Si/Al ratio of 2.5 is extremely hygroscopic, and approximately 27 wt% of the fully hydrated zeolite is from adsorbed water. Solid-state NMR is highly sensitive to the local surroundings of the studied nuclei, hence the presence of water molecules around studied nuclei affects the spin properties, *i.e.*, mobility of extraframework cations, quadrupolar broadening of ^{27}Al, and longitudinal relaxation times of ^{29}Si. Therefore, to obtain the atomic-level structural information of Pt-NaY materials without the effects of water molecules, solid-state NMR measurements were conducted on dehydrated materials, which also closely resemble the state of the Pt-NaY catalysts under reaction conditions compared to hydrated materials. Calcined and dehydrated samples were sealed in a glass ampule and transferred into a glovebox under dry Ar, where samples were packed in NMR rotors. Silicone plugs were used to seal the open end of the rotor before placing the rotor cap, and dry N_2 was used for MAS. Conventional solid-state ^{1}H and ^{29}Si MAS-NMR were conducted on 11.7 T Bruker AVANCE-II NMR spectrometer, operating at 12.5 kHz MAS at 298 K using a Bruker 4 mm probe head and zirconia rotors with Kel-F^{TM} caps. Low-temperature MAS (LTMAS) measurements (95 K) provide significantly enhanced NMR signal sensitivity that allows the detection and analysis of ^{29}Si-O-^{27}Al covalent-bonding environments and ^{29}Si -^{23}Na$^+$ cation interactions in zeolite framework at a natural abundance of ^{29}Si (4.7%). LTMAS measurements were conducted on a Bruker

ASCEND 400 NMR spectrometer with a 9.4 T superconducting magnet equipped with low temperature 3.2 mm triple-resonance MAS probe head operating at frequencies listed in Table S1. ^{23}Na MQMAS spectra were obtained at ultra-high field (35.3 T) Series-Connected Hybrid Magnet at the National High Magnetic Field Laboratory. A Triple-quantum MAS pulse sequence with two hard pulses followed by a *z*-filter was used. Single-pulse excitation of 0.42 us corresponding to π/12 flip angle was used for quantitative ^{23}Na experiments with a recycle delay of 0.5 s.

Thermogravimetric analyses (TGA) were used to identify the decomposition temperature regime of tetraamine complex in ion-exchanged Pt-NaY and the temperature at which the parent hydrated NaY zeolite losses adsorbed water. TGA was conducted on fully hydrated NaY and 15 wt% ion-exchanged $Pt(NH_3)_4^{2+}$-NaY to obtain the tetraamine decomposition temperature from the pronounced effects in higher concentration Pt. TA Discovery Thermo-Gravimetric Analyzer was used for TGA measurements. **Figure 2.1** shows the weight percent of the samples as a function of sample temperature. As temperature increases fully hydrated zeolite loses adsorb water until it reaches equilibrium when most of the water is desorbed. Approximately 27 wt% of fully hydrated NaY is due to adsorbed water, which mostly is removed heating at 673 K (trace i). The decomposition of the $Pt(NH_3)_4^{2+}$ complexes start around 573 K, as manifested by the sudden mass loss between 573 and 673 K (trace ii) corresponding to the highlighted grey region.

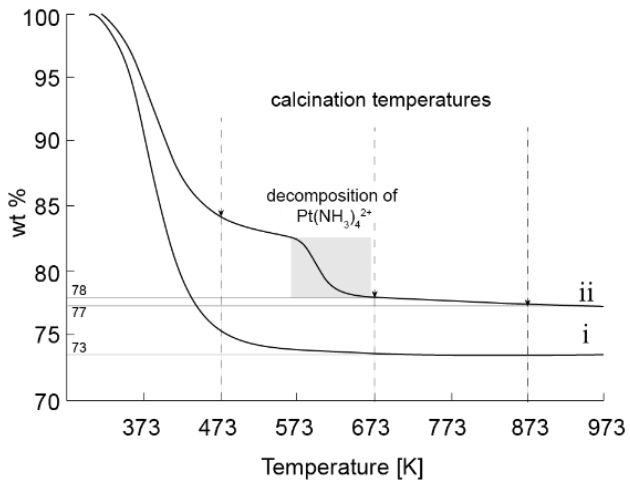

Figure 2.1. Thermogravimetric (TGA) analyses of (i) initially fully hydrated NaY and (ii) and initially ion-exchanged 15 wt% Pt(NH3)42+-NaY during calcination in air at 5 ml/min g sample at a heating rate 10 K/min

X-ray photoelectron spectroscopy (XPS) was used to identify and quantify Pt located on the outer few nanometers of the zeolite crystal. The electron mean free path, EMFP, determines the sampling depth, which depends on the kinetic energy of the photoelectrons and the material of the study. The sampling depth for crystalline zeolite materials is within a few nanometers. NaY zeolite used in this study has crystals with a diameter of a micron, so XPS only probes the surface of the Pt-NaY materials. The high-resolution XPS spectra of 1 wt% Pt-NaY calcined at 873 K (a) at 673 K (b) are shown in **Figure 2.2**. XPS Signals from the zeolite support appear at 74 eV from Al 2p, which overlaps with a signal from Pt $4f_{7/2}$ photoelectrons at 77 eV, making an unambiguous resolution of the signals challenging.

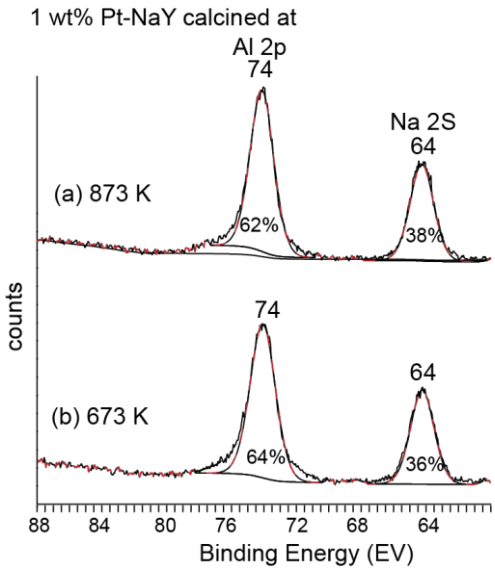

Figure 2.2. Regional XPS spectra of 1 wt% Pt-NaY calcined at (a) 873 K and (b) 673 K, A Shirley background is used to remove the contribution of the inelastically scattered electrons. Due to lower loadings of Pt and overlapping signals from Pt $4f_{7/2}$ and Al 2p photoelectrons, XPS signals from 1 wt% Pt-NaY cannot identify differences between Pt-NaY calcined at 673 and 873 K

2.4 Results and Discussion

Reaction properties of Pt-zeolite catalysts depend on dispersions and locations of metal sites, which are directly influenced by treatment conditions.[2,14] To maximize the use of precious metals supported on zeolite catalysts, it is crucial to carefully control the dispersions of metals and avoid the formation of large metal clusters. Detailed understandings of locations and identities of Pt metal species of Pt-zeolites treated at different conditions are necessary to control the dispersion of Pt on NaY zeolite. Here, ion-exchanged $Pt(NH_3)_4^{2+}$-NaY is calcined at different temperatures, which are chosen based on the tetraamine salt decomposition temperature regimes, to result in Pt species with different identities, *i.e.*, Pt particles or Pt single atom cations, and located in different cages, *i.e.*, small hexagonal prisms, sodalite cages, or larger

supercages Y zeolite. The calcination temperatures were chosen before the tetraamine salt decomposition (473 K), following decomposition of $Pt(NH_3)_4^{2+}$ (673 K), and at a higher temperature (873 K) to identify the locations and speciation of Pt-NaY calcined at different temperatures.

Calcination temperatures below the temperature of the tetraamine salt decomposition result in an intact square planar $Pt(NH_3)_4^{2+}$ structure as expected, hence, 473 K calcined Pt-NaY contain platinum tetraamine cations, presumably inside the supercages of the NaY zeolite. Calcination at 673 K yields complete decomposition of $Pt(NH_3)_4^{2+}$ precursor and formation of oxidized Pt clusters residing inside the supercages or on the surface of the zeolite crystallites, which were revealed by X-ray diffraction refinement analyses and HRTEM images. When calcined at 873 K, Pt species disperse even more and reside in smaller cages of the Y zeolite as Pt^{2+} cations. The presence of such single atom cation sites stabilized by the zeolite framework oxygen atoms was identified by their effects on zeolite framework sites which were revealed by analyses of 2D $^{27}Al\{^{29}Si\}$ NMR results, and the Pt-O coordination with framework oxygen atoms by EXAFS analyses, and finally, the single Pt atoms are shown by HRTEM images. Furthermore, the locations of such Pt^{2+} cations are deduced from the relative distributions of Na^+ cation sites located in different cages of Y zeolite quantified from ^{23}Na NMR. Moreover, the color of the 873 K calcined Pt-NaY sample is much lighter (light grey even at very high 15 wt% Pt loading) compared to the sample calcined at 673 K (dark grey) with Pt loadings of 15 and 1 wt%, indicating that Pt moieties are small and well dispersed in 873 K calcined Pt-NaY. Larger particles scatter light more effectively,[19] thus the darker sample color

is an indication of larger Pt cluster formation. Structural diagrams of Pt-NaY calcined at the chosen temperatures are shown in **Figure 2.3**. Different cages of the Y zeolite are highlighted in **Figure 2.3a**: supercages with 0.7 nm aperture opening and 1.2 nm diameter cage, sodalite cage with a diameter of 0.6 nm, and small hexagonal prism with a diameter of 0.3 nm. Square planar tetraamine complexes of Pt are depicted in **Figure 2.3a** inside the supercages results and analyses of these different Pt species formed inside NaY zeolite under different calcination temperatures. Firstly, the results and analyses of Pt-NaY calcined at 873 K will be discussed to establish the identification of such single atom species, their effects on the local environments of zeolite support, and distributions of Na^+ cations. Then, the following sections will discuss the comparisons of analyses obtained from 673 K calcined Pt-NaY.

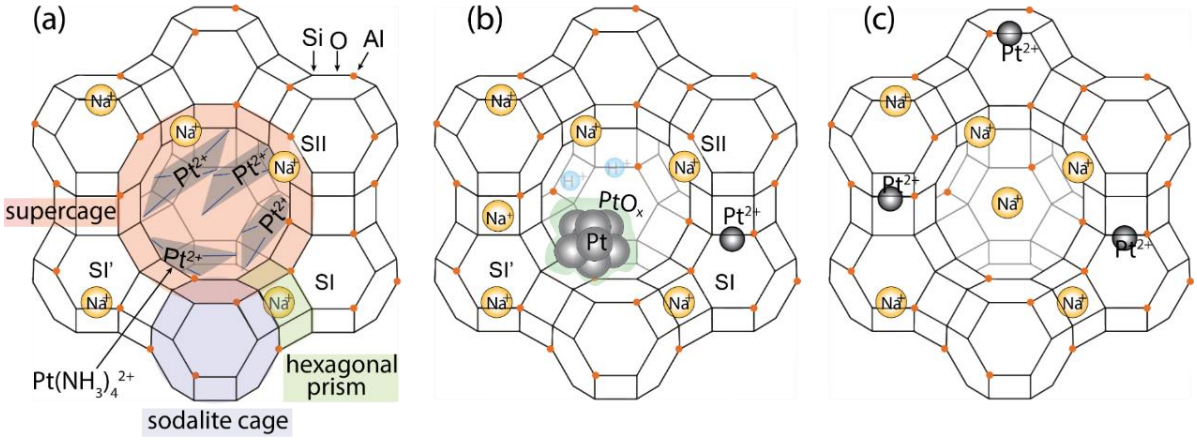

Figure 2.3. Structural diagrams of Pt-NaY following calcination at (a) 473 K, (b) 673 K, and (c) 873 K, which show different types and locations of Pt species that result

2.4.1 Single-atom Pt^{2+} cations coordinated with framework oxygens of Y zeolite: 873 K calcined Pt-NaY. The identities and locations of Pt in zeolites are determined by the preparation process, *e.g.*, final calcination temperature. At certain calcination conditions, NaY zeolite with high Al content (Si/Al = 2.5) can stabilize single-atom cation Pt^{2+} species, which are coordinated with four framework oxygen atoms of zeolite Y. High-resolution TEM images show single Pt atoms located inside the zeolite cages. Based on the DFT calculations, the most energetically favorable locations of Pt^{2+} cations are at the center of the 6-membered ring and coordinated with four oxygen atoms. Moreover, the coordination environment of Pt centers with four oxygen atoms is confirmed by EXAFS analyses. Finally, the direct detection of broadband ^{195}Pt NMR reveals chemical shift anisotropy (CSA) consistent with Pt in well-defined environments as discussed below.

Differences in framework ^{29}Si-^{27}Al interactions of NaY and Pt^{2+}-NaY. The differences in the local-bonding-environments of framework zeolite NaY and calcined Pt-NaY revealed the effects of Pt species on the support zeolite framework sites. ^{29}Si-O-^{27}Al through-bond interactions of NaY zeolite are elucidated by two-dimensional (2D) solid-state *J*-mediated ^{27}Al{^{29}Si} Heteronuclear Multiple Quantum Coherence (HMQC) NMR measurements. **Figure 2.4** shows ^{29}Si{^{27}Al} *J*-HMQC spectra of 873 K calcined parent NaY, 15 and 1 wt% Pt-NaY. The contour plots indicate through-bond interactions between framework ^{27}Al and ^{29}Si sites, whose signals are plotted along the horizontal and vertical axes, respectively. Although such through-bond correlations from the dilute natural isotopic abundance of ^{29}Si (4.7%) and weak ^{29}Si–O-^{27}Al *J*-couplings (<20 Hz) are challenging, they are feasible at low temperature (95

K) conditions under which Boltzmann sensitivity is enhanced[17] and thermal noise is decreased[18]. Firstly, the local environments of the parent NaY are identified by the 2D ^{27}Al{^{29}Si} *J*-HMQC experiment (**Figure 2.4a**). NaY zeolite was calcined to 873 K under flowing oxygen, the same as the process of calcination of Pt-NaY, to only observe the effects of Pt on the framework sites, not the preparation conditions. Well-resolved ^{29}Si signals at -91, -95, and 00 ppm are associated with Q^4(3Al), Q^4(2Al), and Q^4(1Al), where Q^4(*m*Al) denotes tetrahedral ^{29}Si sites with *m* numbers of neighboring Al atoms. These ^{29}Si species are through-bond correlated with tetrahedral ^{27}Al with a broadly distributed signal at ca. 54 ppm. To identify the effects of the Pt on the zeolite sites, higher (15 wt%) Pt-NaY is used as a guide to reveal subtle differences observed in ^{29}Si-O-^{27}Al environments of lower and industrially relevant loading of Pt (1 wt%).

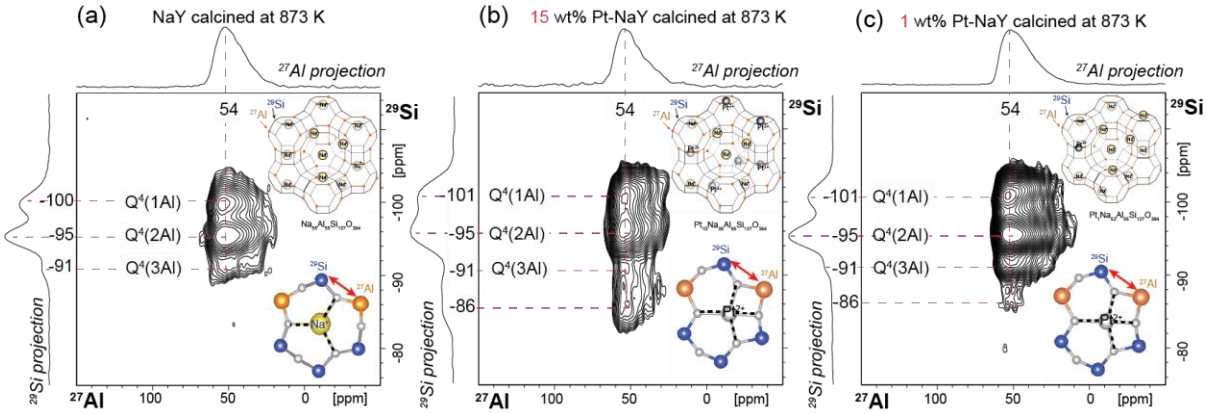

Figure 2.4. Solid-state 2D *J*-mediated (through-covalent-bond) ^{27}Al{^{29}Si} HMQC NMR correlation spectra of (a) dehydrated NaY zeolite, (b) 15 wt%, and (c) 1 wt% Pt-NaY calcined at 873 K. The spectra are acquired at 9.4 T, 95 K, and 8 kHz MAS. The structural schematics show through-bond interactions of ^{29}Si and ^{27}Al sites charge-balanced by a. Na^+ in dehydrated NaY and (b,c). Pt^{2+} in Pt-NaY calcined at 873 K. The chemical shifts of ^{29}Si sites (vertical axes) are labeled alongside their respective NMR signals. Projections of ^{27}Al sites are shown on the horizontal axes.

Similar to the parent NaY, Pt-NaY samples reveal ^{29}Si sites with one, two, and three Al neighbors with signals at -101, -95, -91 ppm for both loadings of Pt (**Fig. 2.4b**) 15 wt%, and 1 wt% (**Fig. 2.4c**). Compared to ^{29}Si signals of $Q^4(1Al)$ of the parent NaY, the ^{29}Si chemical shift is slightly at a higher field (by 1 ppm), suggesting the effects of Pt incorporation on $Q^4(1Al)$ sites. Moreover, the new ^{29}Si signal at -86 ppm is only present in calcined Pt-NaY and assigned to ^{29}Si sites proximate to Pt^{2+}, which changes the electronic environment of the nearby sites as well the bond angle between T-O-T connections as depicted in the structural diagrams of **Figure 2.4b,c**. The intensity of such new ^{29}Si peak at -86 ppm is much higher for 15 wt% calcined Pt-NaY, but still present in 1 wt% Pt-NaY calcined at 873 K. Moreover, the dilute amount of such small Pt species interacting strongly with the framework is also found in 673 K calcined Pt-NaY as discussed below.

These Pt^{2+} monoatomic species in calcined Pt-NaY were directly observed by HRTEM images. **Figure 2.5** shows HRTEM ADF images of 873 K calcined 1 wt% Pt-NaY along [112] direction (**Fig. 2.5a**) and higher resolution image along [110] direction (**Fig. 2.5b**). Obtaining high-resolution TEM images of porous materials is challenging due to radiation damage on the material. Hence, to minimize beam damage, low electron doses are used. The images were acquired by Annular dark-field high resolutions transmission electron microscopy (ADF HRTEM), which detects the electrons transmitted to higher angles, to enhance the contrast between heavier Pt and zeolite framework atoms. The iDPC images (**Figure S2.1**), which are more sensitive to the zeolite framework structures, were separately acquired to confirm extraframework species observed in ADF images are Pt atoms. In 1 wt% Pt-NaY

calcined at 873 K, Pt atoms are sprinkled throughout the images (**Fig. 2.5a**) acquired along [112] direction and appear along the zeolite lattice axis, indicating that these Pt species are residing inside the zeolite cages. ADF image showing the zeolite lattice along the [110] direction was resolved and Pt species appear in whiter contrast in **Figure 2.5b**. Pt single atoms in hexagonal prisms are pointed by red arrows, and a few Pt clusters are indicated by white arrows. The features with brighter contrasts are ~1Å in diameter, consistent with single atoms. The majority of the Pt in 873 K 1 wt% Pt-NaY materials are Pt single atom cations, while there are still a small fraction of Pt clusters with 4-5 atoms present as evidenced by TEM analyses. These single-atom Pt cations can be either Pt^{+}, Pt^{2+}, Pt^{3+}, and/or Pt^{4+}, which are the most stable Pt oxidation states. Pt^{+} and Pt^{3+} are paramagnetic such that they can be directly detected by Electron Paramagnetic Resonance (EPR) techniques. It has been shown by Akdogan et al.[17] that calcination of Pt-Y zeolite under an oxygen-deficient environment results in paramagnetic Pt moieties, *e.g.*, Pt^{+} and Pt^{3+}. However, Pt-NaY materials in this study are calcined under flowing dry air, hence resulting in only diamagnetic Pt species as evidenced by EPR measurements. Only EPR signals observed from these air-calcined samples (even at high 15 wt% loadings) were from a dilute amount of Fe^{3+} impurity of the parent zeolite. As a control, Pt-NaY samples were also prepared under flowing N_2, and the samples clearly show a broad EPR signal (**Figure S2.2**) corresponding to paramagnetic Pt species, Pt^{+} and/or Pt^{3+}. Therefore, Pt single atom cations present in air-calcined Pt-NaY are confirmed to be either Pt^{2+} or Pt^{4+}. However, based on DFT calculations of EXAFS measurements, the most stable cation present in the Pt-NaY is Pt^{2+} that are charge-balanced by negative-charge bearing oxygen

atoms bonded to tetrahedral Si and Al sites in Y-zeolite. Moreover, these Pt^{2+} cation species behaving as a charge balancing cations of the Y zeolite influence the distributions of the other cation, Na^{+}, present in the Y zeolite, which is evidenced by ^{23}Na NMR measurements discussed in the following section.

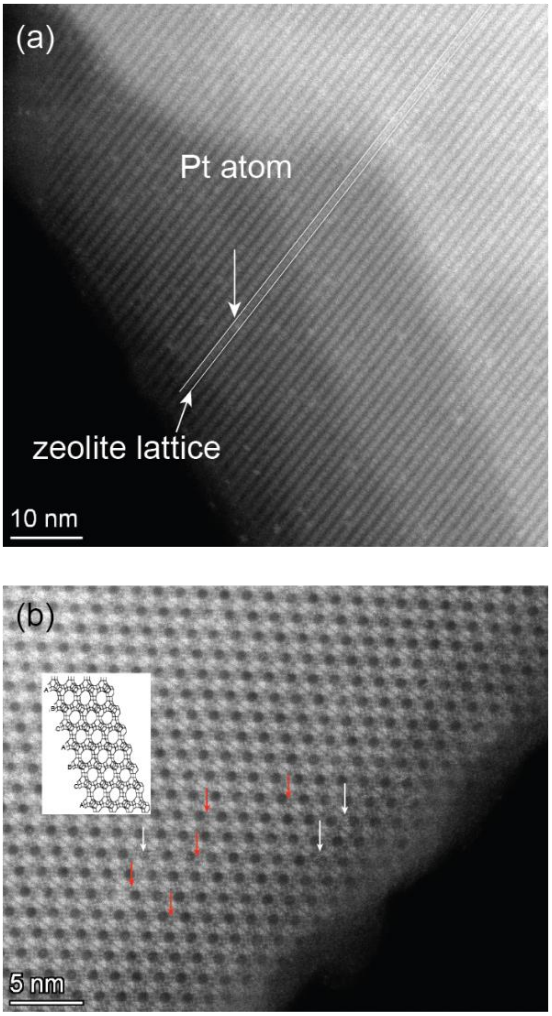

Figure 2.5. Annular Dark Field High-Resolution TEM images of 1 wt% Pt-NaY calcined at 873 K view along (a) [112] and (b) [110] direction. < 3Å Pt species are located along the zeolite lattice in (a). In the higher resolution image (b), distributions of Pt species are located inside the FAU framework. The majority of the Pt are single atoms indicated by red arrows and clusters of 4-5 Pt atoms are pointed by white arrows

Correlated distributions of Na^+ and Pt^{2+} cations in Pt-NaY zeolite. Relative populations of ^{23}Na cations located at different sites in the framework zeolite are identified by quantitative ^{23}Na NMR of dehydrated zeolites. Although ^{23}Na nuclei have almost 100% natural abundance, the quadrupolar nature of the nuclei makes the resolution of the signals challenging due to overlapping signals from broad quadrupolar lineshapes. Fortunately, quadrupolar interaction scales inversely with the external magnetic field, B_o,[20,21] thus high-field measurements in combination with spin manipulation methods such as Multiple Quantum Magic Angle Spinning (MQMAS) enable the resolution of the signals. ^{23}Na MQMAS NMR spectrum at 35.2 T (highest magnetic field available for solid-state NMR measurements)[22] of dehydrated NaY zeolite is shown in **Figure 2.6a**. With the Si/Al ratio of 2.5, FAU zeolite contains 55 charge balancing exchangeable cation sites per unit cell, *i.e.*, $Si_{137}Al_{55}Na_{55}O_{384}$. There are seven locally different sites that extraframework cations can be located.[23] However, only six of them are energetically favorable locations for Na^+ for a given Si/Al ratio, and there are three main distinct environments from which ^{23}Na signals can be resolved. The charge balancing Na^+ cations can reside at site SI, the center of the double-6-ring; SII, near the 6-ring to the supercage side; and SI', near the 6-ring to the sodalite cage side as illustrated in **Figure 2.1a**. ^{23}Na cations located in different cages of dehydrated zeolite are surrounded by different electronic environments, hence these ^{23}Na cations exhibit different chemical isotropic shifts and quadrupolar broadening.[24–27]

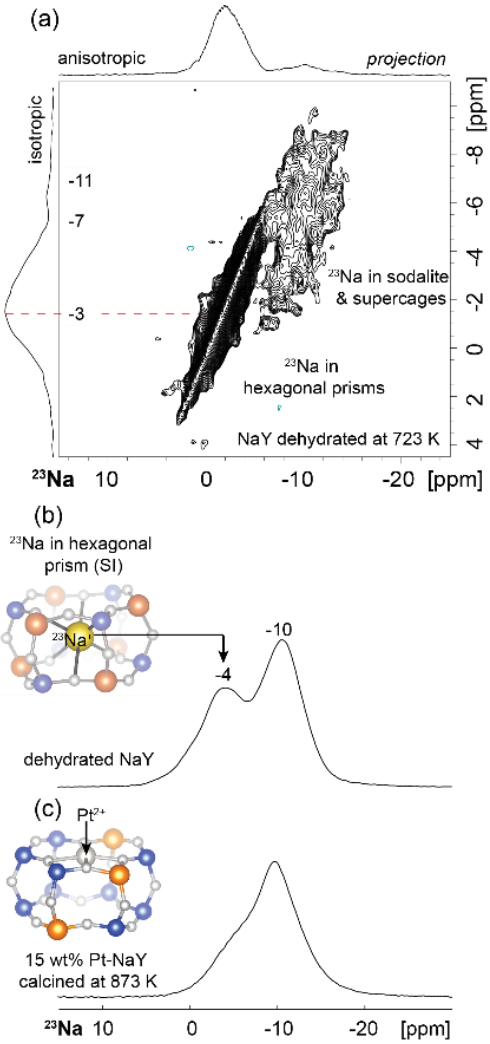

Figure 2.6. Differences in ^{23}Na distributions between dehydrated NaY and calcined Pt-NaY. Solid-state ^{23}Na (a) MQMAS and (b) single-pulse spectra of dehydrated NaY zeolite, (c) single-pulse spectrum of 15 wt% Pt-NaY calcined at 873 K acquired at 35.2 T, ^{29}8 K, and 24 kHz MAS.

In contrast, ^{23}Na cations in hydrated NaY zeolite are solvated in adsorbed water molecules, and the ^{23}Na spectrum of hydrated zeolite has one sharp peak at -3 ppm (**Figure S2.3**) almost identical to a solution-state spectrum. The MQMAS spectrum in **Figure 2.6a** shows anisotropic dimension in the horizontal axis and isotropic distribution in the vertical axis, which reveals distinct isotropic signals from ^{23}Na at -4,

-7, and -11 ppm. The signal at -4 ppm arises from ^{23}Na cations located at SI-site in hexagonal prisms. Because of their octahedrally symmetric local structure, ^{23}Na in hexagonal prisms have negligible quadrupolar coupling constant, thus exhibiting a ^{23}Na signal with a Gaussian lineshape instead of a quadrupolar broadened signal pattern. The broad signal that appears at ca. -10 ppm in the anisotropic dimension is due to an overlapping signal from ^{23}Na cations at SI' and SII sites, which are well-resolved in the isotropic dimension of the MQMAS conducted at high-field.

To understand the effects of Pt species in 873 K calcined Pt-NaY on the distributions of ^{23}Na cations, ^{23}Na spectra of the pristine dehydrated NaY zeolite, and 873 K calcined Pt-NaY are compared in **Figure 2.6b**,**c**. Higher loading of 15 wt% Pt-NaY calcined at 873 K is used to show the promoted differences in signal intensities of NaY and Pt-NaY. The relative intensities of ^{23}Na signals from hexagonal prism sites are significantly reduced in 873 K calcined 15 wt% Pt-NaY, indicating that Na^+ at site SI are absent, which was also consistent with XRD refinement analyses discussed below. This change in distributions of ^{23}Na cations in calcined Pt-NaY zeolite is due to the formation of Pt^{2+} occupying the hexagonal prism sites and charge balance the zeolite framework Al sites as illustrated in **Figure 2.6b**. The effects of such Pt^{2+} cation species strongly interacting with the zeolite framework sites are also identified by ^{27}Al{^{29}Si} 2D NMR analyses (**Fig. 2.4**) discussed in the previous section. Pt^{2+} cations residing at the center of the 6-membered ring repels the Na^+ in the site SI (**Fig 2.6b** schematics) due to charge repulsion, resulting in a vacancy of ^{23}Na at the center of the double six-ring, which was manifested by decreased signal intensities of -4 ppm peak. This result is consistent with the refinement analyses, which revealed that SI-

site is empty in 873 K calcined Pt-NaY. Redistribution of ^{23}Na cations at different sites in 873 K calcined Pt-NaY suggests competition between Pt^{2+} and Na^{+} cations at certain sites, and further enforces the suggested structure of energetically favorable Pt^{2+} at the center of 6-ring in the prism.

To further analyze the interactions between distinct ^{29}Si sites and ^{23}Na cations located at different, ^{23}Na-^{29}Si through-space mediated 2D NMR measurements are conducted. 2D dipolar-mediated HMQC NMR spectra of parent NaY, 15 wt%, and 1 wt Pt-NaY calcined at 873 K are shown in **Figure 2.6**. Moreover, the ionic nature of the interaction between the extraframework $^{23}Na^{+}$ and ^{29}Si sites are corroborated by the resulting null signal in *J*-mediated $^{23}Na\{^{29}Si\}$ HMQC experiments, but well-resolved correlated intensities in dipolar-mediated $^{23}Na\{^{29}Si\}$ measurements. **Figure 2.4a** shows 2D $^{23}Na\{^{29}Si\}$ *D*-HMQC NMR spectrum of dehydrated NaY. ^{29}Si signal is resolved along the horizontal axis. ^{29}Si signals at -90, -94, -99, and -102 ppm arise due to $Q^4(3Al)$, $Q^4(2Al)$, $Q^4(1Al)$, and $Q^4(0Al)$ ^{29}Si sites respectively. As discussed previously, the ^{23}Na signal at -4 ppm is from ^{23}Na cations located at the center of the double-6-ring, and ^{23}Na sites in the supercages and sodalite cages give rise to signal at -15 and -20 ppm. Well-resolved correlated intensities from dehydrated parent NaY reveal unambiguous through-space interactions between distinct ^{29}Si sites, including siliceous ^{29}Si species and ^{23}Na sites. Different $^{23}Na\{^{29}Si\}$ interactions are identified in calcined Pt-NaY compared to calcined parent NaY. For both 15 wt% and 1 wt% Pt-NaY (**Fig. 2.8b,c**), distinct ^{29}Si sites give rise to signal at -104, -101, -95, and -89 ppm correspond to $Q^4(3Al)$, $Q^4(2Al)$, $Q^4(1Al)$, and $Q^4(0Al)$ ^{29}Si sites respectively. Notably, the new ^{29}Si signal at -86 ppm, which arises ^{29}Si sites near Pt^{2+}, interacts only with

^{23}Na sites in supercages and sodalite cages, *i. e*. no interaction between ^{23}Na cations located in the middle of double-6-ring and new ^{29}Si sites proximate to Pt (**Fig. 2.8b**). This is consistent with the DFT calculations and refinement analyses of X-ray diffractions, in which Pt^{2+} is energetically most favorable when coordinated with 4 framework oxygen atoms of the 6-membered ring and occupancies of SI sites (center of the double-6-ring) are empty in 873 K calcined Pt-NaY, respectively. The conclusion is still consistent for lower 1 wt% Pt-NaY calcined at 873 K (**Fig. 2.8c**), such that only ^{23}Na cations are located in the supercages and sodalite cages (with ^{23}Na signal centered ca. -18 ppm) interact with the new ^{29}Si sites with a signal at -86 ppm.

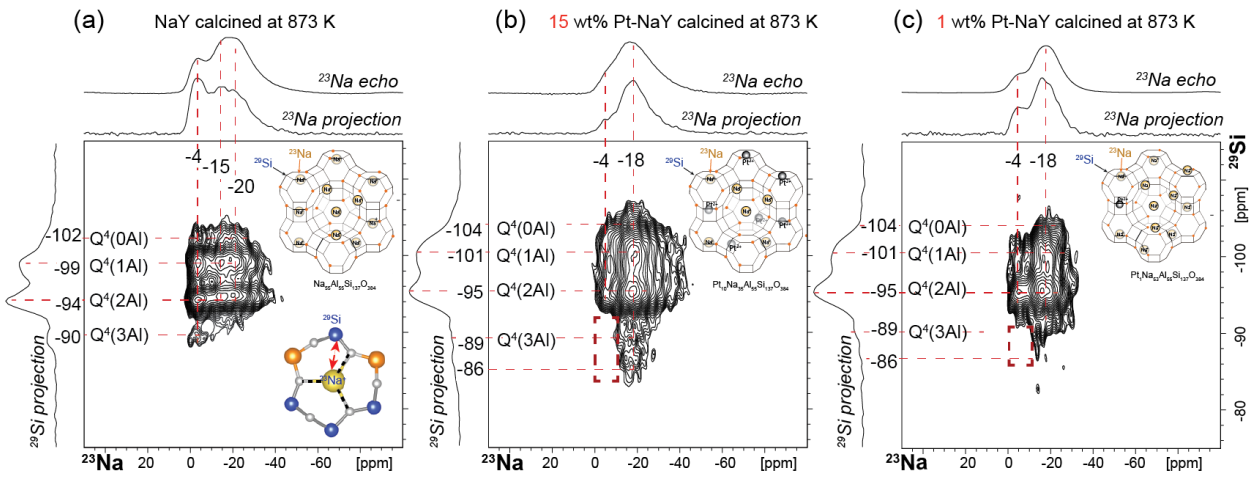

Figure 2.7. Solid-state 2D dipolar-media ted (through-space) ^{23}Na{^{29}Si} HMQC NMR correlation spectra of a. dehydrated NaY zeolite, b. 15 wt%, and c. 1 wt% Pt-NaY calcined at 873 K. The spectra are acquired at 9.4 T, 95 K, and 8 kHz MAS, with $sr4^2_1$ dipolar recoupling pulse with a recoupling time of 5 ms. 1D Hahn-echo ^{23}Na spectra acquired under the same conditions are shown along the horizontal axes of each corresponding spectrum for comparison with the projections of the 2D spectra.

Different locations of Pt species in the FAU framework in Pt-NaY are identified by X-ray powder diffraction. Noticeable differences in intensities of XRD powder patterns of NaY and Pt-NaY calcined at different temperatures are observed when Pt loading was high 15 wt% (**Fig. S2.4**). For lower and industrially relevant Pt loading of 1 wt%, detailed refinement analyses are necessary to identify locations of heavy Pt atoms in the FAU framework. The WAXS powder patterns of 1 wt% Pt-NaY calcined at 873 K were acquired and analyzed by Rietveld refinement methods to identify occupancies of extraframework charges, *i.e.*, Na^+ and Pt^{2+} cations, in Pt-NaY. The unit cell matches the $Fd\bar{3}m$ cell for FAU framework of NaY zeolite, indicating that the bulk crystallinity of the zeolite is not affected by the addition of Pt and calcination under the conditions.

Significant differences in the intensities of some reflections between the powder patterns of the Pt-NaY calcined at 873 K, caused by different electron density occupancies of non-framework cation sites. **Figure 2.8a** shows WAXS powder patterns of 1 wt% Pt-NaY calcined at 873 K. Crystal structure refinement analyses found that electron density of extraframework cations in 873 K calcined Pt-NaY is ca. 25% more than that of parent NaY. This indicates the presence of heavier Pt inside the zeolite framework of Pt-NaY treated at higher temperatures because the electron density of one Pt equals seven Na atoms. Moreover, refinement analyses revealed occupancies of cation sites, either Pt^{2+}, Na^+, or H^+, in calcined Pt-NaY. Interestingly, cation positions in the center of the double-6-ring (SI site) were empty in 873 K calcined Pt-NaY. Based on DFT calculations Pt^{2+} is most stable when it is coordinated with four oxygen atoms of the 6-membered rings of the framework structure. Therefore, it is likely that Pt^{2+} occupies its most energetically favorable position, which

is at the center of the 6-membered ring and repels Na^+ cations from the center of the double-6-ring. Difference electron density maps were analyzed to locate the non-framework species. Electron density of extraframework species is expressed in terms of Na equivalent charge densities. While parent NaY has extraframework electron density corresponding to 55 equivalent Na cations, Pt-NaY calcined at 873 K has 70 equivalent Na cation charge densities indicating successful encapsulation of heavier Pt^{2+} cations (7 Na^+ cation density is equivalent to 1 Pt^{2+}) inside the cages of Y zeolite.

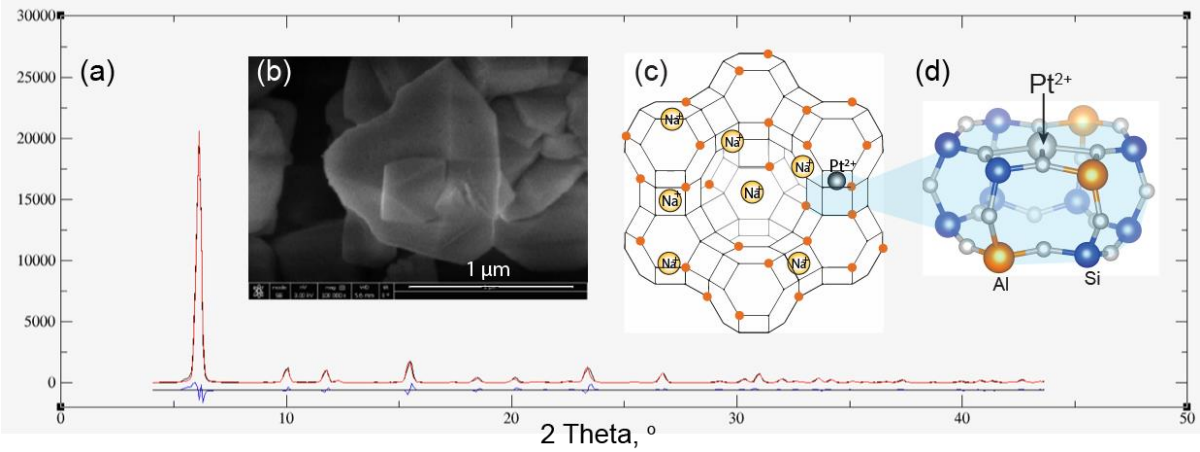

Figure 2.8. WAXS pattern of (a) 1 wt% Pt-NaY calcined at 873 K. Black line is the data, red is simulated powder pattern with Pt^{2+} located at the center of the 6-membered ring as shown in (c) and zoomed in (d), blue is the difference between data and calculated powder pattern. (b) SEM image of NaY zeolite

The electron densities corresponding to cation sites in the center of the hexagonal prisms have disappeared in 873 K calcined Pt-NaY. Consequently, cation site density on the sodalite cage side of the D6R has increased, indicating that electron-dense cations, *e.g.*, Pt^{2+}, have occupied the D6R site, which is consistent with what we have observed from ^{23}Na NMR analyses. Also, a new position on the sodalite cage side of the single 6-ring has appeared due to Pt cations. The SII and SII' positions (on the supercage and sodalite cage sides of the single 6-ring) cannot be occupied

simultaneously by cations (they would be too close to one another with a distance of 2.95 Å), so the presence of Pt might explain that apparent discrepancy. The results obtained from the refinement analyses agree with the ^{23}Na NMR results and the effect of Pt^{2+} cations revealed by ^{27}Al{^{29}Si} NMR measurements obtained from 873 K calcined Pt-NaY. The following sections will discuss the comparisons between these analyses acquired from 873 K calcined Pt-NaY with 673 K calcined Pt-NaY, which contains mainly Pt clusters instead of Pt^{2+} cations.

2.4.2 Pt particles in supercages of Y zeolite: 673 K calcined Pt-NaY. Broad distributions of Pt species, *e.g.*, clusters of Pt with 4-5 atoms located inside supercages of the zeolite Y and a small amount of Pt^{2+} cation species when Pt-NaY is calcined at milder temperatures compared to previous cases of 873 K. High-resolution transmission electron microscopy (HRTEM) images of 1 wt% Pt-NaY calcined at 673 K is shown in **Figure 2.10**. The images were acquired by Annular Dark Field (ADF) mode, which detects the electrons transmitted to higher angles, to enhance the contrast between heavier Pt and zeolite framework atoms. For both images, zeolite lattice along the [112] direction was resolved and Pt species appear in whiter contrast. However, the sizes and distributions of Pt on the zeolite are significantly different compared to Pt-NaY materials calcined at 873 K, which was discussed in previous sections. 673 K calcined Pt-NaY contains larger Pt clusters (1-3 nm) and a few smaller (<3 Å) Pt positioned along the zeolite lattice (**Fig. 2.10b**). These larger Pt particles are either residing on the surface of zeolite crystallite or inside the larger supercages of the Y zeolite. 873 K calcined single Pt-atom containing sample color is almost white compared to a darker-grey colored sample of 673 K

calcined Pt-NaY, which contains Pt clusters. Small Pt atoms are located inside the zeolite lattice, which is indicated by parallel lines. **Figure 2.9** shows HRTEM images with higher resolution in zeolite framework atoms and distributions of Pt species. The sizes and distributions of Pt on the zeolite are significantly different between Pt-NaY materials calcined at 873 K and 673 K. The majority of the Pt in 673 K calcined Pt-NaY form surface oxided Pt clusters, which would have a negligible influence on the framework T-sites compared to Pt^{2+} coordinated with framework oxygen atoms.

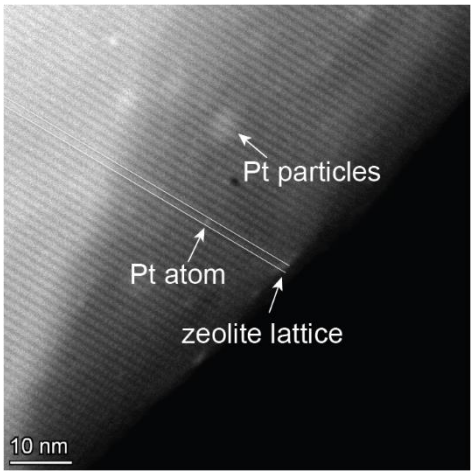

Figure 2.9. Representative annular dark-field high-resolution TEM image of 1 wt% Pt-NaY calcined at 673 K viewed along the [112] direction. Most of the Pt appears to be present as 1-3 nm diameter particles. Heavy Pt atoms appear as brighter contrasts

The differences in the local-bonding-environments of framework zeolite NaY and calcined Pt-NaY revealed the effects of Pt species on the support zeolite framework sites. ^{29}Si-O-^{27}Al through-bond interactions of NaY zeolite are elucidated by two-dimensional (2D) solid-state *J*-mediated ^{27}Al{^{29}Si} heteronuclear multiple quantum ^{27}Al{^{29}Si} HMQC NMR spectra of 673 K calcined (a) NaY, (b) 15 wt% Pt-NaY, and (c) 1 wt% Pt-NaY. Correlated signal intensities of each spectrum show an unambiguous through-bond correlation between framework ^{27}Al and ^{29}Si sites. The directly detected

^{27}Al signal is depicted along the horizontal axis, while the indirectly detected ^{29}Si signal stays along the vertical axis. ^{27}Al signal for all three spectra is broad distributions with a center peak around 55 ppm, which corresponds to 4-coordinated ^{27}Al. The absence of a ^{27}Al signal around 0 ppm, which arises from octahedral extraframework ^{27}Al sites, indicates ^{27}Al signals in calcined NaY and Pt-NaY are zeolite, 15 wt%, and 1 wt% Pt-NaY calcined at 873 K are shown in **Figure 2.5**. Pt^{2+} influences the local electronic environments of nearby ^{29}Si and ^{27}Al sites. When Pt is present, ^{29}Si sites with 1, 2, and 3 Al neighbors are resolved at -101, -95, -91 ppm for both loadings of Pt, (**Fig. 5b**) 15 wt%, and 1 wt% (**Fig. 2.5c**). The new ^{29}Si signal at -86 ppm is only present in calcined Pt-NaY and assigned to ^{29}Si sites proximate to Pt^{2+}, which changes the electronic environments of the nearby sites as well as the bond angle between T-O-T connections. The intensity of such new ^{29}Si peak at -86 ppm is much higher for 15 wt% calcined Pt-NaY, but still present in 1 wt% Pt-NaY calcined at 873 K. Moreover, the dilute amount of such small Pt species interacting strongly with the framework is found in 673 K calcined Pt-NaY. This is consistent with the refinement analyses and HRTEM images. The majority of the Pt in 673 K calcined Pt-NaY form surface oxided Pt clusters, which have a negligible influence on the framework T-sites compared to Pt^{2+} coordinated with framework oxygen atoms.

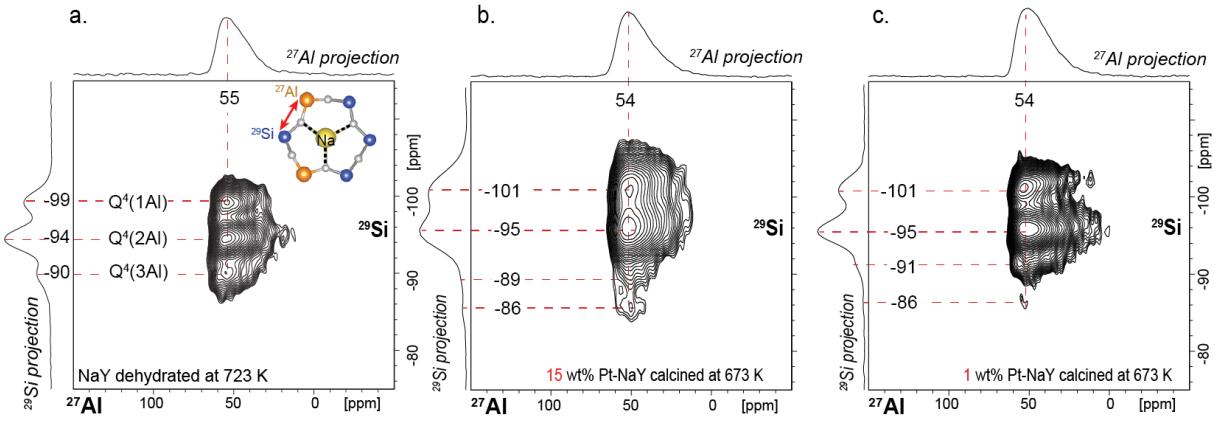

Figure 2.10. Solid-state 2D *J*-mediated (through-covalent-bond) ^{27}Al{^{29}Si} HMQC correlation spectra of a. NaY zeolite dehydrated at 723 K, b. 15 wt%, and c. 1 wt% Pt-NaY calcined at 673 K. The spectra are acquired at 9.4 T, 95 K, and 8 kHz MAS.

Interactions between distinct ^{29}Si sites and ^{23}Na cations located at different sites are identified by ^{23}Na-^{29}Si through-space mediated experiments. 2D dipolar-mediated ^{23}Na{^{29}Si} HMQC NMR spectra of parent NaY, 15 wt%, and 1 wt% Pt-NaY calcined at 873 K are shown in **Figure 2.11**. Moreover, the ionic nature of the interaction between the extraframework $^{23}Na^{+}$ and ^{29}Si sites are corroborated by the resulting null signal in *J*-mediated ^{23}Na{^{29}Si} HMQC experiments, but well-resolved correlated intensities in dipolar-mediated ^{23}Na{^{29}Si} measurements. **Figure 2.11a** shows 2D ^{23}Na{^{29}Si} *D*-HMQC NMR spectrum of dehydrated NaY. ^{29}Si signal is resolved along the horizontal axis. ^{29}Si signals at -90, -94, -99, and -102 ppm arise due to Q^4(3Al), Q^4(2Al), Q^4(1Al), and Q^4(0Al) ^{29}Si sites respectively. As discussed previously, the ^{23}Na signal at -4 ppm is from ^{23}Na cations located at the center of the double-6-ring, and ^{23}Na sites in the supercages and sodalite cages give rise to signal at -15 and -20 ppm. Correlated intensities from dehydrated parent NaY reveal unambiguous through-space interactions between distinct ^{29}Si sites, including siliceous ^{29}Si species and ^{23}Na sites.

Different $^{23}Na\{^{29}Si\}$ interactions are identified in calcined Pt-NaY compared to calcined parent NaY. For both 15 wt% and 1 wt% Pt-NaY (**Fig. 2.8b, c**), distinct ^{29}Si sites give rise to signal at -104, -101, -95, and -89 ppm correspond to Q^4(3Al), Q^4(2Al), Q^4(1Al), and Q^4(0Al) ^{29}Si sites respectively. Notably, the new ^{29}Si signal at -86 ppm, which arise due to ^{29}Si sites near Pt^{2+}, interact only with ^{23}Na sites in supercages and sodalite cages, *i.e.* no interaction between ^{23}Na cations located in the middle of double-6-ring and new ^{29}Si sites proximate to Pt This is consistent with the DFT calculations and refinement analyses of X-ray diffractions, in which Pt^{2+} is energetically most favorable when coordinated with 4 framework oxygen atoms of the 6-membered ring and occupancies of SI sites (center of the double-6-ring) are empty in 673 K calcined Pt-NaY, respectively. The conclusion is still consistent for lower 1 wt% Pt-NaY calcined at 673 K (**Fig. 2.11c**), such that only ^{23}Na cations that are located in the supercages and sodalite cages (with ^{23}Na signal centered ca. -18 ppm) interact with the new ^{29}Si sites with a signal at -86 ppm, which arises due to ^{29}Si moieties close to Pt^{2+} cations. The above analyses are focused on identifying the influences of different types of Pt on the zeolite support and extraframework Na^+ cation distributions. The following sections will discuss the advantages and challenges of directly probing Pt species by techniques such as ^{195}Pt NMR and EXAFS measurements

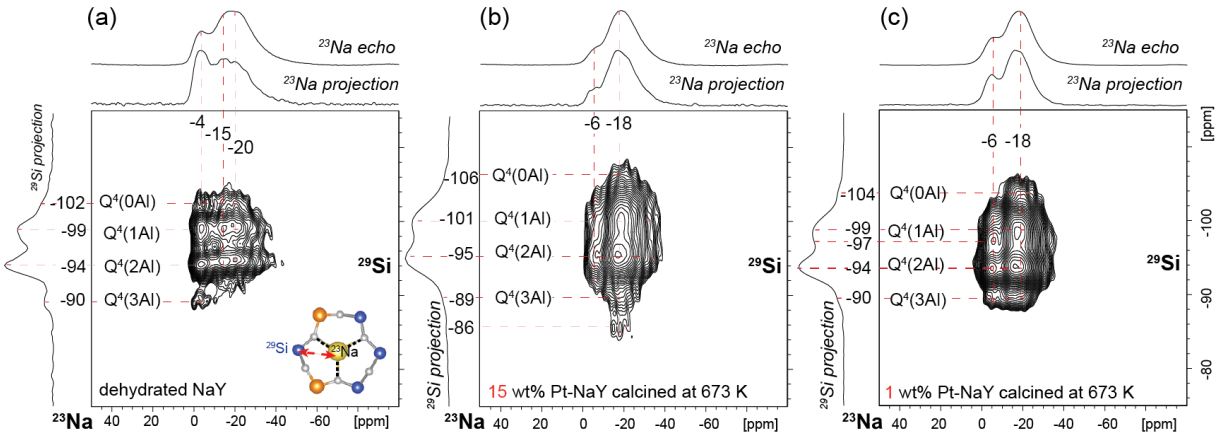

Figure 2.11. Solid-state 2D dipolar-media ted (through-space) ^{23}Na{ Si} HMQC NMR correlation spectra of a. dehydrated NaY zeolite, b. 15 wt% and c. 1 wt% Pt-NaY calcined at 673 K. The spectra are acquired at 9.4 T, 95 K, and 8 kHz MAS, with SR4$^{2}_{1}$ dipolar recoupling pulse with a recoupling time of 5 ms. 1D Hahn-echo ^{23}Na spectra acquired under the same conditions are shown along the horizontal axes of each corresponding spectrum for comparison with the projections of the 2D spectra

2.4.3 Direct detection of Pt in NaY

Pt species supported on NaY zeolite can be directly probed by techniques that are sensitive to electronic environments of Pt species, such as EXAFS and ^{195}Pt NMR. The coordination of Pt^{2+} with the framework oxygen in calcined Pt-NaY was identified by EXAFS analyses. **Figure 2.12** shows EXAFS spectra of 1wt% Pt-NaY calcined at 873 K. By fitting the experimental data, the coordination number of Pt-O was found to be four, which is consistent with the most stable coordination of Pt^{2+} located at the center of the 6-membered ring of the zeolite framework. In contrast, when Pt-NaY is calcined at 673 K, the EXAFS spectrum contains features for both Pt-Pt metal coordination as well as Pt-O coordination (**Fig. S2.5**) which makes it challenging to deconvolute and assign coordination numbers of broad distributions of Pt species.

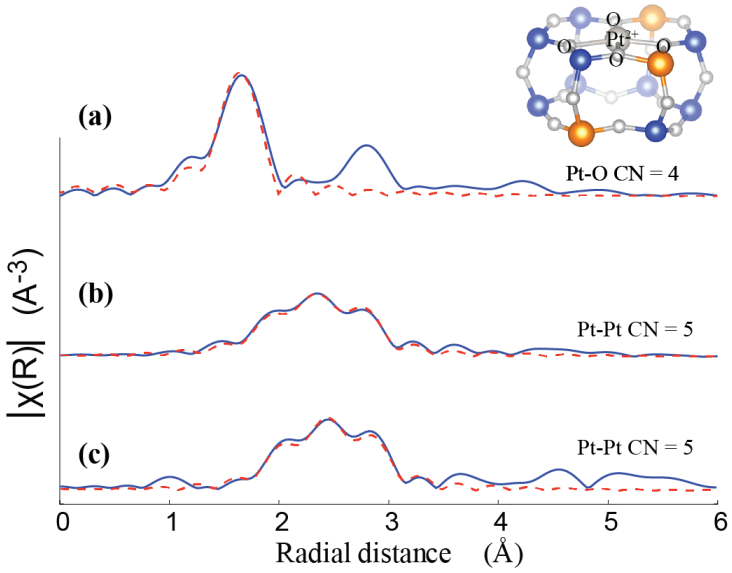

Figure 2.12. FT-EXAFS spectra of 1 wt% Pt-NaY calcined at (a) 873 K and (b) after in-situ H_2 reduction at 673 K (c) after in-situ reduction-oxidation-reduction cycle. Red dashed lines are (a) Pt-O and (b,c) Pt-Pt fitted contributions to the experimental data.

Table 2.1. Pt-O and Pt-Pt coordination numbers (*N*), interatomic distances (*R*) for 1 wt% Pt-NaY calcined at (a) 873 K and (b) after in-situ H_2 reduction at 673 K, (c) after in-situ reduction-oxidation-reduction[a]

	N	*R*, Å
Pt-O	3.5±0.5	2.02±0.02
Pt-Pt	5±0.5	1.9±0.02
Pt-Pt	6.7 ±0.4	2.7±0.03

[a] EXAFS data at the Pt-L_3 edge

Local environments of platinum active sites can be probed by direct detection of ^{195}Pt NMR, which is expected to provide valuable information about the electronic structures of Pt species. However, molecular heterogeneity of small Pt particles and strong hyperfine interactions between ^{195}Pt nuclei and conducting electrons make the ^{195}Pt chemical shift very broad (~MHz) due to the metallic nature of Pt (known as the Knight shift) and broad distributions of electronic environments[28–36] compared to conventionally measured nuclei such as ^{13}C (~kHz). Moreover, the low loading of Pt in the heterogeneous catalysts (<1 wt%) further increases the challenges of acquiring ^{195}Pt NMR spectra. Due to these challenges, not many studies on direct-detection of ^{195}Pt-NMR of heterogeneous Pt-zeolite catalyst are present in the literature.[31,37–42] Moreover, acquiring solid-state NMR spectra of nuclei with broad lineshapes can be challenging due to the limited ability of a standard rectangular radiofrequency pulse to excite a broadband spectrum. Some earlier works of ^{195}Pt NMR of 10 wt% Pt on alumina supports have used a technique called point-by-point, in which only a small part (~ kHz) of the full spectrum is excited by ^{195}Pt spin-echo experiment, and the entire manifold of the spectrum was constructed by sampling at multiple offset frequencies. These experiments are tedious and take a long time (~over a month to acquire the spectrum of 10 wt% Pt - alumina). Advanced pulse-sequence methods developed by Kupce and Freeman,[43] make it possible to uniformly excite broadband spectra by using adiabatic pulses instead of hard rectangular pulses.

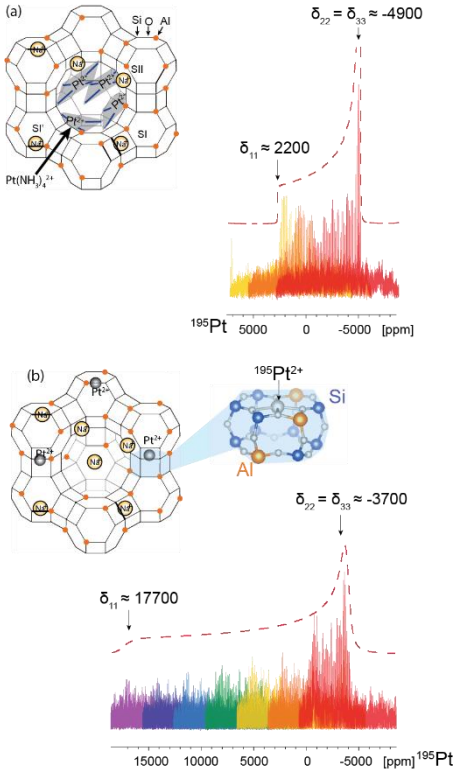

Figure 2.13. ^{195}Pt WURST-CPMG spectra of 15 wt% Pt-NaY calcined at (a) 473 K and (b) 873 K. The spectra are acquired at 9.4 T, $^{29}8$ K. The simulated chemical shift anisotropy (CSA) powder patterns are shown as a dotted line and overlayed on top of each spectrum. The CSA tensors values of ^{195}Pt spectrum of 473 K calcined Pt-NaY match the values of Pt-tetraamine salt (**Fig. 2.9**), indicating that $Pt(NH_3)_4Cl_2$ are intact at 473 K calcination. ^{195}Pt moieties in 873 K calcined Pt-NaY reveal axial symmetry, which agrees with the assignment of Pt species in well-defined environments.

Structural insights of platinum species in Pt-NaY are acquired by direct detection of ^{195}Pt NMR using adiabatic pulse-sequences, known as wideband-uniform-rate-smooth-truncation (WURST) CPMG techniques. The ^{195}Pt WURST-CPMG spectra of Pt-NaY calcined at 473 K and 873 K, which are shown in **Figure 2.13a, b**. Each colored subsection in the spectrum is a separate measurement at varying offset frequencies. ^{195}Pt NMR of 473 K calcined Pt-NaY reveals broad ^{195}Pt signals consistent with platinum tetraamine salt complex. As revealed by TGA analyses 473

K calcination temperature is not enough to decompose Pt-tetraamine precursor, hence the results are consistent with expectations. In contrast, the ^{195}Pt NMR spectrum of 873 K calcined Pt-NaY reveals a much broader signal, indicating broad distributions of chemical environments, and most importantly a sharp singularity at -3700 ppm. Instead of broad Gaussian lineshape, which would be expected from surface oxided Pt clusters, sharp singularity is an indication of signals from Pt species in a well-defined local environment, such as Pt^{2+} cations located at the center of 6-ring in hexagonal prisms of Y zeolite. The direct detection of ^{195}Pt enables us to confidently assign the types of Pt species present in calcined Pt-NaY materials.

2.5 Conclusions

Catalytic activities of Pt-zeolites are directly influenced by preparation conditions, *i.e.*, calcination a.[2,14] To maximize the use of precious metals supported on zeolite catalysts, it is crucial to carefully control the dispersions of metals and avoid the formation of large metal clusters. Detailed understandings of locations and identities of Pt metal species of Pt-zeolites treated at different conditions are necessary to control the dispersion of Pt on NaY zeolite. Calcination temperature-dependent types and locations of Pt moieties are identified. Detailed structural information was obtained from Pt-NaY calcined at 473 K, 673 K, and 873 K by using a combination of state-of-the-art HRTEM imaging techniques, EXAFS analyses, Rietveld refinement methods of X-ray powder patterns, and advanced solid-state NMR techniques. Square planar $Pt(NH_3)_4^{2+}$ was still intact and presumably residing inside the supercages of the NaY zeolite when Pt-NaY was calcined at 473 K. Higher calcination temperature of 673 K results in surface oxided Pt clusters with a diameter of 1-3 nm supported on zeolite

NaY. In contrast, calcination at 873 K yields well dispersed Pt^{2+} moieties residing inside the hexagonal cages of the zeolite. Pt^{2+} cations charge-balance anionic framework sites and compete with Na^{+} cations, which can be distinguished by their respective effects on the framework sites. Strong interactions between such Pt^{2+} and zeolite framework sites are manifested directly by distinct ^{29}Si-O-^{27}Al moieties and indirectly by ^{29}Si-^{23}Na interactions, as revealed by solid-state two-dimensional (2D) NMR measurements. A mild-calcination temperature (673 K) yields ~1 nm PtOx clusters with broad size distributions and surface heterogeneity, which were revealed by HRTEM, EXAFS, and ^{27}Al{^{29}Si}2D NMR analyses. Such atomic-level insights obtained from an important Pt-zeolite system are unprecedented and expected to guide the preparation of well-dispersed Pt metal species on zeolite catalysts.

Funding Sources

This research was supported by ExxonMobil Research and Engineering (Clinton, New Jersey).

Notes

The authors declare no competing financial interest.

ACKNOWLEDGMENT

The project was supported by ExxonMobil Research and Engineering. The solid-state NMR and WAXS measurements made use of shared facilities of the UCSB MRSEC (NSF DMR1720256), a member of the Materials Research Facilities Network (www.mrfn.org). High-field NMR measurements are acquired at the National High Magnetic Field Laboratory supported by the National Science Foundation through NSF/DMR-1644779 and the State of Florida. Synchrotron EXAFS measurements are conducted at 9-BM of the Advanced Photons Source, a U.S. Department of Energy

(DOE) Office of Science User Facility operated for the DOE Office of Science by Argonne National Laboratory under Contract No. DE-AC02-06CH11357. The authors are grateful to Professor Xiaodong Zou at Stockholm University for providing the opportunity to acquire HRTEM images.

References

(1) Gallezot, P.; Alarcon-Diaz, A.; Dalmon, J.-A.; Renouprez, A. J.; Imelik, B. Location and Dispersion of Platinum in PtY Zeolites. *Journal of Catalysis* **1975**, *39*, 334–349.

(2) Gallezot, P. The State and Catalytic Properties of Platinum and Palladium in Faujasite-Type Zeolites. *Catalysis Reviews Science and Engineering* **1979**, *20*, 121–154.

(3) Chmelka, B. F.; de Menorval, L. C.; Csencsits, R.; Ryoo, R.; Liu, S. B.; Radke, C. J.; Petersen, E. E.; Pines, A. Calcination-Dependence of Platinum Cluster Formation in NAY Zeolite: A ^{129}Xe NMR Study. *Studies in Surface Science and Catalysis* **1989**, *48*, 269–278.

(4) Chmelka, B. F.; Ryoo, R.; S.B. Liu; L.C. de Menorval; Radke, C. J.; Petersen, E. E.; Pines, A. Probing Metal Cluster Formation in NaY Zeolite by Xenon-129 NMR,. *Journal of American Chemical Society* **1988**, *110*, 4465–4467.

(5) de Graaf, J.; van Dillen, A. J.; de Jong, K. P.; Koningsberger, D. C. Preparation of Highly Dispersed Pt Particles in Zeolite Y with a Narrow Particle Size Distribution: Characterization by Hydrogen Chemisorption, TEM, EXAFS Spectroscopy, and Particle Modeling. *Journal of Catalysis* **2001**, *203*, 307–321.

(6) Exner, D.; Jaeger, N.; Möller, K.; Schulz-Ekloff, G. Thermal Analysis of the Decomposition Mechanism of Platinum and Palladium Tetrammine Faujasite X. *Journal of the Chemical Society, Faraday Transactions* **1982**, *78*, 3537–3544.

(7) Elena Pérez-Guevara; Molinillo, J. M. G.; Martínez de la Ossa, E. J.; Frontela, J.; Lázaro, J.; Franco, M. J. Selective Ring Opening of Ethylbenzene on Bifunctional Catalyst Pt–Ir over Hierarchical USY Zeolite. *Petroleum Chemistry* **2020**, *60*, 104–112.

(8) Thybaut, J. W.; Laxmi Narasimhan, C. S.; Marin, G. B.; Denayer, J. F. M.; Baron, G. v.; Jacobs, P. A.; Martens, J. A. Alkylcarbenium Ion Concentrations in Zeolite Pores during Octane Hydrocracking on Pt/H-USY Zeolite. *Catalysis Letters* **2004**, *94*, 81–88.

(9) Ma, Z.; Ghosh, A.; Asthana, N.; van Bokhoven, J. Visualization of Structural Changes During Deactivation and Regeneration of FAU Zeolite for Catalytic Fast Pyrolysis of Lignin Using NMR and Electron Microscopy Techniques. *ChemCatChem* **2018**, *10*, 4431–4437.

(10) Vieira Dos Santos, B. R.; Montoya Urbina, M.; Souza, M. J. B.; Garrido Pedrosa, A. M.; Silva, A. O. S.; Sobrinho, E. v.; Velasco Castedo, R. Preparation and Characterization of Pt-Dealuminated y Zeolite by TG/DTA and TPR. *Journal of Thermal Analysis and Calorimetry* **2015**, *119*, 391–399.

(11) Tzou, M. S.; Teo, B. K.; Sachtler', W. M. H. *Formation of Pt Particles in Y-Type Zeolites The Influence of Coexchanged Metal Cations*; 1988; Vol. 113.

(12) Vedrine, J. C.; Dufaux, M.; Naccache, C.; Imelik, B. X-Ray Photoelectron Spectroscopy Study of Pd and Pt Ions in Type Y-Zeolite Electron Transfer between Metal Aggregates and the Support as Evidenced by X-Ray Photoelectron Spectroscopy and Electron Spin Resonance. *Journal of the chemical society Faraday Transaction 1* **1978**, *74*, 440–449.

(13) Noviikov, J. , Kubelkovi, L., Brabec, L., Bastl Z., Jaeger , N. , Schulz-Ekloff, G. Pt0 in Alkali Faujusites. 1. Preparation by Thermal Decomposition of PtTA Ion in Vacuum. *Zeolites* **1996**, *16*, 173–183.

(14) Chmelka, B. F.; Went, G. T.; Csencsits, R.; Bell, A. T.; Petersen, E. E.; Radke, C. J. Oxidation of Reduced Platinum Clusters in Pt-NaY. *Journal of Catalysis* **1993**, *144*, 506–524.

(15) Ryoo, R.; Pak, C.; Chmelka, B. F. Macroscopic or Microscopic Information of Y Zeolite from ^{129}Xe n.m.r. Line Splitting. *Zeolites* **1990**, *10*, 790–793.

(16) Zilm, K. W.; Bonneviot, L.; Hamilton, D. M.; Webb, G. G.; Haller, G. L. Carbon-13 NMR Studies of CO Adsorbed on Supported Platinum and Palladium Catalysts Using Magic Angle Sample Spinning. *The Journal of Physical Chemistry* **1990**, *94*, 1463–1472.

(17) Akdogan, Y.; Vogt, C.; Bauer, M.; Bertagnolli, H.; Giurgiu, L.; Roduner, E. Platinum Species in the Pores of NaX, NaY and NaA Zeolites Studied Using EPR, XAS and FTIR Spectroscopiesw. *Physical Chemistry Chemical Physics* **2008**, *10*, 2952–2963.

(18) Ravel, B.; Newville, M. Synchrotron Radiation ATHENA, ARTEMIS, HEPHAESTUS: Data Analysis for X-Ray Absorption Spectroscopy Using IFEFFIT. *J. Synchrotron Rad* **2005**, *12*, 537–541.

(19) Wan, W.; Su, J.; Zou, X. D.; Willhammar, T. Transmission Electron Microscopy as an Important Tool for Characterization of Zeolite Structures. *Inorg. Chem. Front* **2018**, *5*, 2836.

(20) Ashbrook, S. E.; Sneddon, S. New Methods and Applications in Solid-state NMR Spectroscopy of Quadrupolar Nuclei. *Journal of the American Chemical Society* **2014**, *136*, 15440–15456.

(21) Amoureux, J.-P.; Pruski, M. MQMAS NMR: Experimental Strategies and Applications. *Encyclopedia of Magnetic Resonance*; 2008; p 1.

(22) Gan, Z.; Hung, I.; Wang, X.; Paulino, J.; Wu, G.; Litvak, I. M.; Gor'kov, P. L.; Brey, W. W.; Lendi, P.; Schiano, J. L.; Bird, M. D.; Dixon, I. R.; Toth, J.; Boebinger, G. S.; Cross, T. A. NMR Spectroscopy up to 35.2 T Using a Series-Connected Hybrid Magnet. *Journal of Magnetic Resonance* **2017**, *284*, 125–136.

(23) Mortier, W. J. *Compilation of Extra Framework Sites in Zeolites*; Butterworth Scientific Limited: London, 1982.

(24) Feuerstein, M.; Hunger, M.; Engelhardt, G.; Amoureux, J. P. Characterisation of Sodium Cations in Dehydrated Zeolite NaX by ^{23}Na NMR Spectroscopy. *Solid-state Nuclear Magnetic Resonance* **1996**, *7*, 95–103.

(25) Tijink, G. A., H.; Janssen, R.; Veeman, W. S. Investigation of the Hydration of Zeolite NaY by Two-Dimensional ^{23}Na Nutation NMR. *J. Am. Chem. Soc* **1987**, *109*, 61–65.

(26) Jelinek, R.; Ozkar, S.; Ozin, G. Extraframework Sodium Cation Sites in Sodium Zeolite Y Probed by ^{23}Na Double-Rotation NMR. *JACS* **1992**, *114*, 4907–4908.

(27) Hunger, M.; Engelhardt, G.; Koller, H.; Weitkamp, J. Characterization of Sodium Cations in Dehydrated Faujasites and Zeolite EMT by ^{23}Na DOR, 2D Nutation, and MAS NMR. *Solid-state Nuclear Magnetic Resonance Elsevier Science Publishers B.V* **1993**, *2*, 111–120.

(28) Carter, G. C.; Bennett, L. H.; Kahan, D. J. *Metallic Shifts in NMR: A Review of the Theory and Comprehensive Critical Data Compilation of Metallic Materials (Progress in Materials Science)*; Pergamon Press, 1977.

(29) Stokes, H. T.; Rhodes, H. E.; Wang, P.-K.; Slichter, C. P.; Sinfelt, J. H. NMR of Platinum Catalysts. III. Microscopic Variation of the Knight Shifts. *Physical Review B* **1982**, *26*.

(30) Knight, W. D. Nuclear Magnetic Resonance Shift in Metals. *Physical Review* **1949**, *76*, 1259–1261.

(31) Slichter, C. P. NMR Study of Pt Catalysts. *Surface Science* **1981**, *106*, 382–396.

(32) Slichter, C. P. The Discovery and Renaissance of Dynamic Nuclear Polarization. *Reports on Progress in Physics* **2014**, *77*, 1–15.

(33) Carvert, T. R.; Slichter, C. P. Polarization of Nuclear Spins in Metals. *Physical Review* **1953**, *92*, 212–213.

(34) Ansermet, J. P.; Slichter, C. P.; Sinfelt, J. H. Solid-state NMR Techniques for the Study of Surface Phenomena. *Properties in NMR Spectroscopy* **1990**, *22*, 401–421.

(35) Rhodes, H.; Wang, P.-K.; Stokes, H.; Slichter, C. P. NMR of Platinum Catalysts I. Line Shapes. *Physical Review B* **1982**, *26*, 3559–3569.

(36) Rhodes, H. E.; Wang, P.-K.; Makowka, C. D.; Rudaz, S. L.; Stokes, H. T.; Slichter, C. P.; Sinfelt, J. H. NMR of Platinum Catalysts. II. Relaxation. *Physical Review B* **1982**, *26*, 3569–3574.

(37) Rees, G. J.; Orr, S. T.; Barrett, L. O.; Fisher, J. M.; Houghton, J.; Spikes, G. H.; Theobald, B. R. C.; Thompsett, D.; Smith, M. E.; Hanna, J. v. Characterisation of Platinum-Based Fuel Cell Catalyst Materials Using ^{195}Pt Wideline Solid-state NMR. *Physical Chemistry Chemical Physics* **2013**, *15*, 17195.

(38) Appleton, T.; Hall, J.; Ralph, S.; Thompson, C. Reactions of Platinum(II) Aqua Complexes. 2. ^{195}Pt NMR Study of Reactions between the Tetraaquaplatinum(II) Cation and Chloride, Hydroxide, Perchlorate, Nitrate, Sulfate, Phosphate, and Acetate. *Inorganic Chemistry* **1984**, *23*, 3521–3252.

(39) Soorholtz, M.; Jones, L. C.; Samuelis, D.; Weidenthaler, C.; White, R. J.; Titirici, M.-M.; Cullen, D. A.; Zimmermann, T.; Antonietti, M.; Maier, J.; Palkovits, R.; Chmelka, B. F.; Schü, F. Local Platinum Environments in a Solid Analogue of the Molecular Periana Catalyst. *American Chemical Society Catalysis* **2016**, *6*, 2332–2340.

(40) Bucher, J. P.; van der Klink, J. J. Electronic Properties of Small Supported Pt Particles: NMR Study of ^{195}Pt Hyperfine Parameters. *Physical Review B* **1988**, *38*, 11038–11047.

(41) Tong, Y. Y.; Yonezawa, T.; Toshima, N.; van der Klink, J. J. Pt NMR of Polymer-Protected Pt/Pd Bimetallic Catalysts. *Journal of Physical Chemistry* **1996**, *100*, 730–733.

(42) Tan, F.; Du, B.; Danberry, A. L.; Park, I.-S.; Sung, Y.-E.; Tong, Y. A Comparative in Situ ^{195}Pt Electrochemical- NMR Investigation of PtRu Nanoparticles Supported on Diverse Carbon Nanomaterials. *Faraday discussions* **2008**, *140*, 139–153.

(43) Kupce, Ē.; Freeman, R. Stretched Adiabatic Pulses for Broadband Spin Inversion. *Journal of Magnetic Resonance, Series A* **1995**, *117*, 246–256.

SUPPORTING INFORMATION

Table S2.1. Properties of nuclei studied by solid-state NMR

	Nuclear spin	Natural abundance, %	Frequency (MHz)				Spectral reference
			9.4 T	**11.7 T**	**18.8 T**	**35.2 T**	
^{1}H	1/2	99.98	400	500	800	1500	^{1}H of TKS at 0.25 ppm
^{29}Si	1/2	4.7	80	99	160	299	^{29}Si of TKS at 9.85 ppm
^{27}Al	5/2	100	104	130	209	390	1 M $Al(NO_3)_3$ sol.in D_2O
^{23}Na	3/2	100	106	132	212	397	1 M NaBr solution in D_2O
^{195}Pt	1/2	34	86	107			1M Na_2PtCl_6 sol. in D_2O

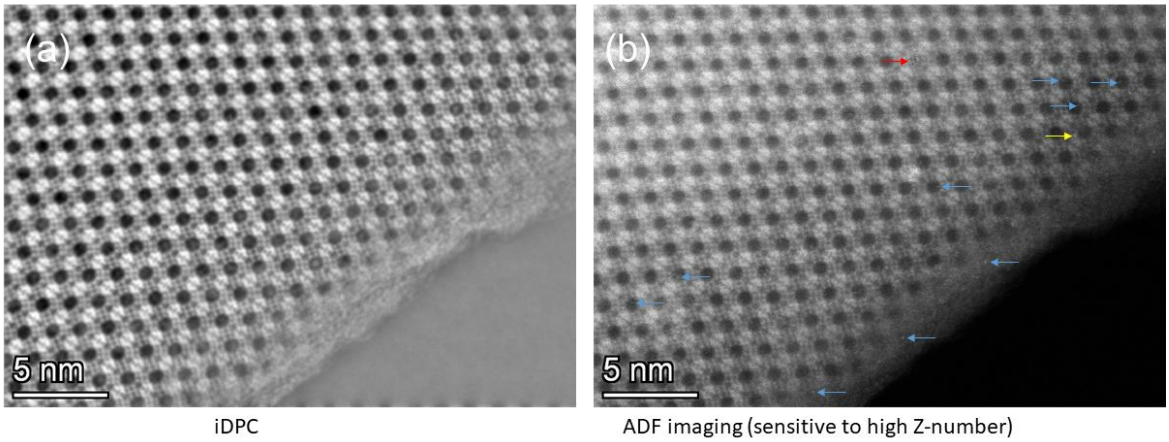

Figure S2.1 – Comparisons of (a) iDPC and (b) ADF images of 873 K calcined 1 wt% Pt-NaY.

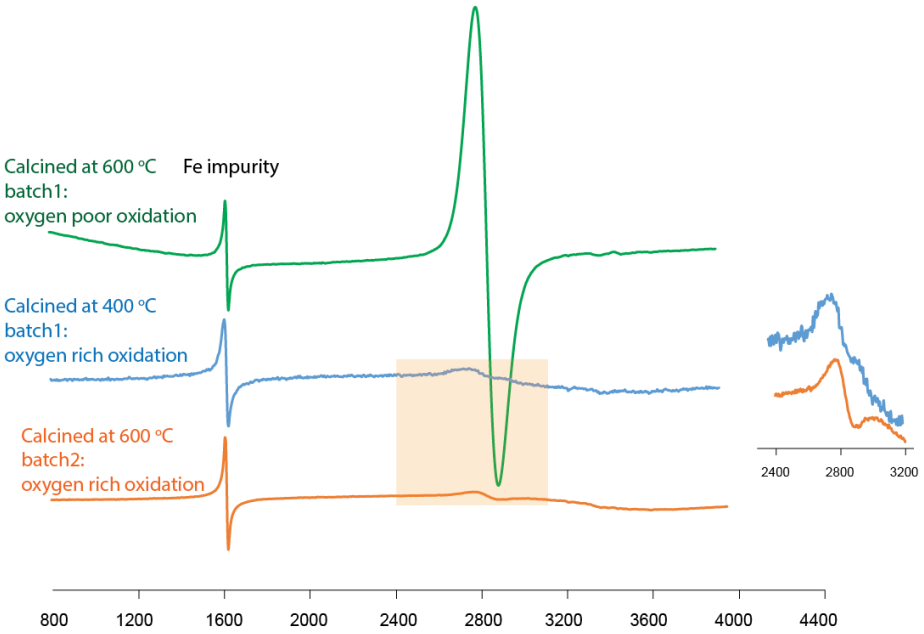

Figure S2.2. EPR spectra of 15 wt% Pt-NaY (a) calcined at 873 K under dry N_2 and (b) calcined at 873 K under flowing air, (c) calcined at 673 K under flowing air.

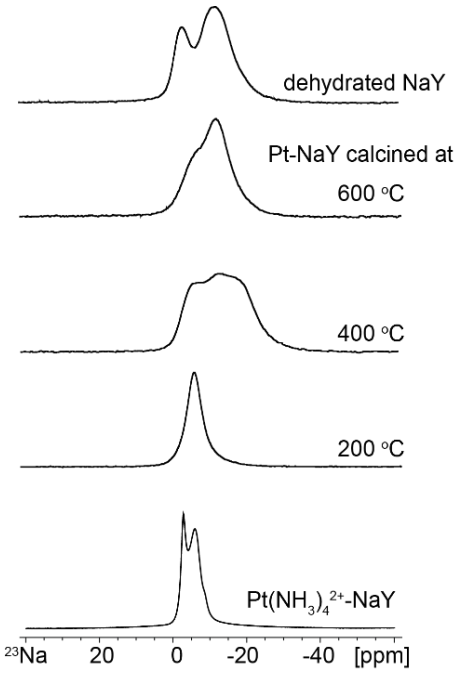

Figure S2.3. Solid-state single-pulse ^{23}Na MAS NMR of 15 wt% Pt-NaY calcined at different temperatures acquired at 18.8 T, 298 K, and 20 kHz MAS.

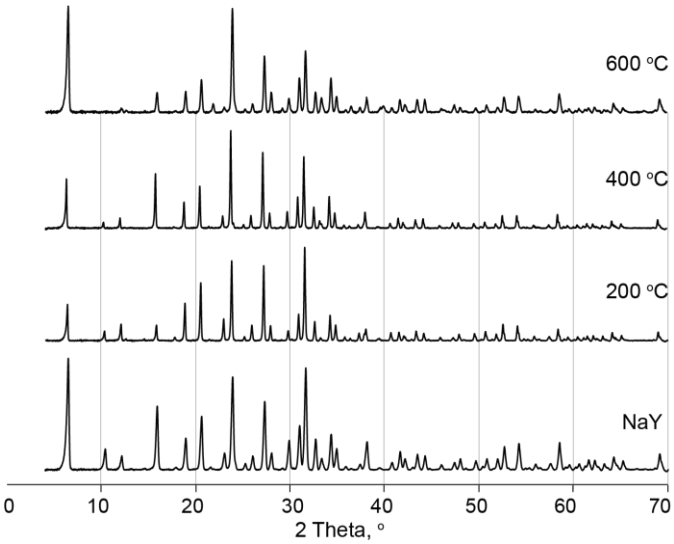

Figure S2.4. XRD powder patterns of 15 wt% Pt-NaY calcined at (a) 873 K, (b) 673 K, (c) 473 K, in comparison with parent (d) NaY. Calcination heating rates are 0.2 K/min with flowing air.

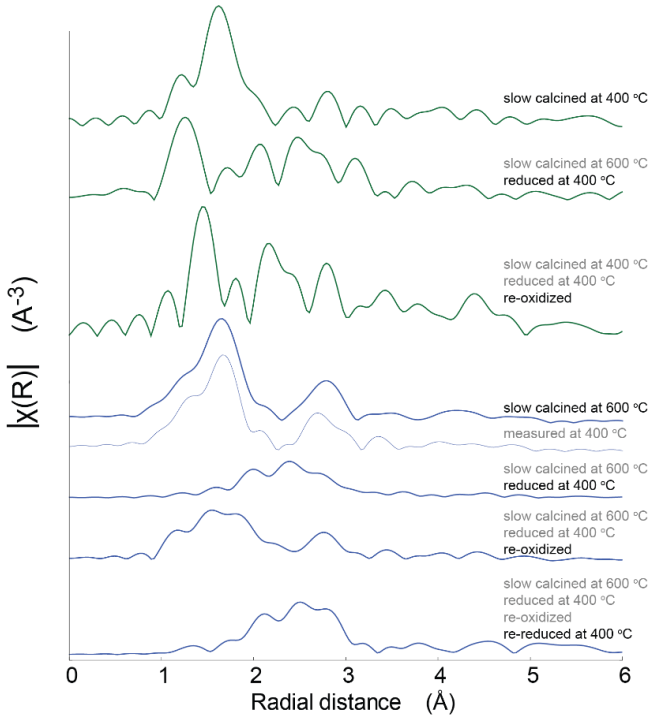

Figure S2.5. EXAFS spectra of 1 wt% Pt-NaY (a) calcined at 673 K, (b) in-situ reduced at 673 K under flowing H_2

Pt clusters with a mean size of 3 nm formed at a fast-heating rate (10 ^{o}C/min), while there was no indication of Pt cluster formation at a slower heating rate (0.2 ^{o}C/min).

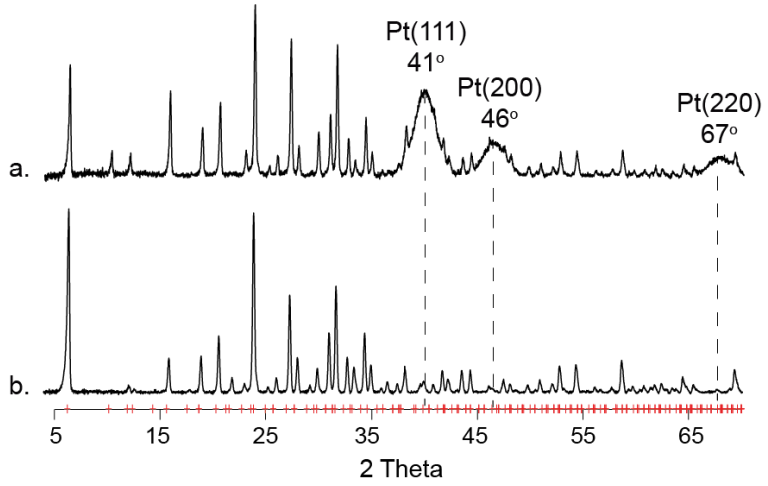

Figure S2.6. XRD powder pattern of 15 wt% Pt-NaY calcined to 873 K with heating rate of a. 10 K/min b. 0.2 K/min

Scherrer equation:

$$d = \frac{K\lambda}{\beta cos\theta}$$

d – mean size of the crystallite domain

K – dimensionless shape factor

λ – X-ray wavelength

β – line broadening at FWHM in radian

θ – Bragg angle

$$d = \frac{0.95 \cdot 1.54\ \text{Å}}{3 \cdot \frac{\pi}{180} cos\frac{41^{\circ}}{2}} = 2.98\ nm\ \approx 3\ nm$$

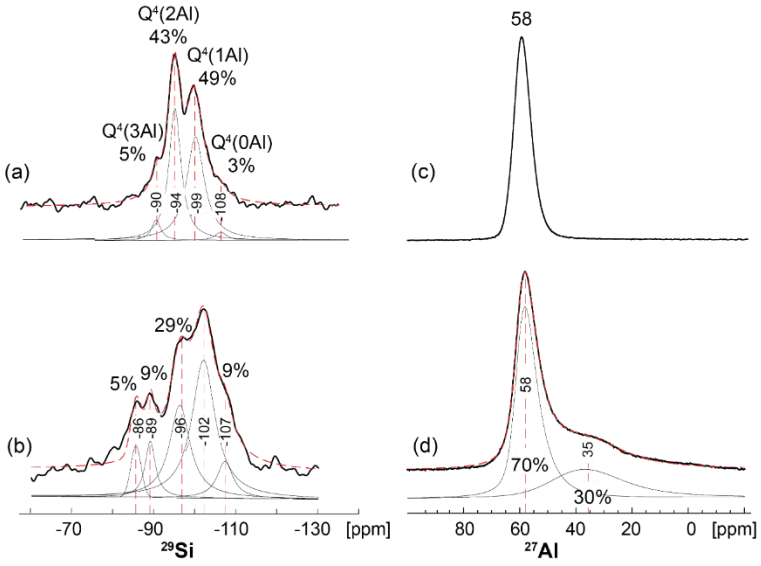

Figure S2.7. Solid-state single-pulse ^{29}Si MAS NMR of a. dehydrated NaY, b. 15 wt% Pt-NaY calcined at 873 K using 11.7 T, at 298 K, 12.5 kHz MAS under dry N_2. Solid-state single-pulse ^{27}Al MAS NMR of c. dehydrated NaY, d. 15 wt% Pt-NaY calcined at 873 K acquired at 18.8 T, 298 K, 20 kHz MAS under dry N_2. Dotted lineshapes are addition of deconvoluted signals, which provide the relative quantities of distinct (a & b) ^{29}Si and (d) ^{27}Al sites

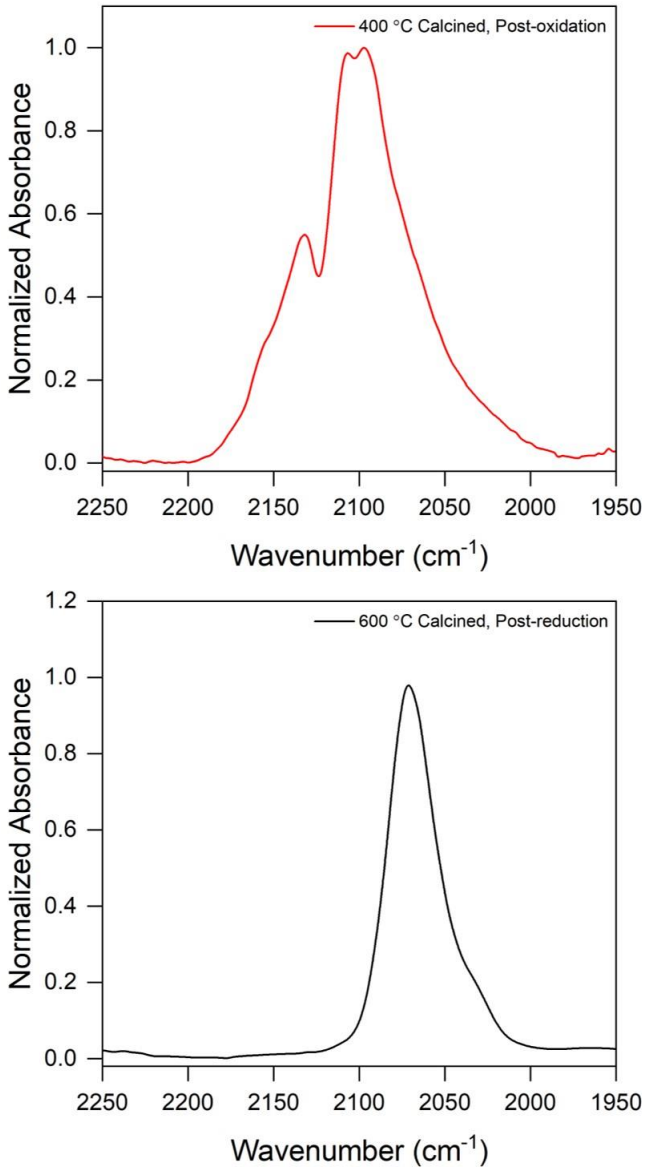

Figure S2.8. CO FTIR spectra of 1 wt% Pt-NaY calcined at (a) 673 K and (b) 873 K

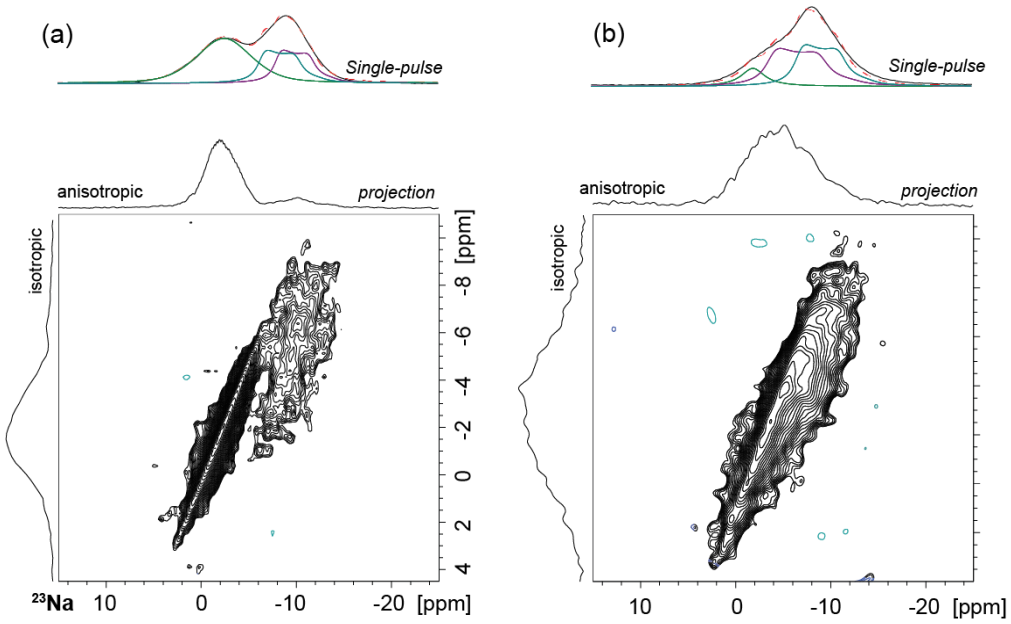

Figure S2.9. Solid-state ^{23}Na MQMAS spectrum of (a) dehydrated NaY zeolite (b) 15 wt% Pt-NaY calcined at 873 K acquired at 35.2 T, 298 K, and 24 kHz MAS. 1D single-pulse ^{23}Na spectrum acquired under the same conditions is on top of the anisotropic axis along with deconvoluted spectra.

CHAPTER 3

3. Correlating atomic-level compositions and structures with the aromatization properties of fluorine-promoted Pt/KL zeolite catalysts

*Tsatsral Battsengel,[1] Zachariah J. Berkson,[1] Joseph Bergmeister,[2] Gabriela Alvez-Manoli,[2] Sikander Hakim,[2] Steven Lim,[2] Masud M. Monwar,[2] Cori A. Demmelmaier,[2] Bradley F. Chmelka[1,] **

[1] Department of Chemical Engineering, University of California, Santa Barbara, California 93106 U.S.A.

[2] Chevron-Phillips Chemical Company, Kingwood, Texas 77339 U.S.A.

Keywords: Solid-state NMR of zeolite, catalyst characterization, 2D NMR

3.1 Abstract

The promoting effects of dilute fluorine additives on industrially significant Pt-KL catalysts for aromatization reactions are demonstrated, along with atomic-level analyses of the catalyst compositions and structures that account for their properties. Specifically, at least three distinct types of fluorine species are present in fluorine-promoted reduced Pt,/F-KL catalysts, including F species that are bonded to framework Al sites. Detailed insights on the compositions and structures of Pt/KL-zeolite catalysts with and without fluorine are obtained from advanced solid-state NMR

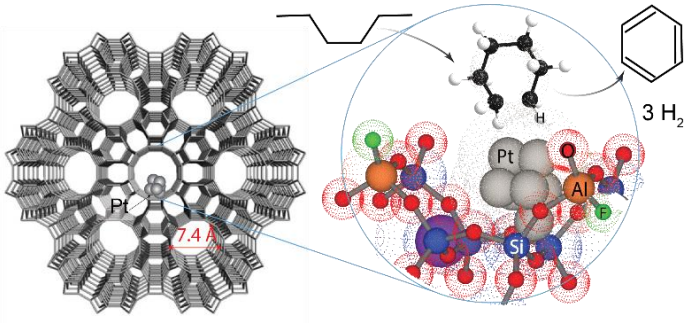

techniques, which can be correlated to their reaction properties. Specifically, 2D ^{27}Al{^{29}Si} *J*-mediated NMR spectra enable distinct ^{29}Si-O-^{27}Al zeolite framework sites to be unambiguously resolved and identified. Furthermore, 2D ^{27}Al{^{19}F} *J*-mediated NMR spectra of fluorine-containing Pt-KL catalysts establish that certain fluorine moieties are covalently bonded to tetrahedral Al sites in the zeolite framework and remain in the spent catalyst. In combination with 1D direct-excitation ^{19}F NMR analyses, the relative quantities and distributions of ^{19}F species and their interactions with the zeolite framework are determined at different stages of catalyst preparation. Importantly, Al framework sites with covalently bonded fluorine atoms appear to be crucial to stabilizing Pt precursors within the zeolite nanopores and are important to aromatization of *n*-hexane over Pt,F-KL zeolite. The atomic-scale analyses yield new compositional and structural insights on the roles of dilute guest species, in particular the beneficial effects of dilute fluorine, on the macroscopic reaction properties of Pt/F-KL catalysts.

3.2 Introduction

Platinum supported on K^+-exchanged L-zeolite (Pt/KL) is used for commercial alkane-aromatization processes.[1,2] Such Pt/KL zeolite catalysts often convert low-value alkanes into high-value aromatic compounds with significantly higher selectivity compared to Pt supported on ot0her types of zeolites or oxides.[2–5] High aromatization activities of monofunctional Pt/KL catalysts are attributed to lack of acidity of KL zeolite,[6,7] steric constraints of unidimensional nanopores of L-zeolite,[8] and highly dispersed nanoscale Pt particles.[9–12] The reactivity and selectivity of Pt-KL catalysts

can furthermore be enhanced by the addition of dilute promoters, *e.g.*, various cations,[9,13] transition metals,[14,15] or halides.[1,10,11,16] Although halides have been commonly used to improve the dispersion of metal particles on zeolite supports, detailed understandings of the types and distributions of different halide moieties present in zeolites and whether these halide moieties have direct effects on catalytic reactions on Pt-zeolites are not fully established.[11,17] Here, the aromatization activity, selectivity, and catalyst stability of Pt/KL are shown to be improved by adding a dilute amount of ammonium fluoride during catalyst preparation to yield <1 wt% F in reduced Pt/F-KL without affecting the overall dispersion of Pt.

While there have been numerous studies on fluorine-modified zeolite and oxide catalysts,[12,16,18–21] the majority of them have investigated fluorine-promoted acidic H^+-zeolite catalysts. For example, Becker *et al.* have reported that fluorination of H^+-Y zeolite resulted in increased acidity which led to improved catalytic activity involving acid sites, such as cracking, isomerization, and alkylation.[18] It was suggested that some of the surface hydroxyl groups may be replaced by F, leaving the remaining -OH groups with higher acidity due to the electron-withdrawing effect of nearby electronegative fluorine atoms. In contrast, fluorine-promoted non-acidic Pt/KL catalysts are a special case, where enhanced acidic properties are undesirable for the aromatization of hydrocarbons. The presence of strong acidic sites in zeolite KL would otherwise result in cracking of paraffin feedstocks and correspondingly lower selectivity for benzene formation. Furthermore, the overall Pt dispersions measured by CO chemisorption were not affected by the addition of fluorine for Pt-KL and Pt/F-KL catalysts. Hence, the improved reaction properties of P/F-KL catalysts are

attributed to chemical changes caused by the fluorine additives, rather than enhanced Pt dispersion of the catalysts.

Identifying the types, relative populations of fluorine species and obtaining detailed atomic-scale structural information of fluorine-promoted catalysts has been challenging due to their dilute compositions and heterogeneous distributions of fluorine moieties. Here, one-dimensional (1D) and two-dimensional (2D) solid-state NMR ^{1}H, ^{19}F, ^{29}Si, and ^{27}Al nuclear magnetic resonance (NMR) spectroscopy analyses are used to obtain atomic-scale structures of this complicated catalyst material. Specifically, interactions between fluorine moieties and the zeolite framework, and distinct ^{19}F-^{19}F interactions are unambiguously revealed by correlation NMR analyses, which enable distinct types of fluorine species to be identified and their relative populations established, among which are those that are thought to contribute to the enhanced aromatization properties of Pt/F-KL catalysts. The local environments of the ^{19}F species are found to be sensitive to the hydration state of the material, which is important to understand the preparation and storage of the catalyst. Complementary transmission electron microscopy, X-ray diffraction, H_2 chemisorption analyses yield atomic-scale structural insights on types of fluorine species that affect the aromatization reaction on industrially significant Pt/F-KL catalysts.

3.3 Materials and methods

Catalyst preparation. Commercially purchased zeolite KL (Si/Al = 3) was impregnated with an aqueous $Pt(NH_3)_4Cl_2$ solution at room temperature using incipient wetness techniques. The Pt/KL catalyst was then dried at 373 K, calcined under flowing air at 533 K and reduced under flowing hydrogen at 783 K. The fluorine-

promoted Pt/F-KL catalyst was prepared under otherwise identical conditions, except for the addition of NH_4F solution during impregnation of the platinum precursor.

Material characterization. Elemental analyses of the Pt/KL and Pt/F-KL catalysts were obtained by X-ray fluorescence spectroscopy on a Bruker S8 wavelength dispersive XRF spectrometer, with the results tabulated in **Table 3.1**. After calcination, both catalysts contained ~1 wt% Pt and ~0.35 wt% residual Cl from the Pt precursor, $Pt(NH_3)_4Cl_2$. The surface area and nanopore dimensions of the zeolite support have crucial influences on the overall catalytic properties of Pt-zeolite systems. The pore volumes and surface areas of Pt/KL and Pt/F-KL were acquired by using a Micromeritics TriStar II porosimeter and are shown in **Table 3.1**. Both catalysts have a total pore volume of 0.18 cm^3/g, of which 0.12 cm^3/g are from micropores. A high surface area of ca. 300 m^2/g in KL zeolite was maintained after fluorination, indicating that no significant structural disintegration occurred during the fluorine treatment, consistent with maintained bulk crystallinity evidenced by the XRD powder diffractions of Pt/KL and Pt/F-KL. Bulk Pt dispersion of Pt/KL and Pt/F-KL were measured by Micromeritics ASAP 2020C Instruments by CO chemisorption method, and results are listed in **Table 3.1**. Both catalysts have similar Pt dispersions of ~55%, indicating that the different catalytic activities observed are not due to improved Pt dispersions in fluorinated Pt/F-KL rather from the effects of fluorine promoters. Scanning electron micrographs (SEM) of Pt/KL catalysts were obtained using an FEI XL40 Sirion FEG digital scanning electron microscope at 15000× magnification and 5 kV electron beam voltage. SEM images of platelet-shaped KL zeolite particles are shown in **Figure 3.1**. It is worth mentioning the significant amount of research efforts that enabled the

syntheses of LTL zeolites with low aspects ratios, *i.e.*, disc-like shape with a small ratio of diameter to length of the cylinder. Reduced pore length in c-axis [001] of LTL zeolite promotes diminished diffusion limitation of reactants and products, hence platelet-shaped KL zeolites exhibit higher catalytic performance.[22,23]

Table 3.1. Comparison of bulk elemental compositions, Pt-dispersion, surface area, and pore volume of Pt/KL and Pt/F-KL catalysts

		oxidized Pt/KL	oxidized Pt/F-KL
Elemental analyses, wt%	Pt	1.02	0.9
	F	None detected	0.67
	Cl	0.34	0.36
Total pore volume, cm^3/g		0.18	0.18
Micropore volume, cm^3/g		0.12	0.12
Surface area, m^2/g		296	291
Pt dispersion		59%	53%

The crystallinity of Pt/KL and Pt/F-KL catalysts were probed by X-ray diffraction (XRD) methods. The XRD patterns in **Figure 3.1 b,c** were collected with a scanning rate of 5 ^{o}/min over a range of 2θ angles from 5^o to 70^o using a Panalytical empyrean powder diffractometer. The reflection patterns of fluorinated catalyst Pt/F-KL were unchanged compared to Pt/KL within the detection limits of the measurement. Previous studies on fluorinated zeolites have shown excessive dealumination and framework destructions upon fluorine treatment.[18,19,21] However, the long-range order of the zeolite KL was retained following treatment with <1 wt% fluorine. Furthermore, the absence of reflection patterns from Pt indicates well-dispersed Pt species which are

too small to be detected by XRD, consistent with observed TEM images and measured Pt dispersions. Transmission electron microscopy (TEM) images of reduced Pt/KL and Pt/F-KL were collected by FEI Titan 300 kV instrument with 30 electrons/$Å^2$·s. The samples were exposed to the beam for 5–10 s to decrease the beam damage.

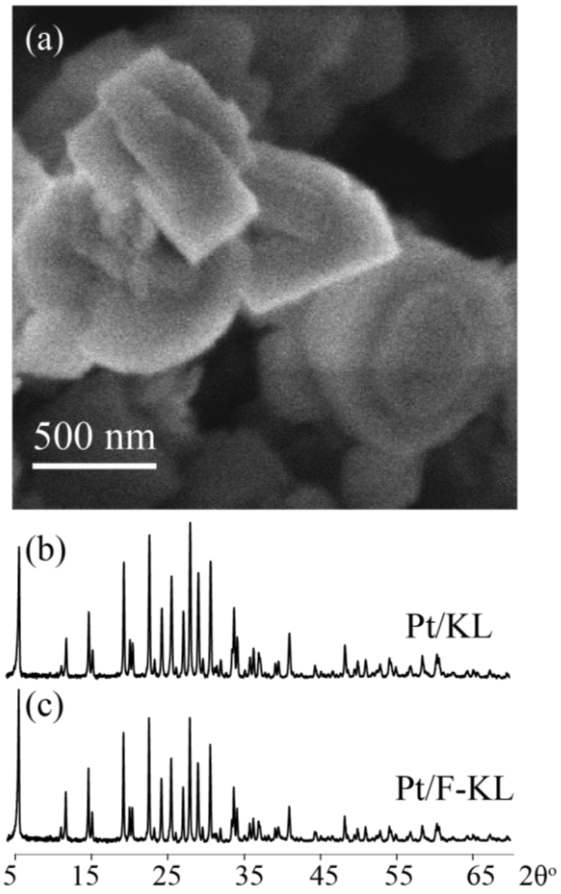

Figure 3.1. SEM and XRD of KL zeolite (a) Scanning electron micrograph of zeolite KL showing platelet-shaped crystallites. Powder X-ray diffraction patterns of reduced (b) 1 wt% Pt/KL and (c) 1 wt% Pt/F-KL show reflections consistent with zeolite KL unaffected by the addition of 0.7 wt% fluorine.

Local chemical environments and interactions between fluorine species and zeolite framework sites were revealed by solid-state NMR spectroscopy. One-dimensional (1D) and two-dimensional (2D) NMR correlation spectra were acquired on various NMR spectrometers depending on the types of experiments and nuclei being investigated. Prepared samples were carefully transferred into a dry, O_2-free glovebox without exposure to air, and packed into rotors for magic-angle-spinning (MAS) NMR measurements. The rotors were subsequently transferred in a secondary glass vial from the glovebox and quickly inserted into the MAS probehead, and spun under dry N_2 gas. Solid-state 1D single-pulse ^{19}F fast-MAS, ^{29}Si MAS experiments, and dipolar-mediated $^{27}Al\{^{19}F\}$ Heteronuclear Multiple Quantum Coherence (HMQC) NMR measurements were conducted using a Bruker AVANCE-II NMR spectrometer with an 11.7 T wide-bore superconducting magnet, operating at frequencies of 500.13, 470.59, 99.36, and 130.32 MHz for ^{1}H, ^{19}F, ^{29}Si, and ^{27}Al, respectively. The 1D ^{29}Si MAS spectra were acquired at room temperature and 12.5 kHz using 4-mm zirconia rotors with Kel-F^{TM} caps in a triple-resonance H-X-Y MAS probehead. The 1D ^{19}F MAS experiments were conducted at room temperature and spinning at 50 kHz using 1.3-mm zirconia rotors with Kel-F^{TM} caps in an H-X double-resonance MAS probehead. 1D single-pulse ^{19}F MAS experiments were performed using a 90^{o} pulse length of 2.5 μs with a recycle delay of 10 s. The ^{19}F background was collected with an empty rotor under the same experimental conditions and number scans and subtracted from the ^{19}F NMR signal collected from the sample. 2D $^{19}F\{^{19}F\}$ single quantum-double quantum (SQ-DQ) correlation experiments are conducted by using rotor encoded homonuclear Back-to-Back (BABA-*xy*16) pulse sequences[24] using

optimized 90º pulses with 4864 transients and with STATES-TPPI acquisition mode in the indirect dimension. Double quantum modulation data, *i.e.*, normalized signal intensities as a function of double quantum evolution time, was acquired using the same pulse sequence. Spin dynamics simulation of the collected double-quantum modulation data was carried out using the SIMPSON package version 4.1.1. The best fit simulated data provide the ^{19}F-^{19}F dipolar interaction strength, from which the average distances between coupled fluorine spins were calculated.

2D ^{27}Al{^{19}F} dipolar-mediated *D*-HMQC measurements were conducted on the same 11.7 T instrument equipped with 4 mm HX probe at 12.5 kHz MAS by using symmetry-based $SR4_1^2$ dipolar recoupling sequence,[25,26] which was shown to be one of the most robust methods specifically suited for recoupling dipolar interactions between a spin 1/2, *e.g.*, ^{19}F and ^{29}Si, and a quadrupolar nucleus, *e.g.*, ^{27}Al. ^{27}Al{^{19}F} *D*-HMQC NMR spectrum was acquired using 1024 transients with recoupling of 12 rotor periods (corresponding to 1.5 ms). Low-temperature MAS (LTMAS) measurements (95 K) provide significantly enhanced NMR signal sensitivity that allows the detection and analysis of ^{29}Si-O-^{27}Al covalent-bonding environments in zeolite framework at a natural abundance of ^{29}Si (4.7%). Variable-temperature MAS measurements were conducted on a Bruker ASCEND 400 NMR spectrometer with a 9.4 T superconducting magnet equipped with a low temperature 3.2 mm triple-resonance MAS probehead operating at frequencies 400.13, 376.49, 79.49, and 104.26 MHz corresponding to ^{1}H, ^{19}F, and ^{29}Si, and ^{27}Al resonances, respectively. ^{27}Al{^{29}Si} *J*-mediated HMQC correlation spectra were acquired with 1024 transients, rotor-synchronized incremental step size of 12 μs, 128 increments in the indirect ^{29}Si

dimension, and a recycle delay of 0.5 s. The half echo delay before and after the evolution period was experimentally optimized to 11.3 ms, during which a 90° ^{29}Si pulse was applied to refocus the weak ^{27}Al-O-^{29}Si *J*-couplings. STATES mode was applied for the indirect dimension. ^{1}H heteronuclear decoupling with SPINAL-64 sequence was applied during 2D ^{27}Al{^{29}Si} *J*-HMQC experiment, though for dehydrated sample ^{1}H decoupling did not show any observable effects on the sensitivity and the spectrum. ^{27}Al NMR spectra were collected on 19.6 and 35.2 T instruments at the National High Magnetic Field Laboratory. Samples were packed in 3.2 mm rotors with 15 or 24 kHz MAS. Central transition selective single-pulse excitation of 0.42 us corresponding to π/12 flip angle was used for quantitative ^{27}Al experiments with a recycle delay of 2 s. 2D ^{27}Al MQ-MAS spectra were acquired using the *z*-filtered 3QMAS pulse sequence,[27] with 2048 transients, 20 rotor-synchronized t_1 increments, and 0.5 s of recycling delay on the 35.2 T instrument. The MQMAS data was processed with a Q-shear transformation to expand isotropic spectral width. The ^{1}H and ^{29}Si chemical shifts were referenced to tetramethylsilane (TMS) at 0.0 ppm, using tetrakis(trimethylsilyl)-silane (TKS) as a secondary external reference at 0.25 ppm for ^{1}H and 9.84 & -135.4 ppm for ^{29}Si. The ^{27}Al shifts were referenced to a 0.5 M solution of $Al(NO_3)_3$ at 0.0 ppm as an external reference. The ^{19}F chemical shifts were referenced to trifluoroacetic acid (TFAA) at -76.55 ppm.

H_2 temperature-programmed-reduction (TPR) analyses of Pt/KL and Pt/F-KL were used to identify the differences in reducibility of Pt species. H_2 TPR measurements were conducted by Micromeritics ASAP 2020C. Calcined Pt-zeolite in a tubular glass reactor was heated from 273 to 9743 K at a constant heating rate. The 5% H_2/95% Ar

was used as the reducing gas and passed through the catalyst bed. H_2 concentration at the outlet was detected and recorded.

Reaction test conditions. Calcined Pt/KL and Pt/F-KL zeolite powder catalysts were granulated by pressing a disk at 15,000 pounds, the resulting disk was gently crumbled and sieved to about 20-40 mesh (US), reduced in hydrogen at 774 K before reaction. Reaction tests were conducted at 75 psi and 774 K, H_2/hydrocarbon molar ratio of 2, with liquid hourly space velocity 6/h in a plug-flow reactor. The aliphatic hydrocarbon feed contained a proprietary mix of convertible C6 and C7 species. Products were analyzed by gas chromatography and the selectivity and yield for aromatization were calculated as described in the SI eq (1) and eq (2), respectively.

3.4 Results and Discussions

3.4.1 Improved aromatization properties of Pt/F-KL compared to Pt/KL

Aromatization properties of Pt/KL catalysts were enhanced by the addition of a dilute amount (<1 wt%) of NH_4F during the preparation of the zeolite catalyst. Fluorine-promoted Pt/F-KL exhibits enhanced aromatic selectivity and prolonged catalyst life. **Figure 3.2** shows catalytic test results of *n*-hexane and *n*-heptane aromatization at a constant reaction temperature of 774 K. Aromatization selectivity in mol% is plotted as a function of reaction time on stream for Pt/KL and Pt/F-KL in **Figure 3.2a**. For both catalysts, the selectivity rapidly increases within the first 10 h of run-time, and within the first 30 h of reaction time, the maximum stable selectivity of 96% for Pt/F-KL and 87% for Pt/KL were obtained and maintained until the end of the reaction test. Increased aromatization selectivity of Pt/F-KL catalyst leads to a slower rate of carbon deposit formation due to cracking, hence, the fluorine-promoted catalyst stays active

much longer than Pt/KL. The aromatic yield was measured and plotted in **Figure 3.2b** as a function of reaction time. For Pt/KL catalyst, the yield decreases almost linearly from 80% to 70% as the reaction progresses from the beginning to at the end of 80 h. On the contrary, fluorine-promoted Pt/F-KL catalyst already started with a higher yield of ca. 85% and maintained its yield without significant loss until the end of the reaction test at 80 h. As seen from the catalytic reaction tests of *n*-hexane and *n*-heptane aromatization, fluorine added Pt/F-KL shows higher aromatization selectivities compared to Pt/KL. The following sections will discuss analyses of the atomic-scale origins of such improvements in the reaction properties of Pt/F-KL catalyst.

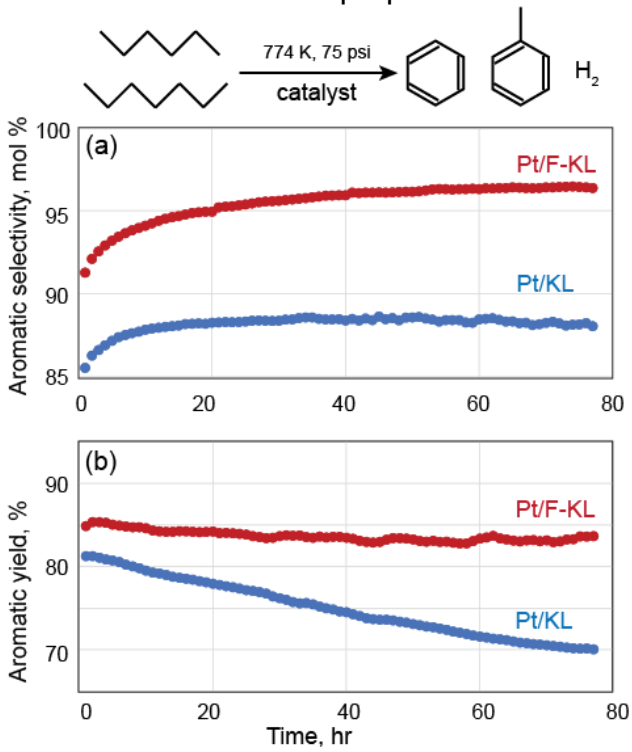

Figure 3.2. Comparisons of (a) aromatic selectivity, (b) aromatic yield loss for fluorine-promoted Pt/F-KL (red) and Pt/KL (blue) zeolite catalysts, as functions of time on stream. The reaction tests were conducted at 75 psi and 774 K, liquid hourly space velocity of 6/h in a plug flow reactor. The feed was a mixture of *n*-hexane, *n*-heptane, and H_2 with an H_2/hydrocarbon ratio of two.

3.4.2 Types and distributions of Pt metals on F-KL and KL zeolites

The atomic-scale origins of the catalytic activities of Pt/KL and Pt/F-KL catalysts depend on the types and distributions of Pt species, which are the active sites of monofunctional Pt/KL catalysts, as well as the electronic environments and atomic compositions of support zeolites. Detailed understandings of types and distributions of Pt, local environments, and compositions of KL support are analyzed by different techniques as discussed below. First, the sizes of Pt particles on F-KL and KL are identified by acquiring the TEM images. Representative images of which are shown in **Figure 3.3a**,**b**. Both catalysts contain mostly small <3 nm diameter Pt particles, some of which are indicated by white arrows, along with a small number fraction of somewhat larger ~5-10 nm diameter Pt particles, which are indicated by red arrows. For catalysts with <1 wt% fluorine, the sizes of Pt particles observed by TEM and the average Pt dispersion, as measured by CO chemisorption (**Table 3.1**), are not affected by the presence of fluorine.

However, Pt species supported on F-KL and KL zeolites exhibit different temperature-dependent H_2 reduction behaviors, indicating the effects of fluorine on the reducibility of Pt species. Different H_2-TPR maxima and distributions reveal differences in the strength of the interactions between Pt and the support as well as different oxidation states of Pt.[28] For example, Pt particles supported on quartz reduces easier at a lower temperature compared to small Pt particles on zeolites due to strong Pt-zeolite interactions.[29] **Figure 3.3c** shows the normalized molar consumption of H_2 plotted at different temperatures over the range of 273 K to 973 K for Pt/KL (blue) and Pt/F-KL (red) catalysts. Firstly, the H_2-TPR signal acquired from

fluorine-promoted Pt/F-KL shows a small maximum at a lower temperature of 320 K, which was not observed from Pt/KL. The easily reducible Pt species present in fluorinated catalyst is likely due to the presence of Pt^{2+} cations associated with F^- anions.[30] Fluorine cations associated with Pt^{2+} are expected to exhibit a distinct chemical environment, and observation of such ^{19}F species was evidenced by ^{19}F NMR as discussed below. Secondly, both catalysts show a majority of the H_2 consumption with TPR maxima at ca. 470-490 K, indicating that most of the Pt species are reduced within this temperature range, and are likely due to the reduction of platinum oxide species. [29]

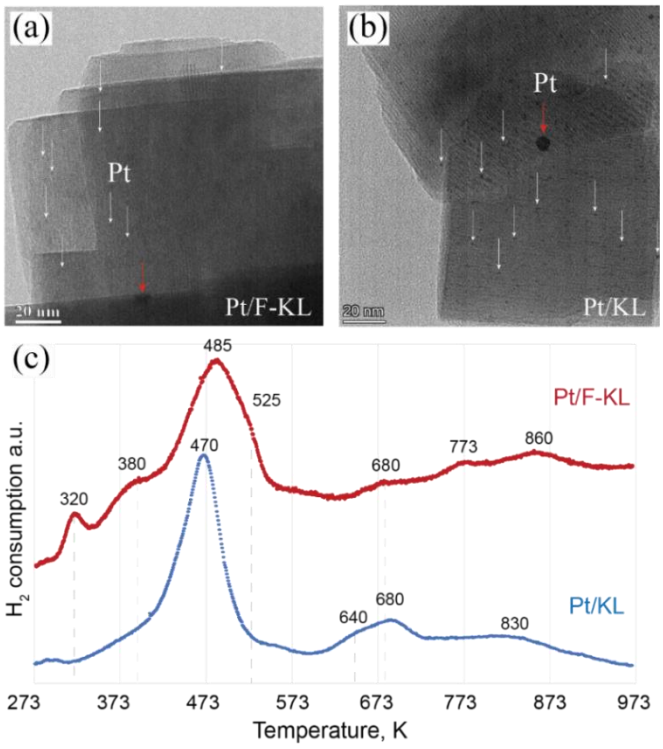

Figure 3.3. Transmission electron micrographs of (a) Pt/F-KL and (b) Pt/KL catalysts show darker contrast from highly dispersed Pt particles. Red and white arrows point at Pt clusters with sizes larger than 3 nm, and smaller than 1 nm, respectively. (c) H_2 temperature-programmed reduction profiles of Pt/F-KL (red) and Pt/KL (blue)

Slightly higher TPR maxima at 485 K in Pt/F-KL compared to 470 K in Pt/KL indicates that platinum oxide species supported on fluorinated zeolite is harder to reduce suggesting stronger Pt-zeolite interactions in the fluorinated catalyst. Other H_2-TPR signals with smaller intensities at 680 K with and broad signal at 830 K are observed in Pt/KL. Such higher temperature reduction occurs due to the presence of Pt species that exhibit strong metal-support interactions, such as Pt^{2+} in small cages of zeolite coordinated with framework oxygen atoms. Higher temperature TPR signals (680-860 K) are also present in the fluorinated catalyst, but with more intensities at 860 K, suggesting stronger interactions between the Pt and the F-KL zeolite. Increased metal reduction temperatures were also observed in other types of fluorinated Pt-zeolite systems,[31] and hypothesized to be due to stronger metal-support interactions induced by fluorine. Such enhanced metal-zeolite interactions can make the adsorption of reactants easier,[20] hence expected to affect the catalytic reactions occurring on the surface of the metal sites. Therefore, it is of great interest to understand the effects of the fluorines on the zeolite framework, which enable stronger Pt-zeolite interactions in F-KL compared to KL. The discussions below will bring interesting atomic-scale structural insights into the types and distributions of fluorine species and their interactions with the zeolite framework.

3.4.3 Framework aluminum sites in Pt/F-KL zeolite frameworks

Zeolite Al sites have crucial roles in stabilizing charge-balancing cations and behaving as a source of ion-exchange sites during Pt incorporation. Moreover, Al sites are preferrable tetrahedral sites for fluorine promoters to get attached to compared to Si sites in fluorinated Pt/KL catalysts.[32] Therefore, detailed structural insights of Al

sites in LTL zeolite are necessary to understand the effects of fluorine on catalytic activities. Although X-ray diffraction (**Figure 3.1 b,c**) shows reflection patterns of crystalline material, solid-state NMR reveals almost glass-like broad distributions of local environments of zeolite framework tetrahedral sites. Framework ^{27}Al in zeolites can be directly probed by ^{27}Al NMR, which can distinguish between 4-, 5-, and 6-coordinate sites.[33] Moreover, it is possible to identify crystallographically distinct tetrahedral ^{27}Al T-sites by high-resolution ^{27}Al NMR measurements.[34,35] However, resolving ^{27}Al NMR of zeolite materials is challenging due to the broad distributions of local ^{27}Al environments and the quadrupolar nature of the ^{27}Al nuclei with spin 5/2. Quadrupolar broadening of NMR spectrum of nuclei with spin greater than ½ arises from the coupling of the nonspherical charge distribution of the nuclei with the electric field gradient of the surrounding electrons.[36] The quadrupolar interaction contains higher-order orientational terms of significant magnitude compared to first-order interactions. Therefore, implementing more complex manipulation of the spin magnetization, *e.g.*, Multiple-Quantum Magic-angle Spinning (MQMQAS) or motions of the sample, *e.g.*, DOuble Rotation (DOR) and Dynamic Angle Spinning (DAS)[37] are necessary to achieve higher resolution. In addition, the second-order quadrupolar interaction is inversely proportional to the external field,[36] hence high field measurements of quadrupolar nuclei enable improved resolution of NMR spectrum by reducing quadrupolar broadening.

To identify types of ^{27}Al species in KL zeolite, both high-field (35.2 T, the highest magnetic field available for solid-state NMR measurements)[38] and MQMAS measurements are used. **Figure 3.4** shows the solid-state ^{27}Al NMR spectra of

reduced 1 wt% Pt/F-KL acquired at different magnetic field strengths, which exhibits the influence of increasing magnetic field strength, B_o, on the narrowing of the ^{27}Al NMR spectrum. This signal narrowing behavior indicates the presence of a strong second-order quadrupolar coupling, which is inversely proportional to B_o, of the tetrahedral ^{27}Al nuclei in reduced (dry) zeolite. It should be noted that the highest possible MAS was used for each instrument operating at different fields to minimize the first-order broadening which can be averaged by magic angle spinning. 8 kHz MAS was sufficient for that purpose, which was demonstrated by measuring the sample at different spinning speeds at the same magnetic field (**Figure S3.1**). Therefore, the effects of spinning speed on the narrowing of the ^{27}Al spectra in **Figure 3.4** is negligible, and the field strength is solely responsible for the narrowing behavior. The ^{27}Al signal acquired at 9.4 T (**Figure 3.4a**) shows a signal at 60 ppm, a region that corresponds to tetrahedral ^{27}Al species, and a broad signal that ranges from 50 to 20 ppm. Just with this 1D spectrum acquired at low field, interpretation of the data would be uncertain. However, by combining different NMR methods, *e.g.*, high-field MQMAS and 2D $^{27}Al\{^{29}Si\}$ measurements, the two types of the framework tetrahedral ^{27}Al sites are unambiguously identified.

The ^{27}Al spectrum narrows and the resolution improve significantly at a higher field of 19.6 T (**Figure 3.4b**). The spectrum reveals at least two isotropic distributions of tetrahedral ^{27}Al environments in the zeolite. LTL zeolite framework has two types of tetrahedral T-sites; T_1 from tetrahedral sites located at the 12-membered ring, and T_2 from other sites[39] as illustrated in the structural schematics in **Figure 3.4d**. ^{27}Al NMR spectrum of zeolite is sensitive to its local bonding environments, *e.g.*, average O-Al-

O bond angle and Al-O bond distance,[40] which are different for crystallographically different two types of tetrahedral T-sites in dehydrated KL zeolite. However, fully hydrated KL zeolite exhibits a ^{27}Al signal with only one broad asymmetric Czjezk lineshape,[41] a model derived from the statistical isotropy inherent to disorder, as shown in **Figure S3.2**. Comparisons of ^{27}Al signals from dehydrated, partially and fully hydrated KL zeolites are shown in **Figure S3.2**. At 35.2 T, signals from Al sites converge due to negligible quadrupolar induced shifts[35] (**Fig. 3.4c**). At this high field, the quadrupolar broadening is almost negligible, which is revealed by the MQMAS spectrum in **Figure 3.4d**. The MQMAS spectrum was conveniently analyzed by applying a shearing transformation, which yields an isotropic axis along the vertical axis. The MQMAS signal is along the chemical shift axis, indicating a negligible quadrupolar broadening at a high field, which enabled to deconvolute the signal by Gaussian distributions. The 1D ^{27}Al spectrum is deconvoluted into two Gaussian distributions at 60 and 58 ppm with relative integrated intensities of 35±2% and 65±2%, respectively, which is consistent with the stoichiometric ratio of the two T-sites (T_1:T_2 = 1:2).[39] Addition of 1 wt% Pt and < 1wt% F did not show any observable effects on the ^{27}Al spectrum (**Fig. S3.3**) of the KL due to their dilute amount, thus the analyses ^{27}Al signals of the reduced 1wt% Pt/F-KL catalyst can be confidently applied to structural analyses of the dehydrated KL zeolite. Identifying the crystallographically distinct two types of Al T-sites located in different zeolite ring structures is crucial to further understand how added fluorine is interacting with these different T-sites, hence affecting the aromatization reaction occurring on/in the zeolite structures.

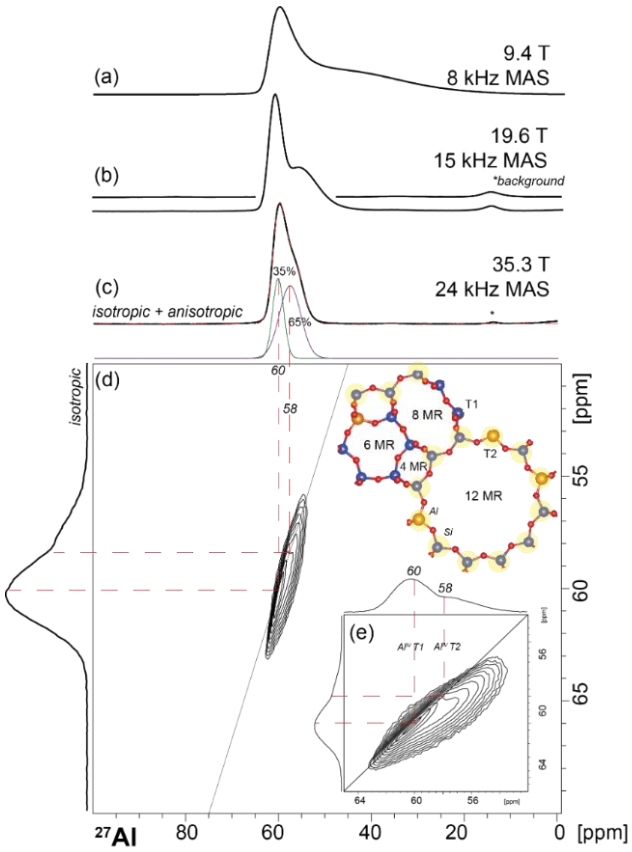

Figure 3.4. Solid-state single-pulse 1D ^{27}Al MAS NMR spectra of reduced 1 wt% Pt/F-KL acquired at (a) 9.4 T with 8 kHz MAS, (b) 19.6 T with 15 kHz MAS, and (c) 35.3 T with 24 kHz MAS. (d) ^{27}Al MQMAS spectrum acquired at 35.3 T showing isotropic shift axis in the y-axis. Deconvoluted ^{27}Al signals from two distinct T-sites are shown under the spectrum with corresponding relative intensities. (e) Close-up signal region of the MQMAS spectrum in (d), that shows signals from T_1 and T_2 sites (which was highlighted with transparent yellow circles) of zeolite LTL with the structure composed of 4, 6, 8, and 12- membered rings (MR) as shown in the schematics.

3.4.4 Framework connectivities of zeolite Pt/F-KL catalyst

With the understandings of the ^{27}Al NMR signals from two types of the Al T-sites, the connectivities of such Al species with the Si tetrahedral sites can be identified by 2D ^{27}Al{^{29}Si} NMR measurements. **Figure 3.5a** shows a 2D ^{27}Al{^{29}Si} *J*-mediated, *i.e.,* through-bond, the correlation NMR spectrum of reduced 1 wt% Pt/F-KL catalyst. The

^{27}Al sites that are directly bonded to different framework ^{29}Si species through bridging oxygen atoms give rise to signal intensities shown as a contour plot on the 2D spectrum. The projection of the ^{27}Al and ^{29}Si signals of the correlated species are shown on the horizontal and vertical axes, respectively. A broad ^{27}Al signal spanning from at ca. 60 ppm to 20 ppm arises from 4-coordinated ^{27}Al located at two types of T-sites of the zeolite framework as identified in previous sections. Correlated signal intensities are observed from such ^{27}Al sites bonded to Q^4(1Al), Q^4(2Al), and Q^3(1Al) ^{29}Si sites with signals at -100, -96, and -92 ppm, respectively, where $Q^m(n\text{Al})$ refers to tetrahedral ^{29}Si sites that are covalently bonded to *m* other Si or Al atoms through bridging O atoms, of which *n* are numbers of Al neighbors. Relative quantities of ^{29}Si species are obtained by 1D ^{29}Si MAS NMR spectrum as shown in **Figure 3.5b.** Signals at -92, -96, -101, and -108 pm arise from 10% Q^3(1Al), ^{29}% Q^4(2Al), 50% Q^4(1Al), and 11% Q^4(0Al), respectively. The 2D ^{27}Al{^{29}Si} correlation spectrum reveals that the Q^4(1Al) and Q^4(2Al) ^{29}Si sites are bonded to tetrahedral ^{27}Al species located at both T_1 and T_2 with signals at 60 ppm and 58 ppm, respectively, and not surprisingly for a given low Si/Al ratio of three. Interestingly, signals from ^{29}Si at Q^3(1Al) show a correlation with only the ^{27}Al signals at 59 ppm from ^{27}Al at T_2 sites, indicating that local environments of surface Q^3(1Al) species are similar to that of T_2 sites. Surface species are surrounded by fewer numbers of oxygen atoms, so do the T-sites that are located in larger membered rings, *e.g.*, T_2 sites at 12-MR, compared to T-sites located in smaller rings which are crowded by electron clouds of bridging oxygen atoms. Therefore, both ^{27}Al located at T_2 sites and surface Q^3(1Al) experience similar local electronic environments, resulting in ^{27}Al signal at the same region. Such information

can only be acquired by 2D correlational NMR measurements, and the analyses will provide information on identifying specific Al sites that are associated with F sites.

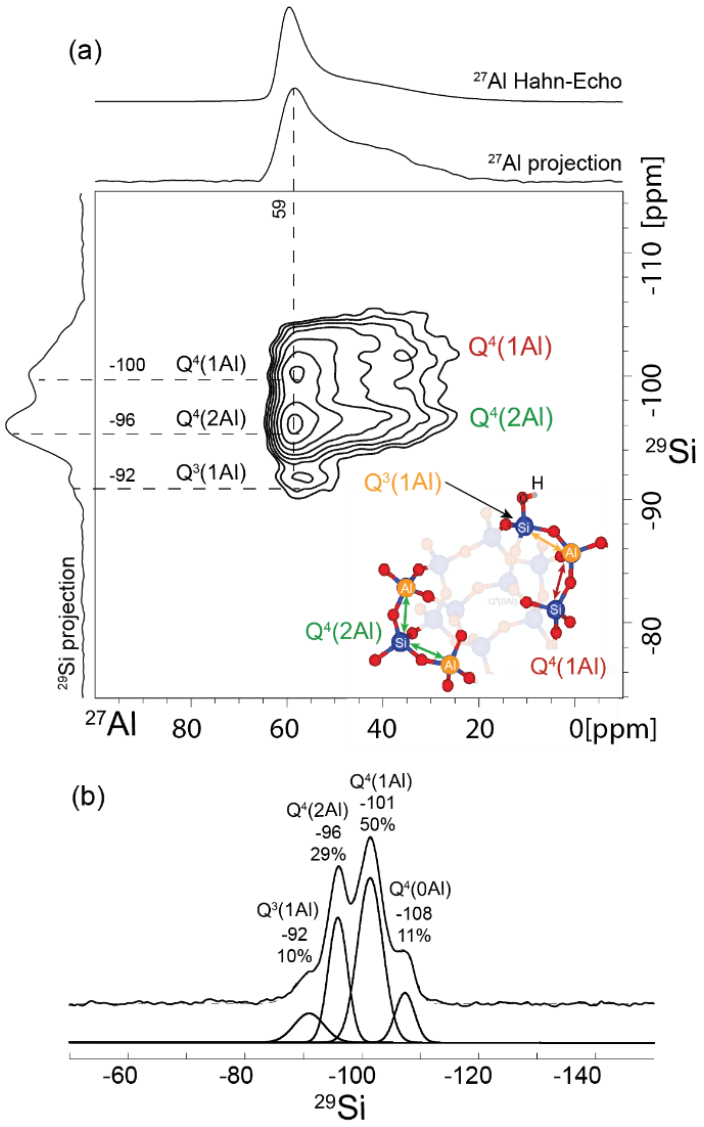

Figure 3.5. (a) Solid-state 2D *J*-mediated (through-covalent-bond) ^{27}Al{^{29}Si} HMQC NMR correlation spectrum of 1 wt% Pt/F-KL reduced at 773 K. The spectrum was acquired at 9.4 T, 95 K, and 8 kHz MAS. The schematic diagram depicts through-bond interactions of tetrahedral framework ^{27}Al sites with distinct Q^4(2Al), Q^4(1Al), and Q^3(1Al) ^{29}Si moieties that are consistent with the 2D spectrum. 1D ^{27}Al Hahn-echo spectrum is shown on the top horizontal axis for comparison. (b) Quantitative 1D single-pulse ^{29}Si MAS spectrum acquired for the same sample at 11.7 T, 298 K, and 12.5 kHz MAS showing partially resolved and deconvoluted signals from different framework ^{29}Si moieties.

3.4.5 Identifying types of fluorine species and their interactions with zeolite framework

Types and distributions of fluorine species and the effects of Pt on the ^{19}F moieties are revealed by ^{19}F single-pulse fast-MAS measurements. ^{19}F NMR is desirable because of its high natural abundance of almost 100%, hence even at dilute loading (< 1 wt%), distinct types of ^{19}F environments can be revealed. However, ^{19}F nuclei have a high gyromagnetic ratio, which leads to exhibit strong ^{19}F-^{19}F dipolar interactions and a broad signal from ^{19}F moieties that are experiencing homonuclear dipolar interactions. Therefore, to average out the strong dipolar interactions, faster MAS is necessary to acquire well-resolved signals. Fortunately, with the advent of NMR hardware development, smaller NMR rotor sizes (1.3 mm OD) enable a fast MAS rate (~50 kHz).[42] **Figure S3.4** shows a comparison of ^{19}F MAS spectra at 12.5 kHz and 50 kHz, the latter shows a narrower signal from ^{19}F moieties experiencing stronger dipolar interactions. A wide distribution of ^{19}F signals obtained from fluorinated Pt/F-KL catalyst indicates a presence of a variety of fluorine species, *e.g.*, fluoride ions located in different cages of the zeolite and fluorine atoms attached to the zeolite framework. The goal is to find out which of these fluorine species are responsible for the promoting effects observed in Pt/F-KL catalysts.

Although fluorine is widely used to promote zeolite catalysts, almost always it is used to improve the acidic properties of H^+-zeolites.[18–20,43] However, the presence of acidic sites is undesirable for monofunctional Pt/KL catalysts for the aromatization of *n*-alkanes due to the cracking properties of zeolite H^+ species. The acidity of the reduced 1 wt% Pt/F-KL catalyst is not more acidic than catalyst without fluorine. Moreover, the amount of fluorine added to the catalyst needs to be optimum, above or below which

the Pt/F-KL catalyst does not exhibit the promoting effect of the added fluorine. The promoting effects of added fluorine somewhat linearly increase up to the optimum amount of fluorine of 0.7 wt%, which corresponds to an Al/F molar ratio is 12. At extreme high loading of fluorine (*i.e.*, 5 wt% F), Pt/F-KL performance even decreases compared to Pt/KL. This suggests that there are competing effects of fluorine, *i.e.*, while some fluorine species have promoting effects on catalysis, some of which are having adverse effects on the aromatization reaction of Pt/KL catalysts. Before discussing which fluorines have promoting effects and which ones might have demoting effects, different types of fluorine species and their relative quantities will be identified in the following discussions.

One hypothesis of how fluorine species improve the reaction activities of Pt/F-KL zeolite catalysts is that some fluorine moieties directly interact with Pt sites to influence the local electronic structures of dispersed Pt atoms or clusters. Therefore, to identify the effects of Pt species on the distributions of ^{19}F species, analyses of ^{19}F fast MAS spectra from F/KL are compared with spectra from Pt/F-KL at different stages of catalyst preparation. Distributions of ^{19}F moieties in F-KL zeolite and Pt/F-KL catalyst at different stages of preparation are revealed by quantitative 1D ^{19}F fast-MAS NMR measurements. As F-KL (**Figure 3.6** left column) and Pt/F-KL (**Figure 3.6** right column) are treated at different stages of preparation, *i.e.*, calcined at 373 K (**Figure 3.6 a,d**), 523 K (**Figure 3.6 b,e**), and reduced at 773 K (**Figure 3.6c, f**), the observed change in the ^{19}F signals reflects the different chemical environments of fluorine moieties present at each stage of the zeolite treatment. Identifying types of fluorine moieties at different preparation stages of F-KL and Pt/F-KL enables us to understand

the evolution of ^{19}F moieties in reduced Pt/F-KL, which eventually lead to improved catalytic activities for Pt/F-KL.

Figure 3.6. Solid-state 1D single-pulse ^{19}F fast-MAS NMR spectra of 1 wt% F-KL and

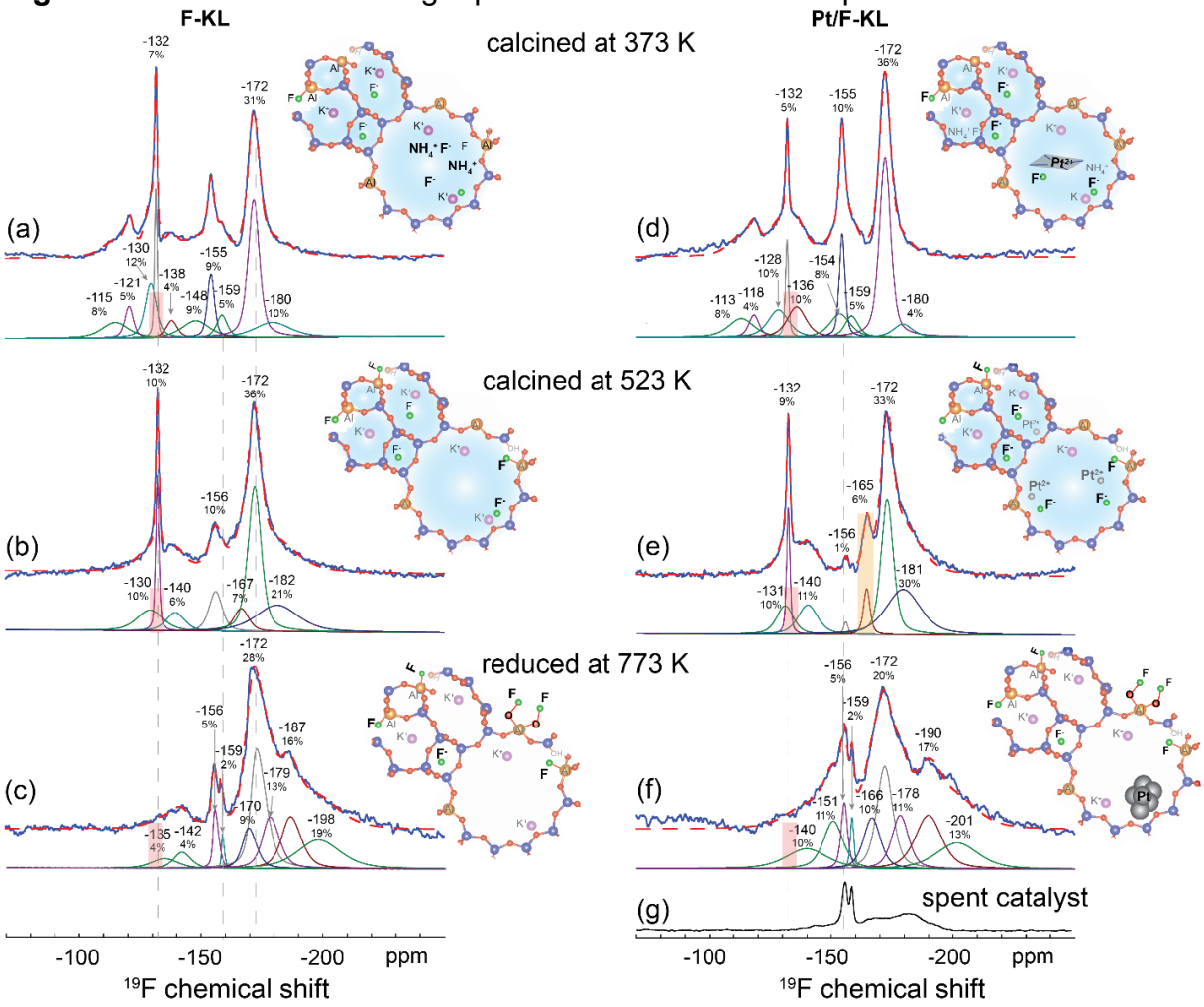

1 wt% Pt/F-KL acquired at 11.7 T, 298 K, and 50 kHz MAS, showing ^{19}F signals from different fluorine species that result from F-KL (a-c) and Pt/F-KL (d-g), respectively, after different post-synthetic treatments: (a,d) calcined at 373 K (b,e) calcined at 523 K, and (c,f) reduced at 773 K, and (g) in spent Pt/F-KL after 60 h on stream at the same conditions (75 psi, LHSV 6/h) used in **Figure 3.1**.

Interpretation of ^{19}F NMR in zeolite has been challenging due to the wide variety of possible fluorine species that can form in fluorinated zeolites. Previous studies on

fluorinated aluminosilicates have reported ^{19}F chemical shifts ranging from -100 ppm to -200 ppm,[44–49] similar to the results of this study. Previously reported DFT calculations have shown numerous possible configurations and their calculated ^{19}F NMR chemical shifts of fluorinated zeolites, *e.g.*, terminal fluorine, corner-shared fluorine, and edge-shared fluorine species.[46] Despite the tremendous efforts of calculating the chemical shifts of these fluorine moieties, the signal assignments have always been inconclusive due to a strong correlation between the chemical composition of the environment and ^{19}F NMR. Hydration level, presence of cations, and metallic Pt species nearby affect the electronic environments of ^{19}F spins, hence the chemical shift will be extremely challenging to predict. Fortunately, some advanced characterization techniques, such as 2D correlational NMR measurements used in this study enable unambiguous identification of fluorine species that are through-space (within <0.5 nm, but not necessarily bonded) or through-bond correlated with tetrahedral ^{27}Al sites, *e.g.*, $^{27}Al\{^{19}F\}$, and fluorine moieties that are proximate to other fluorines, *e.g.*, $^{19}F\{^{19}F\}$. The resolved signals acquired from the analyses of 2D NMR are used to deconvolute quantitative 1D ^{19}F fast-MAS spectra. However, even with the help of resolved signals from correlational 2D NMR results, ^{19}F spectra are composed of multiple overlapping signals, hence the spectra are deconvoluted to the best of our abilities to obtain approximate relative quantities of different fluorine species.

Starting from a lower calcination temperature of 373 K, ^{19}F spectra of F-KL and Pt/F-KL (**Fig. 3.6a,d**) show signals at ca. -120, a narrow signal at -132, a broader signal at -136, a well-resolved signal at -155 with a shoulder at -159, and the majority of the

signal at -172 ppm with a broad shoulder at -180 ppm. Even at this low-temperature treatment, distributions of signals from different ^{19}F moieties are present due to complex chemical compositions and structural cages that induce different chemical environments in the zeolite. The signals from -120 to -135 ppm correspond to F^- ions, which are small enough to be located in any of the cages of zeolite L.[45]. The structure of the zeolite L consists of a double 6-ring (d6r), cancrinite cage (CAN), and a large cage formed by 12-membered rings (LTL) that builds the unidimensional pore of zeolite L. The signal at -121 ppm arises from F^- ions associated with NH_4^+, because at a higher calcination temperature (523 K, **Fig. 3.6b,e**) when NH_4^+ is decomposed the ^{19}F signal at -121 ppm is not present. Also, the chemical shift of -121 ppm is shifted to a more deshielded higher frequency compared to fluorine ion associated with K^+ at -132 ppm. The narrow signal at -132 ppm corresponds to the F^- anion dissolved in adsorbed water. The narrow signal is an indication of motional averaging due to freely moving fluorine species and is consistent with the presence of adsorbed water at the relatively low calcination temperature. Signals at -155 ppm in calcined F-KL are ^{19}F species interacting with the zeolite framework Al sites, which are established by 2D NMR below. Approximately 40% of the ^{19}F signal arises from fluorine species that resonate at -172 and -180 ppm. These fluorine species exhibit the strongest ^{19}F-^{19}F dipolar interactions revealed by 2D SQ-DQ $^{19}F\{^{19}F\}$ NMR measurements, indicating that there are at least two fluorine atoms in proximity. The difference in ^{19}F NMR spectra between 373 K calcined F-KL and Pt/F-KL is observed for ^{19}F signal Although it appears that the signal intensity at -155 ppm is higher in Pt/F-KL compared to that of F-KL, the relative integrated intensities of the two signals, 9% in F-KL and 10% in

Pt/F-KL are almost identical. The signal at -148 ppm in F-KL is shifted to a higher field to -154 ppm in Pt/F-KL due to the presence of $Pt(NH3)_4^{2+}$, and overlapped with the signal at -155 ppm. There is no significant difference in ^{19}F spectra of F/KL and Pt/F-KL calcined at 373 K, mostly due to dilute loadings of both $Pt(NH3)_4^{2+}$ and NH_4F, as well as the presence of adsorbed water which act as an electronic screen between the cations and anions present in the KL zeolite. These broad distributions of fluorine species present in low-temperature calcined F-KL and Pt/F-KL provide crucial information on types of fluorine moieties that will eventually evolve into different fluorine species present in reduced catalysts.

After calcination at higher temperatures of 523 K, most of the initial ^{19}F signals are still present in F-KL and Pt/F-KL. This includes the signal from dissolved $^{19}F^-$ ion at-132 ppm, because of the non-negligible amount of water in the zeolite after heat treatment at 523 K as evidenced by TGA analyses shown in **Figure S3.3**. The signal at -172 ppm was broadened due to slight dehydration of the zeolite, which led to ^{19}F species with the signal at -172 ppm to experience stronger ^{19}F-^{19}F dipolar interaction without significant motional averaging due to the presence of adsorbed water. The broadening of this signal becomes much more enhanced after reduction at 773 K (**Figure 3.6c**). The signal at ca. -120 ppm, which was present in 373 K calcined F-KL and Pt/F-KL, is not present in higher temperature calcined F-KL, consistent with the assignment of fluorine ions from $NH_4^+F^-$ that decompose during calcination at 523 K. A noticeable difference in ^{19}F spectra of 523 K calcined F/KL and Pt/F-KL is the signal at -165 ppm (highlighted in yellow) which is present only in Pt/F-KL. Calcination is a crucial step in the distribution of Pt precursors. Especially, calcination temperature

close to the tetraamine decomposition temperature leads to diffusion of Pt^{2+} species into different cages of the zeolite. Zeolite framework Al has an important role in stabilizing these Pt^{2+} cations, hence any effect of fluorine moieties on the zeolite Al site is expected to affect the distributions of Pt. From the TPR analyses discussed above, fluorinated Pt/F-KL exhibit a new TPR peak at 320 K (**Figure 3.3**), which was assigned to Pt^{2+} cations associated with fluorines. It appears that the signal at -156 ppm, which was assigned to fluorines attached to tetrahedral Al sites, present in F/KL shifted to -165 ppm in Pt/F-KL. This new peak is an indication of the presence of Pt affecting the chemical environments of ^{19}F species in Pt/F-KL. The chemical environments of ^{19}F species that are interacting with the framework ^{27}Al could be altered by the presence of $Pt^{2+,}$ which would preferentially be attracted to negatively charged 4-coordinated Al sites of the zeolite. This suggests that the addition of fluorine influence the diffusion of Pt^{2+} cations during the calcination.

The reduced Pt/F-KL is the final stage of the treatment process in the catalyst preparation, hence, identifying ^{19}F species in reduced Pt/F-KL is the most important step that will lead to the understanding of promoting effects of fluorine additives in these catalysts. When the fluorinated zeolite is treated with H_2 at 773 K (**Figure 3.6c,e**), new signals emerge and some signals disappear compared to calcined samples (**Figure 3.6b,e**). Firstly, the signal at -172 ppm becomes broader compared to low-temperature calcined samples, consistent with the assignment of ^{19}F moieties with strong ^{19}F-^{19}F dipolar interactions, which was evidenced by significant signal narrowing at higher MAS spinning speeds compared to other ^{19}F moieties. Moreover, the broadening of these signals at -172 ppm was extremely sensitive to water content

in the zeolite compared to the other signals at -154 and -156 ppm, due to motional averaging caused by the presence of water. This also indicates that fluorine moieties that give rise to signal at -172 ppm are sensitive to the amount of adsorbed water, and susceptible to freely moving in the presence of water compared to ^{19}F sites with a signal at -154 ppm and -156 ppm, which were unambiguously found to be correlated to the framework ^{27}Al sites. The narrow peak at -132 ppm (highlighted in red) from freely moving F^- ions are not present in high-temperature treated F-KL, which contains almost no adsorbed water. Interestingly, two distinct signals at -156 and -159 ppm started emerging, which are from ^{19}F species interacting with framework tetrahedral ^{27}Al sites. 2D $^{27}Al\{^{19}F\}$ correlational NMR analyses unambiguously reveal such interactions, which will be discussed below. The broad signals at -174 ppm are due to clusters of fluorine species, whose signal broadens significantly upon dehydration as observed here and in previously reported literature.[46,47] The difference between ^{19}F signals of H_2 treated F-KL (**Fig. 3.6c**) and Pt/F-KL (**Fig. 3.6e**) arises from the broadened signal at -151 ppm, which appears to be the ^{19}F signal that resonates at -142 ppm in F-KL is high-field shifted due to the presence of reduced Pt species. The ^{19}F chemical shift differences between F-KL and Pt/F-KL indicate that reduced Pt species, which are commonly referred to as the catalytic active sites, influence the chemical environments of ^{19}F promoters.

The interactions between added fluorine and zeolite framework ^{27}Al sites are directly identified in the 2D $^{27}Al\{^{19}F\}$ dipolar- and *J*-mediated HMQC NMR correlation spectrum shown in **Figure 3.7**. The contour plot selectively shows the signals from ^{19}F moieties unambiguously correlated with ^{27}Al sites through-space (not necessarily directly

covalently bonded, but nearby <0.5 nm) (**Figure 3.7a**) and through-bond (**Figure 3.7b**) with 4-coordinated ^{27}Al with a signal at 60 ppm. The experiment was conducted at low 95 K, to take advantage of the increased signal sensitivity from higher population differences in magnetic spins at high and low energy states, which enables to successfully acquire the correlated intensities from dilute ^{19}F moieties and framework zeolite sites. ^{19}F moieties with signals at -156 and -159 ppm are bonded to the zeolite framework ^{27}Al sites and the ^{19}F species with the signal at -166 ppm are through-space interacting with the tetrahedral ^{27}Al with a signal at 60 ppm. A separately acquired ^{19}F echo-MAS spectrum along the vertical axis shows signals from all ^{19}F moieties, including those that are not interacting with ^{27}Al sites. In **Figure 3.7a**, the correlated signal intensities in the 2D spectrum arise from ^{27}Al moieties interacting through-space with ^{19}F species. Such ^{19}F species are covalently bonded to framework ^{27}Al sites, as revealed by *J*-mediated through-bond ^{27}Al{^{19}F} experiments (**Figure 3.7b**), and still present in the spent catalyst due to strong bonding with the zeolite framework sites. Because the experiment is conducted at a low temperature, the MAS spinning is at a much lower 8 kHz, compared to quantitative 1D fast MAS experiments shown in **Figure 3.6**, ^{19}F signals are broader than the signals shown in **Figure 3.6f**. Among these fluorine species identified from the previous 1D ^{19}F fast MAS NMR, and ^{27}Al-^{19}F correlational experiments, some of the fluorine moieties show a strong narrowing of the signals at faster MAS frequency, an indication of inhomogeneous broadening due to dipolar interactions. The fluorine species that are bonded to the zeolite framework can influence the local environments of the Pt metals supported on F-KL zeolite.

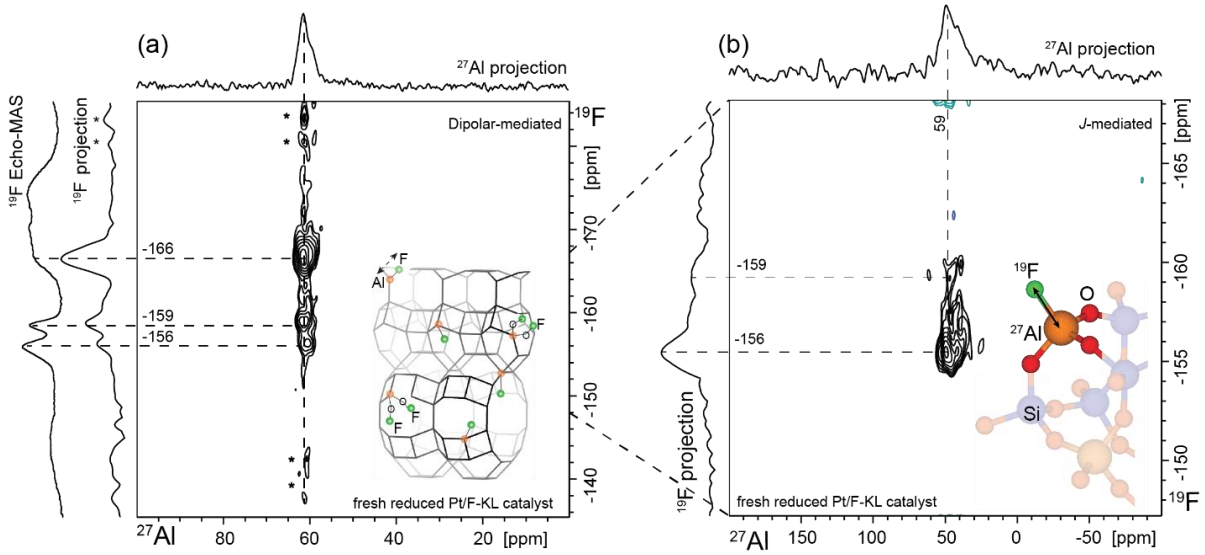

Figure 3.7. Solid-state 2D ^{27}Al{19F} (a) dipolar-mediated (b) *J*-mediated NMR spectrum of reduced 1 wt% Pt/F-KL. The spectrum is acquired at 9.4 T, 95 K, 8 kHz MAS. The solid-state 1D ^{19}F echo MAS NMR spectrum acquired under the same conditions is shown along the vertical axis, for comparison with the 1D projections of the 2D spectra.

Although five-coordinated Si-F species have been identified in fluorinated siliceous zeolites,[45,48] in aluminosilicates F preferentially and exclusively coordinates to Al,[32] consistent with our simple thermodynamic calculation shown in *eqs. 3-6* of SI. Also, no observable signal was acquired by ^{29}Si{^{19}F} CPMAS at short contact times. Moreover, ^{29}Si chemical shift of 5-coordinated ^{29}Si appears at -144 ppm,[48] which was not present in fluorinated Pt/F-KL catalyst.

Interestingly, there is an optimum amount of fluorine, ~1 wt%, in Pt/F-KL catalysts, below which the improvement of the catalytic activities is not at its maximum, and above which the aromatization selectivities even decrease compared to regular Pt/KL catalysts. This suggests that the fluorine additives are exhibiting competing behaviors

of promoting and demoting the catalytic behaviors. Therefore, among these different types of fluorine species identified by ^{19}F NMR measurements, only some are proposed to be responsible for the enhanced aromatization activities of the Pt/F-KL catalysts. In the spent Pt/F-KL catalyst, ^{19}F moieties that are bonded to the zeolite framework are still present with the signal at -156 and -159 ppm, while other fluorine species that are not strongly bonded to the zeolite framework are already removed. This spent catalyst had been on stream for 40 hours (at the end of the catalytic run shown in **Figure 3.1**) and still exhibits superior catalytic activities compared to Pt/KL catalyst. The electron-withdrawing fluorine atoms are expected to modify the local electronic environments of the framework Al sites with which they are associated, thereby influencing the reaction properties of Pt/F-KL.

Specifically, the broad ^{19}F signal at -172 ppm, which further broadens upon zeolite dehydration, was assigned to AlF_3 species. To further analyze the nature of these ^{19}F species and identify the interactions between ^{19}F-^{19}F moieties, 2D $^{19}F\{^{19}F\}$ single-quantum double-quantum (SQ-DQ) correlational analyses were conducted on freshly reduced and spent 1 wt% Pt/F-KL catalysts. For example, the 2D $^{19}F\{^{19}F\}$ SQ-DQ correlational NMR spectra in **Figure 3.8** show signals from correlated ^{19}F-^{19}F moieties of freshly reduced 1 wt% Pt/F-KL. Single-quantum ^{19}F chemical shifts are plotted along the horizontal axis and the vertical axis shows a double-quantum dimension, where signals appear at the sum of the single-quantum chemical shifts of two correlated ^{19}F-^{19}F moieties. Separately collected single-pulse ^{19}F MAS NMR spectrum, which is the same spectrum shown in **Figure 3.5f** for fresh catalyst and **Figure 3.5g** for the spent catalyst, were overlayed on top of the single-quantum

dimension, for comparison with the 1D projections of the 2D spectra. ^{19}F pairs that are dipolar-coupled within 0.5 nm selectively give rise to the correlated signal intensities on the 2D SQ-DQ spectra. Broadly distributed ^{19}F species that give a signal at -190 ppm are correlated with each other (**Figure 3.8a**), indicating that there are at least two ^{19}F moieties that are dipolar-coupled within a 5 Å distance. Interestingly, a weak correlational signal arises from ^{19}F resonating at -156 ppm, which is assigned to two ^{19}F moieties close to the framework ^{27}Al, which were identified from $^{27}Al\{^{19}F\}$ experiments (**Fig. 3.7**). In the spent catalyst, the majority of the signal intensities from AlF_3 are not present (**Fig. 3.8b**), indicating that these species are removed during the packed flow reaction. Fluorine species that are strongly interacting with the zeolite framework are likely responsible for the improved reaction properties of Pt/F-KL catalysts, as it is still present, and presumably still affecting the catalytic reactions, in 60 h spent catalyst. Moreover, based on these extensive studies of identifying fluorine species and finding the presence of a significant amount of AlF_3, the addition of AlF_3 instead of NH_4F as the fluorine precursor was used to test the catalytic activities. However, AlF_3 added Pt/KL zeolites did not show improved aromatization behaviors. This indicates that fluorine moieties that are responsible for enhanced reactivity are not AlF_3, but rather the other fluorine species, which were found to be ^{19}F strongly interacting with the zeolite framework Al-sites.

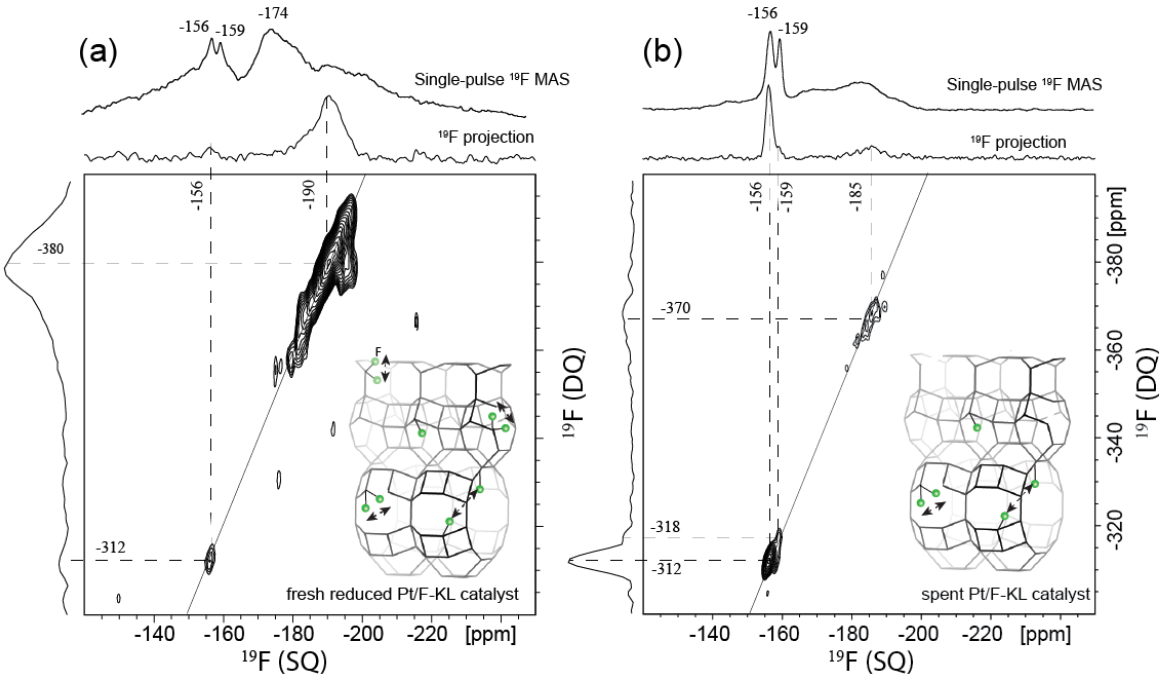

Figure 3.8. Solid-state 2D $^{19}F\{^{19}F\}$ SQ-DQ spectrum of (a) fresh-reduced and (b) spent 1 wt% Pt/F-KL after 60 h on stream at the same conditions (75 psi, LHSV 6/h) used in **Figure 3.1**. The spectrum is acquired at 9.4 T, 95 K, 50 kHz MAS. The correlated signal intensities arise from dipole-dipole coupled ^{19}F moieties that are within ~1 nm. 1D single-pulse ^{19}F MAS spectra were acquired separately and are shown along the top horizontal axes for comparison.

In summary, in reduced Pt/F-KL catalyst, there are three main distributions of ^{19}F moieties present:

1. -110 to -135 ppm signal arises from F- ions associated with different cations, *e.g.*, K_+ and NH_4^+, in different cages of the zeolite
2. -156 and -159 ppm signal arises from ^{19}F moieties covalently bonded to tetrahedral ^{27}Al sites of zeolite KL

3. A broad signal from -172 to -200 ppm arises from fluorine clusters, *i.e.*, at least two fluorine moieties in proximity (<0.5 nm)

The electron-withdrawing fluorine atoms interacting with the zeolite Al sites are expected to modify the local electronic environments of the framework sites with which they are associated, thereby influencing the reaction properties of Pt/F-KL. The detailed compositional and structural information provides new insights on the roles of such species, in particular the beneficial effects of dilute fluorine species, on the macroscopic reaction properties of Pt/F-KL catalysts.

3.4.6 Effects of hydration on distributions of fluorine species in Pt/F-KL catalysts

Aluminosilicate zeolites are extremely hydrophilic. When exposed to atmospheric conditions, KL zeolite used in this study adsorbs up to 10 wt% (**Fig. S3.5**) water. Therefore, careful handling of the zeolite catalyst during preparation, reaction test, and characterization is important. Especially, in the fluorine-promoted catalysts, the ^{19}F moieties identified in previous discussions are extremely sensitive to adsorbed water. **Figure 3.9** shows the ^{19}F fast-MAS NMR spectra of 1 wt% Pt/F-KL after different hydration levels. As the zeolite partially adsorbs a small amount of water (ca. 5 wt%), ^{19}F signals change significantly. The signals at -156 and -159 ppm, which were assigned to ^{19}F moieties attached to framework ^{27}Al sites, are still present in partially hydrated Pt/F-KL (**Fig. 3.9b**).

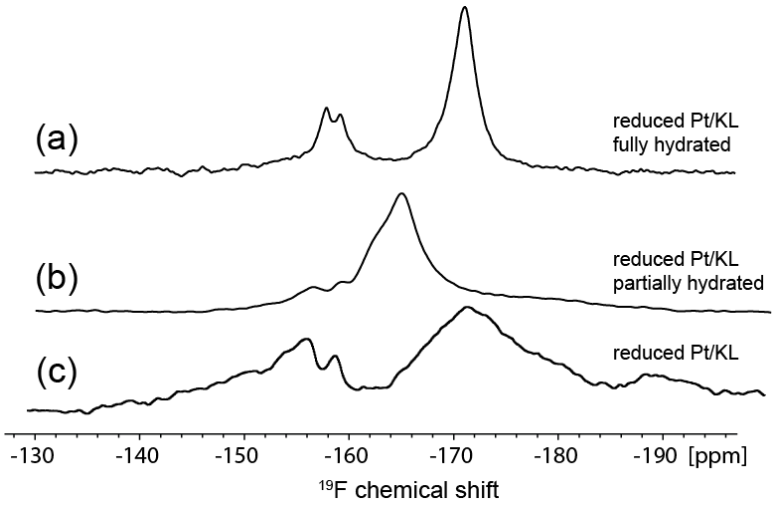

Figure 3.9. Solid-state 1D single-pulse ^{19}F fast-MAS NMR spectra of (a) fully hydrated, (b) partially hydrated, and (c) fresh reduced 1 wt% Pt/F-KL zeolites acquired at 11.7 T, 298 K, and 50 kHz MAS. The chemical shifts of ^{19}F moieties depend strongly on the extent of adsorbed water on the zeolite materials.

However, the broad signal at -180 ppm has shifted to the lower field to a broad distribution at -165 ppm. $^{19}F\{^{19}F\}$ single-quantum double-quantum correlational spectrum of this partially hydrated sample shows that the broad signal at -165 ppm is clusters of fluorines with at least two fluorine atoms that are within 1 nm distance from each other. By acquiring a double quantum build-up curve, it is possible to obtain the average distance between these fluorine atoms. **Figure 3.10b** shows the double quantum buildup curve of the signal at -165 ppm, which gives the strongest signal and enables to acquire double quantum modulation curve. The SIMPSON simulation package was used to simulate the ^{19}F-^{19}F double quantum modulation, which depends on the strength of the dipolar interactions which scales inverse cube of the distance between the coupled nuclei. Based on the SIMPSON simulation, the strength of the dipolar interaction was found to be 1.8 kHz, which corresponds to an average ^{19}F-^{19}F

distance of 3.9 A. It should be noted that this double quantum modulation curve was only possible to acquire in the partially hydrated Pt/KL, but not from the fully dehydrated sample where the signal was too broad. Identifying the distance between these fluorine species in partially dehydrated Pt/F-KL catalysts further confirms the assignments of the fluorines in reduced catalysts.

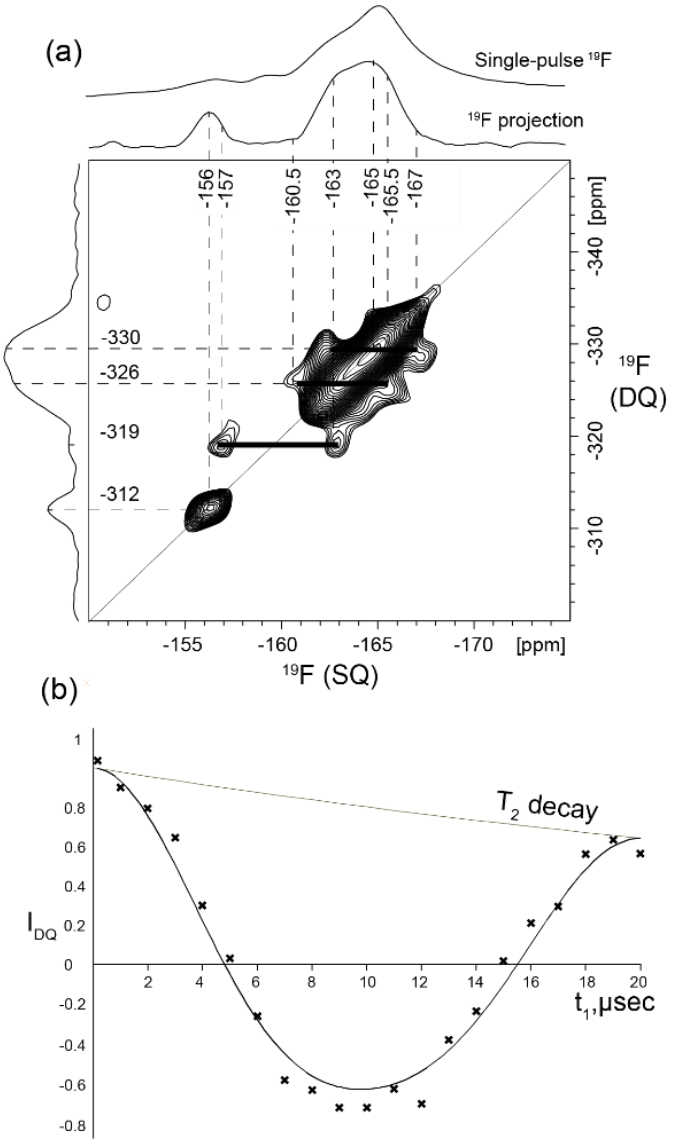

Figure 3.10. (a) Solid-state 2D ^{19}F{^{19}F} SQ-DQ spectrum of reduced 1 wt% Pt/F-KL after partial hydration. The spectrum is acquired at 11.7 T, 298 K, 50 kHz MAS. The correlated signal intensities arise from dipole-dipole coupled ^{19}F moieties that are within ~1 nm. A 1D single-pulse ^{19}F MAS spectrum was acquired separately and is shown along the top horizontal axis for comparison. (b) Double-quantum modulation curve for ^{19}F species with a signal at -165 ppm. The best fit for experimental data is acquired by simulating a double-quantum modulation curve with dipole-dipole interactions strength of 1.8 kHz, which corresponds to a ^{19}F-^{19}F distance of 3.9 Å.

3.5 Conclusions

The selectivity and catalyst longevity of industrially important aromatization catalyst Pt/KL is further improved by adding a small amount of fluorine (<1 wt%) into the Pt/KL catalyst during the catalyst preparation process. Types and distributions of fluorine moieties present in freshly reduced and spent catalysts are identified by using combinations of advanced characterization techniques. Notably, solid-state NMR spectroscopy techniques, including quantitative ^{19}F fast MAS, correlational 2D $^{27}Al\{^{19}F\}$, and $^{19}F\{^{19}F\}$ NMR methods were used to reveal relative quantities of distinct fluorine species, their interactions with the zeolite framework sites, and fluorine moieties with two or more fluorine clusters, respectively. At least three distinct types of fluorine species in fluorine-promoted reduced Pt/F-KL catalysts were identified: Fluorines covalently bonded to zeolite framework Al sites, fluorine clusters with at least two nearby fluorines, and fluorines located in different cages. Among those fluorines, the ones that are attached to framework zeolite appear to be affecting the aromatization activities by increasing the metal-support interactions between active Pt sites and zeolite support. Electronegative fluorine atoms bonded to zeolite framework sites are expected to affect the electronic environments of the support zeolite, hence the interactions between the metal and the support, which was evidenced by observation of higher temperature TPR peaks in fluorine promoted Pt/KL compared to Pt/KL. Moreover, the effects of hydration on distributions of fluorine species are investigated by studying Pt/F-KL catalysts at different hydration states. It was evidenced that some fluorines are becoming more mobile, *e.g.*, fluorines located in different cages in the presence of adsorbed water. Simple dehydration would not

return the state of the fluorines that were observed in reduced Pt/F-KL, indicating the effects of H_2 reduction on certain types of fluorine formation. Such detailed atomic-level structural insights of fluorine-promoted Pt/F-KL catalysts enabled to understand the promoting effects of dilute fluorines and the importance of catalyst handling as even a small amount of adsorbed water hugely affects types of fluorines present in fluorine-promoted catalysts.

ASSOCIATED CONTENT

Equations used to calculate aromatic yield and selectivity of the catalysts, comparisons of reactions energies of F bonded to Si vs Al, comparisons of ^{27}Al-^{29}Si spectra of fully hydrated and dehydrated Pt/F-KL catalysts, ^{13}C NMR and EPR spectra of spent Pt/KL and Pt/F-KL,

ACKNOWLEDGMENTS

The project was funded by Chevron-Phillips Chemical Company. The solid-state NMR, XRD, TEM, SEM measurements made use of the MRL Shared Experimental Facilities, which are supported by the MRSEC Program of the NSF under Award No. DMR 1720256; a member of the NSF-funded Materials Research Facilities Network (www.mrfn.org). The authors thank Dr. Philipp Selter for his guidance on SIMPSON simulation, Dr. Jerry Hu, Jaya Nolt, and Shamon Walker of the Spectroscopy facility at MRL for technical supports on the NMR instrumentations, and Anna Pischer for her reviews and comments of the manuscript.

References

(1) Wu, A.-H. Aromatization Catalyst and Methods of Making and Using Same. US 2004/0259719 A1, 2004.

(2) Bernard, J. R. Method of Dehydrocyclizing Aliphatic Hydrocarbon. US4104320, 1976.

(3) Davis, R. J.; Mielczarski, E. Effect of Catalyst Preparation on the Aromatization of N-Hexane over Pt Clusters Supported on Hydrotalcite. *ACS Symposium Series* **1993**, 327–336.

(4) Miller, J. T.; Agrawal, N. G. B.; Lane, G. S.; Modica, F. S. Effect of Pore Geometry on Ring Closure Selectivities in Platinum L-Zeolite Dehydrocyclization Catalysts. *Journal of Catalysis* **1996**, *163*, 106–116.

(5) Azzam, K. G.; Jacobs, G.; Shafer, W. D.; Davis, B. H. Aromatization of Hexane over Pt/KL Catalyst: Role of Intracrystalline Diffusion on Catalyst Performance Using Isotope Labeling. *Journal of Catalysis* **2010**, 270, 242–248.

(6) Mielczarski, E.; Hong, S. B.; Davis, R. J.; Davis, M. E. Aromatization of N-Hexane by Platinum-Containing Molecular Sieves II. n-Hexane Reactivity. *Journal of Catalysis* **1992**, *134*, 359–369.

(7) Besoukhanova, C. ,; Guidot, J. ,; Barthomeuf, D. ,; Breysse, M. ,; Bernard, J. ,. Platinum-Zeolite Interactions in Alkaline L Zeolites Correlations between Catalytic Activity and Platinum State. *Journal of Chemical Society, Faraday Trans.* **1981**, *77*, 1595–1604.

(8) Derouane, E. G.; Vanderveken, D. J. Structural Recognition, and Preorganization in Zeolite Catalysis: Direct Aromatization of $_n$-Hexane on Zeolite L-Based Catalysts. *Applied Catalysis Letter* **1988**, *45*, L15–L22.

(9) Fukunaga, T.; Ponec, V. The Nature of the High Sensitivity of Pt/KL Catalysts to Sulfur Poisoning. *Journal of Catalysis* **1995**, *157*, 550–558.

(10) Fukunaga, T.; Ponec, V. On the Role of Additives to Platinum Catalysts for Reforming Reactions. *Applied Catalysis A: General* **1997**, *154*, 207–219.

(11) Fukunaga, T.; Katsuno, H. Halogen-Promoted Pt/KL Zeolite Catalyst for the Production of Aromatic Hydrocarbons from Light Naphtha. *Catalysis Survey Asia* **2010**, *14*, 96–102.

(12) Katsuno, H.; Fukunaga, T.; Sugimoto, M. New Modification Method of Pt/L Zeolite Catalyst for Hexanes Aromatization. *Studies in Surface Science and Catalysis* **1993**, *75*, 2419–2422.

(13) Yan, W.; Li, Z.; Zheng, L.; Pan, Z.; Wei, S. XAFS Study of Ce-Enhanced Stability of Pt/KL Catalyst. *Journal of Physics: Conference Series* **2009**, *190*, 1–4.

(14) Song, J.; Ma, H.; Tian, Z.; Yan, L.; Xu, Z.; Liu, Q.; Qu, W. The Effect of Fe on Pt Particle States in Pt/KL Catalysts. *"Applied Catalysis A, General"* **2015**, *492*, 31–37.

(15) Xu, D.; Wang, S.; Wu, B.; Zhang, B.; Qin, Y.; Huo, C.; Huang, L.; Wen, X.; Yang, Y.; Li, Y. Highly Dispersed Single-Atom Pt and Pt Clusters in the Fe-Modified KL Zeolite with Enhanced Selectivity for n-Heptane Aromatization. *ACS Applied Materials and Interfaces* **2019**, *11*, 29858–29867.

(16) Ghosh, A. K.; Kydd, R. A. Acidity and Activity of Fluorinated Mordenites. *Journal of Catalysis* **1987**, *103*, 399–406.

(17) Foger, K.; Jaeger, H. The Effect of Chlorine Treatment on the Dispersion of Platinum Metal Particles Supported on Silica and γ-Alumina. *Journal of Catalysis* **1985**, *92*, 64–78.

(18) Becker, K. A.; Kowalak, S. Zeolite Catalysts Modified with Fluorine. *Studies in Surface Science and Catalysis* **1989**, *52*, 123–132.

(19) Ghosh, A. K.; Kydd, R. A. Fluorine-Promoted Catalysts. *Catalysis Reviews Science and Engineering* **1985**, 27, 539–589.

(20) Yang, H.; Ma, C.; Wang, G.; Sun, Y.; Cheng, J.; Zhang, Z.; Zhang, X.; Hao, Z. Fluorine-Enhanced Pt/ZSM-5 Catalysts for Low- Temperature Oxidation of Ethylene. *Catalysis Science & Technology* **2018**, *8*, 1988–1996.

(21) Lok, B. M.; Gortsema, F. P.; Messina, C. A.; Rastelli, H.; J Izod, T. P. Zeolite Modification-Direct Fluorination. *ACS Symposium Series* **2021**, *22*, 41–58.

(22) Lupulescu, A. I.; Kumar, M.; Rimer, J. D. A Facile Strategy to Design Zeolite L Crystals with Tunable Morphology and Surface Architecture. *Journal of the American Chemical Society* **2013**, *135*, 6608–6617.

(23) Brent, R.; Anderson, M. W. Fundamental Crystal Growth Mechanism in Zeolite L Revealed by Atomic Force Microscopy. *Angewandte Chemie International Edition* **2008**, *47*, 5327–5330.

(24) Saalwächter, K.; Lange, F.; Matyjaszewski, K.; Huang, C. F.; Graf, R. BaBa-Xy16: Robust and Broadband Homonuclear DQ Recoupling for Applications in Rigid and Soft Solids up to the Highest MAS Frequencies. *Journal of Magnetic Resonance* **2011**, *212*, 204–215.

(25) Brinkmann, A.; Kentgens, A. P. M. Proton-Selective 17O-1H Distance Measurements in Fast Magic-Angle-Spinning Solid-state NMR Spectroscopy

for the Determination of Hydrogen Bond Lengths. *Journal of American Chemical Society* **2006**, *128*, 14758–14759.

(26) Hu, B.; Trébosc, J.; Amoureux, J. P. Comparison of Several Hetero-Nuclear Dipolar Recoupling NMR Methods to Be Used in MAS HMQC/HSQC. *Journal of Magnetic Resonance* **2008**, *192*, 112–122.

(27) Amoureux, J.-P.; Fernandez, C.; Steuernagel, S. Z Filtering in MQMAS NMR. *Journal of Magnetic Resonance* **1996**, *123*, 116–118.

(28) Hurst, N. W.; Gentry, S. J.; Jones, A. Temperature Programmed Reduction. *Catalysis Reviews Science and Engineering* **1982**, *24*, 233–309.

(29) Vieira Dos Santos, B. R.; Montoya Urbina, M.; Souza, M. J. B.; Garrido Pedrosa, A. M.; Silva, A. O. S.; Sobrinho, E. v.; Velasco Castedo, R. Preparation and Characterization of Pt-Dealuminated y Zeolite by TG/DTA and TPR. *Journal of Thermal Analysis and Calorimetry* **2015**, *119*, 391–399.

(30) Duan, H.; Tian, Y.; Gong, S.; Zhang, B.; Lu, Z.; Xia, Y.; Shi, Y.; Qiao, C. Effects of Crystallite Sizes of Pt/HZSM-5 Zeolite Catalysts on the Hydrodeoxygenation of Guaiacol. *Nanomaterials* **2020**, *10*, 1–19.

(31) Jongpatiwut, S.; Rattanapuchapong, N.; Rirksomboon, T.; Osuwan, S.; Resasco, D. E. Enhanced Sulfur Tolerance of Bimetallic PtPd/Al2O3 Catalysts for Hydrogenation of Tetralin by Addition of Fluorine. *Catalysis Letters* **2008**, *122*, 241–222.

(32) Karpukhina, N. G.; Werner-Zwanziger, U.; Zwanziger, J. W.; Kiprianov, A. A. Preferential Binding of Fluorine to Aluminum in High Peralkaline Aluminosilicate Glasses. *Journal of Physical Chemistry B* **2007**, *111*, 10413–10420.

(33) van Bokhoven, J. A.; Roest, A. L.; Koningsberger, D. C.; Miller, J. T.; Nachtegaal, G. H.; Kentgens, A. P. M. Changes in Structural and Electronic Properties of the Zeolite Framework Induced by Extraframework Al and La in H-USY and La(x)NaY: A ^{29}Si and ^{27}Al MAS NMR and ^{27}Al MQ MAS NMR Study. *Journal of Physical Chemistry B* **2000**, *104*, 6743–6754.

(34) van Bokhoven, J. A.; Koningsberger, D. C.; Kunkeler, P.; van Bekkum, H.; Kentgens, A. P. M. Stepwise Dealumination of Zeolite Beta at Specific T-Sites Observed with ^{27}Al MAS and ^{27}Al MQ MAS NMR. *Journal of American Chemical Society* **2000**, *122*, 12842–12847.

(35) Chen, K.; Gan, Z.; Horstmeier, S.; White, J. L. Distribution of Aluminum Species in Zeolite Catalysts: ^{27}Al NMR of Framework, Partially-Coordinated Framework, and Non-Framework Moieties. *Journal of American Chemical Society* **2021**, *143*, 6669–6680.

(36) Man, P. P. Quadrupolar Interactions. In *Encyclopedia of Magnetic Resonance*; John Wiley & Sons, Ltd, 2011.

(37) Chmelka, B. F.; Zwanziger, J. W. Solid-state NMR Line Narrowing Methods for Quadrupolar Nuclei: Double Rotation and Dynamic-Angle Spinning. In *Solid-state NMR IV: Methods and Applications of Solid-state NMR*; 1994; pp 79–124.

(38) Gan, Z.; Hung, I.; Wang, X.; Paulino, J.; Wu, G.; Litvak, I. M.; Gor'kov, P. L.; Brey, W. W.; Lendi, P.; Schiano, J. L.; Bird, M. D.; Dixon, I. R.; Toth, J.; Boebinger, G. S.; Cross, T. A. NMR Spectroscopy up to 35.2 T Using a Series-Connected Hybrid Magnet. *Journal of Magnetic Resonance* **2017**, *284*, 125–136.

(39) Rivero, L. G.; Bañuelos, J.; Bizkarra, K.; Izquierdo, U.; Barrio, V. L.; Cambra, J. F.; Arbeloa, I. L. Linde Type L Zeolite: A Privileged Porous Support to Develop Photoactive and Catalytic Nanomaterials. In *Zeolites and Their Applications* ; InTech, 2018.

(40) Lippmaa, E.; Samoson, A.; Mägi, M. High-Resolution ^{27}A1 NMR of Aluminosilicates. *Journal of American Chemical Society* **1986**, *108*, 1730–1735.

(41) d'Espinose de Lacaillerie, J. B.; Fretigny, C.; Massiot, D. MAS NMR Spectra of Quadrupolar Nuclei in Disordered Solids: The Czjzek Model. *Journal of Magnetic Resonance* **2008**, *192*, 244–251.

(42) Nishiyama, Y. Fast Magic-Angle Sample Spinning Solid-state NMR at 60–100 KHz for Natural Abundance Samples. *Solid-state Nuclear Magnetic Resonance* **2016**, *78*, 24–36.

(43) Goa, Y.; Wu, P.; Tatsumi, T. Influence of Fluorine on the Catalytic Performance of Ti-Beta Zeolite. *Journal of Physical Chemistry B* **2004**, *108*, 4242–4244.

(44) Kao, H.-M.; Liao, Y.-C. Direct Solid-state NMR Observation of Tetrahedral Aluminum Fluorides in Zeolite HY Fluorinated by Ammonium Fluoride. *Journal of Physical Chemistry C* **2007**, *111*, 4495–4498.

(45) Kao, H.-M.; Chen, Y.-C. ^{27}Al and ^{19}F Solid-state NMR Studies of Zeolite H-Dealuminated with Ammonium Hexafluorosilicate. *Journal of Physical Chem B* **2003**, *107*, 3367–3375.

(46) Liu, Y.; Tossell, J. Possible Al-F Bonding Environment in Fluorine-Bearing Sodium Aluminosilicate Glasses: From Calculation of ^{19}F NMR Shifts. *Journal of Physical Chemistry B* **2003**, *107*, 11280–11289.

(47) Stebbins, J. F.; Zeng, Q. Cation Ordering at ¯uoride Sites in Silicate Glasses: A High-Resolution F NMR Study. **2000**, *262*, 1–5.

(48) Liu, Y.; Nekvasil, H. Si-F Bonding in Aluminosilicate Glasses: Inferences from Ab Initio NMR Calculations. *American Mineralogist* **2002**, *87* (2–3), 339–346.

(49) Kohn, S. C.; Dupree, R.; Mortuza, M. G.; Henderson, C. M. B. NMR Evidence for Five-and Six-Coordinated Aluminum Fluoride Complexes in F-Bearing Aluminosilicate Glasses. *American Mineralogist* **1991**, *76* (1–2), 309–312.

(50) Zhang, W.; Sun, M.; Prins, R. Multinuclear MAS NMR Identification of Fluorine Species on the Surface of Fluorinated *γ*-Alumina. *Journal of physical chemistry B* **2002**, *106*, 11805–11809.

(51) Shayib, R. M.; George, N. C.; Seshadri, R.; Burton, A. W.; Zones, S. I.; Chmelka, B. F. Structure-Directing Roles and Interactions of Fluoride and Organocations with Siliceous Zeolite Frameworks. *Journal of American Chemical Society* **2011**, *133*, 18728–18741.

(52) Fischer, L.; Harle, V.; Kasztelan, S.; d' Espinose de la Caillerie, J.-B. Identification of Fluorine Sites at the Surface of Fluorinated G-Alumina by Two-Dimensional MAS NMR. *Solid State Nuclear Magnetic Resonance* **2000**, *16*, 85–91.

(53) Koller, H.; Wolker, A.; Eckert, H.; Panz, C.; Behrens, P. Five-Coordinate Silicon in Zeolites: Probing Si02F- Sites in Nonasil and ZSM-5 with ^{29}Si Solid-state NMR Spectroscopy. *Angewandte Chemie International Edition* **1997**, *36*, 2823–2825.

(54) Thivasasith, A.; Maihom, T.; Pengpanich, S.; Limtrakul, J.; Wattanakit, C. Insights into the Reaction Mechanism of N-Hexane Dehydroaromatization to Benzene over Gallium Embedded HZSM-5: Effect of H 2 Incorporated on Active Sites. *Physical Chemistry Chemical Physics* **2019**, *21*, 5359–5367.

(55) Manh Tri, T.; Massardier, J.; Gallezot, P.; Imelik, B. Catalytic and Electronic Properties of Pt Particles in Zeolite- Particle Size and Environment Effects on n-Butane Conversion. *International Congress on Catalysis* **1981**, *7*, 266–287.

(56) Xu, D.; Wang, S.; Wu, B.; Huo, C.; Qin, Y.; Zhang, B.; Yin, J.; Huang, L.; Wen, X.; Yang, Y.; Li, Y. Tailoring Pt Locations in KL Zeolite by Improved Atomic Layer Deposition for Excellent Performance in N-Heptane Aromatization. *Journal of Catalysis* **2018**, *365*, 163–173.

(57) Luo, Y. R. *Comprehensive Handbook of Chemical Bond Energies*; CRC Press: Boca Raton, 2007.

Supporting Information

Correlating atomic-level compositions and structures with the aromatization properties of fluorine-promoted Pt/KL zeolite catalysts

Tsatsral Battsengel,[1] Zachariah J. Berkson,[1] Joseph Bergmeister,[2] Gabriela Alvez-Manoli,[2] Sikander Hakim,[2] Steven Lim,[2] Masud M. Monwar,[2] Cori A. Demmelmaier,[2] Bradley F. Chmelka[1,*]

[1] Department of Chemical Engineering, University of California, Santa Barbara, California 93106 U.S.A.

[2] Chevron-Phillips Chemical Company, Kingwood, Texas 77339 U.S.A

*Corresponding author: bradc@ucsb.edu

Supporting Information

Equations to calculate aromatic selectivity and yield plotted in **Figure 3.2** of main text.

$$\text{Selectivity} = \frac{\text{moles of (benzene + toluene) in effluent}}{\text{moles of [(hexane+heptane) in feed}-\text{(hexane+heptane) in effluent]}} \qquad \textit{eq (3.1)}$$

$$\text{Yield} = \frac{\text{moles of (benzene + toluene) in effluent}}{\text{moles of [(hexane+heptane) in feed}-\text{(hexane+heptane) in effluent]}} \qquad \textit{eq (3.2)}$$

Back of the envelope, thermodynamic calculations show the preferential binding of F to Al.

Reaction energies of fluorine bonded to Si (eq (4)) and Al (eq (6)) sites as shown in reaction eq (3) and eq(4), respectively, reveal that fluorine preferentially bonds to

zeolite Al sites, consistent with previously reported publications on fluorinated aluminosilicates.[32]

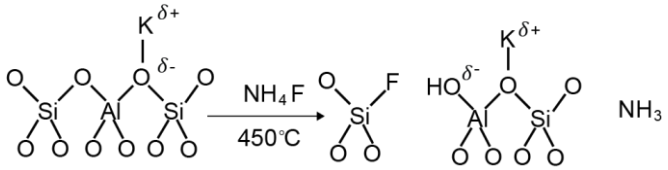

eq(3)

$$\Delta H\ (298\ K) \approx -(\Delta H_{Si-F} + \Delta H_{O-H} - H_{Si-O}) = -207\ kJ/mol \qquad eq(4)$$

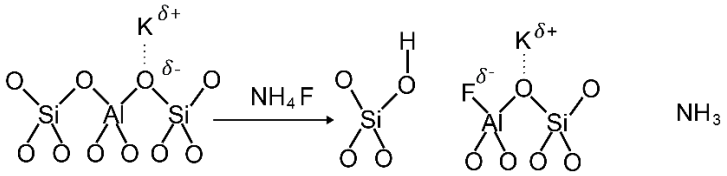

eq(5)

$$\Delta H\ (298\ K) \approx -(\Delta H_{O-H} + H_{Al-F} - H_{Al-O}) = -603\ kJ/mol \qquad eq(6)$$

Table S3.1. Bond energy of possible simple bonding configurations in fluorinated aluminosilicate

	Bond Energy [kJ/mol] at 298 K
Si-O:	799.6 ± 13
Al-F:	675
Al-O:	501.9 ± 11
O-H:	430 ± 0.3
Si-F:	576.4 ± 17

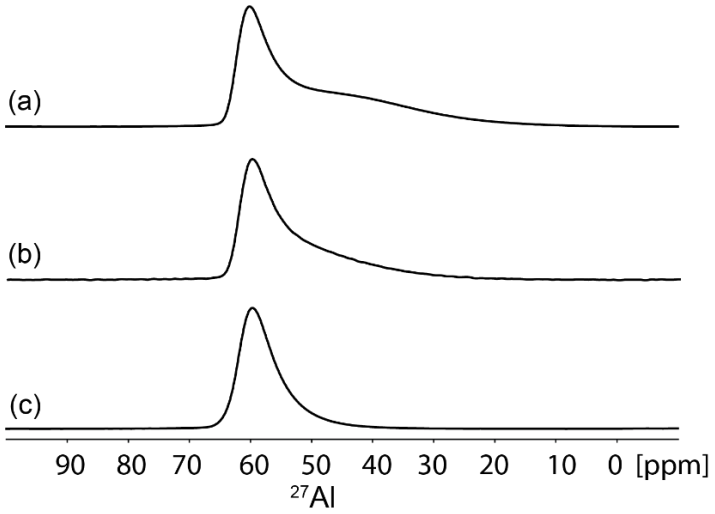

Figure S3.2. Solid-state 1D ^{27}Al Hahn-echo NMR spectra of (a) dehydrated, (b) partially hydrated, (c) fully hydrated 1 wt% Pt/F-KL acquired at 9.4 T, 8 kHz MAS. Fully hydrated KL zeolite exhibits a ^{27}Al signal with only one broad asymmetric Czjezk lineshape.

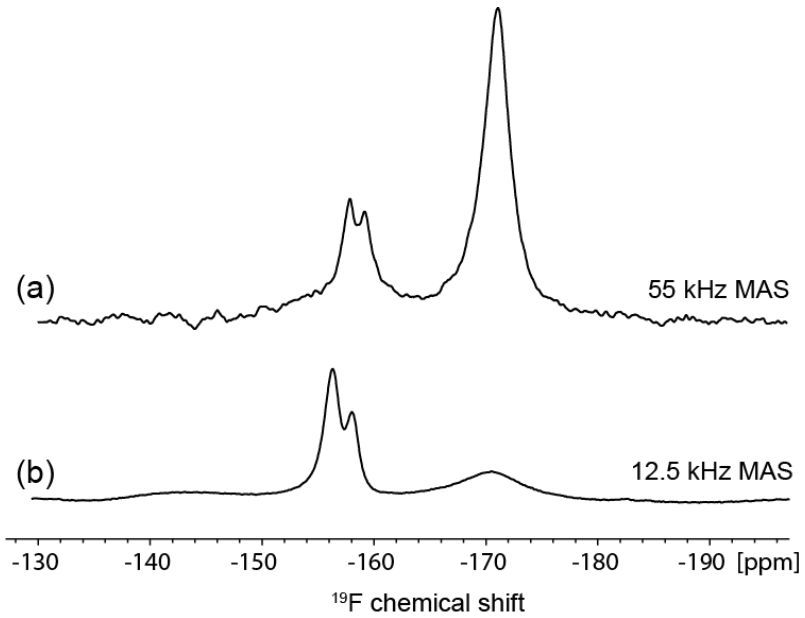

Figure S3.3 shows a comparison of ^{19}F MAS spectra at 12.5 kHz and 55 kHz, the latter shows a narrower signal from ^{19}F moieties experiencing stronger dipolar interactions

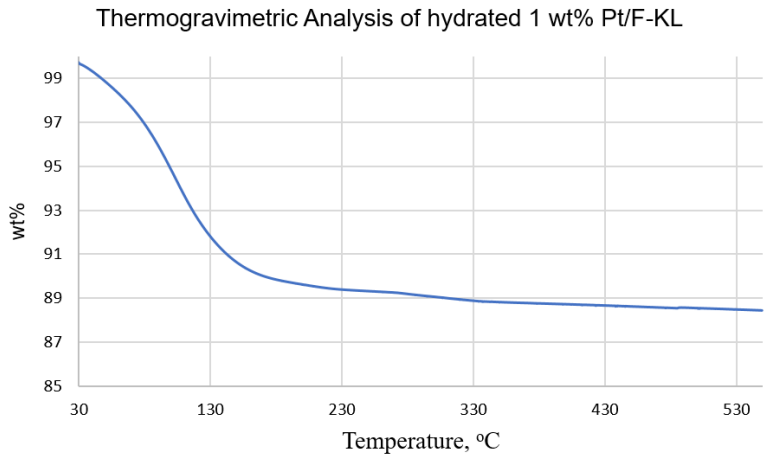

.**Figure S3.4.** Thermogravimetric analyses of fully hydrated 1 wt%Pt/F-KL. Approximately 11 wt% of the fully hydrated zeolite is adsorbed water.

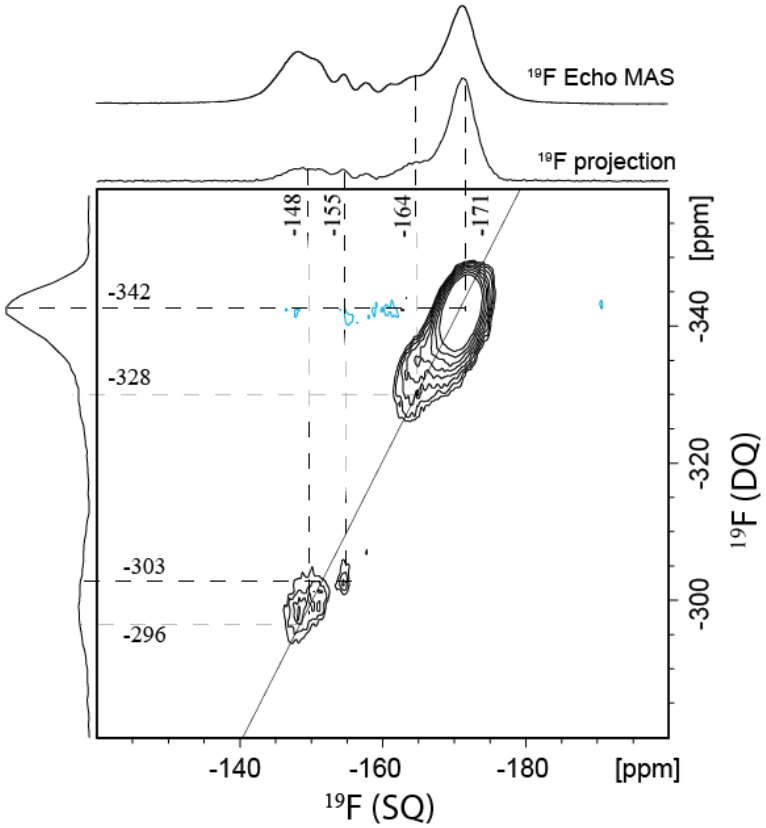

Figure S3.5. Solid-state 2D ^{19}F{^{19}F} SQ-DQ spectrum of AlF_3. The spectrum is acquired at 9.4 T, 95 K, 55 kHz MAS. The correlated signal intensities arise from dipole-dipole coupled ^{19}F moieties that are within ~1 nm. A 1D ^{19}F Echo MAS spectrum was acquired separately and is shown along the top horizontal axis for comparison.

Discussions on spent catalysts.

Figure S3.2 shows ^{13}C spectra of spent catalysts that are used to obtain aromatization selectivities of benzene and toluene shown in **Figure 3.3**. Both Pt/KL and Pt/F-KL contain ca. 0.1 wt% carbonaceous residues after spending the catalyst for 40 hours. ^{13}C species in spent Pt/KL contains a variety of carbon deposits including aromatic ^{13}C moieties with signals around 130 ppm, as well as aliphatic ^{13}C species with signals at 10 – 30 ppm. In contrast, fluorine-promoted Pt/KL catalyst contains mostly only aliphatic ^{13}C species probably due to adsorbed reactants *n*-hexane and *n*-heptane. Both catalysts do not show an indication of any coke formation, which would result in broad featureless signal around 100-150 ppm.

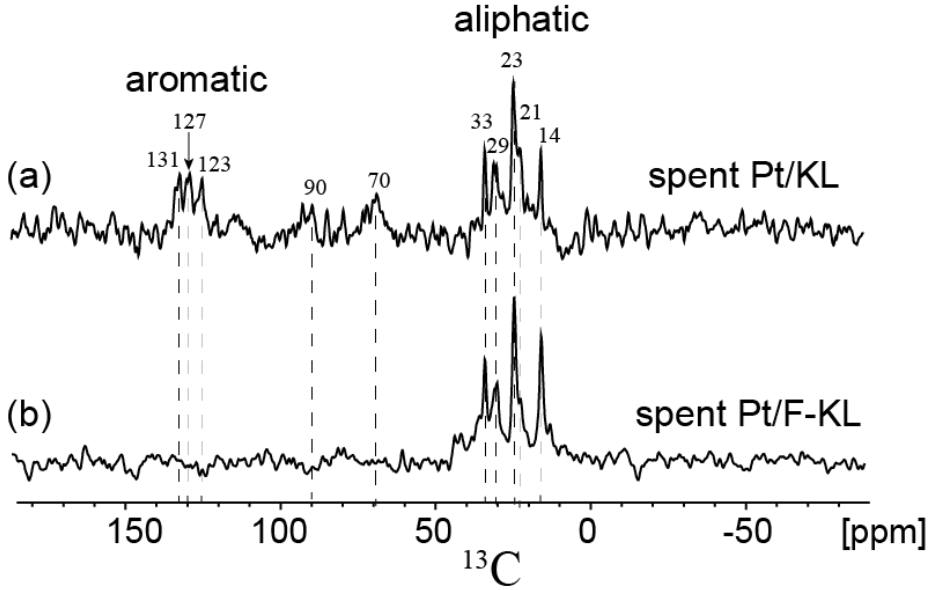

Figure S3.6. Solid-state 1D $^{13}C\{^{1}H\}$ CP-MAS spectra of spent (a) 1 wt% Pt/KL and (b) 1 wt% Pt/1 wt% F-KL zeolite catalysts after 60 h on stream at the same conditions (75 psi, LHSV 6/h) used in **Figure 3.1.** The spectra were acquired at 11.7 T, 298 K, and 10 kHz MAS.

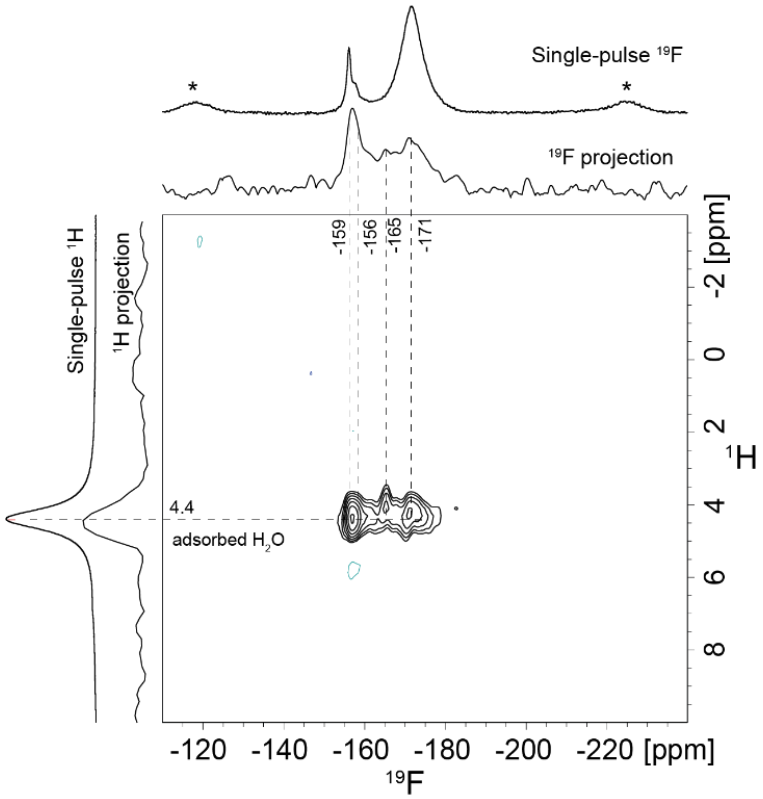

Figure S3.7: Solid-state 2D ^{19}F{^{1}H} HETCOR spectrum of reduced Pt/F-KL after full hydration. The spectrum was acquired at 9.4 T, 298 K, 20 kHz MAS. Dipole-coupled ^{19}F and ^{1}H moieties give rise to correlated signal intensities. 1D single-pulse ^{19}F and ^{1}H MAS spectra were acquired separately and are shown along the top horizontal and left vertical axes, respectively.

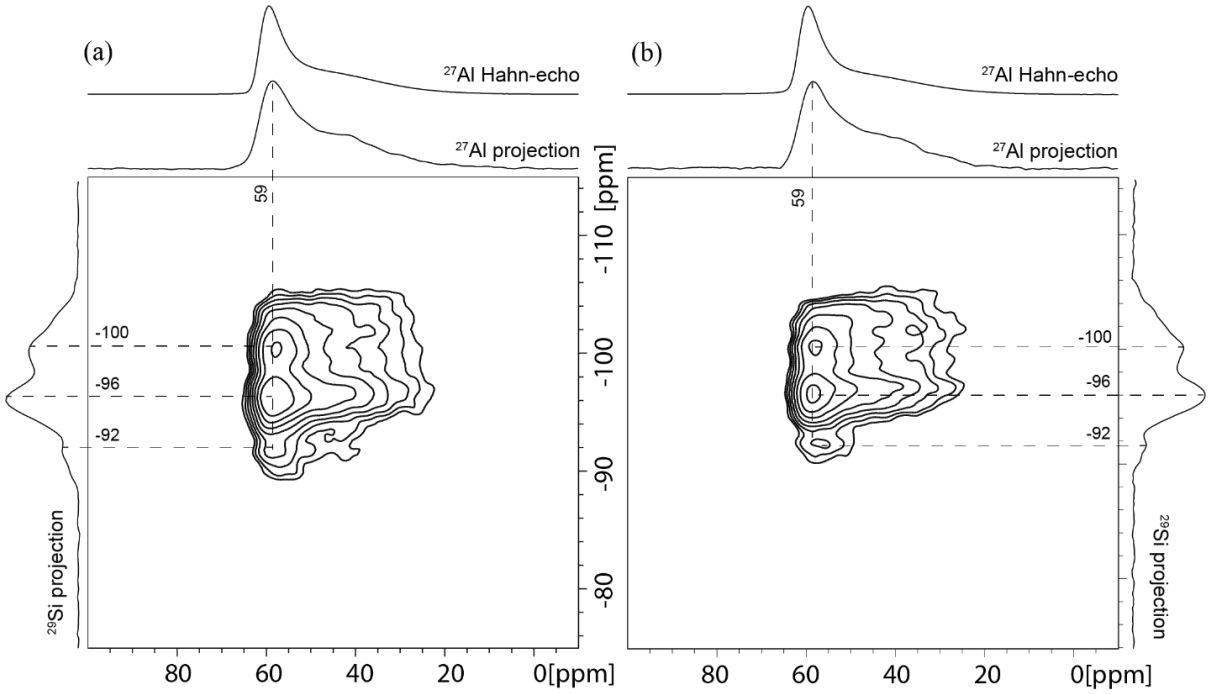

Figure S3.8. Comparisons of solid-state 2D *J*-mediated (through-covalent-bond) ^{27}Al{^{29}Si} HMQC NMR correlation spectra of (a) KL zeolite dehydrated at 723 K (b) 1 wt% Pt/F-KL reduced at 773 K. The spectra were acquired at 9.4 T, 95 K, and 8 kHz MAS. Quantitative 1D single-pulse ^{29}Si MAS spectra acquired at 11.7 T, 298 K, and 12.5 kHz MAS for (c) dehydrated KL and (d)1 wt% Pt/KL

CHAPTER 4

4. Nanoscale compositions, structures, and hydroisomerization properties of bifunctional Pt-H^+-USY zeolite catalysts

Tsatsral Battsengel,[1] Michael Girgis,[2] Stacey Zones,[2] Bradley F. Chmelka[1,*]

[1] Department of Chemical Engineering, University of California, Santa Barbara, California 93106 U.S.A.

[2] Chevron Energy Technology Company, Richmond, CA, 94801, USA

Keywords: Pt-zeolite catalyst, *n*-alkane hydroisomerization, bifunctional catalyst, USY zeolite, solid-state NMR of zeolite catalyst

4.1 Abstract

Two types of dual-function Pt-zeolite catalysts (0.5 wt% Pt-H^+USY with Si/Al molar ratios of 30 or 54) were used for *n*-hexadecane hydroisomerization to identify reaction pathways and correlate atomic-scale structures of these large pore zeolites to their catalytic activities. Though the catalysts have similar Pt loadings and comparable dispersions, they exhibit significantly different hydroisomerization reaction pathways. More interestingly, Pt-H^+USY catalyst with a lower Si/Al ratio (Catalyst A) behaves more like higher Si/Al ratio zeolites, *i.e.*, showing more cracking and less isomerization compared to the

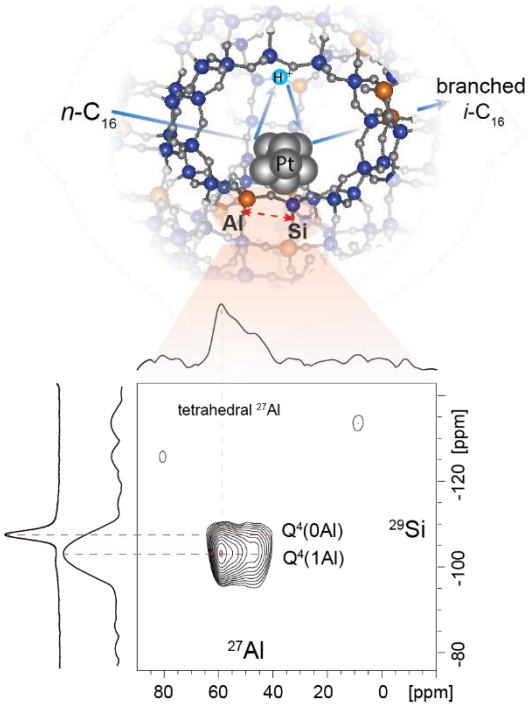

other catalysts with a higher Si/Al ratio (Catalyst B). Atomic-scale origins of such differences in macroscopic behaviors are revealed by a combination of characterization techniques such as X-ray diffraction, electron microscopy, infrared spectroscopy, and solid-state nuclear magnetic resonance (ssNMR) spectroscopy. Among these techniques, ssNMR, in particular, reveals significantly higher quantities of disordered siliceous species present in catalyst A compared to catalyst B, which is expected to influence the different hydroisomerization behaviors observed in two catalysts. Specifically, advanced two-dimensional (2D) NMR provides high-resolution and correlations of zeolite framework sites. For example, 2D ^{29}Si{^{1}H} NMR correlation spectra of Pt-H^{+}USY zeolite catalysts enable to identify of interactions between different ^{29}Si and ^{1}H species, which are crucial for bifunctional catalysts with acid species as one of the active sites. Moreover, recent advancements in NMR instrumentation enabled to conduct *in situ* variable temperature and pressure (up to 200 bar & 240 ^{o}C) ^{13}C MAS NMR measurements, which provide opportunities to identify types of reactants and products under similar reaction conditions. With these detailed insights on the structures and reactivities of Pt-H^{+}USY zeolites, catalytic behavior can be understood and opportunities for improvement can be recognized.

4.2 Introduction

Pt metal supported on ultrastable Y zeolites (USY) is used for a variety of hydrocarbon conversion applications.[1–6] Especially the presence of Pt active sites in combination with Bronsted acid H^{+} sites of the zeolite make Pt-H^{+}USY zeolites a favorable candidate for hydroisomerization, also known as dewaxing, catalyst. The branching of long straight-chain alkanes improves the octane number of gasoline and

enhances the low-temperature performance of diesel or lubricating oils.[7] High-quality lubricating oils have a low melting point and high viscosity indices, *i.e.*, less viscosity changes with temperature, properties that multibranched alkanes possess but not straight alkanes.[8] Therefore, effective hydroisomerization catalysts produce high yields of isoalkanes from *n*-alkanes.[9] Bifunctional Pt-H^+USY catalysts containing the metallic Pt sites for hydrogenation/dehydrogenation and the H^+ acidic sites for isomerization are known to be effective in the hydroisomerization of *n*-alkanes. Here, two types of Pt-H^+USY catalysts with different Si/Al ratios are studied to understand the effects of atomic-scale structures on *n*-hexadecane hydroisomerization. The dehydrogenation and cracking reactions occur sequentially on the bifunctional catalyst as demonstrated in **Figure 4.1**. Reactant *n*-hexadecane diffuses into the pore of the zeolite USY and hydrogenation/dehydrogenation occurs on Pt sites while isomerization proceeds with the help of H^+ sites.[10] The reaction properties of these bifunctional catalysts depend strongly on (i) types and distributions of Pt and H^+ active sites, (ii) the ratio of accessible Pt to acid sites, and (iii) both meso- and nanoscale architectures of the zeolite support. Obtaining the atomic-scale structural information of Pt-H^+USY systems is crucial to understanding the structure-reactivity relationship of industrially significant catalysts, hence developing strategies to improve catalyst performance.

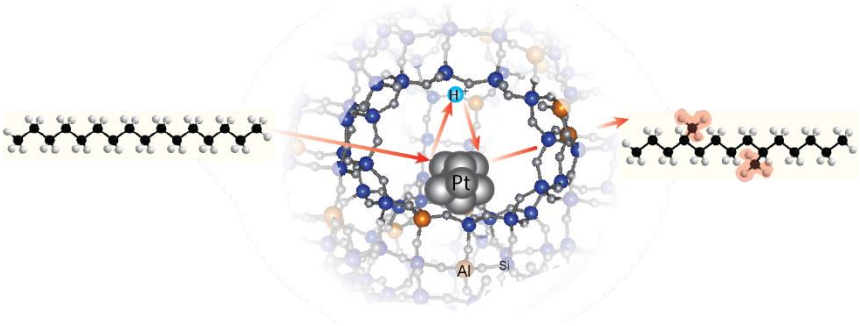

Figure 4. 1. Schematics of Pt-H$^+$USY zeolite catalyst used for n-hexadecane hydroisomerization

Here, a combination of characterization techniques, including X-ray diffraction (XRD), transmission electron microscopy (TEM), Fourier Transformed Infrared Spectroscopy (FTIR), and solid-state Nuclear Magnetic Resonance (ssNMR) spectroscopy are used to understand the structural origins of the n-hexadecane isomerization behaviors of two types of Pt-H$^+$USY catalysts. To effectively implement various characterization methods and analyze the results to obtain detailed structure-function correlation, it is crucial to have a deeper understanding of how the hydroisomerization reaction proceeds on bifunctional catalysts. **Figure 4.2** shows reaction mechanisms of *n*-butane hydroisomerization on Pt-H$^+$USY catalyst. First, the reactant finds its way to a Pt-site, on which dehydrogenation occurs to result in a short-lived olefin intermediate. The olefin finds the nearest Bronsted acidic site of the zeolite to form carbocation, which is charge-balanced by the zeolite framework Al sites, where C-C bond rearrangement, *i.e.*, isomerization, occurs to form in branched carbocation. The final carbocation diffuses away from the Al site of the zeolite to the next active Pt-site to hydrogenate and produce a branched isomer of the starting straight alkane.

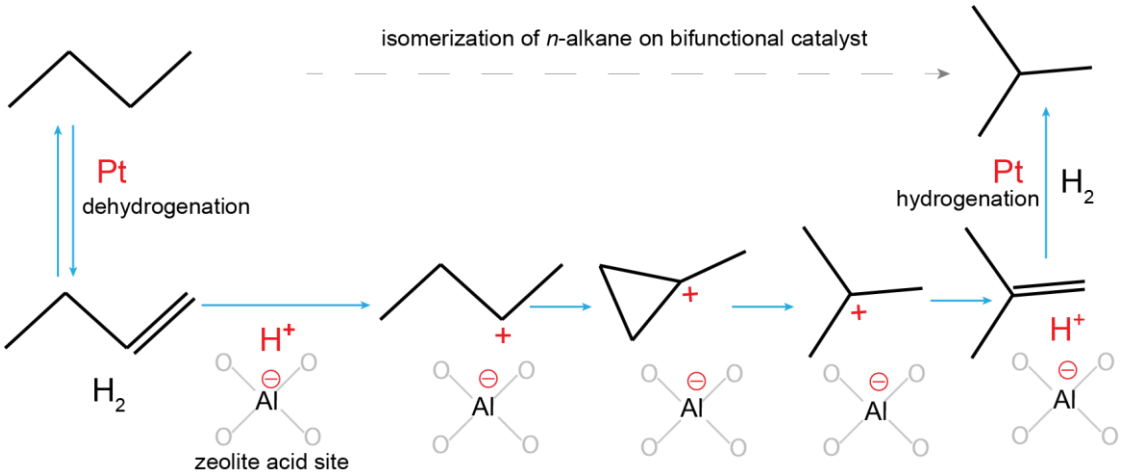

Figure 4.2. Hydroisomerization mechanism of straight alkanes on Pt-H^+USY bifunctional catalyst

This work aims to identify the effects of local chemical environments of the zeolite support on the reaction properties. Two types of Pt-H^+USY with Si/Al molar ratio of 54 (noted as Catalyst A) and 30 (noted as Catalyst B) are investigated for *n*-hexadecane hydroisomerization. The results and analyses of atomic-scale structures of two types of zeolite support revealed that bulk Si/Al ratio alone is not a determining factor of types and relative quantities of ^{29}Si species, *e.g.*, Q^4(*n*Al) zeolite sites, and the presence of dense siliceous species, etc., which affect the accessibility of the H^+ acidic sites thus the reaction properties.

4.3 Materials and methods

Catalyst preparation. 1 g of FAU zeolites used for catalysts were added to a vial along with 5 g of 0.148 M NH_4OH buffer solution and 6 mL of DI water, resulting in a pH of 9-10.5. $Pt(NH_3)_4(NO_3)_2$ was used, instead of $Pt(NH_3)_4Cl_2$ as Pt precursor, to avoid Cl^-, though differences caused by the two precursors are expected to be small. The platinum-containing solution was prepared by dissolving 350 mg of $Pt(NH_3)_4(NO_3)_2$ in 5 g of 0.148 M NH_4OH solution and 32 ml of H_2O. 1 mL of the latter

platinum solution was added to the vial containing the zeolite slurry. The solution was left to stand for 2-3 d at room temperature and subsequently filtered. The platinum-containing zeolite powder was dried at 90°C in an oven for 2-4 h and then placed as a fine powder in a thin glass dish and calcined to 300°C in the air flowing at 20-40 ft^3/min. The following stepped heating program was used: 1. heat at 1°C/min to 120°C, 2. hold for 2 h, 3. heat at 1°C/min to 300°C, 4. hold for 3 h, and finally turn off the heat and allow cooling to room temperature. The catalyst was pressed into a pellet, which was crushed to give solids of a 20-40-mesh size upon sieving. Measurements of Pt dispersion were presented based on strong (dissociative) H_2 chemisorption.

Reaction test. Catalyst powder was pressed into a pellet which was crushed to give 20-40-mesh size solids and diluted with 100-mesh alundum and loaded to 0.25" OD reactor to give a 13-cm bed height. Catalysts are dried by flowing 50 cm^3/min of N_2 over catalyst bed at 120°C for at least 2 h, followed by reducing at 315°C in H_2 flowing at 50 cm^3/min for at least 1 h. H_2 and *n*-hexadecane as was used as the feed (H_2/*n*-C_{16} = 8). The reagent *n*-hexadecane is liquid at reaction temperatures of 280 °C for Pt-H^+USY zeolites. Detailed reaction pathways of *n*-hexadecane were investigated by using the Delplot method,[11] which plots selectivity (yield/conversion) as a function of conversion for each product. The primary products can be identified from the Delplot because they have non-zero initial rates of formation and have finite *y*-intercept at zero conversion. Non-primary products have an initial rate of zero, and thus exhibit a zero intercept on the Delplot. Primary products for two types of Pt-zeolite catalysts were identified using the Delplot method and reaction pathways were deduced.

Material characterization: Scanning electron micrographs (SEM) of H^+USY zeolites were obtained using an FEI XL40 Sirion FEG digital scanning electron microscope at 15000× magnification and 5 kV electron beam voltage. The crystallinity of Pt-H^+USY catalysts was probed by X-ray diffraction (XRD) methods. The XRD patterns were collected with a scanning rate of 5 ^{o}/min over a range of 2θ angles from 5^o to 70^o using a Panalytical empyrean powder diffractometer. Transmission electron microscopy (TEM) images of reduced Pt-H^+USY catalysts were collected by FEI Titan 300 kV instrument with 30 electrons/Å^2·s. The samples were exposed to the beam for 5–10 s to decrease the beam damage.

Table 4.1. Comparison of Si/Al ratio, Pt wt%, and Pt dispersion of catalysts A and B

	Catalyst A	**Catalyst B**
	Pt-H^+USY	Pt-H^+USY
Si/Al molar ratio	54	30
Pt, wt%	0.47	0.43
Pt dispersion	70%	52%

Multinuclear solid-state nuclear magnetic resonance (NMR) spectroscopy experiments were conducted to obtain atomic-scale structural information from Pt-H^+USY materials. Dried, calcined, and reduced samples were sealed in a glass ampule and transferred into a glovebox under dry Ar, where samples were packed in NMR rotors. Silicone plugs were used to seal the open end of the rotor before placing the rotor cap, and dry N_2 was used for MAS. Conventional solid-state ^{1}H and ^{29}Si

MAS-NMR were conducted on 11.7 T Bruker AVANCE-II NMR spectrometer, operating at 12.5 kHz MAS at 298 K using a Bruker 4 mm probe head and zirconia rotors with Kel-F^{TM} caps. Low-temperature MAS (LTMAS) measurements (95 K) provide significantly enhanced NMR signal sensitivity that allows the detection and analysis of ^{29}Si-O-^{27}Al environments at a natural abundance of ^{29}Si (4.7%). LTMAS measurements were conducted on a Bruker ASCEND 400 NMR spectrometer with a 9.4 T superconducting magnet equipped with a low temperature 3.2 mm triple-resonance MAS probe head. A Triple-quantum MAS pulse sequence with two hard pulses followed by a *z*-filter was used. Single-pulse excitation of 0.42 us corresponding to π/12 flip angle was used for quantitative ^{27}Al experiments with a recycle delay of 0.5 s. *In situ* high-temperature high-pressure measurements were conducted at 11.7 T Bruker AVANCE-II NMR spectrometer equipped with 7.5 mm HX probe using specially designed MAS NMR rotor (the WHiMS rotor) capable of operating at pressures up to 400 bar at 20 °C or 225 bar at 250 °C.[12] Background ^{13}C NMR of the empty rotor was collected at each temperature and subtracted from the ^{13}C NMR spectra of the *in situ* measurements of the catalysts. Two terminal carbon-enriched *n*-hexadecane was purchased from Sigma Aldrich (CAS number: 158563-27-0) and used as a reactant for in situ measurements. To make sure the reaction is not mass transport limited, a small amount (80 mg catalyst with 20 µL *n*-hexadecane) of catalyst was used. A specially designed pressurizing chamber was used to pressurize the rotor with 50 bar H_2 at room temperature.

4.4 Results and Discussion

4.4.1 *N*-hexadecane hydroisomerization over Pt-H^+USY catalysts

Using *n*-hexadecane as a probe molecule, a sequential reaction network was deduced for the two types of Pt-H^+USY catalysts (Catalyst A: Si/Al = 30 and Catalyst B: Si/Al = 54), in which *n*-hexadecane, mono- and multi-branched isomers form in series and with cracking products subsequently formed from the latter. Pseudo-first-order rate coefficients for the isomerization and cracking reactions were determined and cracking rates by carbon number were determined. The different *n*-hexadecane hydroisomerization activities of the two Pt-H^+USY catalysts were correlated with distinct local Si and Al environments of the USY zeolite framework and Bronsted acid sites, as characterized by ^{29}Si, ^{27}Al, and ^{1}H NMR methods.

The selectivities and product species differ for each type of catalyst, hence, the reaction pathways of *n*-hexadecane into branched C_{16}-isomers and smaller hydrocarbons can be deduced from quantitative analyses of reactant conversion and product selectivities. **Figure 4.3** shows the mole fraction of reactant and isomer products of hexadecane as a function of contact time, *i.e.*, the inverse of Weight Hourly Space Velocity $(WHSV)^{-1}$. For both catalysts, decreasing mole fraction of the reactant *n*-hexadecane occurs with the increasing fractional conversion of mono- and multi-branched isomers of hexadecanes shown by red and green data points. For Catalyst A, the mole fraction of the reactant decreases almost linearly from 1.0 to ca. 0.35 at the end of the reaction test of 2 h contact time. The amount of monobranched isomers of hexadecane increases up to a mole fraction of 0.2 during the first 1 h of contact time and stayed almost constant until the end of the test. In contrast, multibranched

isomers of hexadecane were produced in less amount compared to monobranched isomers, but the mole fraction of multibranched i-C_{16} kept increasing during the entire period of the test and ended at a mole fraction of 0.1 in 2 h contact time. This suggests that in the first 1 hour of the contact time the rate of formation of monobranched isomer was higher than that of multibranched product, but in the last 1 hour of the contact time, multibranched product formation was at a higher rate than monobranched isomers. Faster formation of multibranched hexadecane towards the end of the reaction test could be due to deactivation of Pt active sites, which can lead to more branching catalyzed by the acidic H^+ sites than dehydrogenation/hydrogenation on Pt.

By comparison, for Catalyst B, *n*-hexadecane is consumed at a much faster rate, *i.e.*, molar fraction decreases to less than 0.1 within the first 2 h of contact time. Similar to reactions on Catalysts A, monobranched *i*-C_{16} forms at a faster rate compared to multibranched *i*-C_{16} at the beginning of the catalytic test, and the trend is reversed at the end of the contact time, *i.e.*, multibranched hexadecane forms at a faster rate than monobranched isomers. However, the molar fraction of monobranched isomer increases to its maximum of 0.3 within 0.5 h of contact time and decreases to ca. 0.1 at the end of the reaction. On the other hand, multibranched isomers increased to a molar fraction of 0.4 within the first 1.5 h of the reaction and slightly decreased to 0.35 for the last 0.5 h of the reaction. Although both catalysts show similar behaviors of forming monobranched at a higher rate at the beginning of the reaction and multibranched isomer at the end of the reaction, Catalyst B with lower Si/Al ratio

H^+USY zeolite exhibit more amount of overall branched isomers of hexadecane compared to Catalyst A.

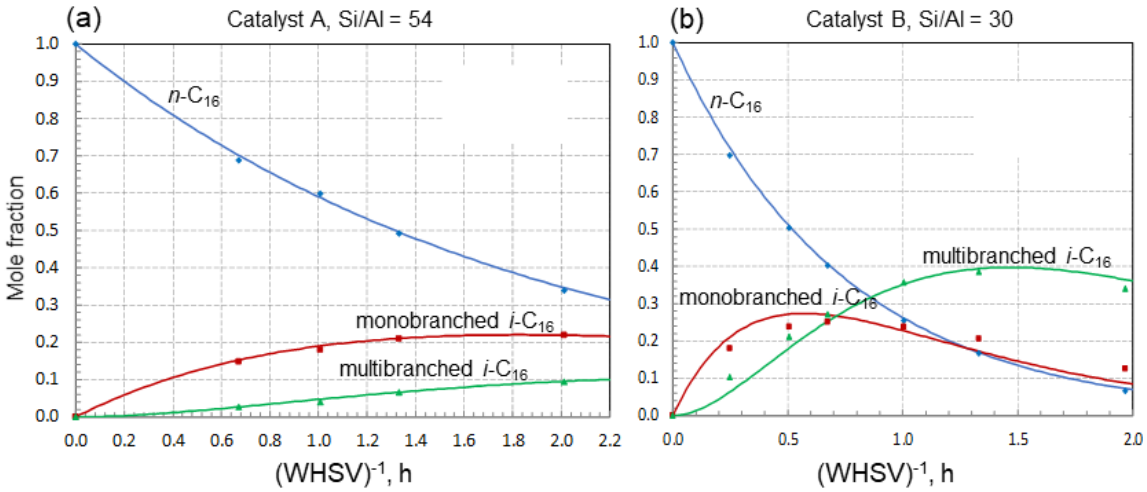

Figure 4.3. Catalytic tests of n-hexadecane hydroisomerization on (a) catalyst A and (b) catalyst B. Fractional conversion as a function of 1/WHSV expressed in h. Feed *n*-hexadecane is in blue, monobranched, and multi-branched hexadecane products are in red and green, respectively. The feed is composed of H_2 and *n*-C_{16} with a ratio of 8, and the reaction proceeds at 280 ^oC. Continuous lines correspond to a fitted model of the experimental data points.

Furthermore, for Pt-H^+USY catalyst with lower acidity (Catalyst A with Si/Al = 54), a parallel set of reaction pathways were identified in which *n*-paraffin cracking products are formed directly from *n*-hexadecane. **Figure 4.4** shows the selectivity for *n*-octane as a function of fractional conversion of the reactant *n*-hexadecane for Catalyst A (green rectangle data points) and Catalyst B (red square data points). For Catalyst A, *n*-octane selectivity reaches its maximum of 0.06 when the reactant fractional conversion was only 0.4 and stayed at 0.06 until the end of the test. In contrast, n-octan selectivity slowly increases from 0 to 0.02 for Catalyst B. By comparison, a Pt/SiO_2 catalyst was less active for catalyzing the formation of *n*-paraffin cracking products. Direct hydrocracking of *n*-hexadecane to *n*-paraffin

products appears to be characteristic of Pt-containing low-acidity zeolites and could provide a new route for hydrogenolytic cleavage of aliphatic carbon-carbon bonds.

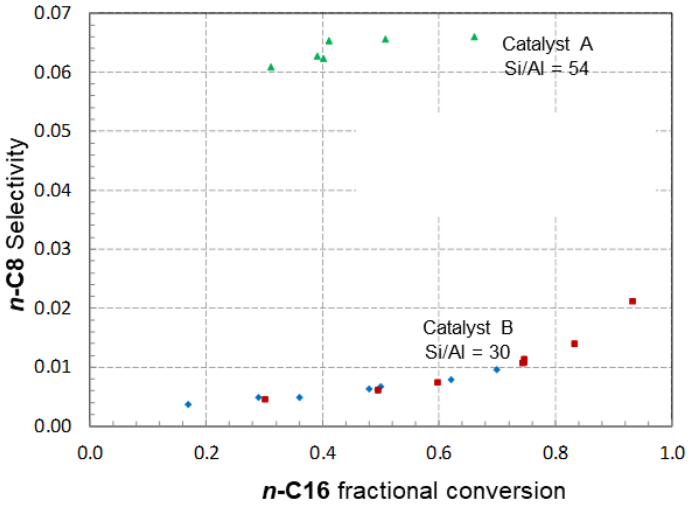

Figure 4.4. *n*-octane product selectivity as a function of feed *n*-hexadecane for catalyst A (green) and catalyst B (red).

Considering the provided Si/Al ratio of the two catalysts, Catalyst A with a higher Si/Al ratio and lower concentrations of Bronsted acidic sites, is expected to have higher isomerization properties compared to Catalyst B. However, the opposite of what is expected is observed, *i.e.*, Catalyst B with a lower Si/Al ratio exhibits more hydroisomerization activities. Moreover, previous studies of bifunctional Pt-H^+USY catalysts have shown the effects of accessible Pt/H^+ ratio on hydroisomerization[10,13–15] and have demonstrated that the catalysts with higher Pt/H^+ yield more isomerization products. The approximate ratio between accessible surface Pt to H^+ sites is 0.054 for Catalyst A and 0.021 for Catalyst B (calculated based on measured Pt dispersion and provided Si/Al ratio). The estimated Pt/H^+ values predict Catalyst A with almost double the Pt/H^+ ratio of Catalyst B to exhibit more isomerization products. The predictions of catalytic activities based on bulk properties, *e.g.*, bulk Si/Al ratio and accessible Pt/H^+

ratio, are not reliable. The results and analyses presented in this work show the importance of obtaining atomic-scale structural information of these materials, which directly influence the catalytic activities.

4.4.2 Size and uniformity of Pt clusters in Pt-H^+USY catalysts.

Dual-functionality of the catalysts originates from the dehydrogenation properties of Pt sites and isomerization functionalities of Bronsted acidic sites of the zeolites. The structural origins of different hydroisomerization behaviors exhibited by Catalyst A and B are investigated by characterizing both Pt active sites and local chemical environments of the H^+USY zeolite supports. First, to characterize the Pt sites and obtain information on the sizes of the Pt present on both types of zeolites, transmission electron micrographs are acquired. **Figure 4.5** shows TEM images of Catalysts A and B, which reveal Pt particles with varying sizes. For both catalysts, small Pt particles shown in darker contrast with a diameter of 1-3 nm are pointed by white arrows. Magnified inlets for each TEM image are shown at the upper right corner to demonstrate the presence of small Pt species. Catalytically active Pt sites for hydroisomerization are likely these small Pt particles residing inside the zeolite cage instead of large Pt particles located on the surface of the zeolite crystallites, because of the necessity to have proximate Pt and H^+ active sites for sequential hydroisomerization reaction. Large Pt clusters with a diameter of 30-50 nm are observed in both catalysts, which are pointed by red arrows. Assuming the particles are closed-packed icosahedron,[16–18] a Pt particle with a 30 nm diameter would contain approximately 931,000 Pt atoms compared to only 34 atoms for a 1 nm particle based on the following equation.

$N_T = \frac{\pi\sqrt{2}}{6}\left(\frac{d}{2r}\right)^3$, where N_T is the total number of atoms in a particle with diameter *d* and *r* is the radius of Pt atom (0.139 nm).

Even at this low 0.5 wt% Pt loading, metal agglomeration is challenging to avoid, and the formation of large particles exponentially decreases the amount of accessible surface Pt species that can participate in the reaction. For Catalyst A with Si/Al ratio of 30, 0.5 wt% Pt corresponds to Al/Pt molar ratio (which can also be estimated for molar Bronsted H^+/Pt ratio) of approximately 21, and for Catalyst B with Si/Al =54, the molar ratio of Al/Pt is 12. However, Al to accessible surface Pt species will be orders of magnitude higher than the calculated molar ratios due to the formation of large Pt particles, resulting in catalysts with much higher relative molar concentrations of acidic sites than surface Pt sites. Regardless of the different Si/Al ratios of the zeolite supports, both catalysts contain similar sizes of Pt particles, *e.g.*, Pt particles with 1-3

nm diameter and Pt particles with a size of 30-50 nm based on the analyses of the TEM results.

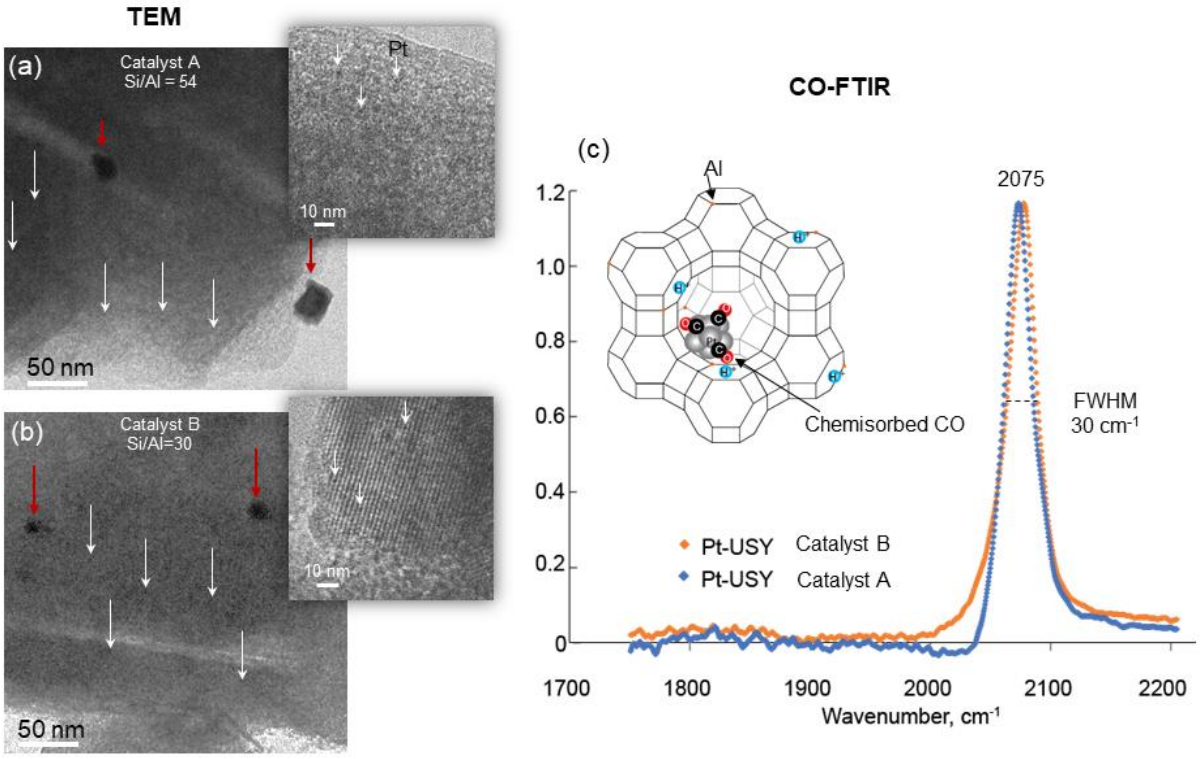

Figure 4.5. Representative TEM images of (a) Catalyst A and (b) Catalyst B. White arrows point at small ca. 1-3 nm Pt particles and red arrows point at larger Pt particles with a diameter of up to 20 – 30 nm. Subsets show magnified sections of TEM images showing small Pt particles that are pointed by white arrows. Darker contrasts are from heavier Pt atoms. (c) FTIR spectra of CO adsorbed on reduced catalyst A (blue) and catalyst B (orange) after evacuation at 293 K.

The types, oxidation states, and locations of Pt species in the zeolites can be probed by complementary Fourier-Transform Infrared Spectroscopy of adsorbed CO on Pt clusters. CO-FTIR results obtained from catalysts A and B. FTIR spectra of CO adsorbed on *in situ* reduced Pt-H^+USY catalysts are shown in **Figure 4.5c**. The IR spectra of CO adsorbed on platinum depend on the. The effects of the dynamic behavior of Pt, *i.e.*, agglomeration, redispersion, or mobility of Pt, upon introduction of

CO[19] should not be completely ignored but minimized by adsorbing the CO at metallic Pt nanoparticles. Moreover, the peak width can be correlated to the uniformity of the chemical environments of adsorbed CO. For example, carbonyls bound to homogenous metal catalysts have very narrow peak widths with FWHM ~10 cm^{-}) while CO on Pt nanoparticles can show signals with FWHM of up to 50 cm^{-1}. [20] Both catalysts reveal CO-FTIR signals with FWHM of 30 cm^{-1}, indicating a presence of similar uniformity of Pt nanoparticles. Furthermore, the analyses of temperature-programmed desorption (TPD) of adsorbed CO in zeolite are shown to be challenging due to the mass transfer limitations of evacuating desorbed CO at elevated temperatures. Nonetheless, the gradual shift of the CO vibration to lower wavenumbers at higher temperatures was observed and is indicative of multiple CO molecules bound to a contiguous Pt surface due to a phenomenon of dipole-dipole coupling. Based on the characterization of the Pt sites by TEM and CO-FTIR, both catalysts A and B contain metallic Pt clusters with similar uniformity and similar sizes. To understand the origins of different catalytic activities observed for the two catalysts, structures of the support H^{+}USY zeolites are discussed in the following discussions.

4.4.3 Crystallinity of the H^{+}USY zeolite supports

Starting with the identification of the bulk crystallinity and zeolite crystal sizes of the two zeolites used to synthesize Catalysts A and B, structural similarities and differences between the supports are revealed. **Figure 4.6** shows the XRD powder diffractions of USY zeolites used for Catalyst A and B. The powder patterns of H^{+}Y zeolite (Si/Al =2.5), which did not go through an extensive dealumination like the H^{+}USY zeolites, are shown in **Figure 4.6a** as a comparison. Reflections of the H^{+}USY

zeolites (**Fig. 4.6b,c**) match the reflection obtained from the H^+Y zeolite, consistent with the FAU framework. Compared to XRD of the H^+Y zeolite, both types of zeolites show broader reflections, which manifest reduced long-range order due to excessive dealumination. Moreover, Catalyst B exhibits less relative intensities of reflections at wide angles compared to that of Catalyst B, suggesting more long-range disorder in Catalyst B.

Crystallite size is one of the many important factors that affect the reaction activities of zeolites, as it affects the mass transfer limitations of the diffusing reactant, intermediates, and products inside or on the mouth of the zeolite pores.[8,21] Scanning electron micrographs of H^+USY zeolites used for Catalyst A and B are shown in **Figures 4.6d** and **e**, respectively. H^+USY of catalyst has relatively larger crystallite sizes of approximately a micron-sized compared to the zeolite used for Catalyst B, which has less than 0.5 μm crystals. Relatively smaller sizes of the H^+USY zeolite crystallites of Catalyst B could contribute to the higher hydroisomerization activities observed for Catalyst B. However, it is challenging to correlate such bulk properties to the observed catalytic activities, which occur on the surface of the metallic and acidic sites and are influenced by the local chemical environments of the zeolite. Therefore, to understand the molecular level origins of the catalytic differences observed in two catalysts, detailed atomic-scale structural insights of the support H^+USY zeolites are studied.

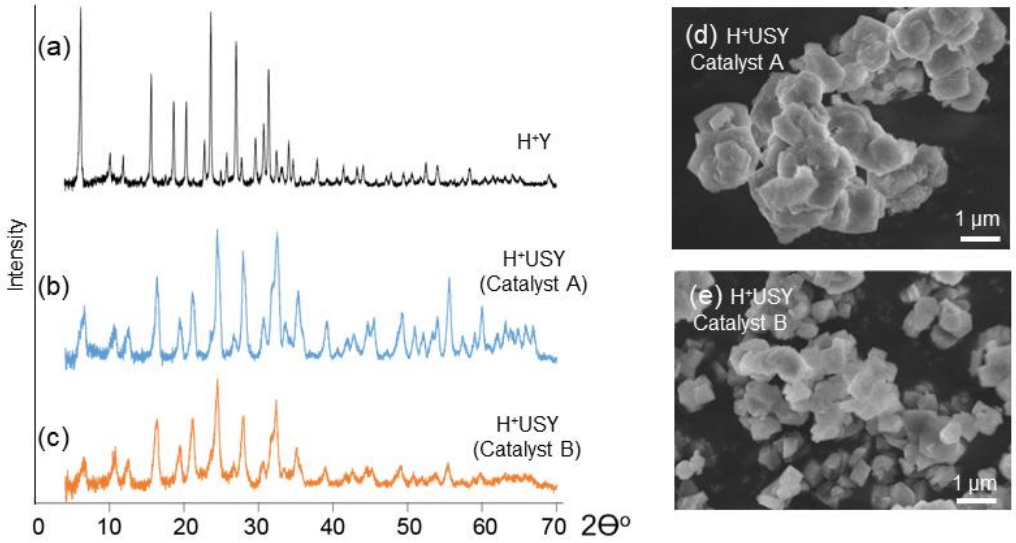

Figure 4.6. XRD powder patterns (a) H+Y zeolite in comparison with H+USY used for (b) catalyst A and (c) catalyst B. SEM images of H^+USY zeolites used for (d) catalyst A and (e) catalyst B

4.4.4 Framework ^{29}Si moieties in H^+USY zeolites

Although both H^+USY zeolites used to make Catalyst A and B have the same FAU framework structure with one type of crystallographic T-site, the two zeolites exhibit strikingly different local chemical environments of ^{29}Si sites. **Figure 4.7** shows quantitative single-pulse ^{29}Si MAS measurements of dehydrated H^+USY zeolites used in the synthesis of (a) Catalyst A (will be noted as H^+USY-A) and (b) Catalyst B (will be noted as H^+USY-B). The majority of the ^{29}Si signals from both zeolites emerge from Q^4(0Al) siliceous sites with a peak at -107 ppm, as expected for low Al content zeolites. Approximately 92% of the total ^{29}Si signal of H^+USY-A is from Q^4(0Al) sites and 8% of the ^{29}Si signal is from Q^4(1Al) sites. In contrast, the ^{29}Si spectrum of H^+USY-B contains 43% Q^4(0Al) species with a signal peak at -107 ppm and 29% Q^4(1Al) moieties with a peak at -102 ppm. The signal at -102 ppm can be either from Q^4(1Al) or Q^3(0Al)

species, so to identify whether the signal is from tetrahedral ^{29}Si sites with one Al neighbor or surface Q^3 site, ^{27}Al{^{29}Si} two-dimensional (2D) experiment is necessary, and will be discussed below. ^{29}Si signal from Q^4(0Al) species of H^+USY-A is significantly narrower compared to that of H^+USY-B, indicating a presence of broad distributions of ^{29}Si chemical environments in H^+USY-B. Moreover, ca. 28% of the ^{29}Si signal of H^+USY-B appears at -111 ppm, which is from disordered siliceous species induced by the dealumination process. Such disordered species, sometimes referred to as dense siliceous, are also reported in other USY zeolites.[22]

In contrast, the ^{29}Si spectrum of H^+USY-B does not reveal any detectable amount of such disordered siliceous species, though ^{29}Si{^{1}H} experiments that selectively enhance ^{29}Si signals close to ^{1}H species show the existence of the signal at -112 ppm from H^+USY-A as discussed below. XRD powder diffractions of the two zeolites do not show any detectable broad reflections that correspond to amorphous phases, suggesting that these siliceous species are not physically separated from the zeolite crystallites. To understand how these disordered siliceous species are coordinated with the rest of the zeolite structures, ^{27}Al{^{29}Si} 2D correlational NMR experiments were conducted.

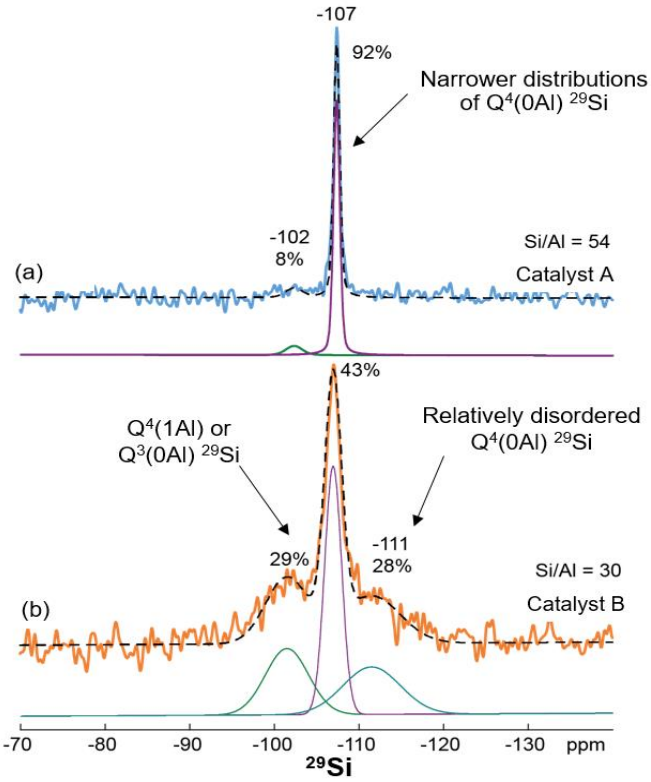

Figure 4. 7. Single-pulse ^{29}Si MAS NMR spectra of dehydrated H+USY used for (a) catalyst A and (b) catalyst B. Deconvoluted signals are shown under each corresponding spectrum. Dashed lines are the sum of the deconvoluted signals.

The framework ^{27}Al sites directly correlate with Bronsted acid sites, which is one of the active sites for bifunctional Pt-H^{+}USY catalyst, hence understanding how framework ^{27}Al atoms are coordinated to the neighboring ^{29}Si sites of the zeolite is crucial to obtaining structure-function correlation of these catalysts. The differences in the local environments two types of zeolites with varying Si/Al ratios are elucidated by 2D solid-state ^{27}Al{^{29}Si} Heteronuclear Multiple Quantum Coherence (HMQC) NMR measurements. **Figure 4.8** shows ^{29}Si{^{27}Al} Dipolar-mediated (through-space) HMQC spectra of H^{+}USY catalysts used for Catalyst A and B. Although the dilute amount of Al and low natural isotopic abundance of ^{29}Si (4.7%) make the acquisition of such 2D

correlation spectrum challenging, it is feasible at low temperature (95 K) conditions under which Boltzmann sensitivity is enhanced and thermal noise is decreased. Correlated signal intensities reveal unambiguous correlations between distinct ^{29}Si moieties and ^{27}Al sites.

H^+USY-A with a high Si/Al ratio (**Fig. 4.8a**) exhibits ^{27}Al signal at 60 ppm, which arise from tetrahedral ^{27}Al species, correlated with ^{29}Si signal at -107 and -102 ppm corresponding to Q^4(0Al) and Q^4(1Al) species, respectively. Separately collected ^{29}Si{^{1}H} Cross-Polarization (CP) spectrum acquired under the same condition is shown on the y-axis as a comparison. The majority of the ^{29}Si signal from H^+USY-A zeolite arises from Q^4(0Al) as shown in ^{29}Si{^{1}H} CP-MAS spectrum, the main signal intensity of ^{29}Si projection of 2D ^{27}Al{^{29}Si} spectrum is centered at -102 ppm, which corresponds to Q^4(1Al) species. Although -102 ppm ^{29}Si signal can be assigned to Q^4(1Al) and/or Q3(0Al) moieties, it is highly unlikely that ^{29}Si signals at -102 ppm correlated with ^{27}Al signal at 60 ppm are arising from Q^3(0Al) species due to dilute ^{27}Al in the framework. Moreover, the strength of the dipolar interaction scales inverse cube of the distance between the two nuclei, hence a weak through-space interaction between surface Q^3(0Al) ^{29}Si sites and framework ^{27}Al sites are not expected to exhibit observed correlated signal intensities. However, the presence of Q^3(0Al) species in these zeolites should not be neglected as they contain a lot of dealumination-induced surface defect sites as depicted by the structural schematics shown in the bottom right of the spectrum. Presence of Q^3(0Al) species are also shown by ^{29}Si{1H} measurements as discussed below. 5- and 6-coordinated ^{27}Al species have signals at ca. 30 and 0 ppm, respectively, which were not observed in 2D ^{27}Al{^{29}Si}

measurements, indicating that ^{29}Si sites are not in proximity with these extraframework Al species. However, these USY zeolite contain 6-coordinated extraframework ^{27}Al species, which were identified by ^{27}Al measurements as shown in **Figure S4.1**.

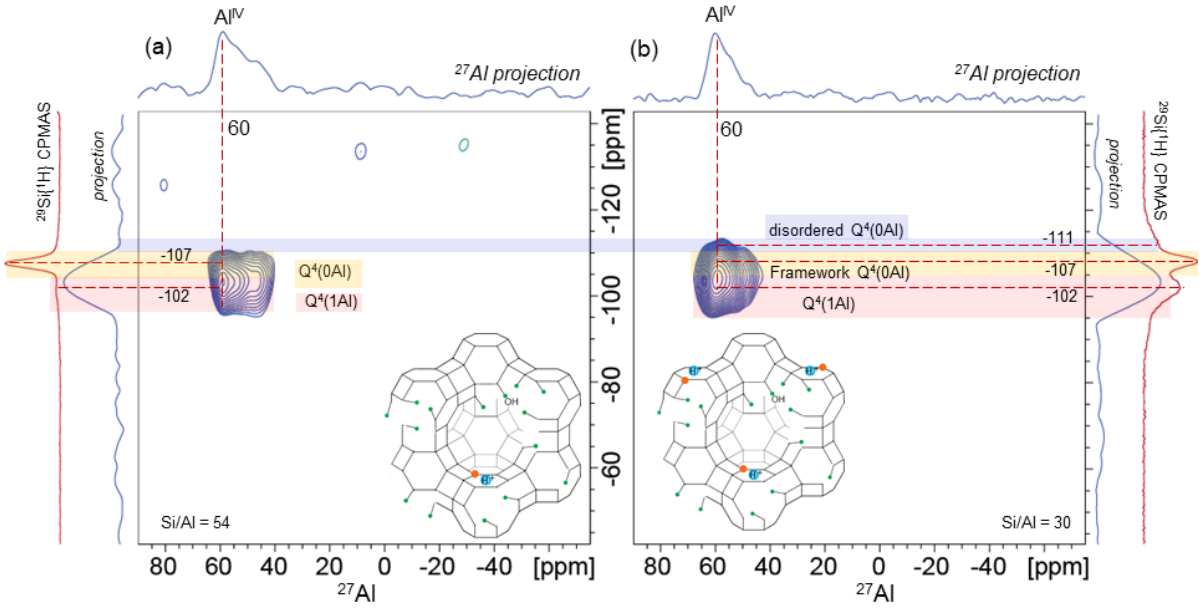

Figure 4.8. Solid-state 2D Dipolar-mediated ^{27}Al{^{29}Si} HMQC NMR correlation spectra of hydrated H+USY zeolite used for (a) Catalyst A (b) Catalyst B. The spectra are acquired at 9.4 T, 95 K, and 8 kHz MAS. The structural schematics of each zeolite structure are shown inside the corresponding spectrum. The chemical shifts of ^{29}Si sites (vertical axes) are labeled alongside their respective NMR signals. Projections of ^{27}Al sites are shown on the horizontal axes.

In comparison, H$^+$USY-B zeolite with a lower Si/Al ratio with a higher concentration of Al (**Fig. 4.8b**) reveals slightly different framework ^{27}Al{^{29}Si} connectivities compared to H$^+$USY-A zeolite. Similar to H$^+$USY-A zeolite, H$^+$USY-B zeolite has framework tetrahedral ^{27}Al sites with a signal at 60 ppm correlated with different ^{29}Si sites with signals at -107 and -102 ppm, which arise from Q^4(0Al) and Q^4(1Al) moieties. ^{29}Si{1H} CP-MAS spectrum overlaid on top of the ^{29}Si axis reveal a high-intensity signal at -

107 ppm from Q^4(0Al) species. ^{29}Si signal at -102 ppm in H^+USY-B has higher signal intensity compared to that of H^+USY due to the larger amount of Q^4(1Al) in low Si/Al ratio zeolite as discussed in previous quantitative 1D single-pulse measurements (**Fig. 4.7**). Interestingly, the ^{29}Si signal at -111 ppm, which was assigned to disordered siliceous moieties formed due to the dealumination process was found to be correlated with framework tetrahedral ^{27}Al sites. Although this signal intensity is subtle, it is clear that the presence of correlation between ^{29}Si signal at -111 ppm and ^{27}Al signal at 60 ppm in H^+USY-B, but the correlated signal intensity is not present in H^+USY-A as shown by the purple highlighted guide across the two spectra. The fact that these disordered siliceous species are close to the framework ^{27}Al site suggests that these disordered species are not separate phases from the zeolite framework but connected to the zeolite crystallites. XRD powder diffractions of two zeolites also do not show detectable reflections from separate amorphous phases (**Fig. 4.6**). Moreover, through-bond ^{29}Si{^{29}Si} correlational spectrum also reveals a presence of covalent-bonding between these disordered species at zeolite framework Q^4(0Al) moieties as shown in **Figure S4.2**. Such disordered siliceous moieties in ultrastable dealuminated Y zeolites have been reported previously and denoted as dense siliceous species. However, without further proof of the denseness of these species, they are simply denoted as “disordered siliceous species” in this work. Based on the experimental observations, the following schematics in **Figure 4.9** are proposed to portray the relative structures of the zeolite framework, disordered siliceous species, and the mesopores, similar to what has been proposed in Van Aelst et al.[22]

USY zeolite, also known as the ultrastable Y zeolite due to its higher stability under high temperature (~400-500 ^{o}C), is synthesized by steam-aging the Y zeolite, which initially starts with high loading of Al in the zeolite (Si/Al ~ 2-3) (**Fig. 4.9a**). By treating the Al-rich Y zeolite at high temperature in presence of water vapor, also known as steam-aging, induces framework Al to be popped out of the zeolite crystals. As a result, USY zeolite contains treatment-induced defects, mesopores, and fewer amounts of Al compared to the parent Y zeolite. Two USY zeolites studied in this work are provided by two different vendors, which presumably implement different steam-aging methods that result in not only different Si/Al ratios but also different amounts of disordered siliceous moieties. ^{29}Si spectra of USY zeolites prepared by the same vendor (**Fig. S4.3**) as USY zeolite used for Catalyst B show that higher extent of dealumination results more quantities of disordered siliceous species, further proving the origin of these species from the steam-aging process. Therefore, it is likely that disordered moieties are located at the surface of the dealumination induced mesopores as shown in the diagrams. Quantitative 1D ^{29}Si spectrum and ^{27}Al{^{29}Si} measurements revealed that H^{+}USY-B zeolite contains a significantly higher amount of disordered siliceous species, thus the structural diagram in **Figure 4.9d** has more of the purple disordered moieties compared to H^{+}USY-A zeolite shown in **Figure 4.9c**. Although Catalyst B contains more Al and H^{+} sites compared to Catalyst A, analyses of *n*-hexadecane hydroisomerization behaviors revealed the formation of more isomer products of hexadecane when Catalyst B was used in comparison to Catalyst A, opposite of what should be predicted based on bulk Si/Al ratio. The reason Catalyst B with higher overall Al content behaving more like low Al content could be due to

siliceous species formed at the surface of the mesopores. Distributions of acid sites in the zeolite are further investigated to understand the hydroisomerization behavior of the catalysts.

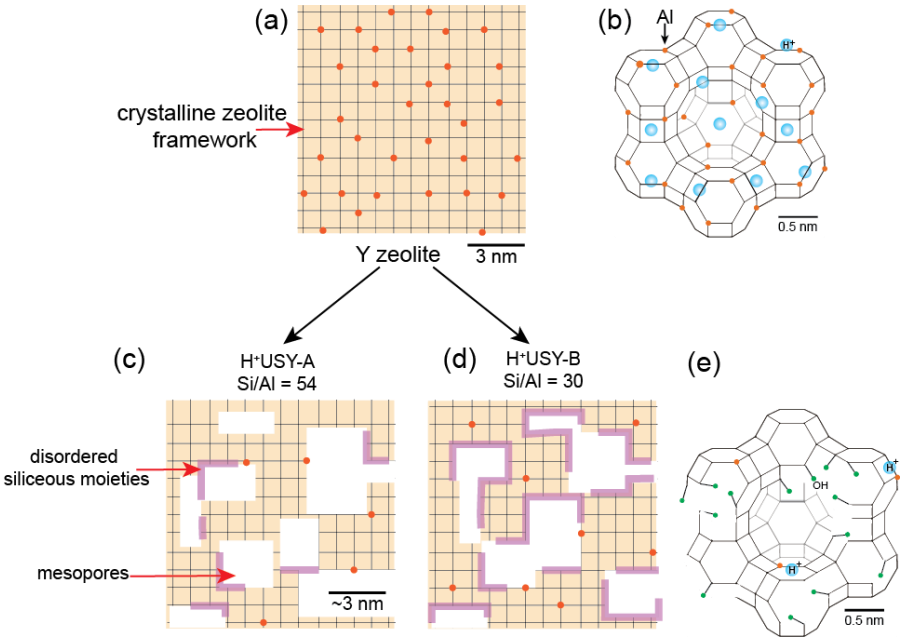

Figure 4.9. Schematic diagrams of crystalline zeolite and dealumination-induced disordered siliceous species at the surfaces of the zeolite mesopores. (a) The crystalline framework of Y zeolite. (b) FAU framework of HY zeolite with Si/Al ~ 2-3. (c) H^+USY-A zeolite with Si/Al =30, (d) H^+USY-B zeolite with Si/Al =54. Disordered siliceous moieties are shown in purple at the surface of the mesopores. (e) H^+USY zeolite framework showing fewer framework Al atoms and surface defect sites. Orange dots represent Al atoms in the crystalline regions of the zeolite framework.

4.4.5 Distributions of acid sites in calcined Pt- H^+USY catalysts

Bronsted acid sites have a crucial role in the dual functionality of the catalysts, hence identifying types of acidic sites and their interactions with the zeolite framework is crucial to obtaining the structure-function relationship of these catalysts. **Figure 4.10** shows $^{29}Si\{^{1}H\}$ HETeronuclear CORrelation (HETCOR) spectra of calcined 0.5 wt% Pt-H^+USY catalysts. Correlated signal intensities arise from distinct ^{29}Si sites

proximate to ^{1}H moieties. ^{29}Si{^{1}H}HETCOR spectrum of calcined Catalyst A in **Figure 4.10a** shows ^{29}Si signals at -91, -101, -107, and -111 ppm, corresponding to Q^2(Al), overlapped signals from Q^4(1Al) and Q^3(0Al), framework Q^4(0Al), and disordered siliceous Q^4(0Al) moieties, respectively. Although quantitative single-pulse ^{29}Si measurement did not reveal any observable disordered siliceous species with a signal at -111 ppm from Catalyst A, ^{29}Si{^{1}H} measurements show signal at -111 ppm which is correlated with ^{1}H species of surface defect Si-OH sites with a signal at 2 ppm. A weak signal from low natural abundance ^{29}Si can be enhanced by transferring polarization from high gyromagnetic ratio, high natural abundance ^{1}H nuclei. Therefore, ^{29}Si signals from these disordered species that are in proximity with surface Si-OH sites are enhanced and detected in ^{29}Si{^{1}H} measurements. Q^4(0Al) species with a signal at -107 ppm is correlated with surface Si-OH and Bronsted acid sites with a signal at 4.7 ppm, suggesting that these Bronsted acid sites are close to the siliceous zeolite framework sites, perhaps inside the large supercages. ^{29}Si signal at -101 ppm, which is an overlapping signal from the Q^4(1Al) sites correlated with Brosnted acid sites with a signal at 4.5 – 7 ppm and Q^3(Al) defect sites correlated with ^{1}H species of Si-OH with a ^{1}H signal at 2 ppm. Interestingly, a presence of Q^2(0Al) surface species with ^{29}Si signal at -92 ppm is also revealed by the HETCOR experiments. ^{1}H signal at 0 ppm arises from Al-OH moieties,[23] which are correlated with surface Q^3(0Al) species. Separately collected ^{1}H Echo MAS spectrum of the calcined Catalyst A is overlayed on top of the ^{1}H projection of the ^{29}Si{^{1}H} experiment for comparison. Different 1H signals from Bronsted acid sites suggest that Catalyst A contains Bronsted acid sites with different local environments, *e.g.*, H^+ located in different cages

of the Y-zeolite. The majority of the ^{1}H signals from calcined catalysts arise from Si-OH species, consistent with dealuminated low Al USY zeolites.

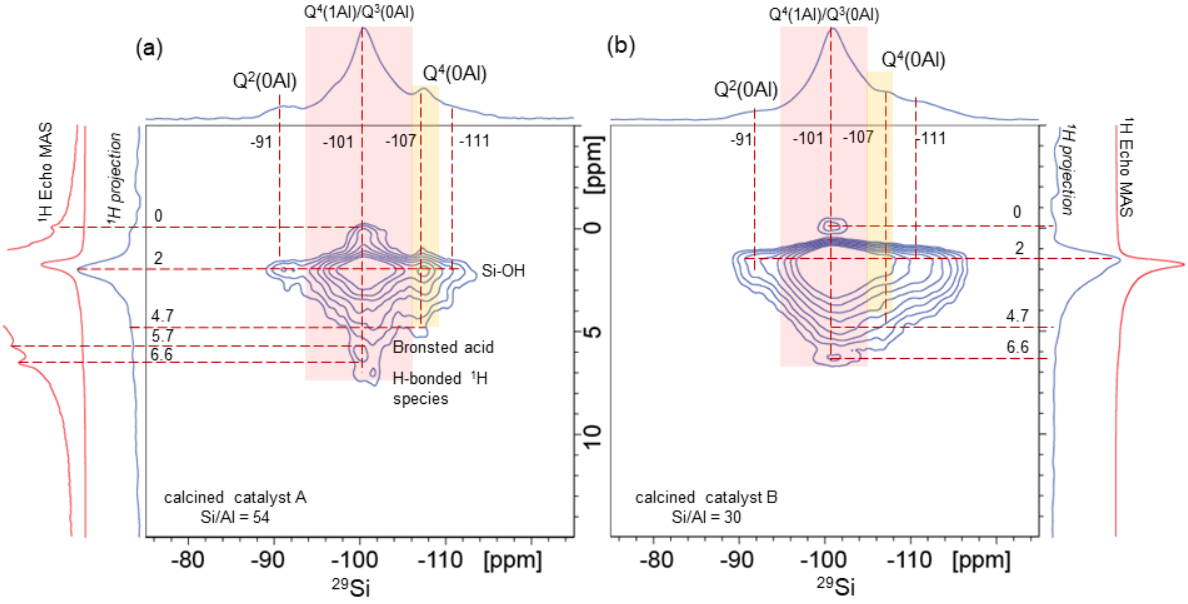

Figure 4.10. $^{29}Si\{^{1}H\}$ HETCOR spectra of calcined (a) catalyst A and (b) catalyst B acquired at 11.7 T with 12.5 kHz MAS with contact time 1.5 ms. ^{29}Si is shown on the *x*-axis, ^{1}H chemical shift is plotted on the *y*-axis. Separately collected ^{1}H Echo MAS spectrum of each catalyst is overlayed on the *y*-axis for comparison.

Similarly, $^{29}Si\{^{1}H\}$ spectrum of calcined Catalyst B (**Fig. 4.10b**) also reveals that the majority of the ^{1}H signal from surface Si-OH species with a signal at 2 ppm. ^{29}Si signals at -91 ppm from $Q^{2}(Al)$, -101 ppm from overlapped signals of $Q^{4}(1Al)$ and $Q^{3}(0Al)$, -107 ppm from framework $Q^{4}(0Al)$, and -111 ppm from disordered siliceous $Q^{4}(0Al)$ moieties are also present in calcined Catalyst B. Compared to Catalyst A, Catalyst B shows broader signals at -111 ppm, consistent with larger quantities of dealumiation-induced disordered siliceous species detected in Catalyst B by single-pulse ^{29}Si NMR measurements. Unlike Catalyst A, Catalyst B does not show any differentiable ^{1}H signals from different Bronsted acid sites. Instead, Catalyst B shows

one broad ^{1}H signal distributions from 5- 7 ppm, suggesting that local environments of Bronsted H^{+} sites are broadly distributed probably due to almost twice more Bronsted acidic sites present in Catalyst B compared to Catalyst A.

4.4.6 *In situ* ^{13}C NMR analyses of *n*-hexadecane on Pt-H^{+}USY

Understanding the atomic-scale reaction mechanisms enables optimization of existing industrial processes, hence it is crucial to identify types of intermediates under reaction conditions. In situ ^{13}C NMR is a powerful technique that can reveal distinct ^{13}C moieties under similar reaction conditions. There are very few studies on *in situ* investigations of solid catalysts in contact with liquid reagents, especially under high pressure as it was conducted in this work. To elucidate the mechanism of *n*-hexadecane hydroisomerization on bifunctional Pt-H^{+}USY heterogeneous catalysts, the reaction intermediates are revealed by *in situ* ^{13}C NMR, which was enabled by a specially designed WHiMS rotor functioning as a small batch system with high temperature (240 ^{o}C) and high pressure (50 bar at room temperature) that is close to reaction conditions used for catalytic tests in **Figure 4.3**. Straight hexadecane with 99 atom% ^{13}C enriched at the two terminal carbons is used as the reactant. ^{13}C NMR of *n*-hexadecane adsorbed on reduced Pt-H^{+}USY catalysts under 50 bar H_2 pressure (at room temperature) are measured at three different temperatures (30, 150, and 240 ^{o}C) to identify types of carbon moieties at varying temperatures.

^{13}C NMR of *n*-hexadecane adsorbed on Catalyst A is shown in the left column of **Figure 4.11**, sequentially measured from low temperature (bottom spectrum) to high temperature (top spectrum). Firstly, ^{13}C signal of 1, 2 ^{13}C-enriched *n*-hexadecane adsorbed on reduced catalyst A acquired at 30 ^{o}C and shown in **Figure 4.11c**. ^{13}C

signals from adsorbed *n*-hexadecane appear at 14, 23, 30, and 33 ppm, which correspond to terminal carbon (purple), carbon number 2 (green), 4 (grey), and 3 (yellow), respectively as shown in hexadecane molecule with numbered carbon atoms in **Figure 4.11g**. Signal intensities from the terminal two carbons at 14 and 23 ppm are larger than the rest of the ^{13}C signals because of the selective ^{13}C-enrichment at the carbon number 1 and 2. Zoomed spectra are overlayed on top of each spectrum to magnify the less intense signals. ^{13}C signals of adsorbed hexadecane are broader compared to solution-state ^{13}C signals (**Fig. S4.4**) due to the presence of broad local environments caused by interactions between the reactant and the zeolite catalysts. A signal at 30 ppm from the middle carbons has higher relative intensity compared to the signal at 33 ppm from the carbon number 3, consistent with the stoichiometric ratio of the carbon moieties.

Even at this low temperature of 30 ^{o}C (**Fig. 4.11c**), there are small signal intensities at 50 and 60 ppm, which are highlighted across the three spectra. These signals arise from alkoxy species formed by carbocation adsorption on zeolite oxygen atoms. As discussed in the reaction mechanisms of bifunctional catalysts in **Figure 4.2**, carbocation species Thermodynamic calculations have shown the formation of energetically favorable alkoxy species in a presence of carbocations adsorbed on negatively charged zeolite framework sites.[24] It should be noted that the observation of alkoxy intermediates is only enabled by pressurizing the NMR rotor under H_2, *i.e.*, without H_2 in the rotor, which resembles a batch reactor, alkoxy species were not observed. Interestingly, two signals are corresponding to alkoxy species, indicating the observation of at least two types of adsorbed species, such as secondary and

tertiary carbons on zeolite, which would be expected to have a chemical shift difference of ca. 10 ppm. To make sure that signals assigned to alkoxy species are not background signals, ^{13}C spectra of the empty rotor are collected at each temperature and shown in **Figure S4.5**. ^{13}C signals of epoxy glue in some homemade NMR probes also appear at 50-60 ppm, which especially becomes narrower and well resolved at high temperatures. No background signals at 50-60 ppm are detected even at 240 °C, leaving the confident assignment of 50 and 60 ppm signals to the alkoxy species.

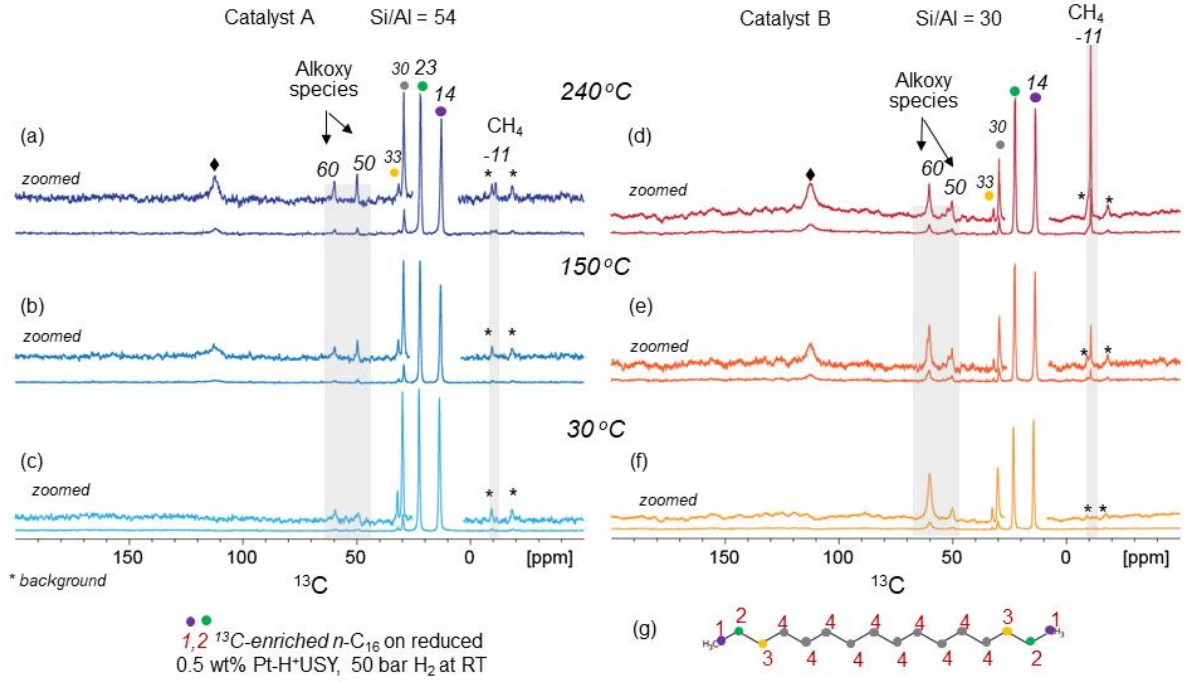

Figure 4.11. In situ single-pulse ^{13}C MAS NMR of ^{13}C enriched n-hexadecane adsorbed on (left column) catalyst A and (right column) Catalyst B under 50 bar H_2 pressure at room temperature. The spectra are acquired at 11.7 T with 4 kHz MAS. The two terminal carbon atoms indicated as carbon numbers 1 and 2 in the structural schematics shown under the spectra, of *n*-hexadecane are 99.99% enriched. ^{13}C NMR spectra acquired at (a,d) 240 °C, (b,e) 150 °C, and (c,f) 30 °C. Low-temperature spectra are acquired first for 10 minutes, and the temperature is increased to the desired value until it was stabilized after 10 minutes to obtain the next spectrum. (g)

hexadecane molecule with numbered & color-coded carbon atoms. * denotes spinning sidebands, ♦ denotes background, which changes at varying temperatures.

At an elevated temperature of 150 ^{o}C (**Fig. 4.12b**), the signals from *n*-hexadecane are still present, but the signals from alkoxy species appear at higher intensity compared to the spectrum collected at 30 ^{o}C indicating the formation of alkoxy species at a higher temperature. As temperature increases, the formation of carbocation moieties are accelerated, which eventually form alkoxy species with signals at 50 and 60 ppm. The measurement at 240 ^{o}C, the maximum capability of the NMR probe, results in increased signal intensities from the alkoxy peaks at 50 and 60 ppm. Notably, the signal intensity between the two peaks are different, *i.e.*, the signal at 50 ppm, which is assigned to secondary carbon alkoxy species, is more intense than the signal at 60 ppm, which is arising from less shielded tertiary carbon alkoxy species. This suggests preferential adsorption of secondary alkoxy intermediate species on Catalyst A, which can correlate with the observed formation of more monobranched isomer formation on Catalyst A as shown in **Figure 4.3**. Moreover, at 240 ^{o}C measurement, a new peak at -11 ppm started emerging, which arises from $^{13}CH_4$. Although a small amount, the presence of a signal at -11 indicates terminal cracking of the *n*-hexadecane. The fact that the signal at -11 ppm of methane is observable suggests that cracking occurred at the ^{13}C enriched terminus.

By comparison Catalyst B exhibits different reaction pathways compared to Catalyst A as evidenced by ^{13}C spectra of *n*-hexadecane adsorbed on Catalyst B at different temperatures (right column in **Figure 4.11**). Starting the measurement at 30 ^{o}C (**Fig. 4.11f**), *n*-hexadecane adsorbed on Catalyst B reveals ^{13}C signals of *n*- C_{16},

similar to Catalyst A, and interestingly signals at 50 and 60 ppm assigned to secondary and tertiary alkoxy species, respectively. The 60 ppm signal appears more intensely than 50 ppm, indicating preferential adsorption and formation of tertiary alkoxy species compared to secondary alkoxy species on Catalyst B. Based on the catalytic testing results discussed in **Figure 4.3**, Catalyst B formed more multibranched hexadecane isomers, which can form from tertiary alkoxy intermediates. Furthermore, at higher temperatures of 150 ^{o}C (**Fig 4.11e**), in addition to the peaks that were observed at 30 ^{o}C, a signal at -11 ppm from methane was detected. In contrast to Catalyst A, which forms a small amount of methane at 240 ^{o}C, Catalyst B forms methane in much more quantity at a lower temperature of 150 ^{o}C. The signal intensity from methane further increased, when the ^{13}C spectrum is acquired at a higher temperature of 240 ^{o}C (**Fig. 4.11d**) due to increased terminal cracking occurring on Catalyst B at an elevated temperature. Compared to Catalyst A, significantly more terminal cracking products (CH_4) on Catalyst B is formed.

For a zeolite with a lower Si/Al ratio and more Bronsted acidic sites, it is consistent that Catalyst B exhibits more cracking compared to Catalyst A. Formation of methane by terminal cracking is likely, not due to classic bifunctionality of Pt-H^+USY catalyst but rather simple cracking due to Bronsted acidic sites. Interestingly, Catalyst B exhibits more hydroisomerization activities due to dual-functionality compared to Catalyst A as discussed in previous sections, but *in situ* NMR results reveal that more terminal cracking occurs on Catalyst B. While both Pt and H^+ sites sequentially participate in hydroisomerization, only H^+ is necessary for terminal cracking. Therefore, an interesting behavior of Catalyst B having more hydroisomerization yet

more terminal cracking could be due to the inhomogeneous distribution of H^+ acidic sites throughout the zeolite crystallite. In other words, Catalyst B possesses more acidic sites on the surface where terminal cracking can easily occur, thus leaving well-balance Pt/H^+ inside the mesopores where hydroisomerization reactions are likely to occur. Identification of differences between intermediate and adsorbed species enabled to understand different catalytic behaviors observed by the two types of Pt-H^+USY bifunctional catalysts.

4.5 Conclusions

Two types of Pt-H^+USY catalysts with different Si/Al ratio (Catalyst A: 54 and Catalyst B: 30) are studied for *n*-hexadecane hydroisomerization. Although Catalyst B has lower bulk Si/Al ratio and higher concentration of Bronsted acid sites which lead to more cracking, Catalyst B exhibits more isomerization behavior compared to Catalyst A. In other words, Catalyst B behaves more like a higher Si/Al ratio zeolite. Analyses of quantitative single-pulse ^{29}Si NMR and correlational ^{27}Al{^{29}Si} 2D NMR results revealed that Catalyst B contains significantly more amount of siliceous disordered species which could be the origin of Catalyst B behaving more like higher Si/Al ratio zeolite for hydroisomerization. Moreover, analyses of *in situ* ^{13}C NMR measurements at high temperature and pressure elucidate the reaction mechanisms of long-chain straight alkanes on two catalysts. Terminal cracking of hexadecane resulted in methane formation under in situ reaction conditions, which was observed by a distinct ^{13}C signal at -11 ppm. Moreover, adsorbed alkoxy species with signals at 50 and 60 ppm revealed different adsorption behaviors of intermediates on two types

of catalysts. Detailed insights on the structures and reactivities enabled to elucidate atomic-level origins of differences in catalytic activities of two types of Pt-H^+USY.

References

(1) Soares, L. W. O.; Pergher, S. B. C. Influence of the Brønsted Acidity on the Ring Opening of Decalin for Pt-USY Catalysts. *Catalysts* **2019**, *9*, 1–12.

(2) Brito, L.; Pirngruber, G. D.; Guillon, E.; Albrieux, F.; Martens, J. A. Hydroconversion of Octylcyclohexane over a Bifunctional Pt/USY Zeolite Catalyst. *Energy & Fuels* **2021**, *35*, 13955–13966.

(3) Elena Pérez-Guevara; Molinillo, J. M. G.; Martínez de la Ossa, E. J.; Frontela, J.; Lázaro, J.; Franco, M. J. Selective Ring Opening of Ethylbenzene on Bifunctional Catalyst Pt–Ir over Hierarchical USY Zeolite. *Petroleum Chemistry* **2020**, *60*, 104–112.

(4) Thybaut, J. W.; Marin, G. B.; Baron, G. v.; Jacobs, P. A.; Martens, J. A. Alkene Protonation Enthalpy Determination from Fundamental Kinetic Modeling of Alkane Hydroconversion on Pt/H-(US)Y-Zeolite. *Journal of Catalysis* **2001**, *202*, 324–339.

(5) Thybaut, J. W.; Laxmi Narasimhan, C. S.; Marin, G. B.; Denayer, J. F. M.; Baron, G. v.; Jacobs, P. A.; Martens, J. A. Alkylcarbenium Ion Concentrations in Zeolite Pores during Octane Hydrocracking on Pt/H-USY Zeolite. *Catalysis Letters* **2004**, *94*, 81–88.

(6) Yasuda, H.; Sato, T.; Yoshimura, Y. Influence of the Acidity of USY Zeolite on the Sulfur Tolerance of Pd-Pt Catalysts for Aromatic Hydrogenation. *Catalysis Today* **1999**, *50*, 63–71.

(7) Corma, A. Transformation of Hydrocarbons on Zeolite Catalysts. *Catalysis Letters* **1993**, *22*, 33–52.

(8) Souverijns, W.; Martens, J. A.; Froment, G. F.; Jacobs, P. A. Hydrocracking of Isoheptadecanes on Pt/H-ZSM-22: An Example of Pore Mouth Catalysis. *Journal of Catalysis* **1998**, *174*, 177–184.

(9) Martens, J. A.; Parton, R.; Uytterhoeven, L.; Jacobs, P. A.; Froment, G. F. Selective Conversion of Decane into Branched Isomers. A Comparison of Platinum/ZSM-22, Platinum/ZSM-5 and Platinum/USY Zeolite Catalysts. *Applied Catalysis* **1991**, *76*, 95–116.

(10) Guisnet, M. “Ideal” Bifunctional Catalysis over Pt-Acid Zeolites. *Catalysis Today* **2013**, *218*, 123–134.

(11) Bhore, N.; Klein, M.; Bischoff, K. The Delplot Technique: A New Method for Reaction Pathway Analysis. *Ind. Eng. Chem. Res* **1990**, 29, 313–316.

(12) Walter, E. D.; Qi, L.; Chamas, A.; Mehta, H. S.; Sears, J. A.; Scott, S. L.; Hoyt, D. W. Operando MAS NMR Reaction Studies at High Temperatures and Pressures. *Journal of Physical Chemistry C* **2018**, *122*, 8209–8215.

(13) Pirngruber, G. D.; Maury, S.; Daudin, A.; Alspektor, P. Y.; Bouchy, C.; Guillon, E. Balance between (De)Hydrogenation and Acid Sites: Comparison between Sulfide-Based and Pt-Based Bifunctional Hydrocracking Catalysts. *Industrial and Engineering Chemistry Research* **2020**, *59*, 12686–12695.

(14) van der Wal, L. I.; de Jong, K. P.; Zečević, J. The Origin of Metal Loading Heterogeneities in Pt/Zeolite Y Bifunctional Catalysts. *ChemCatChem* **2019**, *11*, 4081–4088.

(15) Batalha, N.; Astafan, A.; dos Reis, J. C.; Pouilloux, Y.; Bouchy, C.; Guillon, E.; Pinard, L. Hydroisomerization of N-Hexadecane over Bifunctional Pt-HBEA Catalysts. Influence of Si/Al Ratio on Activity Selectivity. *Reaction Kinetics, Mechanisms and Catalysis* **2015**, *114*, 661–673.

(16) Bucher, J. P.; van der Klink, J. J. Electronic Properties of Small Supported Pt Particles: NMR Study of ^{195}Pt Hyperfine Parameters. *Physical Review B* **1988**, *38*, 11038–11047.

(17) Bucher, J. P.; Buttet, J.; van der Klink, J. J.; Graetzel, M. Electronic Properties and Local Densities of States in Clean and Hydrogen Over Pt Particles. *Surface Science* **1989**, *214*, 347–357.

(18) Bucher, J. P.; Buttet, J.; van der Klink, J. J.; Graetzel, M.; Newson, E.; Truong, T. B. ^{195}Pt NMR Studies of Supported Catalysts. *Colloids and Surfaces* **1989**, *36*, 155–167.

(19) Avanesian, T.; Dai, S.; Kale, M. J.; Graham, G. W.; Pan, X.; Christopher, P. Quantitative and Atomic-Scale View of CO-Induced Pt Nanoparticle Surface Reconstruction at Saturation Coverage via DFT Calculations Coupled with in Situ TEM and IR. *Journal of American Chemical Society* **2017**, *139*, 4551–4558.

(20) Kale, M. J.; Christopher, P. Utilizing Quantitative in Situ FTIR Spectroscopy To Identify Well-Coordinated Pt Atoms as the Active Site for CO Oxidation on Al2O3 -Supported Pt Catalysts. *American Chemical Society Catalysis* **2016**, *6*, 5599–5609.

(21) Radhakrishnan, S.; Goossens, P. J.; Magusin, P. C. M. M.; Sree, S. P.; Detavernier, C.; Breynaert, E.; Martineau, C.; Taulelle, F.; Martens, J. A. In Situ Solid-state ^{13}C NMR Observation of Pore Mouth Catalysis in

Etherification of β-Citronellene with Ethanol on Zeolite Beta. *Journal of the American Chemical Society* **2016**, *138*, 2802–2808.

(22) van Aelst, J.; Haouas, M.; Gobechiya, E.; Houthoofd, K.; Philippaerts, A.; Sree, S. P.; Kirschhock, C. E. A.; Jacobs, P.; Martens, J. A.; Sels, B. F.; Taulelle, F. Correction to “Hierarchization of USY Zeolite by NH_4OH. A Postsynthetic Process Investigated by NMR and XRD.” *Journal of Physical Chemistry C* **2014**, *118*, 22573–22582.

(23) Huang, J.; Jiang, Y.; Marthala, V. R. R.; Thomas, B.; Romanova, E.; Hunger, M. Characterization and Acidic Properties of Aluminum-Exchanged Zeolites X and Y. *Journal of Physical Chemistry C* **2008**, *112*, 3811–3818.

(24) Wang, W.; Hunger, M. Reactivity of Surface Alkoxy Species on Acidic Zeolite Catalysts. *Accounts of Chemical Research* **2008**, *41*, 895–904.

Supporting Information

A solid-state ^{27}Al MAS NMR spectrum exhibited a broad distribution of ^{27}Al intensity spanning from 75 to -20 ppm for dehydrated H^+USY zeolite. A partially resolved signal centered at ~60 ppm corresponds to 4-coordinated ^{27}Al, while intensity near 0 ppm arises from octahedrally-coordinated ^{27}Al sites. Due to the broad nature of the ^{27}Al signal from the dehydrated zeolite, obtaining the relative quantities of the extraframework and framework ^{27}Al sites was challenging. Therefore, ^{27}Al measurements of hydrated zeolites are conducted to obtain narrower and better resolved ^{27}Al signals from the 4- and 6-coordinated Al sites to facilitate the determination of their relative populations and shown in **Figure S4.3**.

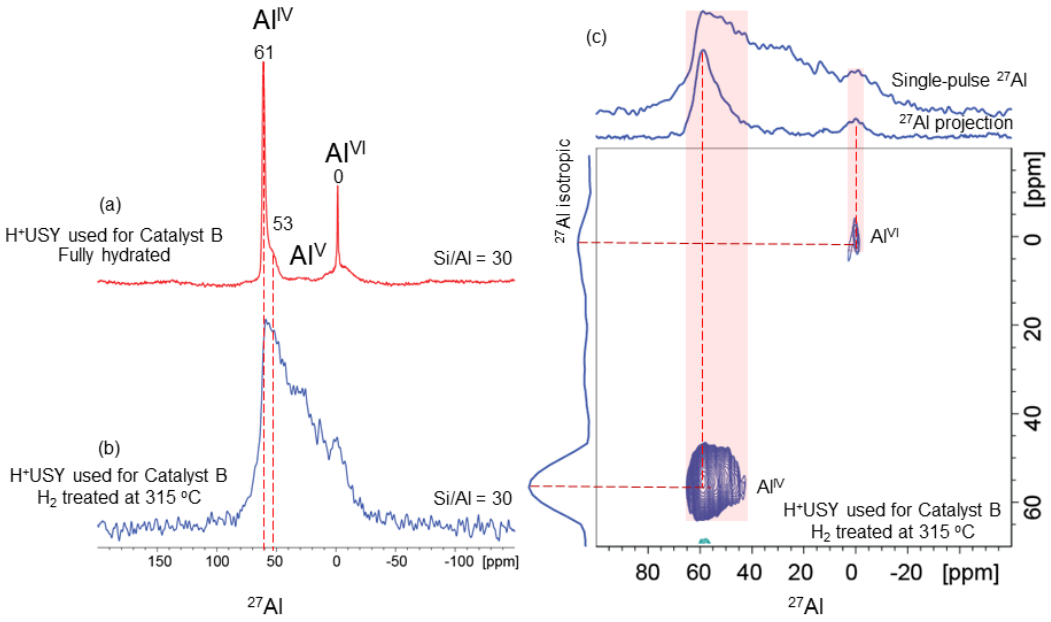

Figure S4.1. Solid-state single-pulse ^{27}Al MAS NMR of H$^+$USY-B (a) fully hydrated and (b) H_2 treated. (c) MQMAS of H_2 treated H$^+$USY-B. The spectra are acquired at 18.8 T, 298 K, and 18 kHz MAS using dry N_2 for MAS.

Disordered siliceous species with signal at -111 ppm is bonded to the framework zeolite crystallites as evidenced by SQ-DQ ^{29}Si{^{29}Si} experiment. Sum of through-bond correlated signal intensities in Single-Quantum dimension appears at the Double-Quantum dimensions. For example, from the first slice of SQ dimensions shown on the right, -222 ppm (purple spectrum) corresponds to intra-correlations between ^{29}Si species with signal at -111 ppm. Similarly, the second slide (green spectrum) shows DQ signal at -213 ppm, which is a sum of -102 ppm corresponding to Q^4(1Al) moieties and -111 ppm arising from siliceous disordered species. This correlation unambiguously reveals the bonding environment between the dealumination-induced siliceous species and the zeolite crystallite, consistent with the suggested structural diagrams shown in **Figure 4.9** of the main text.

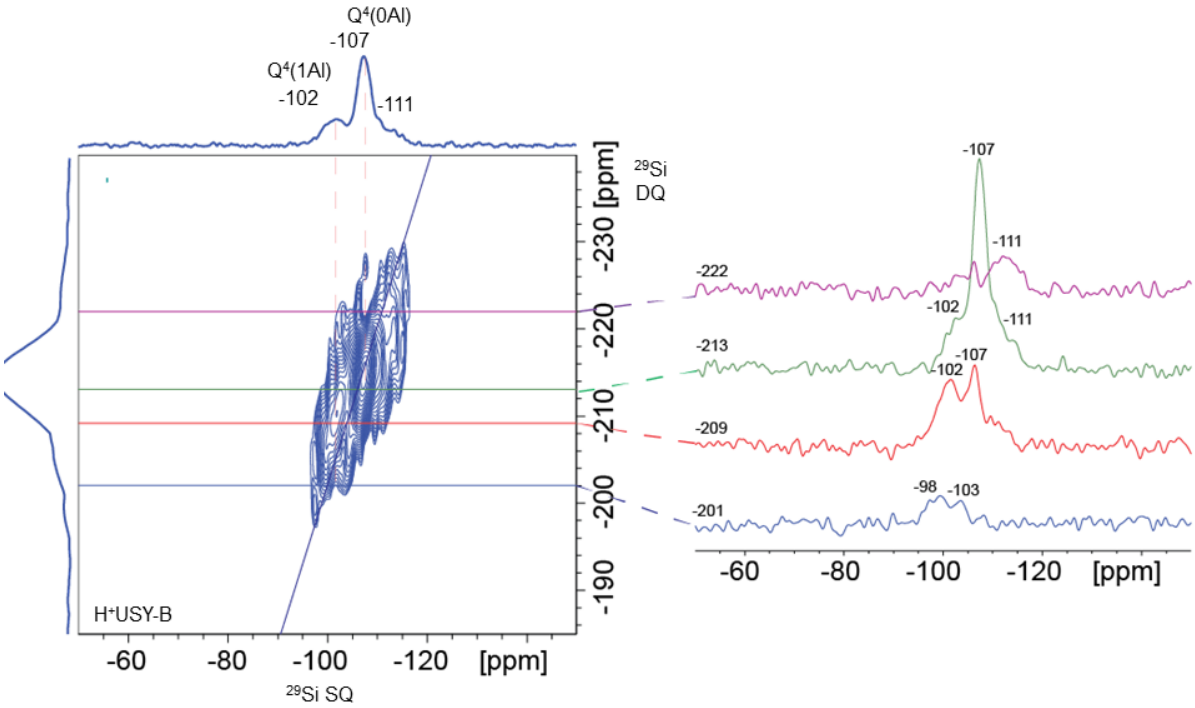

Figure S4.2. Single-Quantum Double-Quantum (SQ-DQ) ^{29}Si{^{29}Si} through-bond correlation experiment acquired by *J*-mediated INADEQUATE method of hydrated H^{+}USY-B zeolite.

A solid-state ^{29}Si MAS NMR spectrum of dehydrated USY zeolites with varying Si/Al ratio reveal different relative quantities of distinct ^{29}Si moieties, Q*m*(*n*Al), where *m* is the coordination number of ^{29}Si with *n* number of Al neighbors. The zeolites are provided from the same vendor as the zeolite used for Catalyst B with (c) Si/Al = 30. Zeolite with higher Si/Al ratio contains more integrated intensities of -111 ppm signal, indicating the extent of dealumination affects the formation of siliceous disordered species.

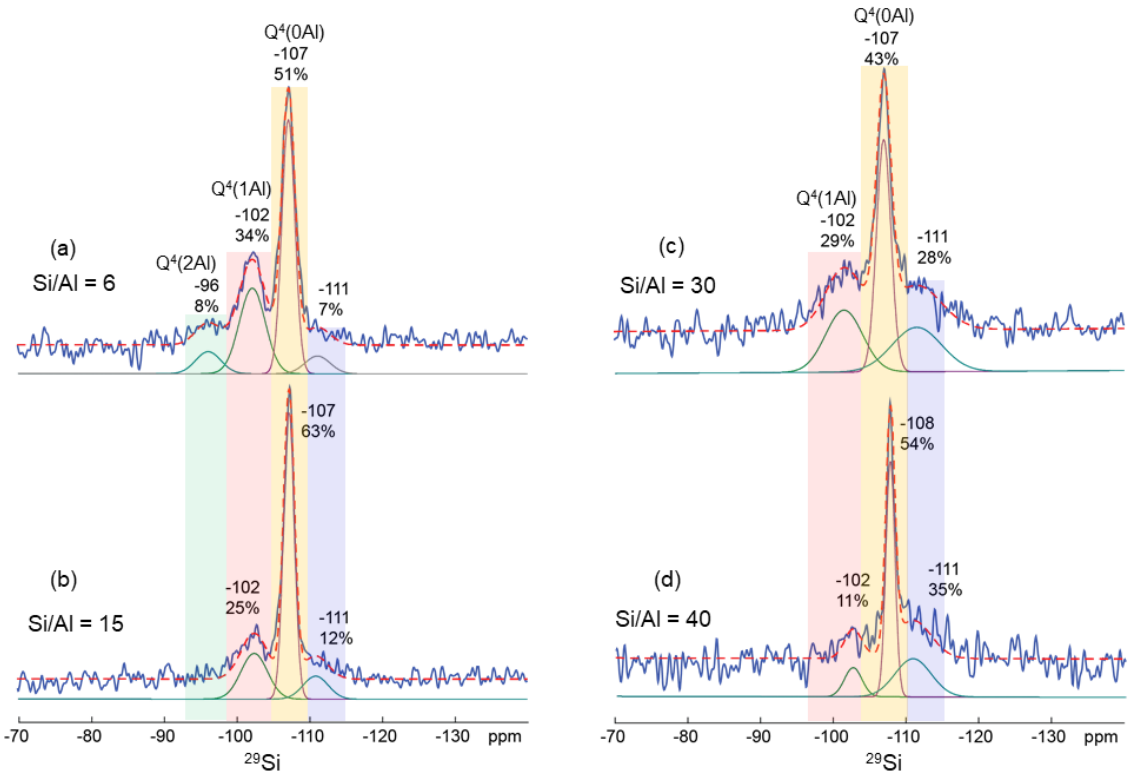

Figure S4.3. Single-pulse ^{29}Si spectra of dehydrated USY zeolites with varrying Si/Al ratio of (a) 6, (b) 15, (c) 30, (d) 40. Deconvoluted signals of different ^{29}Si species are shown below each spectrum. Red dotted lines are the sum of the deconvoluted signals that best fit the experimental spectrum shown in blue. The spectra are collected at 11.7 T at 12.5 kHz MAS.

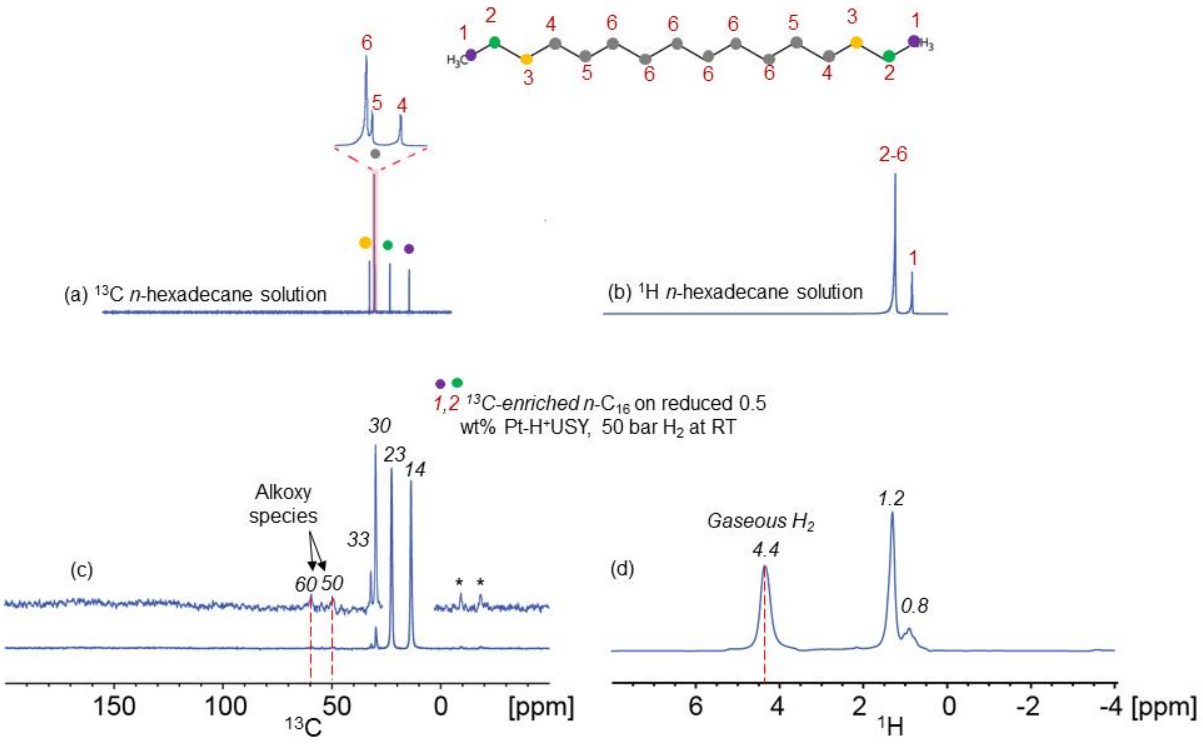

Figure S4.4. Comparisons of ^{13}C and ^{1}H spectra of solution state (non-enriched) *n*-hexadecane and 1,2 -^{13}C enriched n-hexadecane adsorbed on reduced Pt-H$^+$USY Catalyst A. (a) Single-pulse ^{13}C and (b) ^{1}H spectra of solution state *n*-hexadecane acquired at 14.1 T. (c) Single-pulse ^{13}C and (d) ^{1}H spectra of 1,2 ^{13}C-enriched *n*-hexadecane adsorbed on Pt-H$^+$USY under 50 bar H_2.

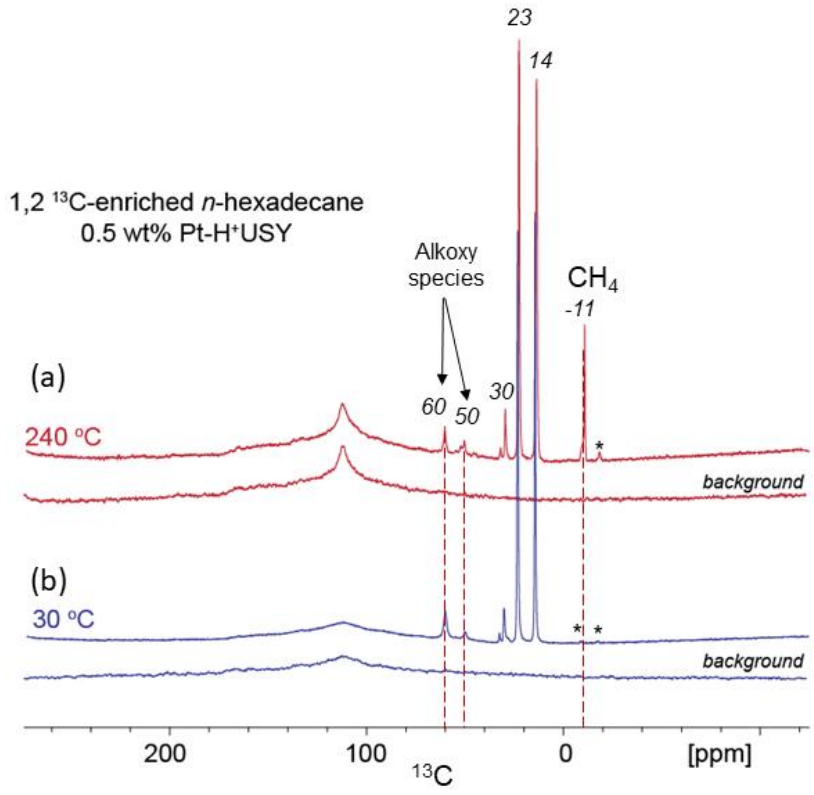

Figure S4.5. Identification of ^{13}C background signal of in situ NMR probe at different temperatures. Single-pulse ^{13}C NMR spectrum of 1,2 ^{13}C-enriched *n*-hexadecane adsorbed on Pt-H^+USY under 50 bar H_2 at room temperature (a) at 240 °C and (b) at 30 °C. Background signals acquired under the same condition from an empty rotor are shown below each spectrum. Background signal at ca. 110 ppm narrows and intensity increases at high temperature measurements. However, signals at 50 and 60 ppm, assigned to alkoxy species, are not present in the background signal. The spectra were acquired at 11.7 T with 4 kHz MAS.

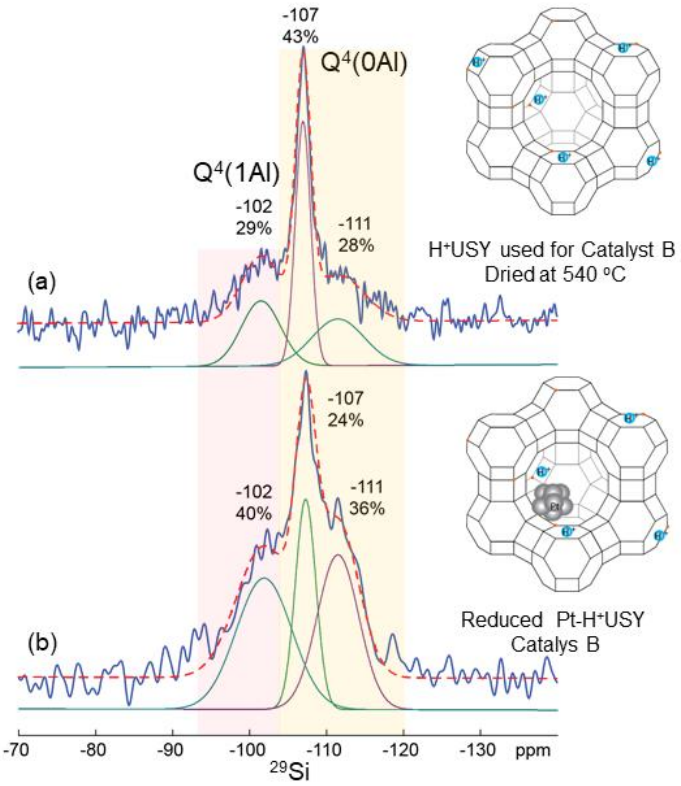

Figure S4.6. Comparisons of single -pulse ^{29}Si MAS NMR of parent H^+USY zeolite and reduced Pt-H^+USY catalyst B.

CHAPTER 5

5. Identifying paired-Al sites in CHA zeolite framework

*Tsatsral Battsengel,[1] Randall Meyer,[2] Allen Burton,[2] Robert Carr,[2] Pedro Serna,[2] Mobae Afeworki,[2] Bradley F. Chmelka[1, *]*

[1] Department of Chemical Engineering, University of California, Santa Barbara, California 93106, United States

[2] ExxonMobil Research and Engineering Co., Annandale, New Jersey 08801, United States

Keywords: Small pore zeolite, CHA zeolite, NMR of zeolite, paired Al sites in zeolite

5.1 Abstract

Chabazite is a small pore zeolite used for various industrial applications, including selective catalytic reduction of NOx with NH_3, methanol to olefin, and selective hydrogenation of olefins. Reaction properties of CHA zeolites strongly depend on distributions of Al sites, specifically the amount of paired Al where two Al tetrahedral sites are separated by at least one Si tetrahedral site in the ring structures of the zeolite. Zeolite crystallization methods influence the distribution of Al sites in CHA zeolites. Here, two types of CHA zeolites with the same bulk Si/Al ratio of 14 synthesized in two different crystallization mediums: with *N,N,N*-trimethyl-1-admantylammonium ($TMAda^+$) and with $TMAda^+$ and Na^+, are studied by solid-state multinuclear magnetic resonance methods to obtain detailed atomic-scale structural differences between the two CHA zeolites. The analyses of quantitative one dimensional (1D) ^{29}Si NMR and two dimensional (2D) $^{29}Si\{^{29}Si\}$ correlational

measurements reveal that CHA zeolite synthesized with $TMAda^+$ and Na^+ is shown to contain higher quantities of Q^4(1Al) moieties, which can lead to paired Al sites (Al-Si-Si-Al), compared to CHA zeolite synthesized with only $TMAda^+$. Moreover, 2D $^{27}Al\{^{29}Si\}$ and $^{29}Si\{^1H\}$ correlational measurements unambiguously revealed higher quantities of Q^4(2Al) ^{29}Si species, which is the source of paired Al-Si-Al sites, in CHA zeolite synthesized with both $TMAda^+$ and Na^+ compared to the CHA zeolite synthesized to result in "random" distribution of Al sites. Such direct characterization of paired Al sites in CHA zeolites using 2D NMR methods is unprecedented and the methods used in this study enable to elucidate correlations between zeolite crystallization methods and atomic-level structures of industrially significant materials.

5.2 Introduction

Chabazite zeolite is used commercially in their H^+ form to catalyze methanol to olefin reaction,[1] Cu and Fe-exchanged form to be used for NO and NO_2 selective catalytic reduction,[2,3] and with supported Pt-CHA zeolite is used for selective reduction of olefins.[4] The distributions of Al sites have crucial to stabilize the exchanged cations and supported metals. For example, paired Al sites in the ring structures are capable of stabilizing divalent cations such as Cu^{2+} and Pt^{2+}, which have crucial effects on the catalytic activities. The Al sitings in the zeolite framework depend on the zeolite crystallization conditions (types of structure-directing agents, alkaline cations, sources of Si and Al, pH, pressure, and temperature)[5–10] and post-treatment conditions.[11] For example, two types of catalysts discussed in Chapter 4 of this dissertation, both have the same framework structure of Y zeolite, but exhibit significantly different catalytic activities which were originated from the different local structures observed by the

multinuclear solid-state NMR measurements. Therefore, elucidating atomic-scale structures of zeolites, especially identifying paired Al sitings in CHA zeolite, has been a hot topic in the zeolite catalyst field.

Previous efforts have shown that by modifying the crystallization medium, Al sitings can be modified, but not in predictable ways. For example, FER zeolite was synthesized with mixtures of structure-directing agents that differ in size, and direct the locations of framework Al sites in either 8-membered ring or 10-membered ring.[12,13] MFI zeolite synthesized with tetrapropylammonium, (TPA^+) contains more Al atoms in 10 membered-ring intersections, while using both TPA^+ and Na^+ results in MFI zeolite with Al sites located in straight and sinusoidal 10 membered-ring channels.[14] Another study has shown that using both TPA^+ and Na^+ in the synthesis gel to crystallize low Al content MFI zeolite (Si/Al = 22) yields lower fractions of paired Al sites compared to MFI zeolite synthesized with only TPA^+.[15] Synthesis of CHA zeolite using *N,N,N*-Trimethyl-1-Adamantammonium ($TMADa^+$) was first discovered by Zones,[5] and the use of both $TMADa^+$ and Na^+ to crystallize CHA zeolite with predominantly paired Al sites are extensively studied.[16,17] It has been proposed that the presence of both Na^+ and $TMADA^+$ cationic charges in each CHA cage attracts two paired anionic Al tetrahedral sites while using only $TMADA^+$ is predicted to result in randomly distributed Al subject to Lowenstein's rule. This hypothesis should be considered with caution because zeolite crystallization predominantly occurs by a series of kinetically controlled steps. **Figure 5.1** shows the structure of the CHA zeolite and configurations of unpaired and paired Al sites in 6-membered rings. CHA zeolite contains one crystallographically unique T-site and double 6-membered ring building

units that interconnect to form 8-membered ring windows, which limit transport into larger cages with 18 T atoms per cage. 8-MR window has a diameter of 0.38 nm and the large cage has a 0.82 nm diameter. Al atoms in the framework are denoted by orange dots. Unpaired Al in the 6-membered ring is shown in **Figure 5.1b**, where five of the T-sites are Si moieties while only one of them is Al. In contrast, paired Al in the 6-membered ring can either have a structure in **Figure 5.1c**, two Al separated by one Q^4(2Al) Si T-site, or two Al separated by two Q^4(1Al) Si-T-sites. Directly observing the sitings of such Al atoms in zeolite has been challenging, because most of the diffraction techniques only provide average structural information but not on the distribution of Al heteroatoms, which are usually non-periodic. Moreover, other diffraction methods, such as XANES and EXAFS, are not capable of distinguishing Al and Si atoms due to their similar electron densities. Recent breakthrough measurements using X-ray standing-wave single-crystal have shown the possibilities of resolution of Al and Si atoms in Al-rich zeolites.[18] However, a single-crystal method is not suitable for catalyst materials, which are usually small crystallites. Therefore, identification of paired Al sitings in zeolite catalysts is usually conducted by indirect methods such as using other probe molecules as the identifier of paired Al sites[19,20], UV-vis spectroscopy of Co^{2+} exchanged zeolites for detection of paired Al atoms,[15] and simple titration of divalent cations for quantification of paired Al sites.[16,21]

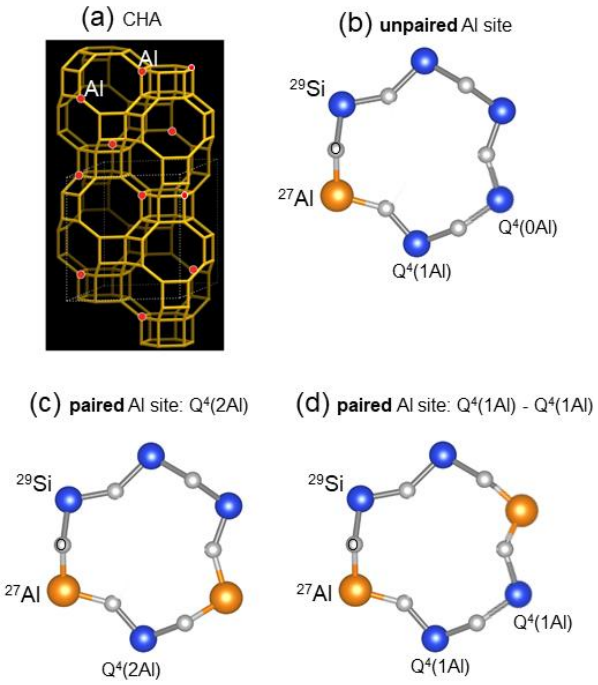

Figure 5.1 Structural diagrams of paired and unpaired Al in 6-membered rings. Structural diagrams of (a) CHA framework, (b) unpaired Al site, (c) paired Al sites separated by one Q^4(2Al) Si site, and (d) paired Al sites separated by two Q4(1Al) Si sites

Solid-state NMR methods are superior to identifying local distributions of heteroatoms directly. For Al-rich zeolites, ^{27}Al double-quantum (2Q) MAS NMR experiments were successfully used to reveal proximity between extra-framework Al species and framework Al atoms. This type of homonuclear correlation pulse sequence can be used to monitor paired Al sites, but due to its challenges arise from quadrupolar ^{27}Al nuclei, this method has not been used to reveal paired ^{27}Al sites in zeolite up to date.[22] Here, multinuclear 2D ^{27}Al{^{29}Si}, ^{29}Si{^{1}H}, and ^{29}Si{^{29}Si} correlational measurements are used to directly identify the paired Al sites and their interactions with the framewok ^{29}Si and Bronsted acid sites. Three types of CHA zeolites synthesized in different crystallization mediums, denoted as CHA1, CHA2, and CHA3 are investigated to

reveal the distributions of Al sites and their interactions with the zeolite framework sites, which are found to be directly affected by the zeolite synthesis methods.

5.3 Materials and methods

Three types of CHA zeolites are synthesized at the Instituto de Tecnologia Quimica (ITQ), denoted as CHA1, CHA2, and CHA3. CHA1 and CHA2 are synthesized in a way to result in "random" distributions of Al, *i.e.*, in a presence of *N,N,N*-trimethyl-1-admantylammonium ($TMAda^+$) as a Structure Directing Agent (SDA). CHA3 was synthesized with the SDA and Na^+ to result in paired Al sites. Hence, CHA3 contains Na, while CHA1 and CHA2 do not have Na. The Si/Al ratio of CHA1 and CHA3 are both 14 to compare the effects of synthesis with and without Na for a CHA zeolite with the same Al content. CHA2 has a Si/Al ratio of 26, which is used as a reference for CHA1 zeolite synthesized by the same method but with lower Al content.

Multinuclear solid-state nuclear magnetic resonance (NMR) spectroscopy measurements were conducted to understand the framework Al distributions of CHA zeolites. Both hydrated and dehydrated samples are studied to obtain acquire framework T-site connectivities, *e.g.*, $^{27}Al\{^{29}Si\}$ and $^{29}Si\{^{29}Si\}$, and interactions between ^{1}H from Bronsted acid sites, Si-OH species, and framework ^{29}Si moieties. Zeolites were hydrated in an 80 % relative humidity environment for 24 hours before measurement. Dehydration was proceeded under vacuum with a heating rate of 1 ^{o}C/min, up to 450 ^{o}C, and held at the temperature for 2 h before slowly cooling down to room temperature. Dried samples were sealed in a glass ampule and transferred into a glovebox under dry Ar, where samples were packed in NMR rotors. Silicone plugs were used to seal the open end of the rotor before placing the rotor cap, and

dry N_2 was used for MAS. Conventional solid-state ^{1}H, ^{29}Si, and $^{29}Si\{^{1}H\}$ CP-MAS NMR were conducted on 11.7 T Bruker AVANCE-II NMR spectrometer, operating at 12.5 kHz MAS at $^{29}8$ K using a Bruker 4 mm probe head and zirconia rotors with Kel-F^{TM} caps. Low-temperature MAS (LTMAS) measurements (95 K) provide significantly enhanced NMR signal sensitivity that allows the detection and analysis of ^{29}Si-O-^{27}Al environments at a natural abundance of ^{29}Si (4.7%). LTMAS measurements, e.g, 2D $^{29}Si\{^{29}Si\}$ and $^{27}Al\{^{29}Si\}$, were conducted on a Bruker ASCEND 400 NMR spectrometer with a 9.4 T superconducting magnet equipped with a low temperature 3.2 mm triple-resonance MAS probe head. A Triple-quantum MAS pulse sequence with two hard pulses followed by a *z*-filter was used for ^{27}Al MQMAS measurements conducted on an 18.8 T instrument equipped with a 3.2 mm HX probe. Single-pulse excitation of 0.42 us corresponding to π/12 flip angle was used for quantitative ^{27}Al experiments with a recycle delay of 0.5 s.

Dynamic Nuclear Polarization (DNP) NMR methods were used to enhance the signal sensitivities. 8 mMol TEKPol in TCE was used as the polarizing agent for fully hydrated zeolite particles, with 263 GHz microwave irradiation. The 2D *J*-mediated $^{29}Si\{^{29}Si\}$ NMR measurements were conducted using the refocused INADEQUATE technique, which probes ^{29}Si-^{29}Si spin pairs that are *J*-coupled (through-covalent bond). The experiments used a 2.5 μs ^{1}H 90° pulse, followed by a 5 ms adiabatic cross-polarization pulse to transfer magnetization to ^{29}Si. 7.2 μs ^{29}Si 180° pulse was used to generate antiphase nuclei. A rotor-synchronized echo (τ-180°-τ) of total duration 2τ = coherences under scalar (*J* Si-Si) coupling evolution while refocusing chemical shift interactions. The antiphase magnetization was converted by a 4 μs ^{29}Si

90° pulse into a mixture of double- and zero-quantum coherences, the latter of which were removed by phase-cycling and the former of which were detected indirectly by incrementation of the evolution period t1. A subsequent ^{29}Si 90° pulse converted the remaining double-quantum components into antiphase coherences. After another delay τ, these were converted by a final 180° pulse into in-phase single-quantum coherences that evolved again under ^{29}Si{^{29}Si} interactions, forming an echo that initiated the detection period t2. The value of τ = 6 ms was established to provide maximum signal intensity. Fourier transformation of the time-domain signals resulted in 2D refocused INADEQUATE ^{29}Si{^{29}Si} NMRspectra that represent frequency maps with single-quantum (SQ) and double-quantum (DQ) dimensions. Signals in the SQdimension (horizontal axis) correspond to isotropic ^{29}Si chemical shifts, ωi (similar to 1D ^{29}Si MAS spectra), while signals in the DQdimension (vertical axis) represent the sum of the chemical shifts of two correlated *J*-coupled ^{29}Si nuclear spins, $\omega_i + \omega_j$. Pairs of signal intensities at (ω_i, $\omega_i + \omega_j$) and (ω_j, $\omega_i + \omega_j$) establish unambiguously that ^{29}Si species with SQisotropic chemical shifts ωi and ωj are bonded covalently (in this case through bridging oxygen atoms).

5.4 Results and analyses

Solid-state NMR is the most suitable technique to directly identify the presence of paired Al sites, especially 2D NMR provides unambiguous correlation between distinct ^{27}Al and ^{29}Si sites which can be used to elucidate the presence of Q^4(2Al) moieties, which is an indication of paired Al sites, *i.e.*, Al-Si-Al. 2D ^{29}Si{^{29}Si} measurement can be used to reveal covalently bonded Q^4(1Al) and Q^4(1Al) species, which lead to paired Al sites separated by two Si sties. Moreover, 2D ^{29}Si{^{1}H} measurements are used to

identify interactions between distinct Bronsted and surface Si-OH protons and ^{29}Si moieties. The analyses of multinuclear NMR methods discussed below elucidate unprecedented atomic-scale structural details on CHA zeolites synthesized to result in “random” distributions of Al and paired Al sites, which are important structural features for industrially significant CHA zeolite catalysts.

5.4.1 Relative quantities of distinct ^{29}Si moieties in CHA zeolites

To identify the effects of treatment conditions and bulk Si/Al ratio on types and distributions of distinct ^{29}Si moieties, quantitative 1D ^{29}Si MAS measurements were conducted on the three types of zeolites. **Figure 5.2** shows 1D ^{29}Si single-pulse MAS NMR spectra of hydrated CHA zeolites. As shown in **Figure 5.2a**, ^{29}Si signals at -102, -105, and -111 ppm in CHA1 correspond to Q^4(0Al), Q^4(1Al), and Q^4(2Al) or Q^3(0Al) ^{29}Si moieties, respectively, where Q^n(*m*Al) denote ^{29}Si sites with *n* numbers of T-site numbers, of which *m* number of them are Al. The majority, 75%, of the ^{29}Si signal arises from Q^4(0Al) moieties, consistent with zeolite with a high Si/Al ratio. 12% of the total signal comes from Q^4(1Al) species. 13% of the total intensities appear at -102 ppm, which are overlapping signals from Q^4(2Al) or Q^3(0Al) species. For this high Si/Al ratio and “random” distribution of Al, CHA1 zeolite is expected to have a small or non-negligible amount of paired Q^4(2Al) moieties, hence the majority of the signal at -102 ppm is expected to be from surface Q^3(0Al) and confirmed by 2D ^{29}Si{^{1}H} and ^{27}Al{^{29}Si} measurements as discussed below. For CHA2 zeolite with a higher Si/Al ratio compared to CHA1, the relative quantities of siliceous species are higher compared to CHA1. 77% of the ^{29}Si signals arise from Q^4(0Al) moieties with a peak at -111 ppm as shown in **Figure 5.2b.** Because of its low Al content in CHA2,

the relative signal intensities from Q^4(1Al) at -105 ppm are only 8% compared to CHA1, which has ca. 12% of the ^{29}Si signal from Si tetrahedral site with one Al neighbor. Relative intensities of the signal at -102 ppm in CHA2 is 15%, which is comparable to CHA1 indicating that changing the total Al content does not significantly affect the quantities of the surface Q^3(0Al) species.

When CHA zeolite is synthesized with both structure-directing agent and Na^+ cation, more paired Al species are expected. CHA3 zeolite has the same Si/Al ratio as CHA1 but crystallized with SDA and Na^+ compared to CHA1, which was synthesized with only SDA. Relative quantities of distinct ^{29}Si moieties in CHA3 are significantly different compared to CHA1. Namely, 20% of the total signal intensities in CHA3 arise from Q^4(1Al), while 12% of the ^{29}Si signal intensities arise from Q^4(1Al) moieties in CHA1. One possible paired Al configuration is having two Al sites separated by two Q^4(1Al) species as illustrated in **Figure 5.1d**. CHA3 with almost double the relative quantities of Q^4(1Al) moieties compared to CHA1 could lead to more paired Al sites. However, the 1D ^{29}Si spectrum simply provides relative quantities of total Q^4(1Al) species, which is not proof of Q^4(1Al) bonded to another Q^4(1Al) to result in paired Al sites. 2D ^{29}Si{^{29}Si} correlational experiments elucidate such information on local bonding environments and will be discussed below. Similar to ^{29}Si signals obtained from CHA1 and CHA2, the majority, 68%, of the ^{29}Si signals of CHA3 arises from siliceous Q^4(0Al) sites, again consistent with high Si/Al zeolite. 12% of the total signal appears at -102 ppm, which can be from Q^4(2Al) and/or surface Q^3(0Al) moieties. To summarize the analyses of quantitative 1D ^{29}Si MAS NMR spectra acquired from three types of zeolites, relative quantities of different ^{29}Si

species are strongly influenced by the zeolite crystallization method, *e.g.*, bulk Si/Al ratio and presence of Na^+ cation in addition to SDA. Notably, relative quantities of Q^4(1Al) species with ^{29}Si signal at -105 ppm decrease as the bulk Si/Al ratio increases when other crystallization parameters are held constant, which is evidenced by comparing CHA1 and CHA2. While the bulk Si/Al ratio is held constant but crystallization medium differs by the presence of Na^+ cation, relative quantities of distinct ^{29}Si moieties differ between two zeolites as evidenced by the comparison of CHA1 and CHA3. This suggests the effects of Na^+ on the distributions of zeolite framework T-sites. To identify the local bonding environments of these different T-sites, correlational 2D NMR methods are implemented and discussed below.

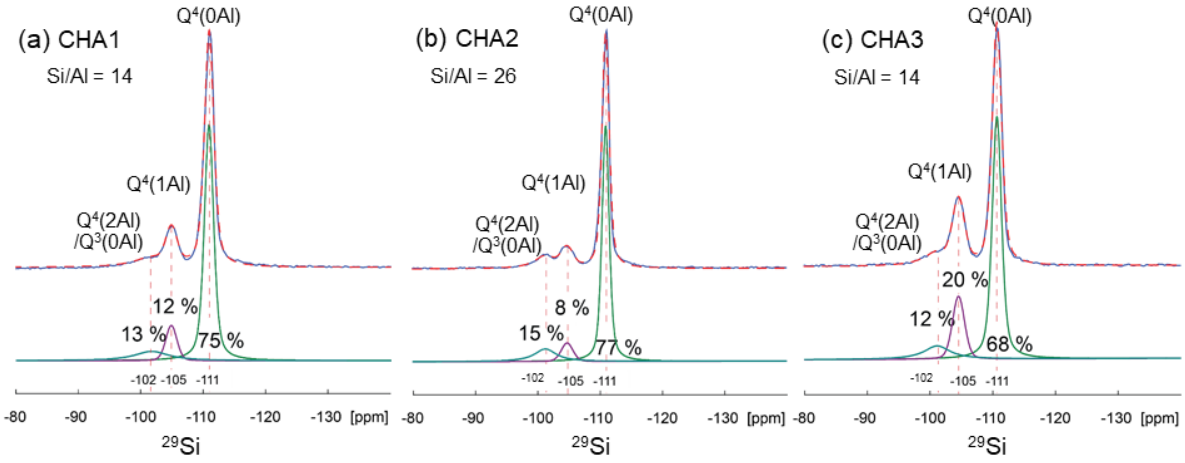

Figure 5.2. Quantitative 1D ^{29}Si single-pulse MAS NMR spectra of hydrated (a) CHA1, (b) CHA2, and (c) CHA3. The spectra are acquired at 11.7 T and 12.5 kHz MAS. Deconvoluted signals with relative quantities are shown under each corresponding spectrum. The sum of the deconvoluted signals shown under each spectrum is shown in red dashed lines.

5.4.2 ^{29}Si{^{29}Si} bonding environments in CHA zeolites

Local bonding environments between distinct ^{29}Si moieties can reveal the presence of Q^4(1Al) ^{29}Si sites bonded to another Q^4(1Al) sites, a direct proof of paired Al sites as illustrated in **Figure 5.1d**. Because of the low natural abundance of ^{29}Si nuclei (4.7%) and weak *J*-coupling between ^{29}Si-^{29}Si, the signal was enhanced by DNP-NMR measurements. *J*-mediated ^{29}Si{^{29}Si} DNP-NMR spectrum of CHA1 zeolite with “random” distributions of Al is shown in **Figure 5.3a**. The Single-quantum dimension is shown on the horizontal axis, and the double-quantum axis is on the vertical axis. Separately collected ^{29}Si{^{1}H} CP-MAS spectrum is overlayed on top of the horizontal axis for comparison. Diagonal peaks on the 2D spectrum indicate intra-correlation of ^{29}Si moieties while cross diagonal peaks arise from inter-correlation between distinct ^{29}Si moieties. Q^4(0Al) sites with the signal at -112 ppm show a diagonal peak, which appears at -224 ppm on the double-quantum dimensions, revealing the covalently bonded Q^4(0Al) species. The signal at -105 ppm corresponds to Q^4(1Al) ^{29}Si species, which are through-bond correlated with Q^4(0Al) siliceous species with the signal at -112 ppm. The correlated signal intensities appear at -217 ppm in the double-quantum dimension, the sum of two correlated intensities at -105 and -112 ppm, which are highlighted by a red line symmetrically divided by the diagonal axis. There are also other distributions of correlated intensities arising from ^{29}Si species with a signal at -109 ppm and siliceous Q^4(0Al) moieties with a signal at -111 ppm. The correlated intensities highlighted by the yellow line appear at -220 ppm, the sum of -111 and -109 ppm. Broad signals of Q^4(1Al) ^{29}Si species at -106 to -109

ppm indicate that CHA1 contains broad distributions of chemical environments caused by “random” distributions of Al sites.

Paired Al moieties separated by two Si atoms can be directly observed by *J*-mediated ^{29}Si{^{29}Si} SQ-DQ experiments. When such paired Al species are present, correlated signal intensities from Q^4(1Al) sites with a signal at -106 ppm should be expected to appear at -212 ppm in the double-quantum dimension. However, for CHA1 zeolite with “random” distributions of Al sites, no correlation intra-correlation was observed, suggesting that Q^4(1Al) moieties are isolated from one another. Moreover, ^{29}Si sites with signals at -101 ppm, which are assigned to Q^4(2Al) and Q^3(1Al), do not show correlated signal intensities, suggesting that these species are not close enough to be covalently bonded to each other.

In comparison to CHA1, CHA3 zeolite synthesized to results in paired Al sites exhibits slightly different local bonding environments of ^{29}Si species. **Figure 5.3b** shows 2D *J*-mediated ^{29}Si{^{29}Si} SQ-DQ spectrum of fully hydrated CHA3. Correlated signal intensities arise from covalently bonded siliceous Q^4(0Al)–O–Q^4(0Al) moieties and from covalently bonded Q^4(0Al)–O– Q^4(1Al) moieties at -224 and -217 ppm in the double-quantum dimension, respectively. Compared to CHA1, CHA3 zeolite does not show a correlated signal at -220 ppm in the double-quantum dimension, as indicated by the grey dashed lines, suggesting narrower distributions of ^{29}Si local environments in CHA3 zeolite compared to CHA1. This could be due to the non-random distribution of Al sites, *i.e.*, a few Al in the framework are paired. However, no observable correlated signal was detected from Q^4(1Al) species bonded to another Q^4(0Al) with a signal -106 ppm. Higher relative quantities of Q^4(1Al) in CHA3 zeolite compared to

CHA1 zeolite as discussed in **Figure 5.2** was suggestive that CHA3 zeolite might contain more of Al-Si-Si-Al paired sites. A presence of a signal is proof of the presence of certain species that give rise to that signal, but an absence of a signal should not be interpreted as an absence of the species that is expected to give the signal. Small quantities of covalently bonded Q^4(1Al)-O-Q^4(1Al) moieties, weak *J*-coupling between ^{29}Si-^{29}Si species (<10 Hz), and low natural abundance of 4.7% ^{29}Si leading to probabilities of 0.22% of all coupled Q^4(1Al)-O-Q^4(1Al) tetrahedral sites with both ^{29}Si-^{29}Si moieties can lead to extremely weak signal that is not observed. Therefore, undetected correlated signal intensities at -212 ppm in the double-quantum dimension should not lead to a conclusion of the absence of Q^4(1Al)-O-Q^4(1Al) moieties that can result in paired Al sites in CHA 3 zeolite. It is also possible that paired Al sites are located in the 8-membered rings separated by three Si T-sites, *i.e.*, Al-Si-Si-Si-Al, hence the relative quantities of Q^4(1Al) species in CHA3 are almost double the amount of Q^4(1Al) in CHA1 zeolite despite the same bulk Si/Al ratio.

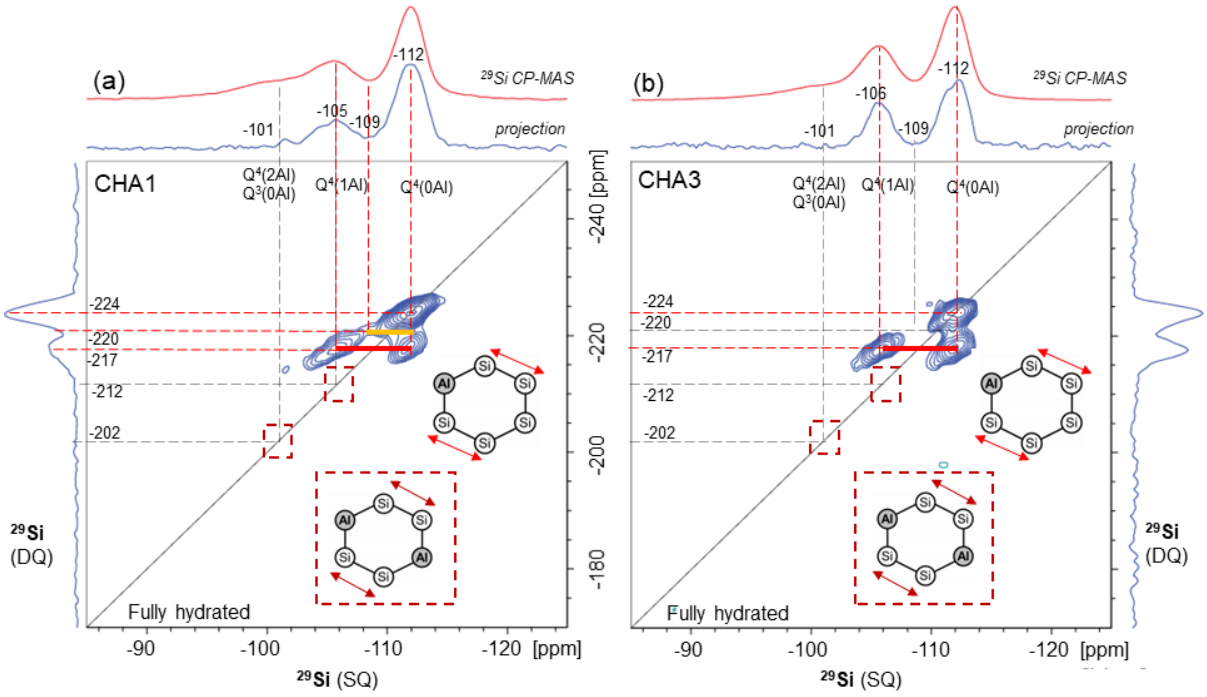

Figure 5.3. Solid-state DNP-enhanced 2D SQ-DQ ^{29}Si{^{29}Si} *J*-mediated INADEQUATE spectra of fully hydrated (a) CHA1 and (b) CHA3 acquired at 9.4 T with 8 kHz MAS. The ^{29}Si{^{1}H} CP MAS spectrum of each zeolite is shown on top of the horizontal axis for comparison.

5.4.3 Framework ^{27}Al{^{29}Si} bonding environments of CHA zeolites

Local environments of framework ^{27}Al and ^{29}Si sites of hydrated CHA1 and CHA3 zeolites are revealed by ^{27}Al{^{29}Si} *D*-HMQC experiments. ^{27}Al signal of dehydrated CHA1 zeolite was broadened beyond detection on 400 MHz instrument, due to severe distortion in the symmetry centered around Al and large 2nd order quadrupole coupling constant of framework ^{27}Al. Although both zeolites have the same bulk Si/Al ratio, ^{29}Si-^{27}Al interactions of the zeolite framework sites are shown to be distinguishable due to different zeolite synthesis methods used for CHA1 and CHA3.

For CHA1 zeolite without Al-pairing, 2D ^{27}Al{^{29}Si} *D*-HMQC spectrum is shown in **Figure 5.4a**. ^{27}Al signals are shown on the horizontal axis and well-resolved ^{29}Si

signals are projected on the vertical axis. Separately collected 1D ^{27}Al Hahn-echo spectrum overlayed on top of the ^{27}Al projection of the 2D spectrum reveals both framework tetrahedral ^{27}Al moieties resonating at 60 ppm, and extraframework octahedral ^{27}Al with a signal at 0 ppm. Correlated signal intensities arise from framework ^{27}Al sites with the signal at 60 ppm and different ^{29}Si sites with the signal at -112, -105, and -99 ppm, corresponding to Q^4(0Al), Q^4(1Al), and Q^4(2Al) moieties, respectively. No through-space interactions between ^{29}Si and Al moieties with a signal at 0 ppm are observed, consistent with the assignment of extraframework ^{27}Al sites for the 0 ppm signal. The signal at -99 ppm can be either from Q^4(2Al) or surface Q^3(0Al) ^{29}Si moieties. However, small correlated signal intensities between tetrahedral ^{27}Al at 60 ppm and ^{29}Si at -99 ppm indicate that there are Q^4(2Al) species present in CHA1 zeolite. Even though CHA1 was synthesized in a way to result in "random" distributions of ^{27}Al, *i.e.*, for a given high Si/Al ratio of 14 majorities of the Al is expected to be isolated, Q^4(2Al) paired Al sites are present, but with significantly smaller amount compared to CHA3 as discussed below.

In comparison, 2D ^{27}Al{^{29}Si} *D*-HMQC spectrum of CHA3 zeolite is obtained and shown in **Figure 5.4b**. Similar to CHA1 zeolite, CHA3 zeolite also exhibits through-space interactions between framework ^{27}Al with a signal at 60 ppm and ^{29}Si species with a signal at -112, -105, and -99 ppm, corresponding to Q^4(0Al), Q^4(1Al), and Q^4(2Al) moieties, respectively. Interestingly, the correlated signal intensities that arise from tetrahedral ^{27}Al and Q^4(2Al) species are much broader and stronger in CHA3 compared to that of CHA1, suggesting that more quantities of paired Q^4(2Al) sites are present in CHA3 than CHA1. Moreover, weakly correlated intensities were observed

from tetrahedral ^{27}Al and ^{29}Si species with a peak at -94 ppm, which are highlighted in purple in **Figure 5.4b**. ^{29}Si signal at -94 ppm can be assigned to either Q^3(1Al) or Q^4(3Al), but a presence of Q^4(3Al) species in a zeolite with Si/Al = 14 is unlikely. Therefore, the signal at -94 ppm is assigned to a small amount of Q^3(1Al) ^{29}Si moieties, which is only revealed by 2D ^{27}Al{^{29}Si} *D*-HMQC measurements, implying that there may be more silanol defects in CHA3 than in CHA1. It is noted that the crystallite size of CHA1 is about 50 nm while the size of CHA3 is about 200 nm according to the images provided by ITQ. Therefore, the higher suggested amount of Q^3(0Al) in CHA3 is not due to increased external silanols.

Although both CHA1 and CHA3 zeolites have the same bulk Si/Al ratios, CHA3 zeolite contains more framework Al sites compared to CHA1 zeolite which was revealed by the single-pulse ^{27}Al spectrum. **Figure S5.1** shows relative quantities of framework tetrahedral ^{27}Al sites with a signal at 60 ppm and extraframework ^{27}Al with a signal at 0 ppm. While 17% of the total ^{27}Al signal arises from extraframework octahedral ^{27}Al sites in CHA1, only 10% of the signal corresponds to octahedral Al in CHA3. This explains the higher relative quantities of Q^4(1Al) moieties based on 1D quantitative single-pulse ^{29}Si measurements and stronger correlated signal intensities

of $^{27}Al^{IV}$ and $Q^4(2Al)$ ^{29}Si sites in CHA3 compared to CHA1 despite the identical bulk Si/Al in the two zeolites.

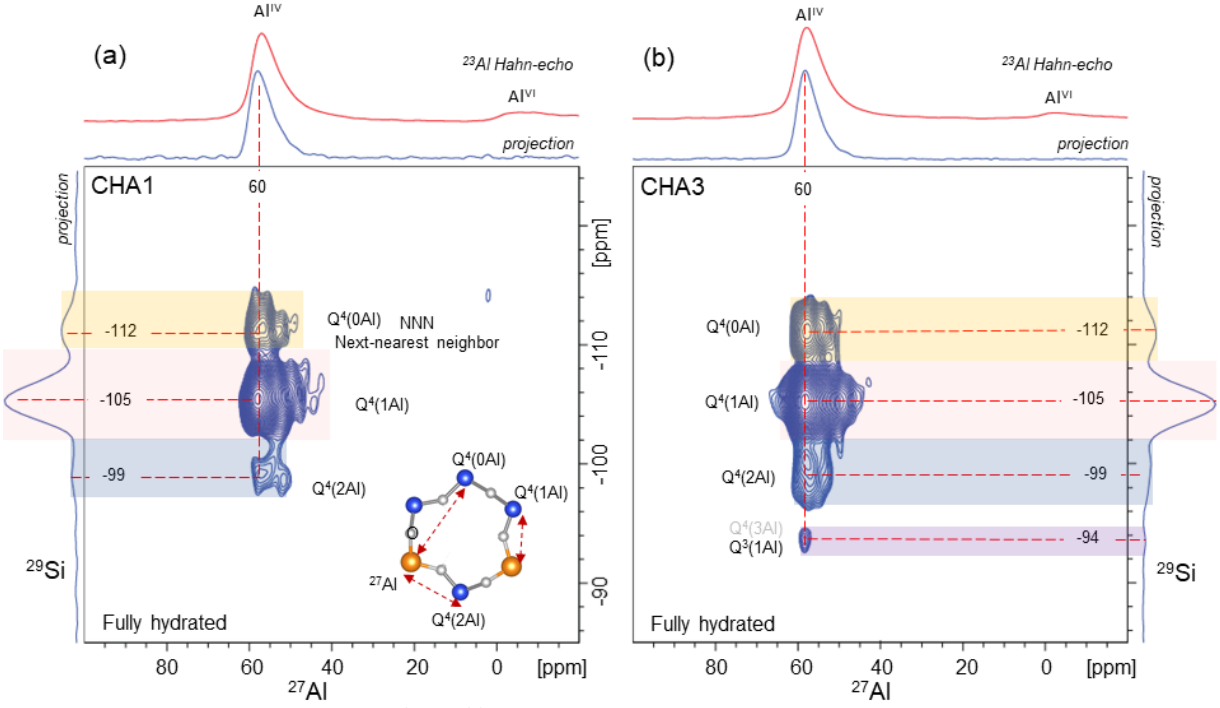

Figure 5.4. Solid-state 2D $^{27}Al\{^{29}Si\}$ *D*-HMQC spectra of fully hydrated (a) CHA1 and (b) CHA 3. The spectra are acquired at 9.4 T, 95 K, and 8 kHz MAS. The structural schematics of each zeolite structure are shown inside the corresponding spectrum. The chemical shifts of ^{29}Si sites (vertical axes) are labeled alongside their respective NMR signals. Projections of ^{27}Al sites are shown on the horizontal axes.

5.4.4 Identifying types of acid sites and surface proton species in CHA zeolites

Types and distributions of ^1H species and their interactions with the zeolite framework sites reveal crucial information on the atomic-scale structural origins of zeolite catalysts. To understand how the ^1H species are distributed throughout the framework of CHA1 and CHA3 zeolites, $^{29}Si\{^1H\}$ cross-polarization (CP) experiments are conducted on hydrated and dehydrated CHA zeolites. In the $^{29}Si\{^1H\}$ CP experiment, polarization transfers from ^1H to nearby ^{29}Si moieties. ^1H species with high natural abundance and high gyromagnetic ratio are used to enhance the signals

from proximate ^{29}Si moieties. As shown by the pulse program in **Figure 5.5a,** ^{1}H nuclei are first excited then polarization transfers from ^{1}H to ^{29}Si, whose signal is collected while ^{1}H is decoupled during the ^{29}Si signal acquisition. In general, signals from ^{29}Si sites with more proximate ^{1}H spins will be enhanced more. By changing the contact time during the polarization transfer, one can probe interactions between ^{29}Si and ^{1}H sites with different local distances. For example, ^{29}Si{^{1}H} CP experiments with shorter contact time reveal ^{29}Si signal enhancements from ^{1}H species closer to ^{29}Si sites (^{1}H species within the red dashed lines in **Figure 5.5b**) compared to CP experiments with longer contact times (^{1}H species within the grey dashed lines in **Figure 5.5b**).

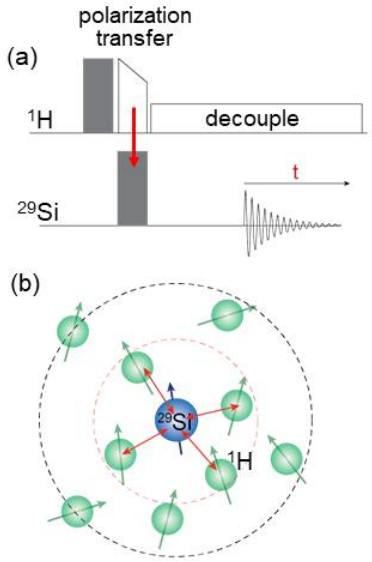

Figure 5.5. ^{29}Si{^{1}H} Cross-polarization pulse sequence with ^{1}H decoupling. (b) Structural diagram of ^{29}Si nucleus surrounded by ^{1}H nuclei. While ^{29}Si{^{1}H}CP experiments with short contact time (red circle) probes interactions between ^{29}Si and ^{1}H in proximity, longer contact time (black circle) can probe longer-range interactions.

^{29}Si species that are proximate to ^{1}H moieties in CHA1 zeolites are revealed by ^{29}Si{^{1}H} CP measurements. **Figure 5.6** shows ^{29}Si{^{1}H} CP spectra with different

contact times obtained from hydrated (left column) and dehydrated (right column) CHA1 zeolite. The same number of scans are used for **Figure 5.6a,b,c**, and **Figure 5.6d,e,f**, thus the signal intensities are comparable for spectra obtained from each sample. At shorter contact times, overall signal enhancement was smaller compared to longer contact times and zoomed spectra are shown on top of the scaled spectrum. Starting with a longer contact time of 5 ms, hydrated zeolite shows $^{29}Si\{^{1}H\}$ CP signals at -111 and -106 ppm, corresponding to Q^4(0Al) and Q^4(1Al) moieties, respectively, as shown in **Figure 5.6a**. The ^{29}Si signal at -101 ppm is an overlapping signal from Q^4(2Al), which was revealed by 2D $^{27}Al\{^{29}Si\}$ measurements shown in **Figure 5.4**, and Q^3(0Al) species. The relative intensities of each $^{29}Si\{^{1}H\}$ CP signals obtained from hydrated CHA1 zeolite at long contact time are similar to relative intensities of ^{29}Si signals obtained from quantitative 1D single-pulse measurements as discussed above. The presence of adsorbed water distributed throughout the zeolite framework zeolite enhances the signal of almost all ^{29}Si species equally, hence the signal intensities of $^{29}Si\{^{1}H\}$ CP spectrum is similar to that of the single-pulse ^{29}Si spectrum. As the contact time decreases to 1 ms and further to 0.2 ms, relative signal enhancements from the siliceous Q^4(0Al) species at -111 ppm decrease as shown in **Figure 5.6 b,c** compared to signals at -101 and -106 ppm. Q^4(1 or 2Al) and Q^3(0Al) species are proximate to H^+ and Si-OH moieties, hence the $^{29}Si\{^{1}H\}$ CP enhancements are relatively higher compared to Q^4(0Al) species, which are weakly coupled to some structural adsorbed water. Polarization transfer from ^{1}H to ^{29}Si occurs via dipolar coupling between the two nuclei. Therefore, ^{1}H moieties from mobile H_2O

are not expected to exhibit dipolar couplings with ^{29}Si species to induce cross-polarization.

In contrast, $^{29}Si\{^{1}H\}$ CP enhancements in dehydrated zeolite provide more structural information compared to the CP spectrum obtained from the hydrated zeolites, because the ^{1}H species that give rise to signal enhancement are Bronsted acid sites and surface Si-OH species instead of structural adsorbed water. **Figure 5.6d,e,f** show $^{29}Si\{^{1}H\}$ CP spectra of dehydrated CHA1. At a longer contact time of 5 ms, ^{29}Si signals at -111, -106, and -101 ppm are observed as presented in **Figure 5.6d**. Although ca. 75% of the total ^{29}Si moieties in CHA1 zeolite are siliceous $Q^{4}(0Al)$ species with a signal at -111 ppm, $^{29}Si\{^{1}H\}$ CP enhancement of the signal at -111 ppm is almost similar to that of signals at -106 and -101 ppm, due to the lack of ^{1}H moieties nearby to the siliceous moieties.

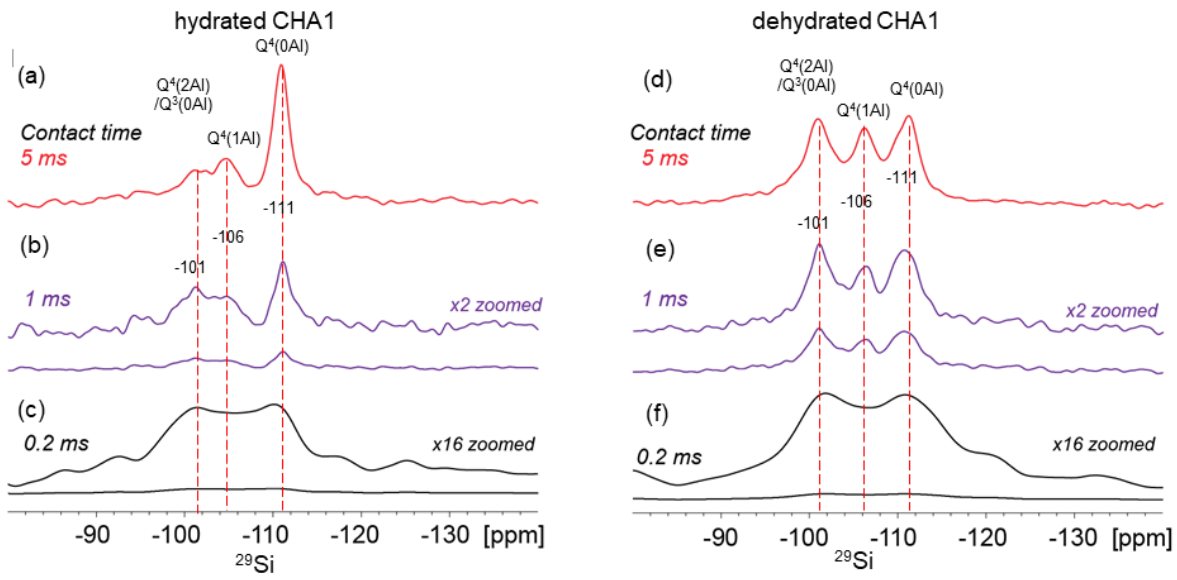

Figure 5.6. Solid-state $^{29}Si\{^{1}H\}$ CP MAS spectra of (a,b,c) hydrated CHA1 with contact time (a) 5 ms, (b) 1 ms, (c) 0.2 ms, (d,e,f) dehydrated CHA1 with contact time (a) 5 ms, (b) 1 ms, (c) 0.2 ms. Zoomed spectra in (b,c,e,f) are shown on top of each spectrum. The spectra are acquired at 11.7 T and 12.5 kHz MAS.

Similarly, $^{29}Si\{^{1}H\}$ CP spectra were collected from hydrated and dehydrated CHA3 zeolite and presented in **Figure 5.7**. The hydrated CHA3 zeolite exhibits almost identical $^{29}Si\{^{1}H\}$ CP spectra (**Fig. 5.7a,b,c**) as hydrated CHA1 zeolite (**Fig. 5.6a,b,c**) at each contact time due to the presence of water which equally enhances ^{29}Si moieties throughout the zeolite framework. However, $^{29}Si\{^{1}H\}$ CP spectra of dehydrated CHA3 exhibit significantly different signals compared to CP spectra of dehydrated CHA1, indicating that CHA1 and CHA3 zeolites contain different distributions of Bronsted acid sites and surface silanol species. Dehydrated CHA3 zeolite exhibits small $^{29}Si\{^{1}H\}$ CP signals at -111 and -106 ppm (**Fig. 5.7d**), corresponding to $Q^4(0Al)$ and $Q^4(0Al)$ moieties. At shorter contact times (**Fig. 5.7e,f**), the overall signal intensities are smaller due to polarization transfer from only the

closest 1H species, but the general trend of the highest signal intensities from the signal at -101 ppm stays the same.

The majority of the signal intensities arise from Q^4(2Al) and Q^3(0Al) moieties at -101 ppm. Higher signal enhancement from these species indicates that more proton species are proximate to ^{29}Si species with a signal at -101 ppm, such as Q^4(2Al) species are close to two H+ sites for charge balancing purposes. Therefore, for CHA3 zeolite, the majority of the ^{29}Si signals at -101 ppm is assigned to be due to Q^4(2Al) sites, which lead to paired Al sites. This is also consistent with analyses obtained from ^{27}Al{^{29}Si} correlational experiments (**Fig. 5.4b**) and ^{29}Si{^{1}H} HETCOR experiments discussed below.

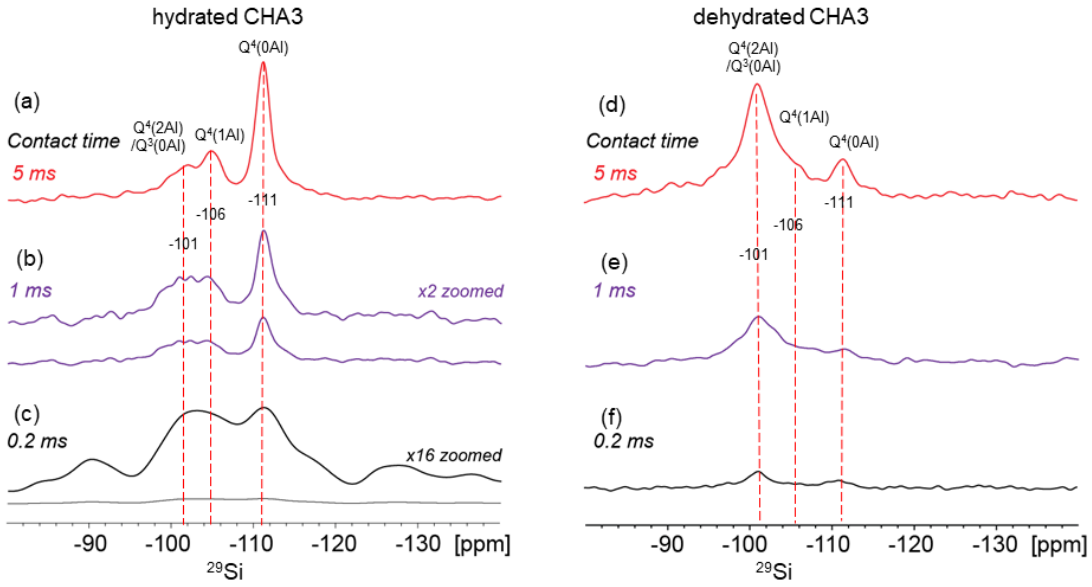

Figure 5.7. Solid-state ^{29}Si{^{1}H} CP MAS spectra of (a,b,c) hydrated CHA3 with contact time (a) 5 ms, (b) 1 ms, (c) 0.2 ms, (d,e,f) dehydrated CHA3 with contact time (a) 5 ms, (b) 1 ms, (c) 0.2 ms. Zoomed spectra in (b,c,e,f) are shown on top of each spectrum. The spectra are acquired at 11.7 T and 12.5 kHz MAS.

Different $^{29}Si\{^{1}H\}$ CP signal enhancements observed in dehydrated CHA1 and CHA3 zeolites led to conclude that local structural differences between the two zeolites can be further elucidated by $^{29}Si\{^{1}H\}$ HETeronuclear CORrelation measurements. 2D $^{29}Si\{^{1}H\}$ HETCOR spectra of CHA1 and CHA3 are presented in **Figure 5.8**. Long contact time (5 ms) was used to maximize the signal sensitivity and resolution. Significantly different $^{29}Si\{^{1}H\}$ correlations observed in CHA1 and CHA3 zeolites indicate different distributions of Si-OH and Bronsted acid sites throughout the zeolite framework.

Dehydrated CHA1 zeolite exhibits well resolved correlated signal intensities arising from ^{29}Si species dipole-coupled to distinct types of ^{1}H moieties as presented in **Figure 5.8a**. Separately collected ^{1}H echo MAS spectrum of dehydrated CHA1 is also shown in red on the vertical axes. ^{1}H spectrum exhibit signals associated with different proton species present: Si-OH species in different cages of the zeolite at -0.9 to -0.4 ppm (highlighted in grey), surface Si-OH moieties at (highlighted in yellow), Al-OH species at 3 ppm (highlighted in purple), and Bronsted acid sites at ~4-4.5 ppm (highlighted in blue). The ^{1}H spectra of hydrated samples are dominated by water but after dehydration, both silanols and Bronsted acid sites can be observed. Surprisingly, the relative intensities of the ^{1}H signal from silanol groups are found to greatly outnumber the Bronsted sites in both CHA1 and CHA3. It is possible that strongly dipolar-coupled Bronsted acid sites in dehydrated zeolites result in very broad ^{1}H signals that are lost in the baseline of the spectrum, and thus understate the ^{1}H signal intensity from Si-(OH)-Al compared to silanols. ^{1}H fast MAS (up to 50 kHz)

experiments can enable to understand whether there is the presence of strong ^{1}H-^{1}H dipolar interactions, which can be averaged by fast spinning.

Defect sites located in different cages give rise to ^{1}H signal at -0.9 and -0.4 ppm, which are correlated with Q^4(0Al), Q^4(1Al), and Q^3(0Al) moieties with signals at -111, -106, and -101 ppm, respectively. Surface silanols with signals at ~1.5-2 ppm show strong correlated signal intensities with ^{29}Si species with a signal at -101 ppm, further confirming that the majority of these ^{29}Si species in CHA1 zeolite is Q^3(0Al). Weak signal intensities from ^{29}Si at -101 ppm and Bronsted ^{1}H moieties at 4.5 ppm confirm the presence of a small amount of Q^4(2Al) ^{29}Si moieties in CHA1 zeolite. Moreover, a weak ^{29}Si signal at -92 ppm and ^{1}H signal at 1.5 ppm give rise to correlated intensities, indicating the small amount of Q^3(1Al) species are present in CHA1 zeolite.

In contrast, CHA3 zeolite exhibits a strikingly different ^{29}Si{^{1}H} HETCOR spectrum compared to CHA1 despite the same bulk Si/Al ratio. Correlated signal intensities in **Figure 5.8b** reveal ^{29}Si moieties proximate to distinct ^{1}H species in dehydrated CHA3 zeolite. Similar to CHA1, CHA3 zeolite contains more amount of Si-OH moieties than Bronsted acid ^{1}H species. Silanol moieties located in different cages of CHA zeolite are correlated with ^{29}Si moieties with Q^4(0Al), Q^4(1Al), and Q^3(0Al) moieties with signals at -111, -106, and -101 ppm, respectively as indicated by the grey highlight in the spectrum. Similar to CHA1 zeolite, CHA3 zeolite also contains Q^3(1Al) moieties with a ^{29}Si signal at -92 ppm, which is correlated with ^{1}H silanols with a signal at 1.7 ppm. However, compared to CHA1 zeolite, the relative amounts of Q^3(1Al) moieties in CHA3 zeolite appears to be slightly higher, which could be caused by the different zeolite crystallization medium used in CHA3 zeolite.

$^{29}Si\{^{1}H\}$ HETCOR spectrum reveals that CHA3 zeolite, which is synthesized to result in “paired” Al sites, definitively contains higher quantities of $Q^4(2Al)$ ^{29}Si sites compare to CHA1. Strongly correlated signal intensities arise from ^{29}Si species at -101 ppm and Bronsted acid ^{1}H moieties at 4.2 ppm. Such correlated signal intensities were weak in CHA1 zeolite as indicated by red dashed lines. The fact that CHA3 zeolite contains higher quantities of $Q^4(2Al)$ ^{29}Si than CHA1 is also consistent with the analyses obtained from $^{27}Al\{^{29}Si\}$ correlational experiments discussed above Furthermore, CHA3 zeolite exhibits a ^{1}H signal at 6.5 ppm (highlighted in red), which correspond to H-bonded ^{1}H species. Hydrogen bonded ^{1}H moieties can be present when Si-OH species are proximate to Bronsted $^{1}H^{+}$ moieties, which were not observed in CHA1 zeolite. The comparisons of $^{29}Si\{^{1}H\}$ HETCOR spectra of CHA1 and CHA3 zeolites reveal significant differences in distributions of ^{1}H moieties, *e.g.*, Bronsted acid sites and Si-OH in different cages, and zeolite ^{29}Si sites, which are caused by different zeolite crystallization mediums used for each zeolite.

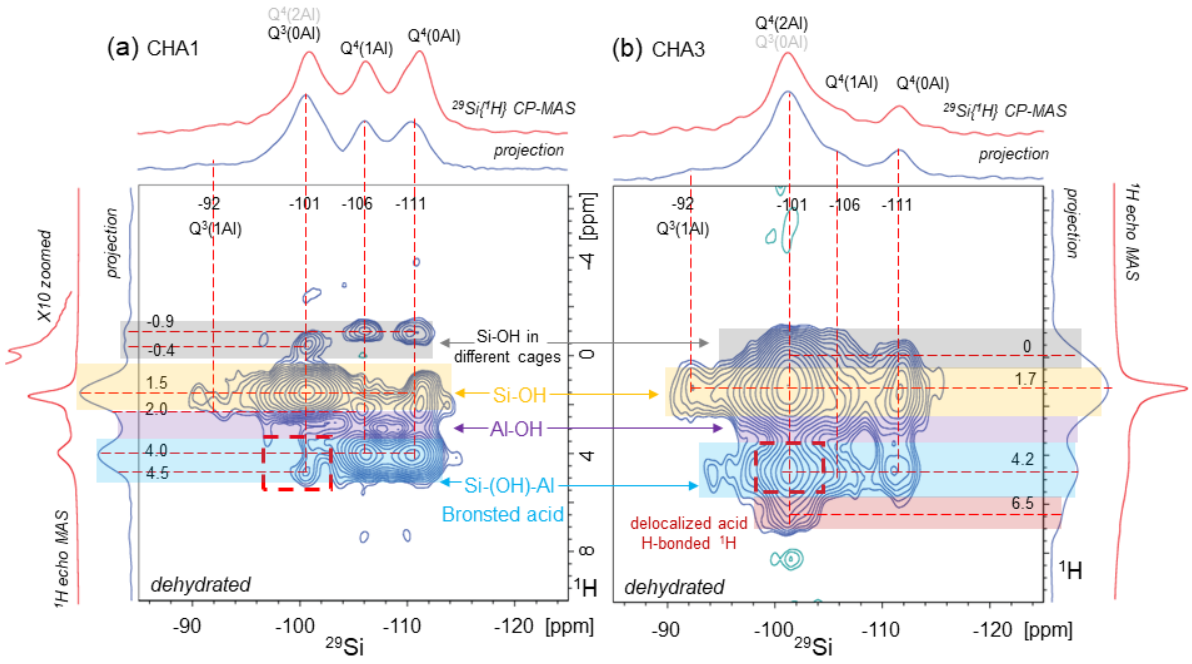

Figure 5.8. Solid-state 2D ^{29}Si{1H} HETCOR spectra of dehydrated (a) CHA1 and (b) CHA3 acquired at 11.7 T with 12.5 kHz MAS with contact time 5 ms. ^{29}Si is shown on the horizontal axis, ^{1}H chemical shift is plotted on the vertical axis. Separately collected ^{1}H Echo MAS spectrum of each zeolite is overlayed on the vertical axis for comparison

5.4.5 Interactions between Na^+ cations and framework ^{29}Si sites in CHA3 zeolite

Among the three different CHA zeolites studied here, only CHA3 zeolite was synthesized with Na^+ and a structure-directing agent. The Na^+ cations are not removed after calcination to identify the interactions between Na^+ and zeolite framework sites. **Figure 5.9** shows ^{23}Na{^{29}Si} *D*-HMQC spectrum of hydrated CHA3 zeolite. Through-space interactions between Na cations with a signal at -8 ppm shown on the horizontal axis and ^{29}Si sites are revealed by correlated signal intensities on the 2D spectrum. Separately collected 1D ^{23}Na Hahn-Echo and ^{29}Si single-pulse spectra are shown on top of the horizontal and vertical axes, respectively. Although the zeolite is hydrated, meaning that Na^+ cations should be solvated and freely

moving, broad distributions of ^{23}Na environments were observed. The ^{23}Na spectrum shows broadened tail at a higher field, similar to Czjeck lineshape, due to distributions of quadrupolar broadened ^{23}Na nuclei, indicating that Na^+ cations are strongly interacting with the zeolite framework sites. Broad distributions of local environments around ^{23}Na nuclei arise from Na^+ cations located at different sites and interacting with different framework sites. The ^{29}Si $Q^4(0Al)$ moieties with a signal at -112 ppm are through-space interacting with Na^+ cations as revealed by the correlated signal intensities highlighted in yellow. A strong signal arises from interactions between Na^+ and $Q^4(1Al)$ ^{29}Si sites with a signal at -105 ppm and $Q^4(2Al)$ ^{29}Si sites with a signal at -99 ppm. Due to attractive electrostatic interactions between positive Na cations and negative framework tetrahedral Al sites, it is expected that Na^+ cations are in proximity to the tetrahedral Al sites as shown in the structural diagrams in **Figure 5.9**. Moreover, the correlated signals from ^{29}Si moieties with a signal at -99 ppm and ^{23}Na species further confirm the presence of $Q^4(2Al)$ ^{29}Si sites that lead to paired Al sites, some of which are charge-balanced by Na^+ cations.

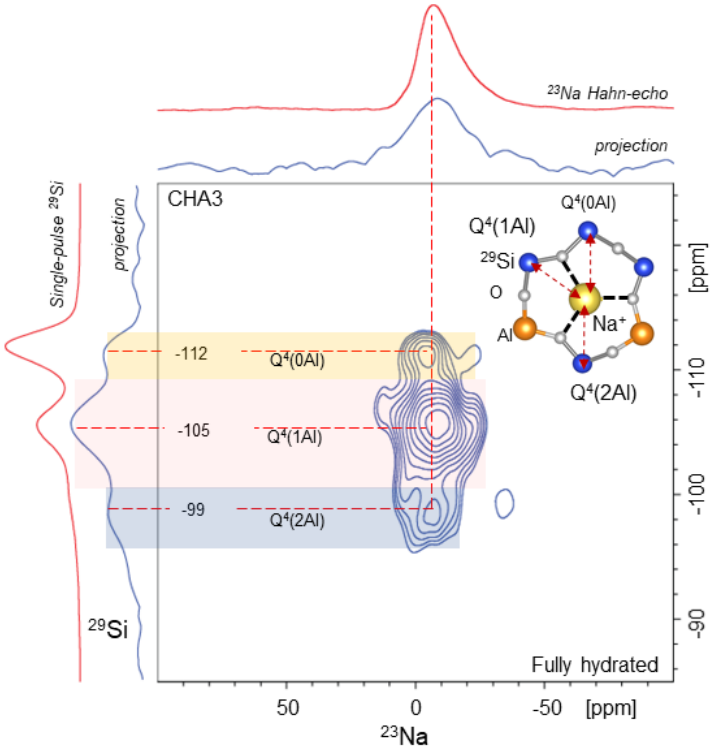

Figure 5.9. Solid-state 2D dipolar-mediated (through-space) ^{23}Na{^{29}Si} HMQC NMR correlation spectra of fully hydrated CHA3. The spectrum is acquired at 9.4 T, 95 K, and 8 kHz MAS, with SR4$^2_1$ dipolar recoupling pulse with a recoupling time of 5 ms. 1D Hahn-echo ^{23}Na spectra acquired under the same conditions are shown along the horizontal axes of each corresponding spectrum for comparison with the projections of the 2D spectra.

5.5 Conclusions

The zeolite crystallization method influences the distributions of heteroatoms and the reaction properties of the zeolite catalysts. Therefore, it is crucial to have detailed understandings of the correlations between zeolite structures and synthesis methods to design catalysts with higher performances. CHA zeolites synthesized in two different crystallization mediums but identical bulk Si/Al ratio of 14 are investigated to elucidate the effects of synthesis methods on distributions of Al sites, *e.g.*, whether the zeolite contains predominantly paired Al sites or randomly distributed Al sites.

Identifying paired Al sites in zeolites has been a hot topic in zeolite studies, and often indirect techniques, *e.g.*, multication titration, UV-Vis of exchanged cations, etc., are used to quantify the paired Al sites. Here, multinuclear solid-state NMR methods are used to directly detect paired Al sites. For example, CHA zeolite synthesized with both $TMAda^+$ and Na^+ (denoted as CHA3) is found to contain larger quantities of $Q^4(1Al)$ moieties, which can lead to paired Al sites (Al-Si-Si-Al), compared to CHA zeolite synthesized with only $TMAda^+$ (denoted as CHA1) based on the analyses of quantitative 1D ^{29}Si NMR and 2D $^{29}Si\{^{29}Si\}$ correlational measurements. Moreover, 2D $^{27}Al\{^{29}Si\}$ and $^{29}Si\{^{1}H\}$ correlational measurements reveal that CHA3 zeolite contains more amounts of $Q^4(2Al)$ ^{29}Si species, which is the source of paired Al-Si-Al sites, compared to CHA1. The methods used in this study to unambiguously identify more amounts of paired Al sites in CHA zeolite synthesized with both $TMADa^+$ and Na^+ are unprecedented, and results and analyses are expected to contribute to the development of a new class of zeolite catalysts with a controlled distribution of the heteroatoms in the framework.

References

(1) Strohmaier, K. G. ; R. S. C. ; L. D. Preparation of High-Silica Chabazite Zeolites and Their Use in the Conversion of Oxygenates into Olefins. US7435863 B2, October 14, 2008.

(2) Peden, C. H. F. Cu/Chabazite Catalysts for 'Lean-Burn' Vehicle Emission Control. *Journal of Catalysis* **2019**, *373*, 384–389.

(3) Bull, I.; Xue, W.; Burk, P.; Boorse, R. S.; Jaglowski, W. M.; Koermer, G. S.; Moini, A.; Patchett, J. A.; Dettling, J. C.; Claude, M. T. United State Patent No: US 7,601,662 B2, 2009.

(4) Moliner, M.; Gabay, J. E.; Kliewer, C. E.; Carr, R. T.; Guzman, J.; Casty, G. L.; Serna, P.; Corma, A. Reversible Transformation of Pt Nanoparticles into Single Atoms inside High-Silica Chabazite Zeolite. **2016**, *138*, 15743–15750.

(5) Zones, S. I. Zeolite SSZ-13 and Its Method of Preparation. *U S Patent* **1985**, No. 4544538A, 4,544,538.

(6) Goel, S.; Zones, S. I.; Iglesia, E. Synthesis of Zeolites via Interzeolite Transformations without Organic Structure-Directing Agents. *Chemistry of Materials* **2015**, 27, 2056–2066.

(7) Zones, S. I.; Darton, R. J.; Morris, R.; Hwang, S. J. Studies on the Role of Fluoride Ion vs Reaction Concentration in Zeolite Synthesis. *Journal of Physical Chemistry B* **2005**, *109*, 652–661.

(8) Zones, S. I.; Lew, C. M.; Xie, D.; Davis, T. M.; Schmidt, J. E.; Saxton, R. J. Studies on the Use of Faujasite as a Reagent to Deliver Silica and Alumina in Building New Zeolite Structures with Organo-Cations. *Microporous and Mesoporous Materials* **2020**, *300*.

(9) Shayib, R. M.; George, N. C.; Seshadri, R.; Burton, A. W.; Zones, S. I.; Chmelka, B. F. Structure-Directing Roles and Interactions of Fluoride and Organocations with Siliceous Zeolite Frameworks. *Journal of American Chemical Society* **2011**, *133*, 18728–18741.

(10) Burton, A.; Darton, R. J.; Davis, M. E.; Hwang, S. J.; Morris, R. E.; Ogino, I.; Zones, S. I. Structure-Directing Agent Location and Non-Centrosymmetric Structure of Fluoride-Containing Zeolite SSZ-55. *Journal of Physical Chemistry B* **2006**, *110*, 5273–5278.

(11) van Aelst, J.; Haouas, M.; Gobechiya, E.; Houthoofd, K.; Philippaerts, A.; Sree, S. P.; Kirschhock, C. E. A.; Jacobs, P.; Martens, J. A.; Sels, B. F.; Taulelle, F. Hierarchization of USY Zeolite by NH4OH. A Postsynthetic Process

Investigated by NMR and XRD. *Journal of Physical Chemistry C* **2014**, *118*, 22573–22582.

(12) Pinar, A. B.; Gómezgómez-Hortigü, L.; Mccusker, L. B.; Pérezpérez-Pariente, J. Controlling the Aluminum Distribution in the Zeolite Ferrierite via the Organic Structure Directing Agent. **2013**.

(13) Román-Leshkov, Y.; Moliner, M.; Davis, M. E. Impact of Controlling the Site Distribution of al Atoms on Catalytic Properties in Ferrierite-Type Zeolites. *Journal of Physical Chemistry C* **2011**, *115*, 1096–1102.

(14) Yokoi, T.; Mochizuki, H.; Namba, S.; Kondo, J. N.; Tatsumi, T. Control of the Al Distribution in the Framework of ZSM-5 Zeolite and Its Evaluation by Solid-state NMR Technique and Catalytic Properties. *Journal of Physical Chemistry C* **2015**, *119*, 15303–15315.

(15) Dědeček, J.; Sobalík, Z.; Wichterlová, & B. Siting and Distribution of Framework Aluminium Atoms in Silicon-Rich Zeolites and Impact on Catalysis. *Catalysis Reviews* **2012**, *54*, 135–223.

(16) di Iorio, J. R.; Gounder, R. Controlling the Isolation and Pairing of Aluminum in Chabazite Zeolites Using Mixtures of Organic and Inorganic Structure-Directing Agents. *Chemistry of Materials* **2016**, *28*, 2236–2247.

(17) Nishitoba, T.; Yoshida, N.; Kondo, J. N.; Yokoi, T. Control of Al Distribution in the CHA-Type Aluminosilicate Zeolites and Its Impact on the Hydrothermal Stability and Catalytic Properties. *Industrial and Engineering Chemistry Research* **2018**, *57*, 3914–3922.

(18) van Bokhoven, J. A.; Lee, T. L.; Drakopoulos, M.; Lamberti, C.; Thie, S.; Zegenhagen, J. Determining the Aluminium Occupancy on the Active T-Sites in Zeolites Using X-Ray Standing Waves. *Nature Materials* **2008**, *7*, 551–555.

(19) Li, S.; Zheng, A.; Su, Y.; Zhang, H.; Chen, L.; Yang, J.; Ye, C.; Deng, F. Brønsted/Lewis Acid Synergy in Dealuminated HY Zeolite: A Combined Solid-state NMR and Theore[ti]cal Calculation Study. *Journal of the American Chemical Society* **2007**, *12*9, 11161–11171.

(20) Li, S.; Huang, S. J.; Shen, W.; Zhang, H.; Fang, H.; Zheng, A.; Liu, S. bin; Deng, F. Probing the Spatial Proximities among Acid Sites in Dealuminated H-Y Zeolite by Solid-state NMR Spectroscopy. *Journal of Physical Chemistry C* **2008**, *112*, 14486–14494.

(21) Yasumura, S.; Ueda, T.; Ide, H.; Otsubo, K.; Liu, C.; Tsunoji, N.; Toyao, T.; Maeno, Z.; Shimizu, K. I. Local Structure and NO Adsorption/Desorption Property of Pd2+cations at Different Paired Al Sites in CHA Zeolite. *Physical Chemistry Chemical Physics* **2021**, *23* (39), 22273–22282.

(22) Yu, Z.; Zheng, A.; Wang, Q.; Chen, L.; Xu, J.; Amoureux, J. P.; Deng, F. Insights into the Dealumination of Zeolitehy Revealed by Sensitivity-Enhanced ^{27}Al DQ-MAS NMR Spectroscopy at High Field. *Angewandte Chemie - International Edition* **2010**, *49*, 8657–8661.

Supporting Information

Comparisons of single-pulse ^{29}Si and ^{27}Al spectra of CHA1 (Si/Al=14), CHA2 (Si/Al=26), and CHA3 (Si/Al=14). Differences in relative intensities of different ^{29}Si species with signals at -102, -105, and -112 ppm, corresponding to Q^4(2Al)/Q^3(0Al), Q^4(1Al), and Q^4(0Al) moieties, respectively, are caused by the different synthesis mediums (structure-directing agent, cations, and amount of Si and Al sources) used to crystallize the three different types of CHA zeolites. Similarly, different relative quantities of framework tetrahedral ^{27}Al with a signal at 60 ppm and extraframework ^{27}Al with a signal at 0 ppm are the results of the different synthesis mediums used in CHA1, CHA2, and CHA3.

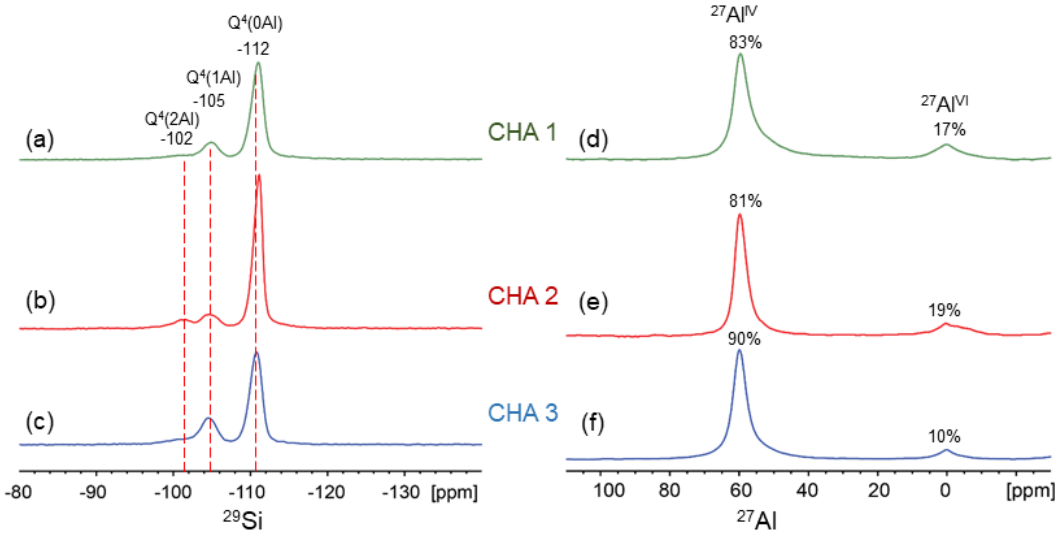

Figure S5.1. Solid-state 1D ^{29}Si Single-pulse MAS spectra of fully hydrated (a) CHA1, (b)

CHA2, (c) CHA3. Solid-state 1D ^{27}Al Echo MAS spectra of fully hydrated (d) CHA1, (e) CHA2, (f) CHA3. The spectra were acquired at 11.7 T with 12.5 kHz MAS.

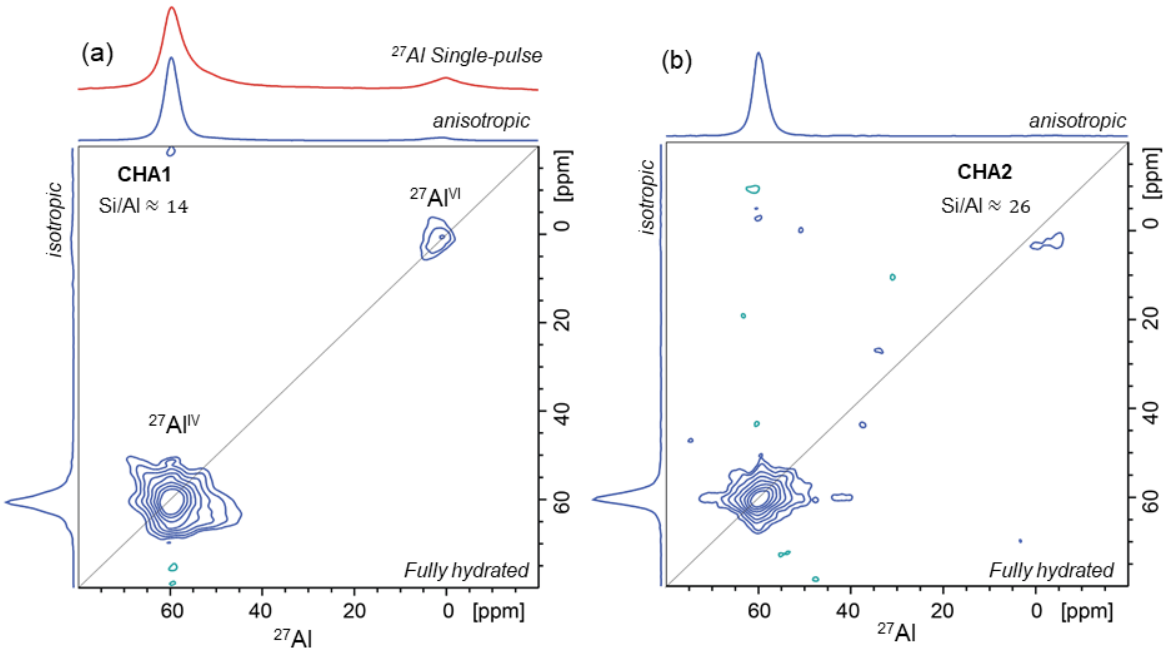

Figure S5.2. ^{27}Al MQMAS spectra of fully hydrated (a) CHA1 and (b) CHA2. The spectra are acquired at 18.8 T, 18 kHz MAS at room temperature.

CHAPTER 6

6. Identifying the local environments of Cu^{2+}sites in chabazite zeolite by EPR

6.1 Introduction

Chabazite zeolite exchanged with Cu^{2+} cations shows exceptional activity for selective catalytic reduction (SCR) of harmful NO_x using ammonia as a reducing agent.[1] There has been significant research effort in understanding the catalytic behavior of the Cu-CHA zeolite, but correlations between atomic-level structures and reaction properties of the catalysts have not been elucidated. To obtain the structure-activity relationship, it is crucial to identify types of coordination environments of Cu^{2+} centers, which are the active sites of the SCR reaction shown below.[2]

$$4NH_3 + 4NO + O_2 \rightarrow 6H_2O + 4N_2$$

Two proximal framework Al atoms, which are the source of the negative charge of the zeolite framework, can be charge-balanced by either a single Cu^{2+} cation or a single Al-site in the zeolite can be associated with $Cu(OH)^+$ cation. Moreover, the coordination environments of Cu-centers change due to the hydration of the Cu^{2+} cations when the zeolite is hydrated. It is crucial to obtain atomic-level insights on types of Cu^{2+} environments and relative quantities of different Cu^{2+} species present in industrially significant Cu-CHA zeolite to further improve the performance of the catalyst. Such detailed information can be obtained by implementing advanced line-shape analyses on the electron paramagnetic resonance (EPR) spectra of Cu-CHA zeolites. EPR analysis results in two parameters: *g*-values and hyperfine coupling

constants. These parameters for interactions between the copper nucleus and the unpaired electron can provide valuable information on the coordination of Cu^{2+} in the zeolite framework. The objective of the project is to identify different coordination environments of Cu^{2+} and understand the effects of hydration on the structure of paramagnetic Cu^{2+} centers by analyzing the EPR spectra of hydrated and dehydrated Cu-CHA materials.

6.2 Materials and methods

Cu-CHA zeolites with varying amounts of Cu loadings are provided by industrial collaborators. Aluminosilicate zeolites are extremely hydrophilic and adsorb a substantial amount of water (up to 30 wt%) when exposed to air. The coordination environments of Cu^{2+} in zeolites are strongly influenced by the presence of adsorbed water, hence it is crucial to control the hydration of zeolites when conducting EPR measurements. Zeolites are dehydrated for 5 hours from room temperature to 450 ^{o}C under vacuum in specially designed glassware with EPR quartz tubes attached. After the treatment, samples are transferred into the EPR tubes without exposure to air and are sealed by glassblowing. Hydrated samples are regularly packed in EPR tubes in ambient conditions. Bruker EMXplus EPR Spectrometer is used to acquire continuous wave (CW) X-band EPR spectra of Cu-CHA catalysts with 3 and 0.8 wt% Cu-loadings in both hydrated and dehydrated states. CW EPR experiments are conducted at both room temperature and 100 K with liquid nitrogen cooling. The spectra are simulated by using EasySpin's fitting function *esfit* to acquire EPR parameters of Cu^{2+} species. Hyperfine couplings of two $^{63/65}$Cu isotopes are not resolved, thus only ^{63}Cu (natural abundance ~ 70%) is considered in the simulation.

6.3 Background of EPR studies on Cu-zeolite materials

The spin Hamiltonian (*eq 1*) of a paramagnetic center depends on the g-values and hyperfine coupling constants. For axial symmetry, $g_{||} = g_{zz}$ and $g_{\perp} = g_{xx} = g_{yy}$, giving a spin Hamiltonian of:

$$H = g||\mu BSzBz + g \perp \mu B(SxBx + SyBy) + A||SzIz + A \perp (SxIx + SyIy) \quad eq(1)$$

where μ_B is the Bohr magneton and the components of the magnetic field are B_z, B_x and B_y. The electronic spin operators are S_z, S_x and S_y, and nuclear spins operators are I_z, I_x and I_y. These parameters depend on the surrounding ligand field and therefore contain important structural information. The software program *EasySpin* used to simulate the EPR spectrum takes into consideration of the above parameters which can be either defined, if known, or can be obtained via the best fit to the experimental spectrum.

EPR is very sensitive and can detect EPR active Cu species in zeolites in a few hundred milligram samples of Cu-zeolites with low Cu concentrations (<0.5 wt%) relevant to catalysis applications, and the EPR techniques have been used to obtain structural information of Cu-zeolites since the 1970s.[5] Cu^{2+} has an unpaired electron in d^9 orbital and has spin doublet ground state which gives rise to the EPR signal. The Cu nucleus has major two naturally occurring isotopes: ^{63}Cu and ^{65}Cu, with a natural abundance of ca. 70% and 30%, respectively. Both $^{63/65}$Cu isotopes have nuclear spin *I* = 3/2 which causes the EPR spectrum to split into four hyperfine lines. Although two isotopes have different effects on the paramagnetic center, the effects are not resolved for EPR line-shapes resulting from Cu-zeolite materials.

Cu^{2+} cations in zeolites strongly interact with the framework oxygen atoms. Based on density functional theory (DFT) calculations it was found that the most stable position of Cu^{2+} in zeolites is on the six-membered ring when two of which are Al sites. For CHA zeolite, all six-membered rings are exposed to the channel systems and are accessible to Cu^{2+}.

Finally, it should be noted that there are some EPR silent Cu species, such as Cu^{+} which have no unpaired electrons, anti-ferromagnetically coupled Cu^{2+} dimers and Cu^{2+} in high symmetric coordination environments such as copper center in trigonal planar structures. Therefore, the presence of such EPR silent species cannot be excluded based on analyses of an EPR spectrum.

6.4 Results and discussions

6.4.1 Establishing the effects of Cu concentrations in CHA zeolite on EPR signal

Different Cu species have sufficiently different spin Hamiltonian parameters and can be resolved from analyses of the EPR spectrum. To obtain g-values and hyperfine splitting constants, which are affected by coordination environments of Cu centers, a well-resolved EPR spectrum needs to be obtained for accurate line-shape analyses. First, Cu-CHA zeolites with Cu-loadings of 3 and 0.8 wt% are studied to determine the effects of Cu concentration on the EPR signal. Comparing the 3 and 0.8 wt% Cu-loadings result results also show which sample has a better-resolved EPR spectrum such that the proper Cu-loading can be chosen for additional analyses. **Figure 6.1** shows EPR spectra of 3 and 0.8 wt% Cu loaded on CHA zeolites at hydrated and dehydrated states acquired on the X-band instrument at room temperature. For 0.8

wt% Cu-CHA, the EPR signal dramatically changes upon hydration (**Fig. 6.1a**). The EPR spectrum of hydrated 0.8 wt% Cu-CHA zeolite shows a broad line shape with poorly resolved anisotropic interactions as well as signatures of isotropic interactions at $g \approx 2.17$, which is the same as g-values of typical Cu^{2+} species found in aqueous solution[6]. This indicates that some Cu^{2+} species are solvated in the adsorbed water. On the other hand, the EPR signal of dehydrated 0.8 wt% Cu-CHA exhibits well-resolved anisotropic interactions, from which the structural information can be (and will be in the following sections) extracted.

For 3 wt% Cu-CHA, the EPR spectra of both hydrated and dehydrated states exhibit broad features (**Fig. 6.1b**), which make the spectra challenging for detailed EPR line-shape analyses. At high concentrations of Cu in CHA zeolite, the EPR signal is broadened due to interactions between paramagnetic centers. These exchange interactions between paramagnetic Cu centers complicate the analyses and decrease the resolution of the EPR spectra. Therefore, in the following sections EPR analyses, only 0.8 wt% Cu-CHA are discussed as it results in a well-resolved EPR signal and enables the extraction of spin Hamiltonian parameters.

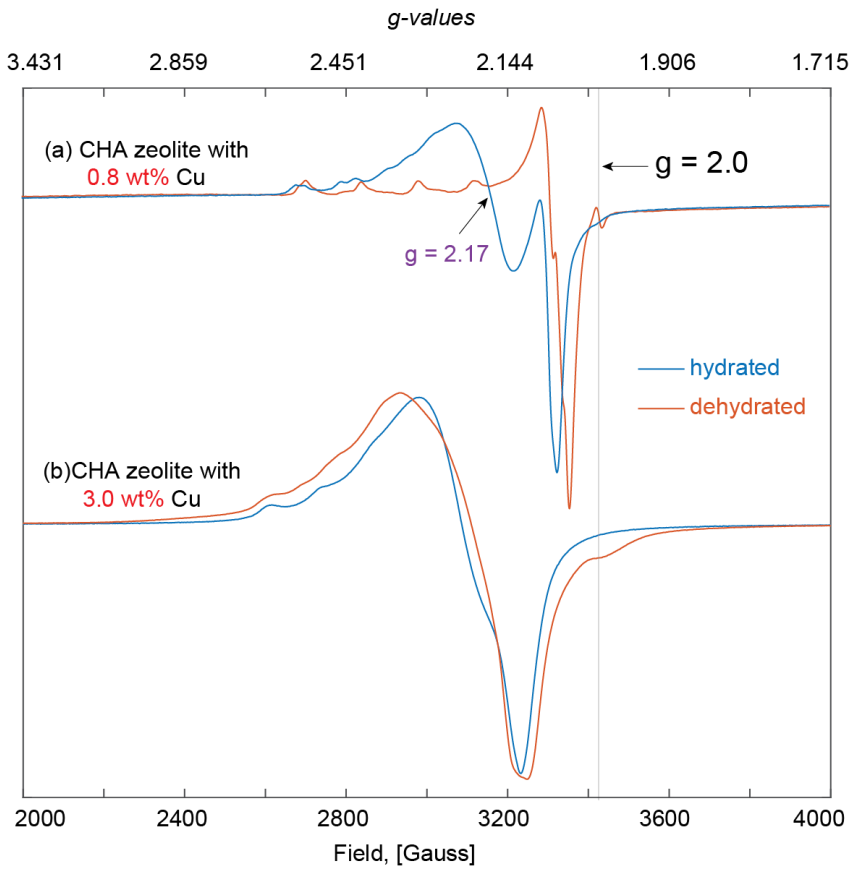

Figure 6.1. Comparison of X-band CW-EPR spectra of (a) 0.8 wt% and (b) 3 wt% Cu-CHA acquired at room temperature. For both Cu loadings, blue spectra are from hydrated Cu-CHA and orange spectra are from dehydrated Cu-CHA. Corresponding g-values to the magnetic field are shown on top of the x-axis.

6.4.2 Revealing coordination environments of Cu^{2+} in 0.8 wt% Cu-CHA zeolites

The information obtained from the EPR signal of hydrated Cu-CHA zeolite is limited as its anisotropic interactions are poorly resolved and the majority of the signal is overwhelmed by signals from aqueous-like isotropic Cu^{2+} species. In contrast, the EPR spectrum of dehydrated 0.8 wt% Cu-CHA exhibit well-resolved signals that can reveal the coordination of Cu inside the zeolite cage. Studying dehydrated zeolite is also more relevant to industrial applications because Cu-CHA catalyst is dehydrated

when operating at the high temperatures found in diesel exhaust environments. Therefore, EPR line-shape analyses are performed on a signal acquired from dehydrated 0.8 wt% Cu-CHA, shown in **Figure 6.2.** The best-simulated fit to the experimental EPR spectrum was found by using *EasySpin* software.

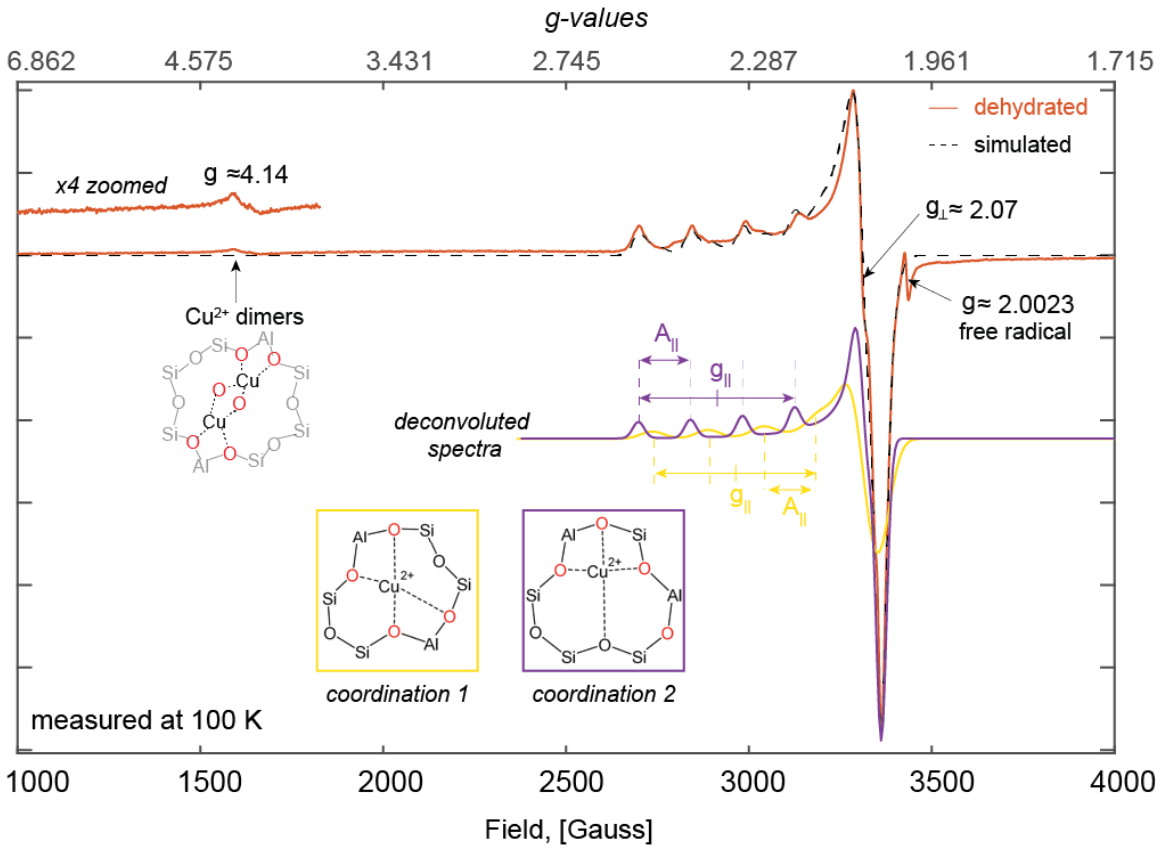

Figure 6.2. X-band CW-EPR spectra of dehydrated 0.8 wt% Cu-CHA acquired at 100 K. The black dashed line is the simulated spectrum which is a sum of the two deconvoluted spectra shown in purple and yellow. Each represents a type of Cu^{2+} coordination environment depicted in the colored boxes. Most negatively charged O atoms are depicted in red. Cu^{2+} transition at half-field (g = 4.14) is observed due to copper-dimers. A small amount of free radical (g = 2.0023) is present in dehydrated Cu-CHA.

The simulated spectrum shown as the dashed line gives the best fit to the experimental EPR spectrum when it is composed of two types of Cu^{2+} coordination with spin Hamiltonian parameters shown in **Table 6.1.** Two types of Cu^{2+} structures shown in yellow (coordination 1) and purple (coordination 2) boxes in **Figure 6.2** correspond to yellow and purple simulated EPR spectrum with different $g_{||}$ and $A_{||}$ values. Both species are assigned to Cu^{2+} in distorted tetragonal planar coordination in six-membered rings with two Al sites. The EPR parameters are assigned to the two structures based on empirical findings of Peisach and Blumberg,[7] which revealed the correlation between the hyperfine coupling constants and electron spin density around the Cu nucleus. The species with the least negative charge on the coordination environment have higher $g_{||}$ and lower $A_{||}$ values. Coordination 2 for Cu-CHA has fewer numbers of negatively charged O atoms strongly bound to the Cu-nucleus (three oxygens shown in red in **Figure 6.2**) than coordination 1 (which has four strongly bound oxygen atoms). Therefore, coordination 2 has higher $g_{||}$ =2.36 and lower $A_{||}$ =468.8 MHz compared to that of coordination 1 with values of $g_{||}$ =2.32 and $A_{||}$ =489.8 MHz. This *g* and A parameter values are consistent with reported values on dehydrated Cu-CHA zeolites.[8]

Table 6.1: Speciation of Cu and Spin Hamiltonian parameters of two types of Cu^{2+} coordination environments of dehydrated 0.8 wt% Cu-CHA. The corresponding simulated spectrum is shown in Figure 6.1.

Cu-coordination type	$g_{\perp}$	$g_{\parallel}$	$A_{\perp}$ (MHz)	$A_{\parallel}$ (MHz)	Weight factor
1	2.0732	2.3154	15.5	489.8	0.41
2	2.0638	2.3564	32.8	468.8	0.87

Interestingly, the EPR signal also shows a sharp signal at $g \approx 2.00$, which corresponds to free electrons. Such species were not present in hydrated Cu-CHA and are tentatively assigned to oxygen radicals in dehydrated aluminosilicate zeolites. Moreover, a small amount of signal at $g \approx 4.14$ is present in dehydrated Cu-CHA zeolites. This signal appears at a half-field (~1655 Gauss) of the anisotropic Cu^{2+} transition (~3310 Gauss) and is a signature for dimeric Cu species.

6.4.3 Discussions on Cu dimers that exhibit half-field transition EPR signal

When two paramagnetic centers form a weak bond it is called the exchange interaction. It is rare to obtain such an exchange regime when two paramagnetic atoms are directly bound. Typically, two paramagnetic metal ions are bridged by diamagnetic atoms which can effectively transmit exchange interaction. Such couplings are referred to as super-exchange.[9] For Cu-dimers in zeolites, the x-y magnetic orbitals of Cu^{2+} ions overlap with the p-orbital of bridging oxygen atoms (as shown in the top Figure) and form structures like Cu^{2+}-O-Cu^{2+} in the bigger cages of the zeolite framework depicted in **Figure 6.2**. When the Cu-O-Cu angle is not equal to 90°, the interaction is ferromagnetic and shows a signature EPR signal at the half-field of the Cu^{2+} transition. Cu^{2+}−O−Cu^{2+}species in zeolites are known to be sensitive to adsorbed water and form monomeric [Cu^{2+}-OH]$^{-}$ species upon hydrolysis. Therefore, the signal at $g = 4.14$ is not present in hydrated Cu-CHA zeolites as shown in **Figure 6.3d**, which will be discussed more in detail in the following sections.

6.4.4 Identifying reversibility of Cu^{2+} structures upon dehydration and rehydration

From the previous sections of the EPR line-shape analyses, it is found that the hydrated and dehydrated zeolites show significantly different EPR signals due to different coordination environments of Cu^{2+} with framework oxygens and adsorbed water. When preparing zeolite catalysts, it is important to know whether the process of dehydration and re-hydration changes the local environments of catalytically active metal ion sites because it governs the overall reaction properties of zeolite catalysts. To obtain insights on the reversibility of Cu environments in Cu-CHA zeolites, the EPR spectra of hydrated, dehydrated, and rehydrated samples of the previously dried Cu-CHA are compared in **Figure 6.3**. The spectra on the left (**Fig. 6.3 a, b, c**, and **d**) are acquired at room temperature, while the spectra on the right (**Fig. 6.3 e, f, g**, and **h**) are acquired at 100 K. The room temperature EPR spectrum of hydrated Cu-CHA (**Fig.6.3a**) shows features for both anisotropic (marked in red lines) and isotropic interactions (marked in purple lines). Hydrated Cu^{2+} species in zeolite exhibit a similar isotropic EPR signal as typical Cu^{2+} found in aqueous solutions with $g \approx 2.17$.[6] Although poorly resolved, there are some anisotropic features present in the EPR signal of hydrated Cu-CHA, indicating that there are some Cu^{2+} moieties strongly bound to the zeolite framework in hydrated states. Interestingly, when the same sample is measured at 100 K, the EPR signal reveals purely anisotropic interactions (**Fig. 6.3e**), indicating that the mobility of hydrated Cu^{2+} species is frozen and can no longer exhibit isotropic interactions. When the zeolite is dehydrated, Cu^{2+} moieties are bound strongly to the framework oxygen atoms. Therefore, the EPR spectrum shows a well-resolved anisotropic line-shape split by the interaction of the unpaired

electron with the $^{63/65}$Cu nuclei. Not surprisingly, the spectra of the dehydrated Cu-CHA acquired at room temperature and 100 K are similar (**Fig. 6.3b, f**) since there are negligible motions due to adsorbed water frozen in the dehydrated Cu-CHA.

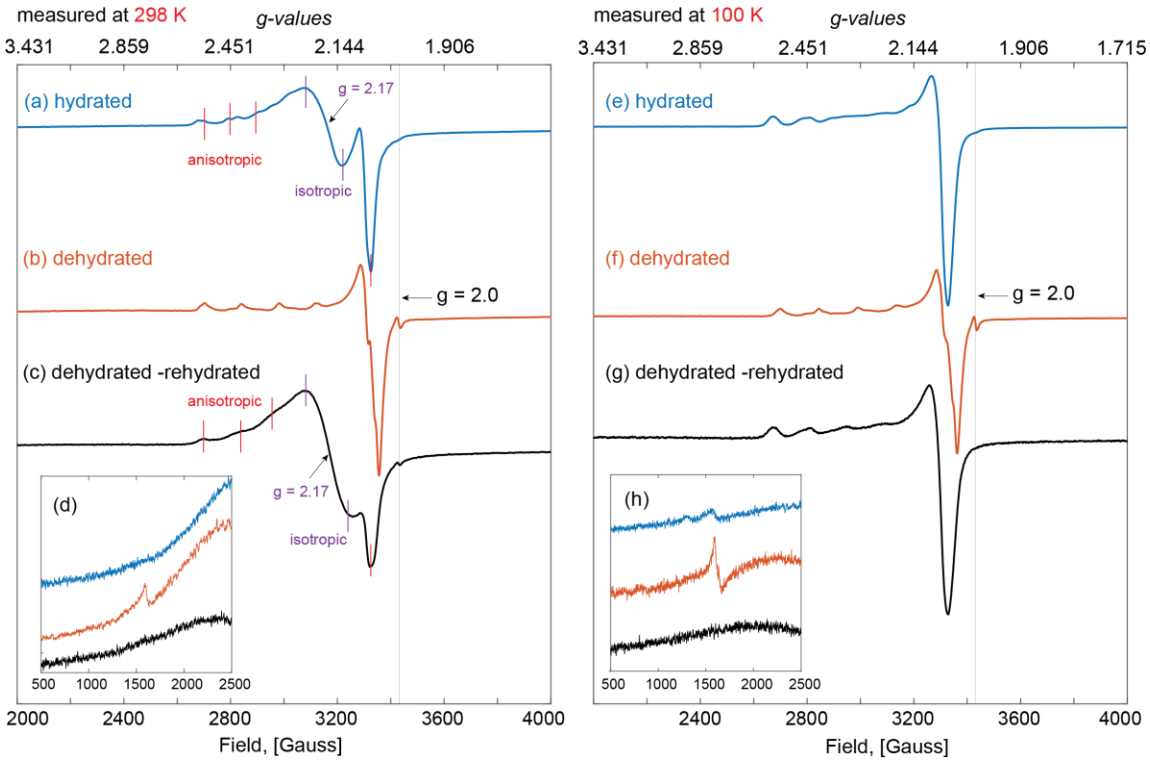

Figure 6.3. X-band CW EPR spectra of (a,e) hydrated, (b,f.) dehydrated, (c,g) dehydrated then rehydrated 0.8 wt% Cu-CHA measured at ^{29}8 K (left) and 100 K (right). Zoomed sections of the half field show EPR signal at ca. 1650 Gauss (d,e). Hydrated Cu-CHA zeolites measured at room temperature, a and c, reveal g-values that correspond to the magnetic fields shown on top of the *x*-axis.

The EPR spectrum of rehydrated Cu-CHA acquired at room temperature also exhibits features for isotropic and anisotropic interactions (**Fig. 6.3c**) like the simply hydrated Cu-CHA samples (**Fig. 6.3a**). Small differences arise due to the number of isotropic contributions present, which could be caused by slightly different amounts of adsorbed water. The low-temperature measurement is consistent with such a

hypothesis. The comparison between the EPR spectra of rehydrated and simply hydrated Cu-CHA samples are almost identical (**Fig. 6.3e, g**) when measured at 100 K, where the mobility caused by the adsorbed water is hindered. The presence of Cu-dimers is revealed by closely investigating the spectra zoomed-in (500 to 2500 Gauss) at the half-field region (**Fig. 6.3d, h**). When EPR measurements are conducted at room temperature, only the spectrum of dehydrated Cu-CHA shows a signal for Cu-O-Cu type dimeric compounds (**Fig. 6.3d** – orange spectrum). Hydrated zeolites do not exhibit features that correspond to such copper-oxo dimers. Interestingly, the low-temperature EPR spectrum of hydrated Cu-CHA show dilute amounts of Cu-dimers. This suggests that the copper-oxo complexes do not fully decompose into a monomeric $Cu^{2+}[OH]^-$ upon hydrolysis when adsorbed water is present in the zeolite. Therefore, at lower temperature measurements where EPR sensitivity is higher than room temperature experiments, the small amounts of residual Cu-dimers give rise to a detectable signal.

6.5 Conclusions

Industrially significant catalyst Cu-exchanged CHA zeolites are studied by CW-EPR line-shape analyses to determine the coordination environments of paramagnetic copper sites, which are the catalytically active sites for deNOx reactions. Information about the coordination environments of Cu-sites is extracted from the spin Hamiltonian parameters obtained from the simulated best-fit to the experimental spectrum. The g-values and the hyperfine coupling constants for the interaction between the unpaired electron and the copper nucleus enabled identification of the speciation of Cu sites in dehydrated Cu-CHA zeolite. Two types of

Cu^{2+} coordinated with oxygen atoms of the zeolite six-membered rings and Cu dimers bonded through bridging oxygen atoms are found in dehydrated Cu-CHA zeolite. Moreover, reversible behavior of Cu-sites upon hydration and dehydration is found by analyzing EPR spectra of Cu-CHA at hydration-dehydration-rehydration cycles. The findings in this report are significant, as the coordination environments and types of Cu sites can be correlated to explain exceptional catalytic activity Cu-CHA for selective reduction of NOx gases.

References

(1) Lomachenko, K. A.; Borfecchia, E.; Negri, C.; Berlier, G.; Lamberti, C.; Beato, P.; Falsig, H.; Bordiga, S.; Topsøe, H. A.; Topsøes Alle, H.; Lyngby, K. *J. Am. Chem. Soc* **2016**, *138*, 44.

(2) Paolucci, C.; Khurana, I.; Parekh, A. A.; Li, S.; Shih, A. J.; Li, H.; Di Iorio, J. R.; Albarracin-Caballero, J. D.; Yezerets, A.; Miller, J. T.; Delgass, W. N.; Ribeiro, F. H.; Schneider, W. F.; Gounder, R. *Science.* **2017**, *357*, 898–903.

(3) Di Iorio, J. R.; Gounder, R. *Chem. Mater.* **2016**, *28*, 2236–2247.

(4) Paolucci, C.; Parekh, A. A.; Khurana, I.; Di Iorio, J. R.; Li, H.; Caballero, J. D. A.; Shih, A. J.; Anggara, T.; Delgass, W. N.; Miller, J. T.; Ribeiro, F. H.; Gounder, R.; Schneider, W. F. **2016**, 6028–6048.

(5) Chao, C.C.; Lunsford, J. H. EPR Spectra of Cu2+in SingleCrystals of Chabazite. *J. Chem. Phys*.**1973**,59, 3920−3925

(6) Giordanino F, Vennestrøm PNR, Lundegaard LF, et al. (2013) Characterization of Cu-exchanged SSZ-13: a comparative FTIR, UV-Vis, and EPR study with Cu-ZSM-5 and Cu-β with similar Si/Al and Cu/Al ratios. Dalton Trans 42

(7) Peisach J, Blumberg WE (1974) Structural Implications Derived from the Analysis of Electron Paramagnetic Resonance Spectra of Natural and Artificial Copper Proteins. Arch Biochem Biophys 165:691–708

(8) Godiksen, A.; Stappen, F. N.; R Vennestrøm, P. N.; Giordanino, F.; Birk Rasmussen, S.; Lundegaard, L. F.; Mossin, S. **2014**, 23126–23138

(9) A. Bencini, D. Gatteschi, EPR of Exchange Coupled Systems, Springer-Verlag, Berlin,**1990**

CHAPTER 7

7. Conclusions

This dissertation elaborately presented correlations between atomic-scale structures and reaction properties of various types of industrially significant zeolite catalysts, with a specific focus on Pt-supported zeolites. The performance of such zeolite catalysts depends strongly on the composition and nanoscale architecture of the zeolite support, and types and locations of metal species within the zeolite pores. Atomic-scale structural insights were obtained by one- and two-dimensional multidimensional solid-state nuclear magnetic resonance spectra (NMR) with sensitivity and resolution enhanced by a high magnetic field (up to 35.2 T), low-temperature measurements, fast Magic Angle Spinning (MAS) methods, dynamic nuclear polarization (DNP) techniques. Results were also complemented by electron paramagnetic resonance (EPR), X-ray powder diffraction (XRD), extended X-ray absorption fine structure (EXAFS), scanning and transmission electron microscopy, and chemisorption methods to acquire long and short-range structural information that is correlated with reaction properties of zeolite catalysts.

Atomic structures of Pt-zeolites prepared under different conditions, zeolite catalysts treated with dilute promoter species, zeolites that are processed through different post-synthesis dealumination methods, and zeolites crystallized in different gel mediums are investigated in this dissertation. In Chapter 2, calcination temperature dependence on types and locations of Pt moieties in different cages of NaY zeolite is revealed. Obtaining detailed understandings of the effects of treatment

conditions on distributions of Pt in the zeolite framework is crucial to control the dispersion of precious metal Pt and design a catalyst with higher performance. In Chapter 3, types of dilute fluorine promoter species, which are responsible for increased aromatization selectivity of Pt/KL catalysts, are identified in fresh and spent catalysts. The specific types of fluorine species attached to the framework zeolite sites are unambiguously revealed and proposed to have promoting effects on *n*-hexane aromatization properties. Chapter 4 investigated structural differences in two types of bifunctional Pt-H^+USY catalysts used for *n*-hexadecane hydroisomerization. Different isomerization activities exhibited by two types of Pt-H^+USY are found to be due to the differences in the amount of siliceous disordered moieties in USY zeolites. In Chapter 5, distributions of Al sitings, specifically paired Al sites in CHA zeolites synthesized in different gel mediums are elucidated. The effects of zeolite crystallization medium, *e.g.*, presence of structure-directing agent and cations, are found to directly influence the distributions of Al sites in CHA zeolite despite keeping the bulk Si/Al ratio. Chapter 6 focused on identifying types of Cu^{2+} coordinations in Cu-CHA zeolite, which is used for deNOx catalysts, by extensive analyses of EPR spectra. Notably, EPR methods revealed two types of Cu coordination and dimers of Cu species, which are all crucial for understanding the catalytic activities of Cu-sites.

In conclusion, the advanced experimental methods used in this dissertation, and results and analyses presented here are expected to be a valuable addition to both fundamental and applicable knowledge of metal-zeolite catalysts, whose performances are directly related to their atomic-level structures. The new insights

obtained from the work presented here can be served as guidance to design zeolite catalysts with better performances.

Appendices

A1. Background of wideline NMR and practical considerations of WURST-CPMG ^{195}Pt NMR experiments

Acquiring solid-state nuclear magnetic resonance spectra of nuclei with broad lineshapes can be challenging due to the limited ability of a standard rectangular radiofrequency pulse to excite a broadband spectrum (> 200 kHz). Anisotropic broadening of the powder pattern can span up to several MHz, which is caused by the coupling between nuclear electric quadrupole moment and the local electric field gradient – quadrupolar interaction, the coupling between conduction band electrons and the nuclei of metals - hyperfine interaction, and sometimes strong chemical shielding anisotropy (CSA). Although difficult to acquire, once obtained, these broad powder patterns provide valuable information about the local electronic environment of the nuclei, thus it is important to investigate advanced pulse techniques that uniformly excite broadband spectra.

Theory of the Knight shifts

In metals, nuclear spins are coupled to unpaired conductions electrons through hyperfine interaction, which gives rise to an additional shift on the chemical shift, known as the Knight shift. The Knight shift is originated from the non-negligible Zeeman energy splitting of conduction band electrons. If we consider a nucleus coupled to one electron, which is spin ½, the NMR spectrum will be a doublet with asymmetric splitting as shown in **Figure 1.8**. However, in reality, the asymmetrically split NMR peaks will collapse into a single peak, because of the very short T_1 relaxation time of the electrons. The position of the Knight shift depends on the

population difference of electronic states, thus it is linearly proportional to external magnetic field strength B_0.

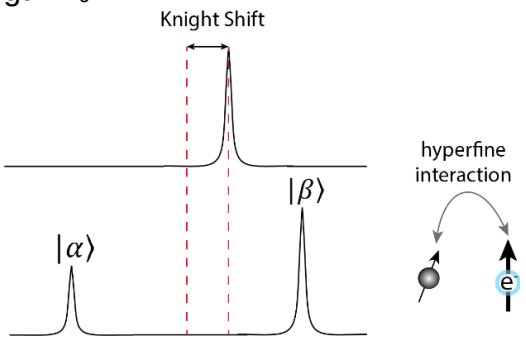

Figure 1.8. Schematic representation of the origin of the Knight shift.

The Knight shift of Pt particles supported on zeolites

In a small supported Pt particle, the Knight shift arises from the Pt nuclei of the interior of the particle far from the surface, where the local environment is bulk-like. On the other hand, surface Pt species of a clean particle with no adsorbed molecules lack neighbors compared to the interior Pt atoms, thus surface Pt exhibits different Knight shifts (2/5 of the Knight shifts of the interior particles). Surface species that are chemically bonded to adsorbed molecules do not give rise to Knight shifts, since the conducting electrons will be tied up to the adsorbed molecules. Instead, these surface species exhibit chemical shifts that are fingerprints of the adsorbed molecules. ^{195}Pt NMR measurements of these small particles are very sensitive to their local environments. Therefore, direct detection of the ^{195}Pt nuclei provides rich information about the electronic environments of the Pt particles, which influence the catalysis phenomenon occurring at the surface of the particles.

A1.1 Excitation profile of a rectangular pulse

The excitation profile of a 10 μs 90^{o} simple rectangular pulse cannot excite a broadband (> 200 KHz) spectrum homogeneously. However, it is capable of exciting a small region of 50 -100 kHz, which is equivalent to 100 – 200 ppm for ^{1}H at 11.7 T instrument. Although this spectral width is enough for commonly studied nuclei, such as ^{13}C and ^{1}H, it is not satisfactory to obtain the full lineshape of nuclei that have spectrum spans to thousands of ppms. **Figure A1.1.1a** shows the excitation profile of a 90^{o} rectangular pulse. As the offset frequency deviates from 0, the ability to excite the signal also decreases. For example, at an offset frequency of 0, the free induction decay starts at maximum strength (**Fig. A1.1.1b** top), while at an offset frequency of 200 kHz, the intensity of free induction decay is almost negligible (**Fig. A1.1.1b** bottom). Therefore, by using a 90^{o} rectangular pulse, only a small portion of the broad spectrum can be excited as indicated by the red highlighted region in **Figure A1.1.1c**, and would not provide complete information on the lineshape of the spectrum. Therefore, an advanced pulse manipulation technique is necessary for broadband excitation.

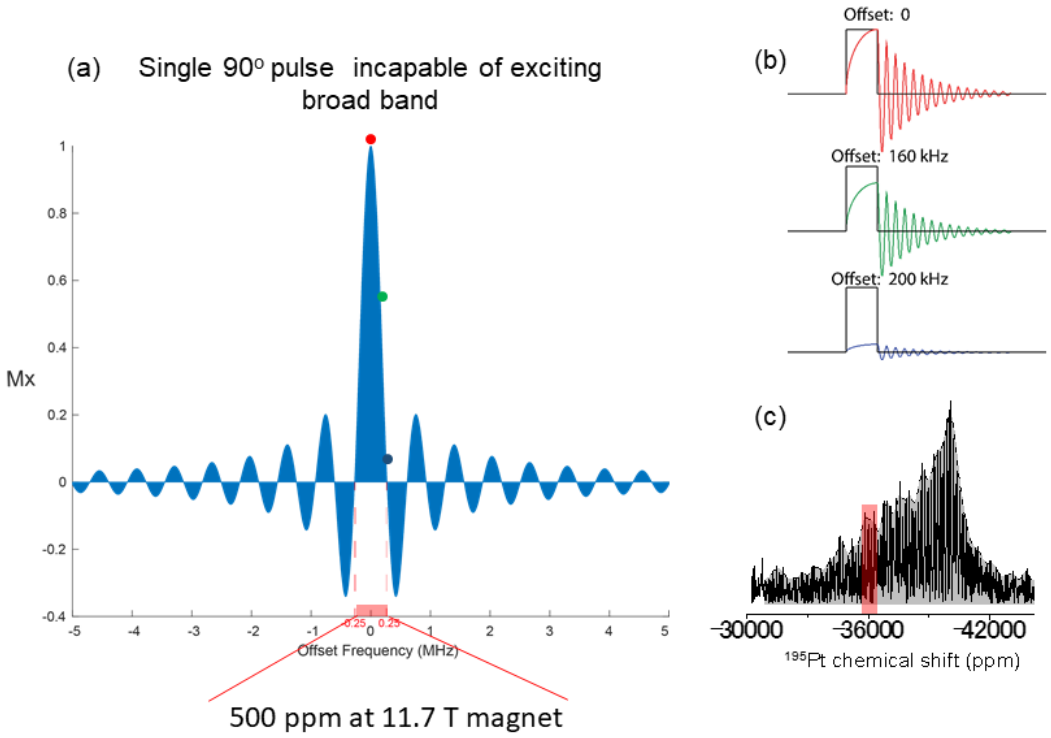

Figure A1.1.1. (a) Excitation profile of 90° rectangular pulse, (b) Free induction decays of 90° rectangular pulse at three different offset frequencies, 0, 160, and 200 kHz indicated by red (top), green (middle), and blue (bottom) respectively. (c) 90° rectangular pulse can excite only the red-highlighted region of the broad ^{195}Pt spectrum obtained from metallic Pt using WURST-CPMG methods.

A1.2 Theory of adiabatic broadband excitation pulses

By applying frequency or amplitude-swept pulses, the nuclear spin magnetization can be manipulated to excite the broadband spectrum. The magnetization vector can be modulated by remaining approximately in alignment with the effective field when the rate of change in the direction of the effective field is slower than the precession frequency. Such manipulation of spin magnetization is known as *adiabatic passage*, or adiabatic magnetization "following" the effective field. To satisfy the adiabatic passage condition, the ratio $\frac{\omega_{eff}}{|d\theta/dt|}$, known as the *adiabacity factor (Q)*, has to be greater than unity.

Magnetization M follows the effective field when $\frac{\omega_{eff}}{|d\theta/dt|} > 1$

$$Q = \frac{\omega_{eff}}{|d\theta/dt|}; \qquad tan\,\theta = \frac{\Omega}{\omega_1}; \qquad \omega_{eff} = (\omega_1^2 + \Delta\omega^2)^{1/2} \;;$$

$$\frac{d\theta}{dt} = \frac{d\arctan\left(\frac{\Omega}{\omega_1}\right)}{dt} = \frac{1}{1+\left(\frac{\Omega}{\omega_1}\right)^2}\left(-\Omega\cdot\frac{1}{\omega_1^2}\frac{d\omega_1}{dt} + \frac{d\Omega}{dt}\cdot\frac{1}{\omega_1}\right) \;;$$

By substituting the $\frac{d\theta}{dt}$ to the first equation 1, the adiabaticity factor can be expressed as:

$$Q = \frac{(\omega_1^2 + \Omega^2)^{3/2}}{\left|\omega_1\frac{d\Omega}{dt} - \Omega\frac{d\omega_1}{dt}\right|}$$

If we look at the denominator of the above equation, two cases can be considered:

1. Constant offset frequency: Ω 2. Constant nutation frequency: ω_1

For each of these two cases to meet the adiabatic inversion (Q ≫1) requirement, the following conditions should be satisfied after substituting $(\omega_1^2 + \Omega^2)^{1/2} = \omega_{eff}$

a. Amplitude- Swept adiabatic passage: b. Frequency-Swept adiabatic passage:

$\left|\Omega\frac{d\omega_1}{dt}\right| \ll (\omega_{eff})^3$ Ω – const $\left|\omega_1\frac{d\Omega}{dt}\right| \ll (\omega_{eff})^3$ ω_1 – const

For Wideband Uniform Rate Smooth Truncation (WURST) pulse, both the nutation frequency and the phase change during the radiofrequency pulse. WURST pulse with such amplitude envelope and phase profile enables to obtain homogeneously excited broadband spectra as can be seen from the excitation profile of a 100 μs WURST pulse in **Figure A1.2.1c**.

By solving the Bloch equation expressed as Ordinary Differential Equation (ODE), the excitation profiles of a 90^o pulse, Chirp pulse with phase modulation, and WURST pulse with both phase and amplitude modulation are plotted in **Figure A1.2.1**. The

Bloch equation is a classical equation that describes the magnetization vector. The Bloch equations describe analytical solutions to the evolution of the bulk magnetic moment in a magnetic field.

$$\frac{dM_X}{dt} = -\Omega M_y(t) + \omega_1 sin\phi M_Z(t) - R_2 M_X(t)$$

$$\frac{dM_y}{dt} = \Omega M_x(t) - \omega_1 cos\phi M_Z(t) - R_2 M_y$$

$$\frac{dM_z}{dt} = \omega_1 [-sin\phi M_x t + cos\phi M_y t] - R_1[M_z t - M0]t$$

Here,

Ω – offset frequency

ω_1 – frequency of the radiofrequency pulse

ϕ – phase of the radiofrequency pulse

t – time during the pulse

M_x, M_y, M_z – magnetization in x, y, z direction

R_1, R_2 – longitudinal and transverse relaxation constants

The second terms in M_x and M_y equations cancel, since we are interested in M_x and M_y *after* the pulse (i.e. $\omega_1 = 0$) Thus, we left with 2 coupled first order ODEs, that can be solved with given Initial Conditions. Longitudinal and transverse relaxation constants (R_1, R_2) are assumed to be negligible during the pulse based on the order of magnitude differences in timescale of the relaxation and the pulse duration.

While 90º pulse can excite only small portion of the broad spectrum (**Fig. A1.2.1a**), both Chirp and WURST pulses are capable of exciting broader range (**Fig. A1.2.1b and c**). However, by modulating both pulse amplitude and phase, WURST can smoothly excite the broader range compared to Chirp pulse.

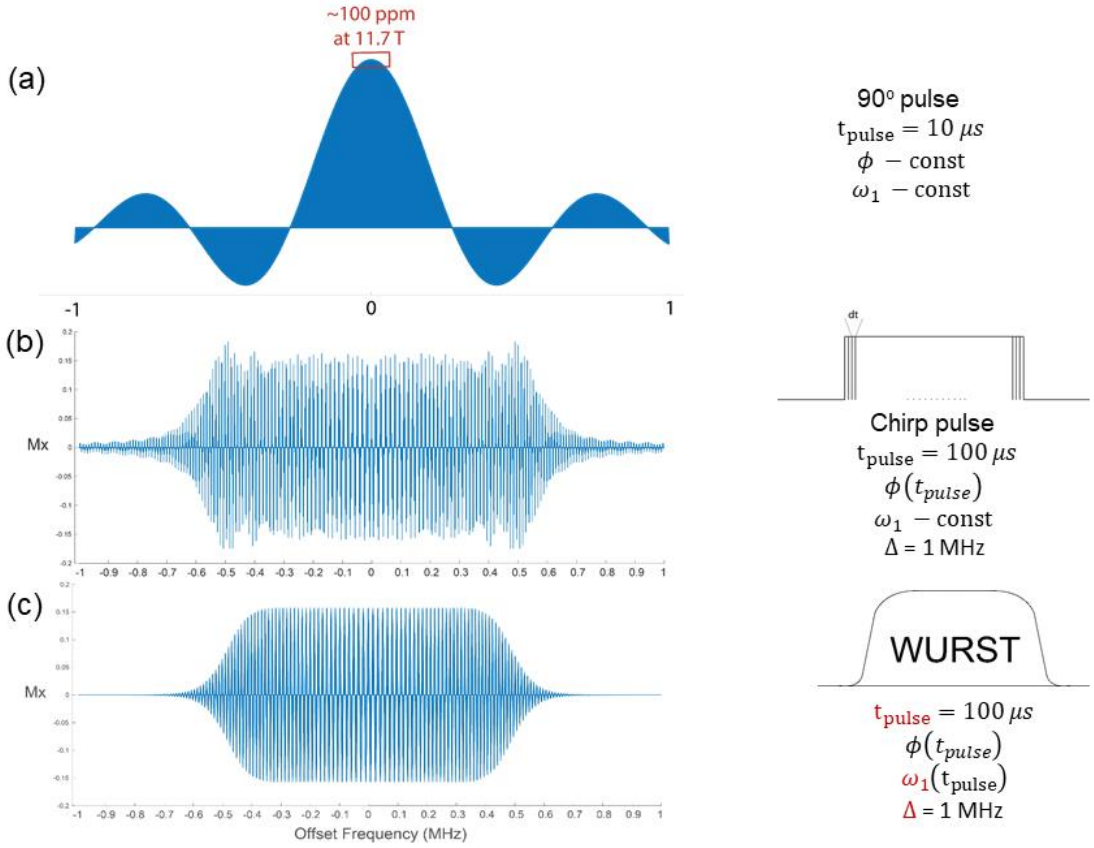

Figure A1.2.1. Comparisons of excitation profiles of (a) 10 µs 90° y pulse, (b) 100 µs Chirp pulse with phase modulation, and (c) 100 µs WURST pulse with 1 MHz sweep width. Each profile is created by Matlab simulation by solving the ODE equation with conditions listed for each pulse

Phase and amplitude of the WURST pulse vary with time during pulse as follows:

$$\phi(t) = 2\pi\left[\left(\Omega + \frac{\Delta}{2}\right)t - \frac{1}{2}\left(\frac{\Delta}{t_{pulse}}\right)(t)^2\right]$$

Sweep Range: Δ [Hz]

$$\omega_1(t) = \omega_{max}\left(1 - \left|\cos\left(\frac{\pi t}{t_{pulse}}\right)\right|^N\right)$$

N – power index

Optimization process of the WURST pulses involve finding the optimum values in the equations, e.g., pulse length t_{pulse}, maximum pulse power ω_{max}, power index N, and sweep range *Δ.*

A1.3 Optimization of ^{195}Pt WURST-CPMG experiments

To acquire broadband spectrum WURST pulse is used with Carr-Purcell Meiboom-Gill (CPMG) to collect as many echo trains as possible. To optimize parameters that result in the highest signal-to-noise ratio spectrum with the lowest number of scans, the following values, and experimental conditions should be carefully considered

- ***Δ*** *- sweep Range*
- $\boldsymbol{t_{pulse}}$ *- pulse length*
- ***N*** *– power index*
- $\boldsymbol{\omega_{max}}$ *– maximum pulse power*
- ***Echo duration****:* too short a value will result in truncation of the echo signal, but too long echo duration will result in an unnecessary increase in noise and a decrease in the number of echo trains
- ***Numbers of echo****:* cutting the number of echoes before full decay will decrease the S/N, but collecting too many echos will result in the unnecessary collection of noise
- ***Relaxation delay vs temperature:*** Low-temperature measurements increase S/N due to larger Boltzmann distributions and decreased thermal noise. Also, for extremely fast relaxing species, which is the case for metallic ^{195}Pt moieties, the cryogenic temperature is beneficial due to higher T_1 relaxation time at lower temperatures which enables to implement broadband excitation methods.

However, one should be careful when choosing the experiment temperature for optimum S/N. Firstly, T_1 is longer at lower temperatures, meaning that the relaxation delay of each scan needs to be longer which can result in a longer experimental time. Secondly, tuning dips of probes usually narrow at lower temperatures, meaning that one might not be able to acquire the broad spectrum at one offset frequency resulting in collection of multiple mosaics for full lineshapes

- ***Choice of probe:*** Not all probes are created equally, *i.e.*, some probes are more sensitive than others due to different arrangements of the electronics, and have broader tuning dips that enable to acquire broad spectrum. One should approach carefully by conducting a series of experiments on available different probes before simply following the theoretical equation to maximize S/N as shown below, *e.g.*, using a probe that is compatible with a magnet at a higher B_0 and capabilities to be used at lower temperatures.

$$\frac{S}{N} = \mathrm{K}\frac{NB_0^{3/2}}{T}\sqrt{NS}$$

where K – constant, B_0 – the strength of the external magnetic field, T- the temperature in K, NS – number of scans.

In more elaborate terms, signal to noise ratio is described as:

$$\frac{S}{N} = \frac{N\gamma_e\gamma_d^{3/2}B_0^{3/2}K}{\sqrt{\Delta\mathrm{f}(T_cR_c + T_a[R_c + R_s] + T_sR_s)}}$$

Noise comes from thermal noise and the noise in the rf coil and preamplifier.

N – number of observed nuclei in the sample- defined by the rotor size, natural abundance of the nuclei, and concentration of the element in the sample – for solid state NMR

γ_e, γ_d- gyromagnetic ratios of excited and detected nuclei, respectively

B_0 – static magnetic field strength

K− factor dependent on the coil

Δf – receiver bandwidth (Hz)

R_c – coil resistance, T_c - coil temperature

T_s – sample temperature, T_a – noise temperature of the preamplifier

R_S - resistance induced by the sample

Resolution of NMR signal linearly increases with B_0, sensitivity increases with $B_0^{3/2}$ Signal averaging longer will increase the S/N ratio as explained in the below equation.To simply explain the equation, noise is random, thus it will increase with $\sqrt{N_s}$. Signal is not random, and it increases linearly with N_s. Overall, S/N ratio increases with $\sqrt{N_s}$. Therefore, increasing the number of scans 16 times, for example, will increase the S/N ratio by a factor of 4.

S/N ratio per unit acquisition time:

$$S/N \propto \frac{N}{T^{3/2}}\ Q\ \gamma^{5/2}\ B_0^{3/2} T_2^{1/2} \left(\frac{t_{max}}{T_c}\right)^{1/2}\ N_s^{1/2}$$

N -number of nuclear spins, T – temperature, Q – coil quality factor, γ – gyromagnetic ratio of the detected nuclei, B_0 – magnetic field, T_2 – relaxation time of the nuclei, T_c - total time between acquisition: pulse length time + recycle delay time

- ***Decoupling ^{1}H or CP (BRAIN-CP)**:* To enhance the signal, decoupling of ^{1}H and/or using cross-polarization (known as BRAIN-CP for broadband CP) should be considered depending on the sample, *e.g.*, a presence of nearby ^{1}H species to ^{195}Pt

- ***Use of Dynamic Nuclear Polarization with BRAIN-CP**:* DNP is a powerful method to enhance the signal, and it has been shown that DNP can be used to enhance broadband ^{195}Pt signal as discussed in the Introduction section of this dissertation. However, not all samples are suitable for DNP measurements, which

exogenously introduces radical species in a solvent. For example, introducing solvent into reduced Pt-zeolite samples will change the local environments of reduced Pt species, which are often times the active sites of interest. Moreover, commonly used biradicals are too bulky to penetrate the pores of the zeolites, inhibiting the signal enhancements from species residing inside the zeolite cages.

TOPSPIN has a built-in feature that enables one to create adiabatic WURST pulses with varying parameters, *e.g.,* pulse length, amplitude power factor, etc. As an example, two WURST pulses with different power factors are shown in **Figure A1.3.1**. Once generated, these pulses can be saved and used for WURST-CPMG experiments by recalling the name of the created pulse.

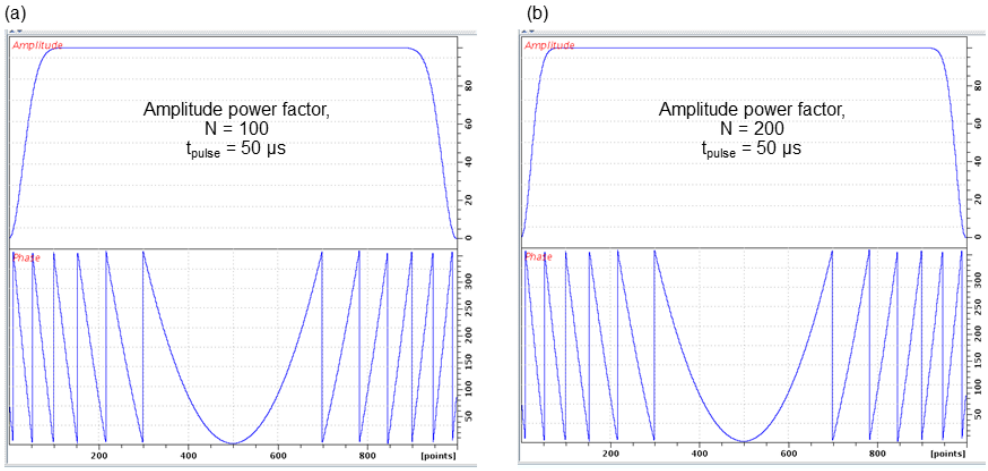

Figure A1.3.1. WURST pulses generated by TOPSPIN (a) amplitude factor N = 100, pulse length = 50 µs, (b) amplitude factor N = 200, pulse length = 50 µs.

As mentioned above, the choice of probe is crucial before setting up a long experiment. As an example, **Figure A1.3.2a** shows a tuning dip of a 7 mm HX probe compatible with 300 MHz instrument (7 T) available at the MRL facility of UCSB. The tuning dip is so narrow, such that it is not capable of exciting the entire lineshape of

the ^{195}Pt spectrum of Pt tetraamine salt. ^{195}Pt WURST-CPMG spectrum at two different offset frequencies is shown in red and blue in **Figure A1.3.2b**.

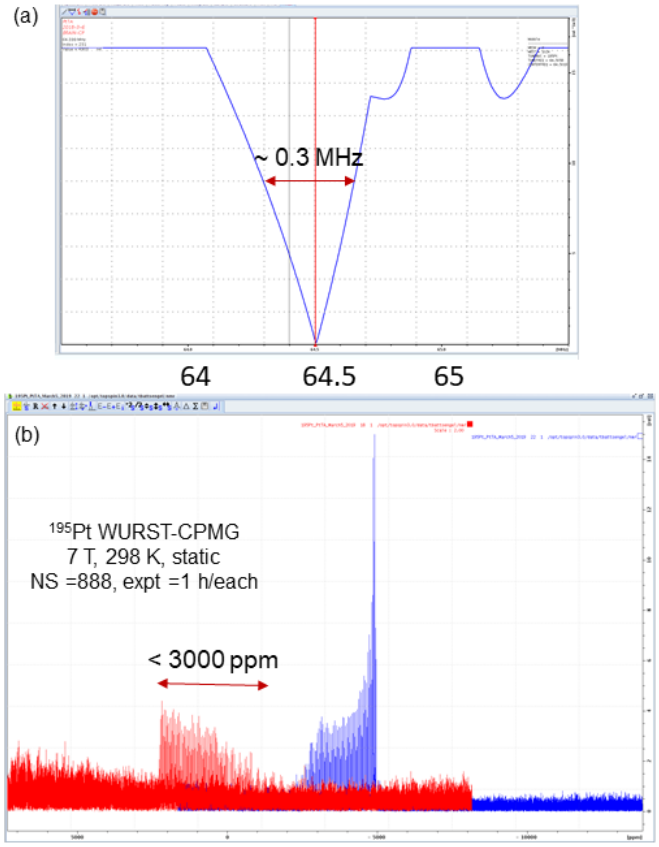

Figure A1.3.2. (a) Tuning dip of the 7 mm HX probe for 7 T magnet. The narrow tuning dip only allows to excite ~3000 ppm of the broad spectrum. Each spectrum in red and blue is acquired for ~1 h.

In comparison, the 7 mm HX probe compatible with the 500 MHz instrument (11.7 T) of the MRL facility at UCSB has a much broader tuning dip as depicted in **Figure A1.3.3**, which can excite the entire spectrum of ^{195}Pt tetraamine salt at one offset frequency. Although lower field (7 T vs 11.7 T) can be beneficial for broad CSA, *i.e.*, CSA is narrower at lower field, the much better performing probe available for 11.7 T was used for the following ^{195}Pt NMR measurements.

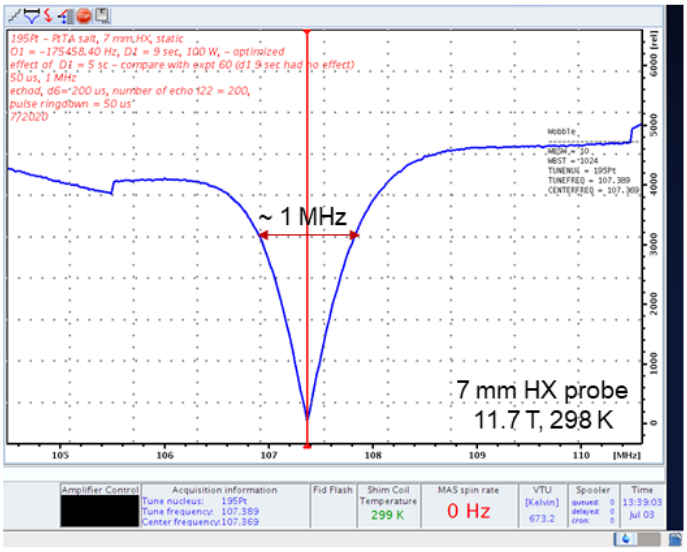

Figure A1.3.3. Tuning dip of the 7 mm HX probe for 11.7 T magnet.

After choosing the best performing probe available, the first parameter that needs to be optimized is the power of the WURST pulse. **Figure A1.3.4** shows the ^{195}Pt spectra using different pulse powers. Each spectrum took 17 minutes with only one sweep. While optimizing the power, one should keep an eye on the percent of the reflected power. Too much power results in reflected power that can damage the coil of the probe. The best power for ^{195}Pt tetraamine salt was found to be 100 W.

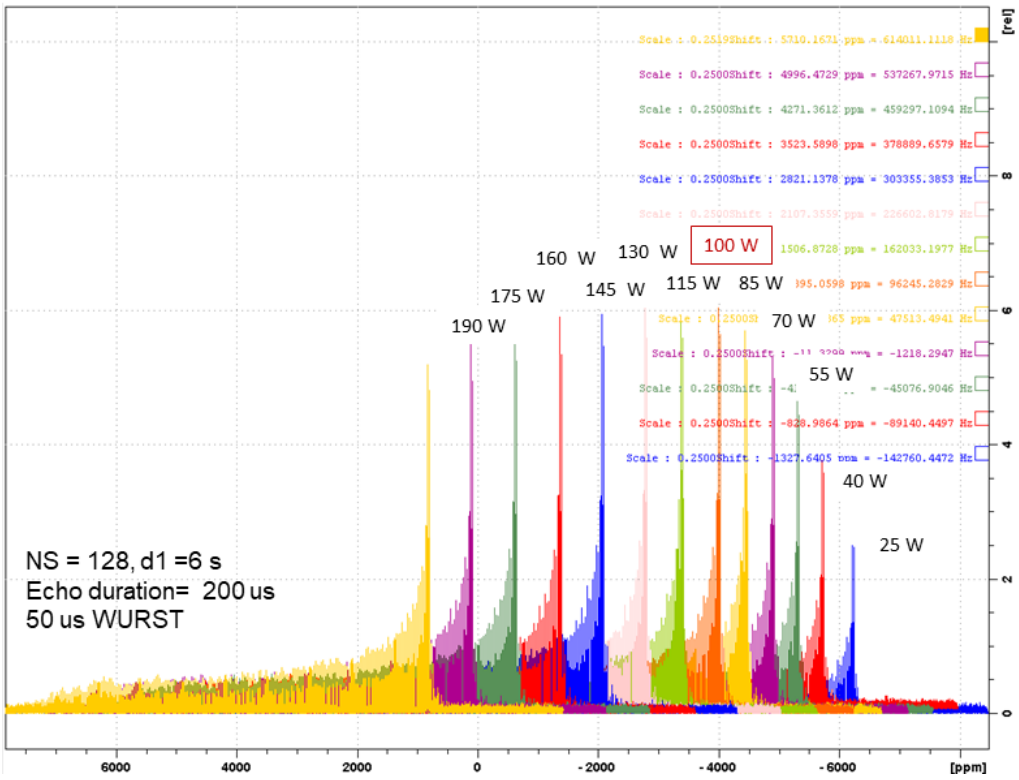

Figure A1.3.4. Optimization of WURST-CPMG pulse power.^{195}Pt NMR spectra of $Pt(NH_3)_4Cl_2$ each acquired in 17 minutes with one sweep at 11.7 T, room temperature, with 7 mm HX probe. Recycle delay, D1 = 6 s, WURST pulse length = 50 µs, WURST pulse sweep width = 1 MHz, Echo duration = 200 µs To show the intensity differences between the lineshapes, each spectrum is manually separated, hence the chemical shift values do not correspond to that of $Pt(NH_3)_4^{2+}$.

Next, the duration of the echo needs to be optimized. Too short echo duration results in truncation of the signal, but too long echo duration results in an unnecessary increase in noise, which can decrease the number of echo trains that can be acquired. **Figure A1.3.5**. shows examples of ^{195}Pt spectra at two different echo duration. After optimization, 200 µs echo duration was found to be optimum.

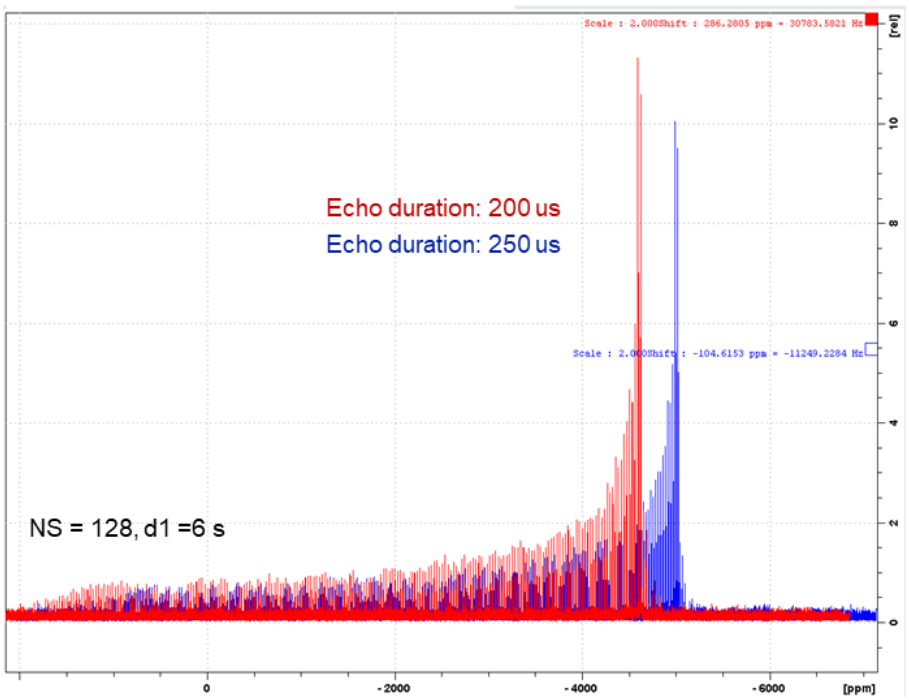

Figure A1.3.5. Optimization of echo duration of WURST-CPMG pulse.^{195}Pt NMR spectra of $Pt(NH_3)_4Cl_2$ each acquired in 17 minutes with one sweep at 11.7 T, room temperature, with 7 mm HX probe. Recycle delay, D1 = 6 s, WURST pulse length = 50 µs, WURST pulse sweep width = 1 MHz, WURST pulse power = 100 W. To show the intensity differences between the two lineshapes, each spectrum is manually separated, hence the chemical shift values do not correspond to that of $Pt(NH_3)_4^{2+}$.

The number of echoes that can be collected needs to be optimized for each sample as well. **Figure A1.3.6** shows the echo trains of the ^{195}Pt WURST-CPMG experiment. In the zoomed subset, each echo with 200 µs is shown, which is just the right length to include the entire echo without extending too much to include unnecessary long noise regions. 200 echo trains are collected, which was based on the signal strength at the end of the last echo. Less than 200, for example 100 echo trains will truncate

the available echo trains that can be collected, but more than 200 echo trains will just acquire more noise.

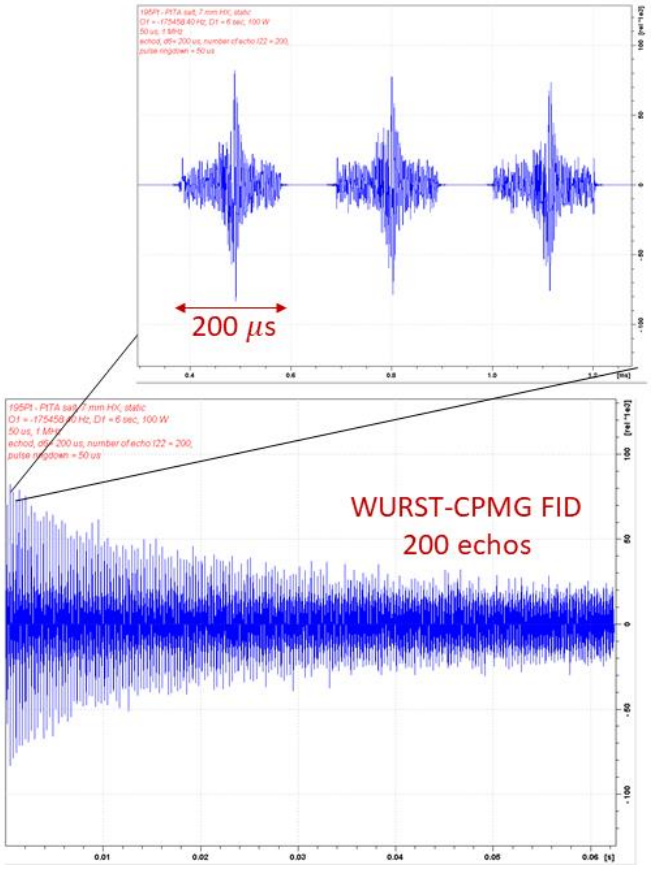

Figure A1.3.6. WURST-CPMG echo trains. 200 echos with each echo length of 200 μs are collected. Three echos are shown in a zoomed subset.

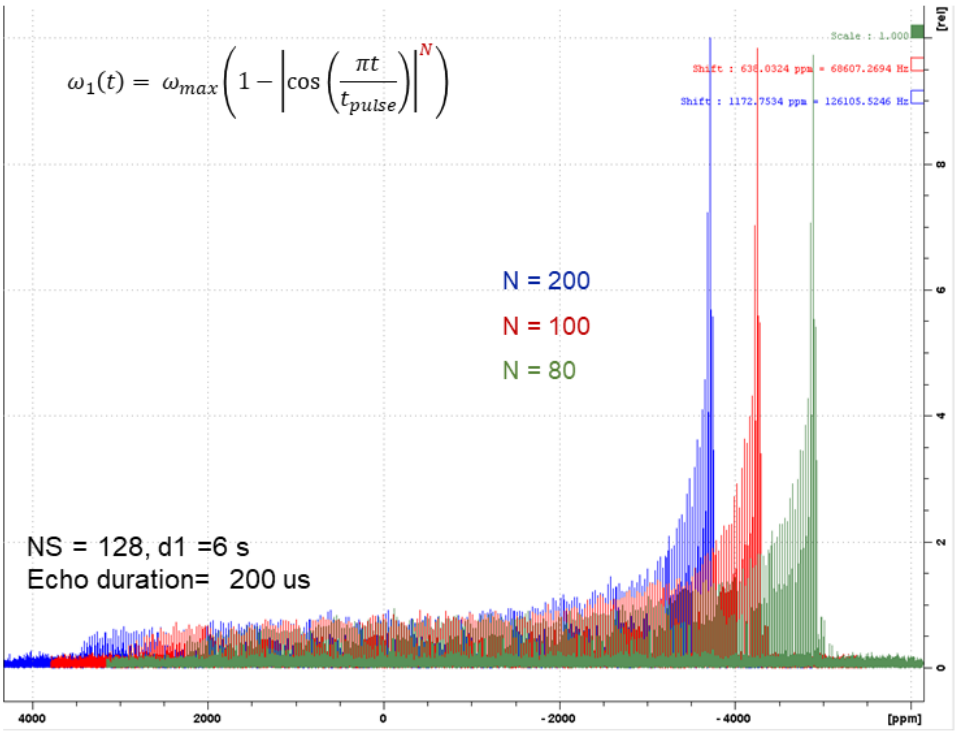

Figure A1.3.7. Optimization of amplitude factor, N, of WURST-CPMG pulse. ^{195}Pt NMR spectra of $Pt(NH_3)_4Cl_2$ each acquired in 17 minutes with one sweep at 11.7 T, room temperature, with 7 mm HX probe. Recycle delay, D1 = 6 s, Echo duration = 200 µs, WURST pulse length = 50 µs, WURST pulse sweep width = 1 MHz, WURST pulse power = 100 W. To show the intensity differences between the three lineshapes, each spectrum is manually separated, hence the chemical shift values do not correspond to that of $Pt(NH_3)_4^{2+}$.

Finally, after optimization of all the parameters, a longer experiment with higher numbers of scans should be collected for a higher S/N spectrum that can provide definite lineshapes, which can be used for structural analyses. **Figure A1.3.8** shows the ^{195}Pt WURST-CPMG spectrum of $Pt(NH_3)_4Cl_2$ acquired in 35 minutes at room temperature. These parameters are a good starting point for measuring ^{195}Pt species in Pt-zeolites that have similar local environments at Pt tetraamine salt, *e.g.,* Pt^{2+}

cations coordinated with four-oxygen atoms of the zeolite lattice. For metallic Pt species, these experimental conditions were unfeasible, likely due to extremely fast relaxing metallic ^{195}Pt moieties. Therefore, to measure ^{195}Pt NMR of metallic Pt moieties, it is recommended to use cryogenic temperature (preferably liquid He temperatures) to acquire broadband ^{195}Pt spectrum. For such measurements, all these parameters need to be optimized for higher sensitivity and lower experimental time possible.

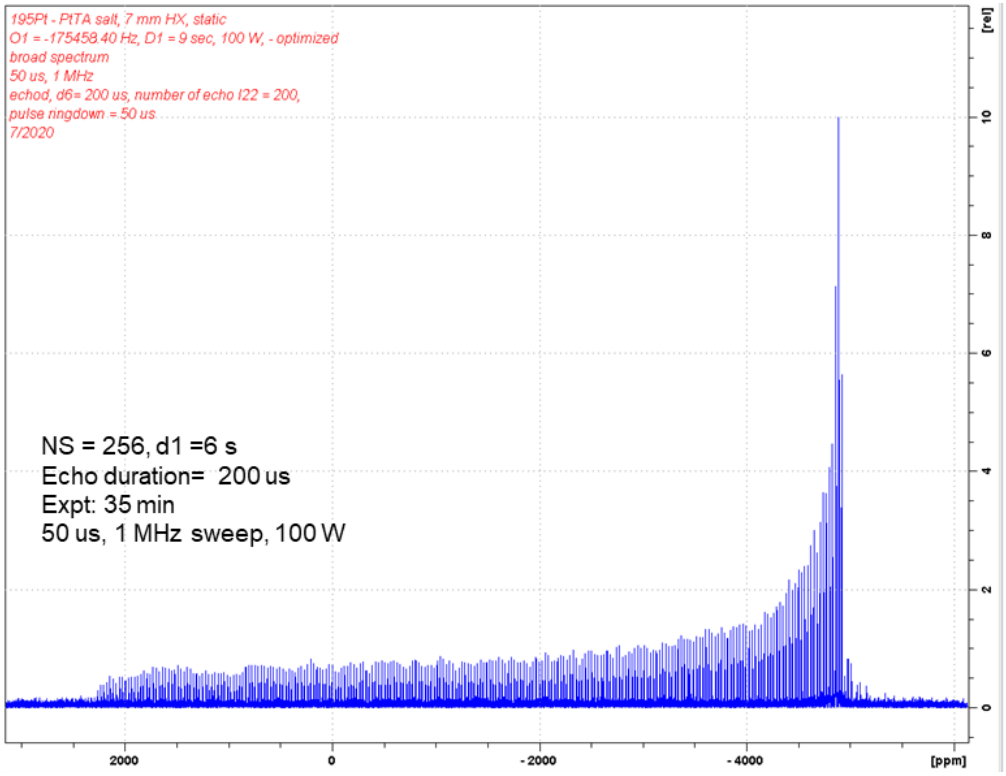

Figure A1.3.8. Optimized ^{195}Pt NMR spectrum of $Pt(NH_3)_4Cl_2$ acquired in 35 minutes with one sweep at 11.7 T, room temperature, with 7 mm HX probe. Recycle delay, D1 = 6 s, Echo duration = 200 µs, WURST pulse length = 50 µs, WURST pulse sweep width = 1 MHz, WURST pulse power = 100 W, WURST pulse amplitude factor N = 200.

A1.3.1. Matlab programs used to simulate excitation profiles

Matlab Software was used to solve the system of ODEs from the Bloch equation with an initial condition of $[M_x, M_y, M_z] = [0, 0, 1]$ and obtained M_x at the end of the pulse at different offset frequencies.

Here is the step-by-step process of the construction of the Matlab code:

1. Define constants:
    - time: pulse length in seconds
    - R2, R1 : relaxation constants (can be assumed to be zero during the pulse)
    - W1 = pi/(2*time): amplitude of the 90 degree rf pulse
    - Phi = pi/2: phase of the pulse, which is 90 for a rectangular pulse
    - Offset_range: range of offset
2. Prepare empty vectors for M_x, M_y, M_z, $M_{transverse}$ with size of the offset frequency range to store each value of the calculated magnetization for each offset frequency

```
Mx_av = zeros(1,offset_range);
My_av = zeros(1,offset_range);
Mz_av = zeros(1,offset_range);
Transverse = zeros(1,offset_range);
```

3. Create **for** loop index **ii** which counts from 1 to the defined offset_range
4. Define a system of ODEs as a matrix **f** with a dimension of [3x1], which is a function of time during the pulse, and magnetization vectors.

$$\boldsymbol{f} = \begin{bmatrix} -Omega * M(2) + w1 * \sin(Phi) * M(3) - R2 * M(1) \\ Omega * M(1) - w1 * \cos(Phi) * M(3) - R2 * M(2) \\ w1 * \big(-\sin(Phi) * M(1) + \cos(Phi) * M(2)\big) - R1 * (M(3) - M0) \end{bmatrix}$$

   Here M(1), M(2), M(3) correspond to M_x, M_y, M_z, respectively. M0 = 1, for initial z magnetization.

5. Solve the system of ODEs using a Matlab built-in ODE solver **ode45** function for each offset frequency, which is denoted as Omega.

*Omega is defined as ii – 1 because the loop counter cannot start from 0, but I want my offset frequency to start from 0.

6. Find the magnetization value at the end of the pulse
    - Solution of the ode45 is a [nx3] (n is automatically defined by Matlab) matrix denoted as **Ma** with each column as a series of numerical solutions of each variable, in my case Mx, My, and Mz. For the excitation profile, I only care about the magnetization value at the end of the pulse, thus the last values of these columns are of my interest. I got the last values of each column and stored them into the vector created in step 2.

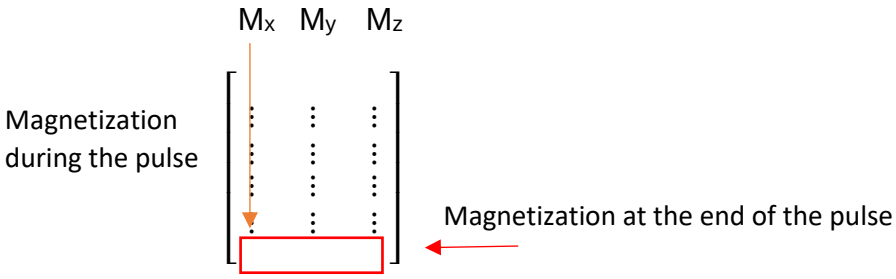

Ma(:,1) is the first column - solution for Mx

Ma(:, 2) is the second column – solution for My

Ma(:, 3) is the third column – solution for Mz

- Since the size of the above matrix is automatically created, I had to find the size of the matrix.

```
[mx,nx]= size(Ma(:,1));
[my,ny]= size(Ma(:,2));
[mz,nz]= size(Ma(:,3));
```

7. Knowing the size of the matrix Ma, I can now extract the magnetization values at the end of each column and store these values in the vector created in step 2.

```
Mx_av(ii) = Ma(mx,1);
My_av(ii) = Ma(my,2);
Mz_av(ii) = Ma(mz,3);
```

8. Steps 4-7 will be repeated until the for loop ends. Now, initially, 0-filled Mx_av, My_av, and Mz_av vectors will be filled with solutions of the ODEs for each offset frequency.

9. Finally, excitation profiles are plotted by:

```
figure
plot( Mx_av);
xlabel('Offset Frequency (Hz)');
ylabel('Mx');
figure
hold on
```

My_av and Mz_av plots can be also plotted to satisfy the curiosity.

The full for loop is shown below:

```
for ii = 1:offset_range
    Omega = ii-1;
    f = @(t,M)[-Omega*M(2)+ w1*sin(Phi)*M(3)-R2*M(1); Omega*M(1)- w1*cos(Phi)*M(3)-R2*M(2);w1*(-sin(Phi)*M(1)+cos(Phi)*M(2))-R1*(M(3)-M0)]
    [t, Ma] = ode45(f, tspan, [0 0 M0]) ;
    [mx,nx]= size(Ma(:,1));
    [my,ny]= size(Ma(:,2));
    [mz,nz]= size(Ma(:,3));
    %%Finding Expectation values of Mx, My, Mz (at the end of the pulse)
    Mx_av(ii) = Ma(mx,1);
    My_av(ii) = Ma(my,2);
    Mz_av(ii) = Ma(mz,3);
    Transverse(ii) = sqrt(Mx_av(ii)^2+My_av(ii)^2);
    if ii == 1      % to plot the evolution of Mx during the 90 pulse in Figure 1
        figure
        plot(t, Ma(:,1),'o-', t, Ma(:,2),'-.', t, Ma(:,3),'m');
        legend('Mx','My','Mz')
        xlabel('time)');
        ylabel('Magnetization buil-up during pulse when offset = 0');
        hold on
    end
end
```

this part is supplemental
Plots the magnetization build up during the pulse when offset frequency is 0

Simulation of CHIRP pulse:

When solving the equation in Matlab using **ode45**, I can still use the same tricks to obtain the magnetization at the end of the pulse I explained on page 3. However, this time I will need two types of zero-filled vectors, and two hierarchical for loops instead of the one I used for the 90^{o} pulse excitation profile.

- One to store the solution for each slice of the pulse: Mx_av = zeros(1, n_slice)
- One to store magnetization at the end of the pulse for each offset frequency:

  Mx_end = zeros(1, offset_range)

There are 2 for loops in this simulation,

- The first for loop (inner loop) with a loop counter ***ii***, which varies from 1 to n_slice. In this loop, the Bloch equation is solved for each slice with a small-time length of t_chirp/n_slice. It is important to carefully define the initial conditions for each slice in this loop. The final value of the magnetization in slice number N is the initial value of the magnetization in slice number N+1.

At the end of the inner for loop, the initial values of Mx, My, and Mz, which are denoted as Mx0, My0, and Mz0, respectively, are set to the final values of the solution of the ODEs calculated for this slice before proceeding to the next slice.

```
Mx0 = Ma(mx,1);
My0 = Ma(my,2);
Mz0 = Ma(mz,3);
```

- The second for loop (outer loop) with a loop counter ***j***, which varies from 1 to offset_range.

After the inner loop ends, initial values have to be reset back to [Mx, My, Mx] = [0,0,1] before the calculation starts at each new offset frequency, and the magnetization value of the very end of the long CHIRP pulse is stored in Mx_end vector for corresponding offset frequency.

```
for j = 1:200:offset_range
    Omega = j-1;
    M0 = 1;
    Mx0 = 0;
    My0 = 0;
    Mz0 = M0;
    N = 20;
    for  ii = 1:n_slice;
         dtime = t_chirp/n_slice;      % Equally spaced time interval
         Phi = 2*pi*((Omega+del/2)*(ii*dtime)-0.5*(del/t_chirp)*(ii*dtime)^2);

         tspan = [0 dtime];
         f = @(t,M)[-Omega*M(2)+ w1*sin(Phi)*M(3)-R2*M(1);
                    Omega*M(1)- w1*cos(Phi)*M(3)-R2*M(2);
                    w1*(-sin(Phi)*M(1)+cos(Phi)*M(2))-R1*(M(3)
         [t, Ma] = ode45(f, tspan, [Mx0 My0 Mz0]);
         [mx,nx]= size(Ma(:,1));
         [my,ny]= size(Ma(:,2));
         [mz,nz]= size(Ma(:,3));
         % Finding Expectation values of Mx, My, Mz (at the end
         Mx_av(ii) = Ma(mx,1);         % These will become the initial condition of the FID
         My_av(ii) = Ma(my,2);
         Mz_av(ii) = Ma(mz,3);
         Mx0 = Ma(mx,1);
         My0 = Ma(my,2);
         Mz0 = Ma(mz,3);
         % Transverse(ii) = sqrt(Mx_av(ii)^2+My_av(ii)^2);
    end
    if  Omega == 0;
        figure
        plot(Mx_av);
        xlabel('time');
        ylabel('Mx');
        hold on
    end
    Mx_end(j) = Mx_av(ii);
end
```

Initial magnetization values have to be reset back to [0,0,1] for the beginning of each offset frequency

Phase changes during pulse as a function of time during pulse, which is dtime*ii

dtime: length of each slice
ii: slice number

Initial value of the next calculation (Mx0) in the inner for loop is the final value of this calculation Ma(mx, 1)

Note: This code is to simulate excitation profile from 0 offset frequency to the defined offset_range frequency. Considering the –offset_range to 0 offset frequency will be the mirror image of the simulated plot, I showed the full excitation profile of 100 μs long chirp pulse with 1 MHz sweep width in **Figure A1.2.1b.

The main disadvantage of the CHIRP pulse is a sudden switching on and off of the rf field, which can violate the adiabatic conversion. Therefore, in the beginning, and at the end of the CHIRP pulse, the amplitude of the rf frequency can be changed with time in the following manner, for smooth adiabatic departure and ending.

$$\omega_1(t) = \omega_{max}\left(1 - \left|\cos\left(\frac{\pi t}{t_{pulse}}\right)\right|^N\right)$$

Wideband-Uniform-Rate-Smooth-Truncation (WURST) pulse with below amplitude envelope and phase profile enables to overcome the issue of not satisfying the adiabatic condition in the beginning and end of the CHIRP pulse.

The excitation profile of a WURST pulse is very similar to that of the CHIRP pulse. The only difference is the nutation frequency has a time-dependent profile in the WURST pulse, as opposed to being constant in the CHIRP pulse. Since the nutation frequency is changing as a function of time during the pulse, the time-dependent w1 equation is placed along with the time-dependent phase equation. Therefore, I can still use 2 for loops, the same as the CHIRP pulse.

The following code is used for plotting the excitation profile of a WURST pulse, and it took more than 5 hours to simulate the positive half of the excitation profile. (from 0 to offset_range)

```
for j = 1:200:offset_range
    Omega = j-1;
    M0 = 1;                              % initial magnetization
    Mx0 = 0;
    My0 = 0;
    Mz0 = M0;
    N = 20;
    for  ii = 1:n_slice;
         dtime = t_chirp/n_slice;        % Equally spaced time interval
         Phi = 2*pi*((Omega+del/2)*(ii*dtime)-0.5*(del/t_chirp)*(ii*dtime)^2);
         w1 = w1max*(1-abs(cos(pi*ii*dtime/t_chirp))^N);
         tspan = [0 dtime];
         f = @(t,M)[-Omega*M(2)+ w1*sin(Phi)*M(3)-R2*M(1);
                    Omega*M(1)- w1*cos(Phi)*M(3)-R2*M(2);
                    w1*(-sin(Phi)*M(1)+cos(Phi)*M(2))-R1*(M(3)-M0)];
         [t, Ma] = ode45(f, tspan, [Mx0 My0 Mz0]);
         [mx,nx]= size(Ma(:,1));
         [my,ny]= size(Ma(:,2));
         [mz,nz]= size(Ma(:,3));
         % Finding Expectation values of Mx, My, Mz (at the end of the pulse)
         Mx_av(ii) = Ma(mx,1);           % These will become the initial condition of the FID
         My_av(ii) = Ma(my,2);
         Mz_av(ii) = Ma(mz,3);
         Mx0 = Ma(mx,1);
         My0 = Ma(my,2);
         Mz0 = Ma(mz,3);
         % Transverse(ii) = sqrt(Mx_av(ii)^2+My_av(ii)^2);
    end
    if  Omega == 0;
        figure
        plot(Mx_av);
        xlabel('time');
        ylabel('Mx');
        hold on
    end
    Mx_end(j) = Mx_av(ii);
end
```

Both the phase and w1 change during pulse as a function of time during pulse, which is dtime*ii

dtime: length of each slice
ii: slice number

The results have shown that the WURST pulse is capable of exciting a broad range with a homogeneous excitation profile at the center region, which will enable to effectively obtain a broadband spectrum.

Summary

In summary, I was able to show the excitation profiles of a rectangular pulse, CHIRP pulse, and WURST pulse by solving the classic Bloch equation in Matlab.

$$\frac{dM_X}{dt} = -\Omega M_y(t) + \omega_1 sin\phi M_Z(t) - R_2 M_X(t)$$

$$\frac{dM_y}{dt} = \Omega M_x(t) - \omega_1 cos\phi M_Z(t) - R_2 M_y$$

$$\frac{dM_z}{dt} = \omega_1 [-sin\phi M_x t + cos\phi M_y t] - R_1[M_z t - M0]t$$

The following summary table highlights the major differences for calculating the Bloch equation for each pulse.

	90 pulse	***CHIRP pulse***	***WURST pulse***
ϕ *phase*	*const*	$\phi(t_{pulse}) = 2\pi\left[\left(\Omega + \frac{\Delta}{2}\right)t_{pulse} - \frac{1}{2}\left(\frac{\Delta}{t_{pulse}}\right)(t_{pulse})^2\right]$ Sweep Range: Δ [Hz]	$\phi(t_{pulse}) = 2\pi\left[\left(\Omega + \frac{\Delta}{2}\right)t_{pulse} - \frac{1}{2}\left(\frac{\Delta}{t_{pulse}}\right)(t_{pulse})^2\right]$ Sweep Range: Δ [Hz]
ω_1 *Nutation frequency*	*const*	*const*	$\omega_1(t) = \omega_{max}\left(1 - \left\|\cos\left(\frac{\pi t}{t_{pulse}}\right)\right\|^N\right)$ *N – power index*
# of for loops	*1*	*2*	*2*

A1.4 ^{195}Pt DNP BRAIN-CP experiments

The sensitivity of the NMR spectrum can be enhanced by Dynamic Nuclear Polarization (DNP) technique, which relies on irradiating the sample with microwaves at the electron Larmor frequency and transferring the highly polarized electron magnetization to the nuclei. Unpaired electrons, oftentimes biradicals, are exogenously introduced to the solid material by the incipient wetness impregnation method. DNP method is feasible for enhancing broadband signals. As an example, ^{195}Pt DNP spectrum of $Pt(NH_3)^4{}_2Cl_2$ is shown in **Figure A1.4.1.** 16 mMol TEKPol in TCE is used as the biradical. Total signal enhancement was 8, which means that using the DNP method 16 times less amount of time can be used to acquire the same S/N ratio spectrum.

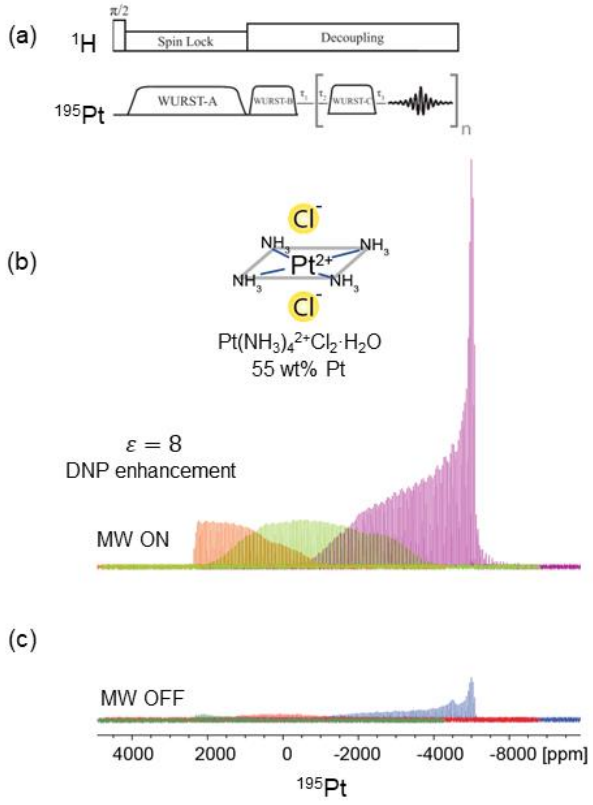

Figure A1.4.1 ^{195}Pt DNP BRAIN-CP spectrum of $Pt(NH_3)^4{}_2Cl_2$ (a) BRAIN-CP pulse sequence, (b) DNP enhanced (MW on) BRAIN-CP, and (c) (MW off) BRAIN-CP spectra of the spectrum of $Pt(NH_3)^4{}_2Cl_2$ acquired at 9.4 T, 100 K, under static conditions, with 16 mMol TEKPol in TCE. Signal enhancement of 8 was achieved by using DNP methods.

References:

(1) Kupce, Ē.; Freeman, R. Stretched Adiabatic Pulses for Broadband Spin Inversion. *Journal of Magnetic Resonance, Series A* **1995**, *117*, 246–256.

(2) Koroleva, V. D. M.; Mandal, S.; Song, Y.-Q.; Hürlimann, M. D. Broadband CPMG Sequence with Short Composite Refocusing Pulses. *Journal of Magnetic Resonance* **2013**, *230*, 64–75.

(3) Harris, K. J.; Lupulescu, A.; Lucier, B. E. G.; Frydman, L.; Schurko, R. W. Broadband Adiabatic Inversion Pulses for Cross Polarization in Wideline Solid-State NMR Spectroscopy. *Journal of Magnetic Resonance* **2012**, *224*, 38–47.

(4) Tannús, A.; Garwood, M. Adiabatic Pulses. *NMR in Biomed* **1997**, *10*, 423–434.

(5) Schurko, R. W.; O'Dell, L. A. QCPMG Using Adiabatic Pulses for Faster Acquisition of Ultra-Wideline NMR Spectra. *Chemical Physics Letters* **2008**, *464*, 97–102.

(6) Slichter, C. P. NMR Study of Pt Catalysts. *Surface Science* **1981**, *106*, 382–396.

(7) Slichter, C. P. The Discovery and Renaissance of Dynamic Nuclear Polarization. *Reports on Progress in Physics* **2014**, *77*, 1–15.

(8) Carvert, T. R.; Slichter, C. P. Polarization of Nuclear Spins in Metals. *Physical Review* **1953**, *92*, 212–213.

(9) Ansermet, J. P.; Slichter, C. P.; Sinfelt, J. H. Solid State NMR Techniques for the Study of Surface Phenomena. *Properties in NMR Spectroscopy* **1990**, *22*, 401–421.

(10) Ansermet, J.-P.; Slichter, C. P.; Sinfelt, J. H. Solid State NMR techniques for the study of surface phenomena. *Progress in NMR Spectroscopy* **1990**, *22*, 401–421.

(11) Rhodes, H.; Wang, P.K.; Stokes, H.; Slichter, C. P. NMR of Platinum Catalysts I. Line Shapes. *Physical Review B* **1982**, *26*, 3559–3569.

(12) Stokes, H. T.; Rhodes, H. E.; Wang, P.-K.; Slichter, C. P.; Sinfelt, J. H. NMR of Platinum Catalysts. III. Microscopic Variation of the Knight Shifts. *Physical Review B* **1982**, *26*.

(13) Rhodes, H. E.; Wang, P.-K.; Makowka, C. D.; Rudaz, S. L.; Stokes, H. T.; Slichter, C. P.; Sinfelt, J. H. NMR of Platinum Catalysts. II. Relaxation. *Physical Review B* **1982**, *26*, 3569–3574.

(14) Bucher, J. P.; Buttet, J.; van der Klink, J. J.; Graetzel, M.; Newson, E.; Truong, T. B. 195Pt NMR Studies of Supported Catalysts. *Colloids and Surfaces* **1989**, *36*, 155–167.

(15) Bucher, J. P.; van der Klink, J. J. Electronic Properties of Small Supported Pt Particles: NMR Study of 195Pt Hyperfine Parameters. *Physical Review B* **1988**, *38*, 11038–11047.

(16) Lucier, B. E. G.; Reidel, A. R.; Schurko, R. W. Multinuclear Solid-State NMR of Square-Planar Platinum Complexes — Cisplatin and Related Systems. *Canadian Journal of Chemistry* **2011**, *89*, 919–937.

(17) Rees, G. J.; Orr, S. T.; Barrett, L. O.; Fisher, J. M.; Houghton, J.; Spikes, G. H.; Theobald, B. R. C.; Thompsett, D.; Smith, M. E.; Hanna, J. v. Characterisation of Platinum-Based Fuel Cell Catalyst Materials Using 195Pt Wideline Solid State NMR. *Physical Chemistry Chemical Physics* **2013**, *15*, 17195.

(18) Appleton, T.; Hall, J.; Ralph, S.; Thompson, C. Reactions of Platinum(I1) Aqua Complexes. 2. 195Pt NMR Study of Reactions between the Tetraaquaplatinum(II) Cation and Chloride, Hydroxide, Perchlorate, Nitrate, Sulfate, Phosphate, and Acetate. *Inorganic Chemistry* **1984**, *23*, 3521–3252.

(19) Kobayashi, T.; Perras, F. A.; Goh, T. W.; Metz, T. L.; Huang, W.; Pruski, M. DNP-Enhanced Ultrawideline Solid-State NMR Spectroscopy: Studies of Platinum in Metal-Organic Frameworks. *J. Phys. Chem. Lett* **2016**. 7, 2322–2327.

A2. Design of an NMR probe head for direct detection of ^{195}Pt NMR

Using the pulse technique mentioned in section A1.2, the feasibility of direct detection of ^{195}Pt was proved on the reference PtO_2 sample. The commercial Bruker NMR probe with a 3.2 mm diameter rotor and temperature of 94 K was used to obtain the ^{195}Pt NMR of PtO_2 within 5 minutes of signal averaging. (**Fig. A.2.1**). However, due to a dilute amount (<1 wt%) of Pt in Pt-zeolite industrial catalysts, signal averaging for 15 hours using the same experimental condition as the PtO_2 showed no signal. Based on the back-of-the-envelope calculation that shows the feasibility (within 3 hours, **Table A2.1**) of obtaining an NMR signal with the same signal-to-noise ratio as the spectrum 7a from the Pt-zeolite catalyst, I was motivated to build an NMR probe-head, which can function at low temperature (liquid He temperature of T ~ 4 K) and have large sample holder (diameter 1cm, length 1.5 cm). It was estimated based on the equation that correlates signal-to-noise ratio to the number of scans (NS), which linearly relates to the experimental time, applied magnetic field (B_o), temperature (T), and a number of nuclei (N) in the sample. $\frac{S}{N} \propto \frac{NB_0^{3/2}}{T}\sqrt{NS}$

Table A2.1: Estimated exp. time of ^{195}Pt NMR at two different experimental conditions

	Commercial 3.2 mm MAS Bruker Probe 94 K, 40 µL	Home-made Probe 20 K, 0.6 mL
PtO_2	5 min	< 1 sec
1 wt% Pt-zeolite	2 years	3 hours

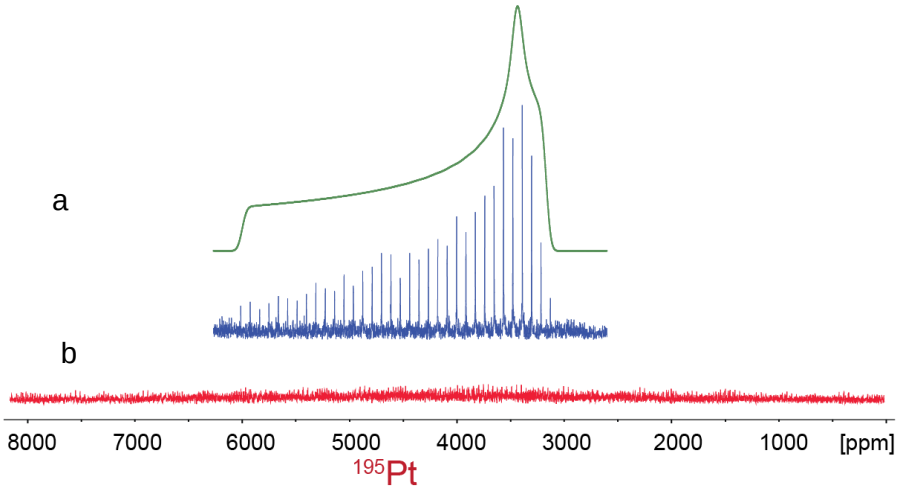

Figure A2.1: ^{195}Pt NMR of a. PtO_2; exp. time: 5 min b. 1 wt% Pt-zeolite; exp. time: 15 hours. The spectra are acquired at 9.4 T, 90 K, static conditions using WURST-CPMG pulse

The efficiency of an NMR experiment is determined by how well the probe can transfer the energy into and out of the sample. The efficient transmission line NMR probehead design[36] has local tuning and matching circuit at the sample end and remote tuning and matching capacitors at the other end, which can be easily accessible to tune and match when the sample end is submerged in liquid helium bath (Fig 16). For successful tuning and matching the circuit impedance has to match with 50 Ω, the impedance of the preamplifier of the NMR instrument.

The impedance of a circuit has resistive (R) and reactive parts (I).

$$Z = R + iI$$

Both capacitors and inductors have reactive impedances ($Z_L = i\omega L$; $Z_C = -i\frac{1}{\omega C}$) with a small amount of internal resistive part. An NMR coil is a homemade copper solenoid with a certain number of turns, length, and diameter for the desired inductance for tuning. The inductance L in μH is expressed as $L = \frac{0.4n^2r^2}{9r+10x}$. Here, n- number of turns,

r – inner diameter in cm, x – length of the coil in cm. The transmission line behaves as an impedance transformer; whether the one end of the transmission line acts as inductive or capacitive depends on the length of the transmission line. If the length is chosen as half of the wavelength, only the resistive part of the transmission line can be considered. The resistive part of the transmission line at one end is: $Z_0 = \frac{60}{\sqrt{\epsilon}} \ln\left(\frac{a}{b}\right)$. Here, a and b are the inner diameter of the outer tube and the outer diameter of the inner tube, respectively. The ratio a/b of the constructed probe is 3.5, and ϵ is the dielectric constant, which is 1 for air. Inner and outer conductors are separated by air dielectric (with Teflon spacers) to minimize dielectric loss. Knowing all the impedance relations of inductors, capacitors, and transmission line, the appropriate value of capacitors (C_{tuning}, $C_{matching}$) and inductance (L) can be calculated to tune to the desired frequency and match to 50 Ω; *i.e.* the total impedance of the probe has zero imaginary part and 50 Ω real part.

The probe will be situated in a vacuum-insulated cryogenic dewar, which can fit inside a wide bore NMR magnet. The dewar (Oxford Instruments) has a temperature sensor and a flow controller for liquid He. The aluminum flange with an O-ring seal holds the probe on top of the cryogenic dewar.

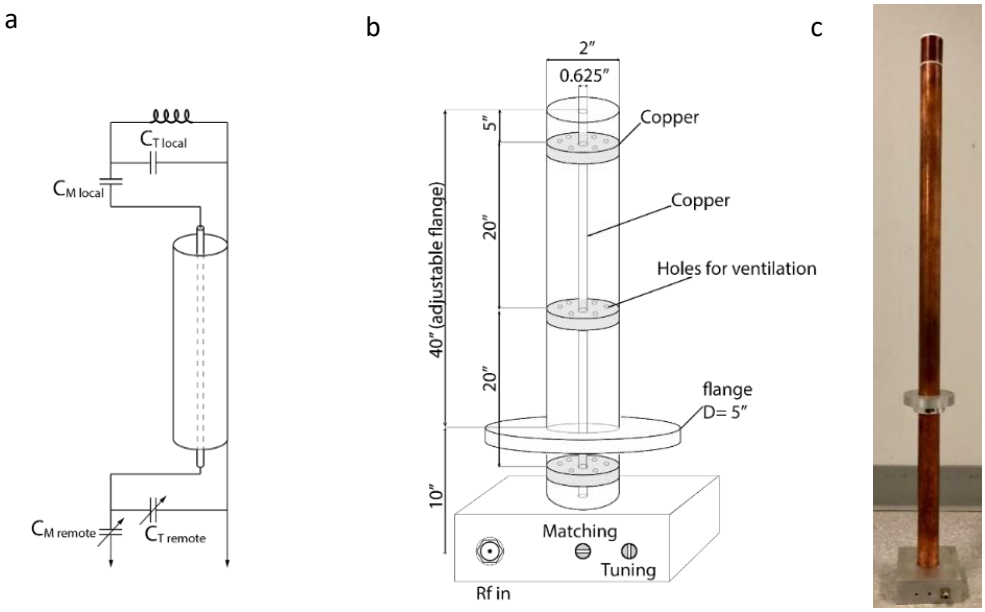

Figure A2.2: Design of a ^{195}Pt NMR probe head. a. Electric circuit design of a single resonance transmission line NMR probe head, known as the “McKay design”, which has both local and remote tuning and matching capacitors. b. Dimensions of transmission line, Teflon spacer, and the flange. c. current construction state of the NMR probe.

A3. Dynamic behavior of Pt catalysts in the native oxide layer of Al nanocrystals: exposing uniform atomically dispersed species via strong metal-support interactions: solid-state ^{27}Al NMR studies

A3.1 Introduction

Controlling the nuclearity, uniformity, and local environment of supported metal species is critical for tuning the reactivity and selectivity of heterogeneous catalysts and mechanistic studies. Recent efforts have focused on developing synthetic approaches for preparing atomically dispersed precious metal species on oxide supports with uniform coordination environments.[1,2] The uniformity of active sites, in particular, is key to defining structure−function relationships that can be inferred by correlating catalytic reactivity to the physical or electronic structure of active sites.[3] Furthermore, uniformity in prepared samples is critical for elucidating how exposure to varying environmental conditions controls the adaptive coordination environment of the metal.[4] In this regard, it is interesting to consider whether the adaptive coordination environment of atomically dispersed species is primarily a result of the active metal moving on the support, or if the support participates in this dynamic behavior as well.

A specific example of oxide support mobility playing a role in controlling the adaptive coordination environment of support metal active sites is the so-called “strong metal-support interaction” (SMSI).[5,6] SMSI refers to a complete or partial encapsulation of metal nanoparticles (NPs) by oxide support overlayers induced by catalyst exposure to H_2 at high temperatures.[7,8,9] This phenomenon has most commonly been reported for Pt group metals deposited on certain reducible oxide supports (TiO_2 and Nb_2O_5), where the driving force for SMSI overlayer formation is

the low free energy of off-stoichiometric oxide layers (*e.g.*, Ti_2O_3) on the metal at low oxygen chemical potentials (reducing conditions).[9,10]

Interestingly, it has been shown that the metal nuclearity, or particle size, can play a critical role in dictating whether SMSI overlayers will form, allowing for control over the types of metal coordination environments exposed.[11] For example, it has been observed that SMSI overlayer growth is more favorable on larger metal nanoparticles and apparently does not occur on sub-nanometer diameter metal clusters.[12] It has further been shown that atomically dispersed metal species (*e.g.* Rh and Pt on TiO_2) do not become encapsulated by SMSI layers under conditions where larger metal nanoparticles do.[13,14] The resistance of very small Pt-group metal species to SMSI overlayer formation likely stems from the lack of a free energy gain through this structural transformation. Recently, there has been a resurgence of interest in SMSI phenomena, where new environments (not high-temperature H_2) have been observed to induce overlayer formation, and overlayer formation has been observed with unexpected metals and supports (*e.g.* Au as metal or BN as support).[14-22] Even with the recent insights into SMSI, the thermodynamic requirements for inducing traditional SMSI formation via high-temperature H_2 treatment dictate that reducible oxides, such as TiO_2 and Nb_2O_5, are uniquely able to participate in such a dynamic reconstruction of supported metals.

Here we provide evidence that the SMSI encapsulation state goes beyond reducible oxide supports by demonstrating the dynamic behavior of Pt catalysts supported with the native oxide layer (AlO_x) that forms on the surface of aluminum nanocrystals (Al NCs). Al NCs are optimal supports for plasmonic photocatalysts, as

the Al localized surface plasmon resonance can be coupled directly to catalytic active sites deposited on the highly porous 2-4 nm thick native oxide layer. Our solid-state nuclear magnetic resonance (NMR) studies revealed different distributions of surface ^{27}Al species in AlNCs compared to the typical γ-alumina indicating that surface oxide layers of AlNCs exhibit unusual support environments, which could lead to unique metal-support interactions that were not previously observed in Pt supported on typical γ-alumina. Using principles of strong electrostatic adsorption, we prepared Pt catalysts with atomically dispersed Pt species and small Pt clusters supported on the native oxide surface of Al NCs. In situ CO probe molecule FTIR, catalytic ethylene hydrogenation, and X-ray absorption spectroscopy measurements suggest that reductive treatment in H_2 at 300 °C results in AlO_x overlayer formation on Pt particles, leaving only uniform atomically dispersed Pt species exposed for adsorption and catalysis. The AlO_x SMSI-state retreats off Pt particles following re-oxidation and can be re-formed upon re-reduction of the catalyst. The unique combination of the plasmonic properties of Al NCs and the ability to dynamically control the nature and characteristics of supported metal active sites on their surfaces offers multiple levers of control over the catalytic functionality of these materials.

A3.2 Magic-angle Spinning Solid-state Nuclear Magnetic Resonance

The solid-state ^{27}Al magic-angle spinning (MAS) NMR experiments were conducted on a high-field 18.8 T Bruker AVANCE-III Ultrashield Plus Spectrometer at room temperature, operating at frequencies of 208.56 MHz for ^{27}Al. Catalysts were treated in a high-temperature Harrick scientific reactor, sealed, and opened in a dry and oxygen-free Ar-filled glovebox, where each powdered sample was packed in a

3.2 mm zirconia NMR MAS rotor with a Kel-F^{TM} cap. The sample-containing rotors were transferred out of the glovebox in a secondary vial filled with dry Ar, and the rotor was quickly inserted into a Bruker 3.2 mm H-X double-resonance probehead for MAS measurements. The ^{27}Al MAS NMR spectra were acquired at ambient temperature spinning at 18 kHz using dry N_2 and at two different center frequencies to capture ^{27}Al signals from surface oxide layers (0–70 ppm) and Knight-shifted ^{27}Al metallic cores (1500–1700 ppm). Single-pulse excitation of 0.42 μs corresponding to π/12 flip angle was used for quantitative ^{27}Al experiments with a recycle delay of 5 s for surface ^{27}Al species and 0.5 s for metallic ^{27}Al. *Dmfit* software was used to simulate and deconvolute the ^{27}Al spectra.[23] The ^{1}H chemical shifts were externally referenced to tetrakis(trimethylsilyl)silane (TKS), and the ^{27}Al chemical shifts were referenced to an aqueous solution of 0.5 M aluminum nitrate.

A3.3 Results and analyses of ^{27}Al NMR of aluminum nanocrystals

γ-Alumina is a dielectric material that has been widely used as catalyst support for anchoring active metal species because of its stability at high temperatures under reactive environments. Theoretical and experimental studies have extensively investigated the presence and nature of metal-binding sites, and metal-support interactions on γ-alumina surfaces.[26-30] In contrast, the recently developed AlNCs with plasmonic and photocatalytic properties have a 2-4 nm thick native oxide layer with a disordered structure on their surface that surrounds the metallic Al core (**Figure A3.1a**). The combination of the plasmonic Al core and native oxide shell enables multifunctional plasmonic and catalytic functionalities. The Al native oxide shell was previously exploited to support metal catalysts species in photocatalytic

applications.[31-34] However, unlike γ-alumina, there is little known about the nature of metal-support interactions in the Al native oxide supported species, which exhibits distinct interaction with acidic and basic probe molecules compared to γ-alumina.[38] In the following section we discuss the interactions and resulting metal structure formed from depositing 1-5 wt% Pt on the native oxide layer of AlNCs.

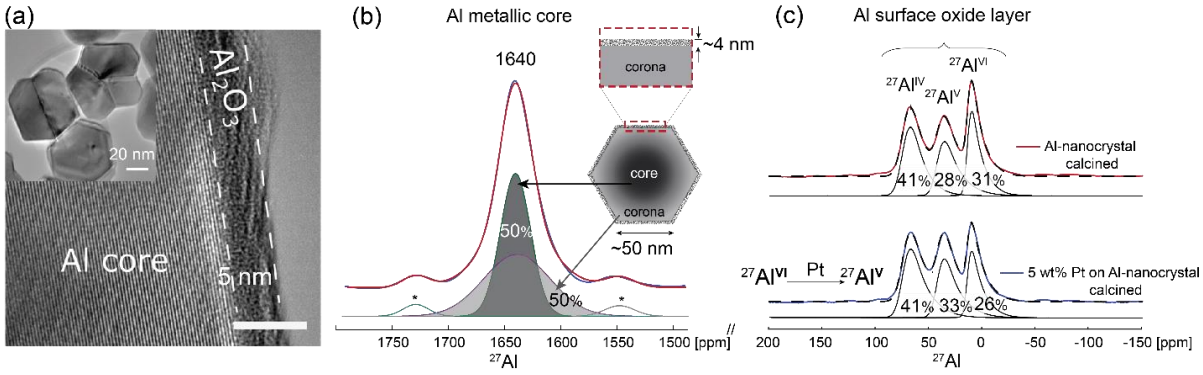

Figure A3.1. Compositions and structures of pristine Al nanocrystals and Pt-loaded Al nanocrystals. (a) High-resolution transmission electron micrographs (TEM) of an aluminum nanocrystal (AlNC) showing the native oxide surrounding the Al metal core. AlNCs are shown in the inset. (b-c) Direct-excitation ^{27}Al MAS NMR spectra of pristine AlNCs (blue) and 5 wt% Pt on AlNCs (red) after calcination at 450 ^{o}C, showing (b) the Knight–shifted ^{27}Al signals from the metallic Al core are centered at 1640 ppm and comprised of 2 types that are attributed to Al atoms in the inner core and outer layer environments and (c) ^{27}Al signals from 4-, 5-, and 6-coordinated ^{27}Al sites of the native oxide layer with peaks centered at ~70, 40, and 10 ppm, respectively. Signals from the thin oxide layers were amplified 40x after integrated intensities of the core and surface layers were normalized. The spectra were acquired at 18.8 T, 18 kHz MAS, and at 298 K. * denotes spinning sidebands.

A.3.4 Local structures of the surface-oxide and core-metallic ^{27}Al species. The local environments of aluminum moieties in the AlNCs were revealed by solid-state

^{27}Al magic-angle spinning (MAS) NMR measurements. The metallic aluminum core and surface aluminum oxide species exhibit significantly different electronic environments, which were manifested by the relative positions, widths, and integrated intensities of ^{27}Al NMR signals in **Figure A3.1b, c**. For example, the Knight-shifted ^{27}Al signal appears at 1640 ppm, which results from hyperfine interactions between the ^{27}Al nuclei in the metallic core and the conduction band electrons of the AlNCs.[35] This signal from the metallic Al core is comprised of two Gaussian components from ^{27}Al atoms of the metallic inner core and outer corona, which are present in approximately equal fractions, as depicted by the dark and light grey regions, respectively, in the schematic AlNC in **Figure A4.1b**. The broader component (70 ppm, full-width-half-maximum, FWHM) from the metallic outer layer indicates a broader distribution of local environments, compared to the metallic inner core (30 ppm FWHM), consistent with a range of ^{27}Al distances within the surface oxide layers to their respective inner metallic cores. Identical overall ^{27}Al NMR signals from the metallic regions of the pristine AlNCs and 5 wt% Pt-supported AlNCs after calcination (at 450 ^{o}C) indicate that the addition of Pt does not affect the ^{27}Al moieties of the metal core. In contrast, the addition of Pt significantly affects the distributions of Al species in the surface oxide layers. This is manifested by the different integrated intensities of partially resolved ^{27}Al MAS NMR signals in **Figure 3.1c** from four-, five-, and six-coordinated Al atoms, respectively, in the surface oxide layers of calcined AlNCs versus 5 wt% Pt/AlNCs. The average ^{27}Al isotropic chemical shift (δ_{iso}), the chemical shift distribution (ΔCS), and the average quadrupolar coupling constant (C_Q) values of different ^{27}Al sites in the oxide layers were obtained using a Czjeck model of the

statistical distributions of parameters that describe the local bonding environments of quadrupolar ^{27}Al nuclei.[36] These parameters obtained from calcined AlNCs and 5 wt% Pt/AlNC are tabulated in **Table A3.1**. The average ^{27}Al isotropic chemical shifts, δ_{iso}, depend on the nearby chemical environments (*e.g.*, Al-O bond lengths and O-Al-O bond angles), ΔCS manifests the distribution of such environments, and C_Q is a measure of local site symmetry. ΔCS and C_Q values progressively decrease from 4- to 5- to 6-coordinated ^{27}Al, as expected for more symmetric ^{27}Al sites with higher coordination. Both the pristine and supported-Pt AlNCs contain 4-, 5-, and 6-coordinated ^{27}Al sites in the surface oxide layer with isotropic ^{27}Al chemical shifts of ca. 75, 41, and 14 ppm, respectively. The relative populations of each type of ^{27}Al site are obtained by deconvoluting the spectra and comparing the integrated signal intensities (**Figure A3.1c**).

Following Pt incorporation, the integrated intensity of the 6-coordinated ^{27}Al signal decreased from 31% to 26%, with a concomitant increase of 5-coordinated ^{27}Al sites from 28% to 33%, while the relative amounts of 4-coordinated ^{27}Al sites remained nearly unchanged (41% Al^{IV}). This suggests the transformation of 6 coordinated into 5-coordinated ^{27}Al species after Pt loading, as the total number of the surface Al sites should remain constant. While obtaining structural information and energetics of Pt-surface oxide interactions for this transformation is non-trivial due to difficulties in modeling the disordered native oxide, we postulate that Pt anchoring via surface oxygen is accompanied by a $^{27}Al^{VI}$-O bond breaking, thus transforming it into a $^{27}Al^{V}$ moiety. Interestingly, the 5% of the total ^{27}Al moieties of the surface oxide converts

from 6- to 5-coordinated ^{27}Al upon addition of Pt corresponds to 1 mole of Pt breaking 1 mole of a $^{27}Al^{VI}$-O bond.

In addition, the quantitative ^{27}Al NMR results revealed a substantially higher number of 5-coordinated sites (~28% of total surface Al sites) in the native oxide layer of AlNCs compared to the typical γ-alumina (< 5 % of total Al, **Figure A3.2**). The 5-coordinated ^{27}Al moieties have been frequently invoked as the anchoring site for Pt dispersion on the γ-alumina surface owing to its strong interaction with metal species.[33,37] Additional comparisons of the integrated intensities of ^{27}Al signals from the metallic core and surface oxide layer (**Figure A3.3**) show that the oxide layers of AlNCs are ca. 5 times less dense compared to the γ-alumina. These differences in local structures and density of the Al native oxide layer compared to the γ-alumina surface and the apparent preferential binding of Pt species to the 6-coordinated ^{27}Al sites on its surface (which results in the formation of 5-coordinated Al species) suggest the presence of a distinct oxide environment surrounding the metallic AlNC core. It also implies that the interaction of Pt species with the native oxide surface could be fundamentally different than that of the typical γ-alumina support, which will be further discussed below.

Table A3.1. ^{27}**Al NMR parameters for the 4-,5-, and 6-coordinated Al sites of the oxide layer**

Sample	^{27}Al coordination	δ_{iso} [ppm]	C_Q [MHz]	ΔCS [ppm]
AlNC	IV	75	8.7	13
	V	42	8.6	11
	VI	14	7.5	6
Pt/AlNC	IV	74	8.7	14
	V	42	8.6	12
	VI	14	7.5	7

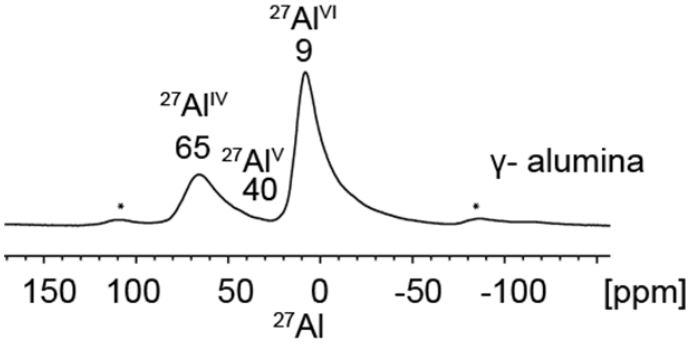

Figure A3.2. ^{27}Al MAS NMR of γ-alumina**.** Solid-state single-pulse ^{27}Al MAS NMR spectra of a typical γ-alumina support. The spectrum is shown to highlight significantly less amount of 5-coordinated ^{27}Al sites in γ-alumina compared to the AlNC (see **Figure 3.1b** for details). Spectrum was acquired at 9.4 T, 12.5 kHz MAS at 298 K. * denotes spinning sidebands.

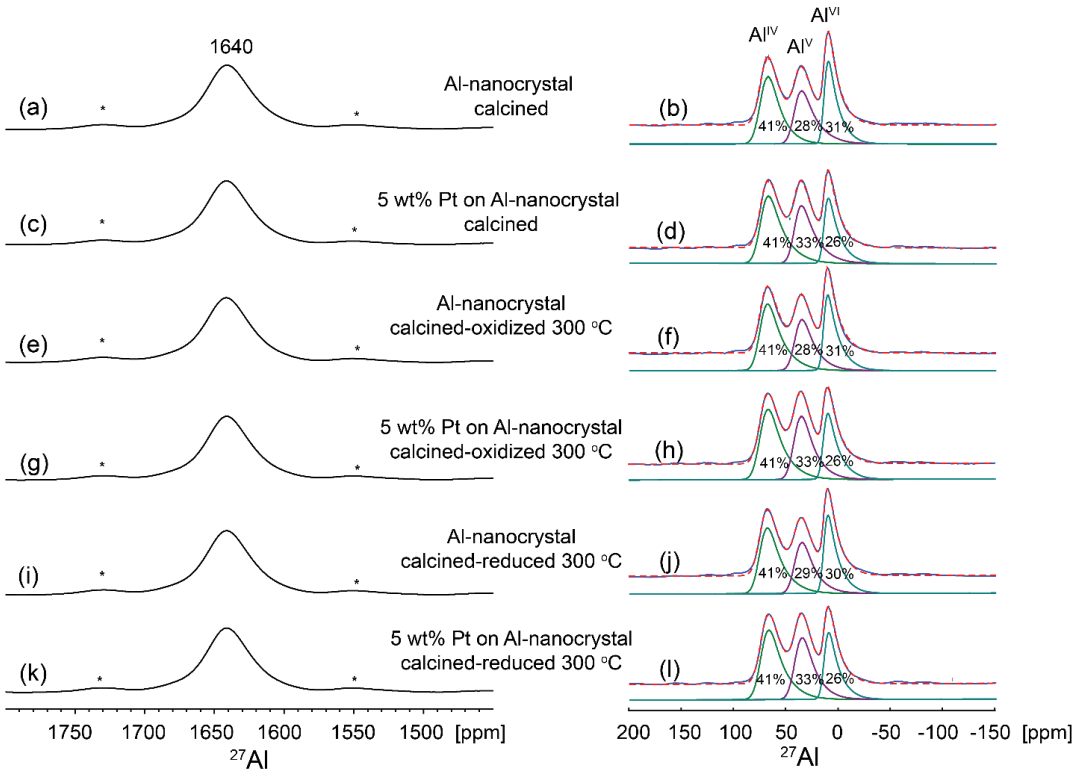

Figure A3.3. ^{27}Al environments of the pristine and Pt-loaded AlNCs following various treatments**.** ^{27}Al MAS NMR spectra of (a) the Al native oxide layer and (b) the metal Al core in the pristine and Pt loaded AlNCs (5 wt% Pt) following catalyst oxidation (300 ^{o}C, O_2) and reduction (300 ^{o}C, H_2). Spectra from the only calcined catalyst without additional pretreatment are also shown. Spectra were acquired at 18.8 T, 18 kHz MAS, and at 298 K. * denotes spinning sidebands. All spectra are nearly identical indicating that the metallic Al core is robust and unaffected by addition of Pt and treatments at different conditions.

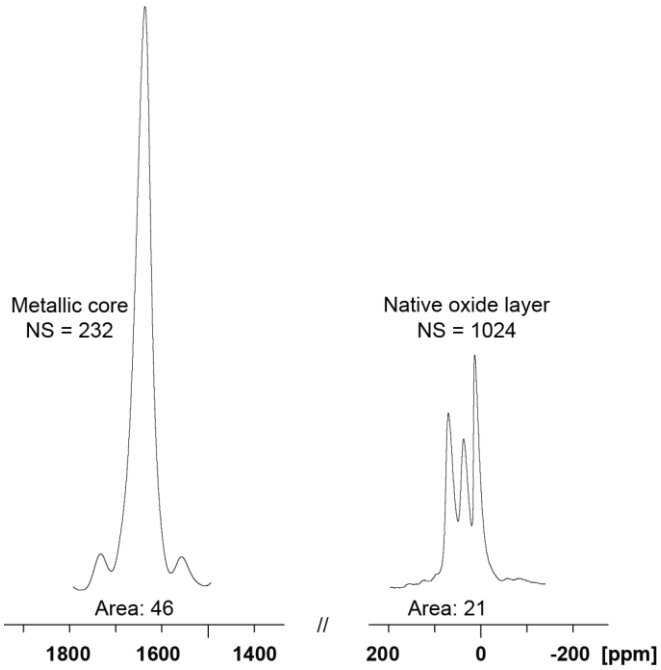

Figure A3.4. Quantitative analyses of ^{27}Al spectra from surface and core Al species. Single-pulse excitation of π/12 flip angle was used for quantitative ^{27}Al experiments with a recycle delay of 5 s for surface ^{27}Al species and 0.5 s for metallic ^{27}Al core. The number of scans (NS) and integrated intensities (Area) of each spectrum are shown above and below the spectra, respectively.

Assuming all ^{27}Al species are NMR visible, for spherical nanocrystals of 50 nm radius with 2 nm oxide layer, surface oxide layer density of AlNCs are ~5 times less dense than regular aluminum oxide, which has a density of ~3.65 g/cm^3. The metallic core density was approximated to be close to the bulk aluminum metal density of 2.7 g/cm^3.

References:

1. Wang, A., Li, J. & Zhang, T. Heterogeneous single-atom catalysis. *Nat. Rev. Chem.* **2**, 65–81 (2018).
2. Ji, S. *et al.* Chemical Synthesis of Single Atomic Site Catalysts. *Chem. Rev.* (2020)
3. DeRita, L. *et al.* Structural evolution of atomically dispersed Pt catalysts dictates reactivity. *Nat. Mater.* **18**, 746–751 (2019).
4. Resasco, J. *et al.* Uniformity Is Key in Defining Structure-Function Relationships for Atomically Dispersed Metal Catalysts: The Case of Pt/CeO_2. *J. Am. Chem. Soc.* **142**, 169–184 (2020).

5. Wang, Y., Widmann, D. & Behm, R. J. Influence of TiO2 Bulk Defects on CO Adsorption and CO Oxidation on Au/TiO_2: Electronic Metal–Support Interactions (EMSIs) in Supported Au Catalysts. *ACS Catal.* **7**, 2339–2345 (2017).

6. Bruix, A. *et al.* A New Type of Strong Metal–Support Interaction and the Production of H2 through the Transformation of Water on Pt/CeO2(111) and Pt/CeO_x/TiO_2(110) Catalysts. *J. Am. Chem. Soc.* **134**, 8968–8974 (2012).

7. Tauster, S. J., Fung, S. C. & Garten, R. L. Strong metal-support interactions. Group 8 noble metals supported on titanium dioxide. *J. Am. Chem. Soc.* **100**, 170–175 (1978).

8. Tauster, S. J., Fung, S. C., Baker, R. T. K. & Horsley, J. A. Strong Interactions in Supported-Metal Catalysts. *Science.* **211**, 1121 LP – 1125 (1981).

9. Dulub, O., Hebenstreit, W. & Diebold, U. Imaging Cluster Surfaces with Atomic Resolution: The Strong Metal-Support Interaction State of Pt Supported on TiO_2. *Phys. Rev. Lett.* **84**, 3646–3649 (2000).

10. Tauster, S. J. Strong metal-support interactions. *Acc. Chem. Res.* **20**, 389–394 (1987).

11. Zhang, S. *et al.* Dynamical Observation and Detailed Description of Catalysts under Strong Metal–Support Interaction. *Nano Lett.* **16**, 4528–4534 (2016).

12. Matsubu, J. C. *et al.* Adsorbate-mediated strong metal-support interactions in oxide-supported Rh catalysts. *Nat. Chem.* **9**, 120–127 (2017).

13. Sakellson, S., McMillan, M. & Haller, G. L. EXAFS evidence for direct metal-metal bonding in reduced rhodium/titania catalysts. *J. Phys. Chem.* **90**, 1733–1736 (1986).

14. Zhang, S. *et al.* Dynamical Observation and Detailed Description of Catalysts under Strong Metal–Support Interaction. *Nano Lett.* **16**, 4528–4534 (2016).

15. Wu, Z., Li, Y. & Huang, W. Size-Dependent Pt-TiO_2 Strong Metal–Support Interaction. *J. Phys. Chem. Lett.* **11**, 4603–4607 (2020).

16. Han, B. *et al.* Strong Metal–Support Interactions between Pt Single Atoms and TiO2. *Angew. Chemie Int. Ed.* **59**, 11824–11829 (2020).

17. Matsubu, J. C., Yang, V. N. & Christopher, P. Isolated metal active site concentration and stability control catalytic CO_2 reduction selectivity. *J. Am. Chem. Soc.* **137**, 3076–3084 (2015).

18. Parastaev, A. *et al.* Boosting CO_2 hydrogenation via size-dependent metal–support interactions in cobalt/ceria-based catalysts. *Nat. Catal.* **3**, 526–533 (2020).

19. Zhang, J. *et al.* Wet-Chemistry Strong Metal–Support Interactions in Titania-Supported Au Catalysts. *J. Am. Chem. Soc.* **141**, 2975–2983 (2019).

20. Chen, M. S. & Goodman, D. W. Interaction of Au with titania: the role of reduced Ti. *Top. Catal.* **44**, 41–47 (2007).

21. McClain, M. J. *et al.* Aluminum Nanocrystals. *Nano Lett.* **15**, 2751–2755 (2015).

22. Hoffman, A. S.; et al., In situ observation of phase changes of a silica-supported cobalt catalyst *J. Synchrotron Radiat.* **25**, 1673−1682 (2018).

23. Digne, M., Sautet, P., Raybaud, P., Euzen, P. & Toulhoat, H. Use of DFT to achieve a rational understanding of acid–basic properties of γ-alumina surfaces. *J. Catal.* **226**, 54–68 (2004).

26. Lee, J., Jang, E. J., Oh, D. G., Szanyi, J. & Kwak, J. H. Morphology and size of Pt on Al2O3: The role of specific metal-support interactions between Pt and Al2O3. *J. Catal.* **385**, 204–212 (2020).

27. Swearer, D. F. *et al.* Transition-metal decorated aluminum nanocrystals. *ACS Nano* **11**, 10281–10288 (2017).

28. Robatjazi, H. *et al.* Plasmon-induced selective carbon dioxide conversion on Earth-abundant aluminum-cuprous oxide antenna-reactor nanoparticles. *Nat. Commun.* **8**, 27 (2017).

29. Swearer, D. F. *et al.* Plasmonic Photocatalysis of Nitrous Oxide into N2 and O2 Using Aluminum–Iridium Antenna–Reactor Nanoparticles. *ACS Nano* **13**, 8076–8086 (2019).

30. Robatjazi, H. *et al.* Plasmon-driven carbon-fluorine (C(sp3)–F) bond activation with mechanistic insights into hot-carrier-mediated pathways. *Nat. Catal.* **3**, 564–573 (2020).

31. Tang, N. *et al.* Coordinatively Unsaturated Al3+ Sites Anchored Subnanometric Ruthenium Catalyst for Hydrogenation of Aromatics. *ACS Catal.* **7**, 5987–5991 (2017).

32. Robatjazi, H. *et al.* Metal-organic frameworks tailor the properties of aluminum nanocrystals. *Sci. Adv.* **5**, 5340 (2019).

33. Thang, H. V., Pacchioni, G., DeRita, L. & Christopher, P. Nature of stable single-atom Pt catalysts dispersed on anatase TiO2. *J. Catal.* **367**, 104–114 (2018).

34. Cao, S. *et al.* High-loading single Pt atom sites [Pt-O$(OH)_x$] catalyze the CO PROX reaction with high activity and selectivity at mild conditions. *Sci. Adv.* **6**, 3809 (2020).

35. Zholobenko, V. L., Lei, G.-D., Carvill, B. T., Lerner, B. A. & Sachtler, W. M. H. Identification of isolated Pt atoms in H-mordenite. *J. Chem. Soc. Faraday Trans.* **90**, 233–238 (1994).

36. Qiao, B. *et al.* Single-atom catalysis of CO oxidation using Pt_1/FeO_x. *Nat. Chem.* **3**, 634–641 (2011).